School of Mechanical, Materials, Manufacturing Engineering and Management

2001

Properties of HVOF sprayed TiC and TiB_2-based cermet coatings

by

Mark Jones, BEng (Hons)

Thesis submitted to the University of Nottingham for the degree of Doctor of Philosophy, November 2001

Abstract

This work reports research concerning the properties of cermet coatings deposited by high velocity oxy-fuel spraying, which are designed to exhibit resistance to abrasive wear and high-temperature oxidation. Cermet powders have been produced by self-propagating high-temperature synthesis (SHS) reaction of elemental powder mixtures of Fe, Cr, Ti and C or B, to produce a cermet, containing an Fe(Cr) binder phase and a hard ceramic phase, TiC or TiB_2. The Ti and C content in the powder mixtures were varied in order to evaluate the effect of the C:Ti ratio of TiC on the overall integrity of three different feedstock powders and coatings produced. Four cermet coatings were produced from these SHS powders, one TiB_2-based and three TiC-based.

Abrasive wear resistance of the coatings was evaluated using a dry sand rubber wheel (DSRW) abrasive wear testing machine, where the coatings were subjected to abrasion by both alumina and silica abrasives. The TiB_2-based coating exhibited superior wear resistance when subjected to both alumina and silica. Of the TiC-based coatings, the equimolar coating exhibited superior resistance when subjected to alumina, and the excess Ti coating exhibited superior wear resistance when subjected to abrasion with silica. When compared with coatings produced from commercially available powders, namely, sintered and crushed WC-Co and blended NiCr-Cr_3C_2, the coatings produced from SHS powders exhibited comparable, and in some cases, better abrasive wear properties.

Preliminary oxidation tests showed that all four coatings performed well at 500°C (the temperature at which WC-Co begins to degrade rapidly). They exhibited some oxidation at 700°C, and at 900°C, exhibited severe oxidation.

Contents

Nomenclature

APD	Agglomerated and Plasma Densified
APS	Atmospheric Plasma Spraying
at%	Atomic Percent
b.c.c.	Body Centred Cubic
BSE	Back Scattered Electron
Cp_l	Specific Heat Capacity of Liquid (J / K / mole)
Cp_s	Specific Heat Capacity of Solid (J / K / mole)
D-Gun	Detonation Gun
DSRW	Dry Sand Rubber Wheel
EDX	Energy Dispersive X-ray
f.c.c.	Face Centred Cubic
FC	Fused and Crushed Powder
ΔG	Change in Gibb's Free Energy of Formation (kJ mol^{-1})
ΔH	Change in Enthalpy of Formation (kJ mol^{-1})
h.c.p.	Hexagonal Close Packed
ΔH_m	Enthalpy of Fusion (kJ mol^{-1})
HVAF	High Velocity Air Fuel
HVIF	Hyper Velocity Impact Fusion
HVOF	High Velocity Oxy-Fuel
LPPD	Low Pressure Plasma Deposition
LPPS	Low Pressure Plasma Spraying
LSE	Laser Surfacing Engineering
PES	Pulsed Electrode Surfacing
PSS	Plasma Spray Synthesis
SE	Secondary Electron
SEM	Scanning Electron Microscopy
SHS	Self-propagating High-temperature Synthesis
T_{ad}	Adiabatic Temperature (°C)
TEM	Transmission Electron Microscope

T_m	Melting Temperature (°C)
UPS	Underwater Plasma Spraying
VPS	Vacuum Plasma Spraying
wt%	Weight Percent
XRD	X-ray Diffraction

Greek Symbols

α-Fe	Ferrite
γ-Fe	Austenite
λ	Wavelength
θ	Diffraction Angle (°)

1 Introduction

Thermal spraying is a widely used technology in the surface coatings industry. It is a process that involves the deposition of molten droplets of powder onto a substrate, which forms a coating. High velocity oxy-fuel (HVOF) thermal spraying is one of the more recent developments in thermal spraying techniques, and the process utilises very high powder velocities with relatively low temperatures, when compared with air or vacuum plasma spraying. As a result, a dense well-bonded coating is produced.

HVOF-sprayed cermet coatings can be produced from a variety of powder forms, such as, sintered and crushed, agglomerated and sintered, or mechanically blended powders. A novel method of cermet powder production is proposed and is called self-propagating high-temperature synthesis (SHS). This process utilizes the exothermic heats of reaction available when certain reactants are mixed and ignited, namely Ti and C, or Ti and B, and produces a highly exothermic reaction which is self-sustaining and propagates through the entire reactant mixture. This process is therefore an economical means, in terms of heat required, for cermet production. Due to the high temperatures that are achieved during the reaction (1200-6000K), many volatile impurities are removed which can improve the hard phase / matrix bonding.

Applications of HVOF-sprayed coatings include protection from wear, high temperatures and chemical attack. Cermet coatings are also produced using this

spray system, namely, WC-Co and NiCr-Cr_3C_2. WC-Co coatings exhibit excellent resistance to wear but are limited to a maximum service temperature of 500°C as they oxidize rapidly (Laul,2000; Somaraju,2000]. NiCr-Cr_3C_2 coatings have excellent oxidation resistance up to 900°C [Wirojanupatump,2001; Valente,2001; Zimmermann,1996] but the Cr_3C_2 phase in the cermet is not very hard (1400 kgf mm^2 c.f. 3200 kgf mm^2 for TiC) and can dissociate into Cr_7C_3 and $Cr_{23}C_6$ during spraying. There is therefore a niche for the development of a material that can operate at temperatures of between 500 and 900°C with comparative, if not better, wear properties than NiCr-Cr_3C_2 and WC-Co coatings.

Two cermet materials proposed for this application are FeCr-TiC and FeCr-TiB_2. Both coatings contain a matrix with a high chromium level to provide oxidation resistance whilst the ceramic phases provide good oxidation resistance and also exhibit high hardness' (TiC = 3200 kgf mm^2 and TiB_2 = 3650 kgf mm^2) which will provide the wear resistance. One TiB_2-based coating and three TiC-based coatings, with variable TiC stoichiometry, have been studied in this work.

The aim of this work is to produce TiC and TiB_2-based cermet coatings, from SHS-produced powders, and to assess the microstructure, room temperature abrasive wear resistance and high-temperature capabilities of the coatings.

2 Self-propagating High-temperature Synthesis (SHS)

2.1 Introduction

Self-propagating High-temperature Synthesis (SHS), also known as combustion synthesis, self-propagating synthesis and self-propagating exothermic reaction [Subrahmanyam,1992], utilises the exothermic heats of reaction available when certain reactants are mixed and ignited, e.g. elemental titanium and carbon, to produce a highly exothermic reaction which is self-sustaining and propagates through the entire reactant mixture (Figure 2.1). The reaction is initiated at the ignition temperature T_{ig}, and propagates to produce a maximum or combustion temperature T_c, in the range of 1200 – 6000 K [Munir,1989]. T_c is commonly referred to as the adiabatic temperature T_{ad}, which assumes adiabatic conditions, and will be referred to in this manner in this work. The adiabatic temperature is therefore an upper limit and it is not usually achieved in practice due to heat loss during the reaction [Moore,1991]. Figure 2.2 shows a schematic representation of a typical time-temperature plot for an SHS reaction [Moore,1995].

Another form of combustion synthesis is known as the thermal-explosion mode and is also known as bulk reaction, reactive sintering and self-ignition mode [Varma,1992]. This type of reaction differs from self-propagating mode in that the whole sample is heated uniformly until the ignition point is reached and a spontaneous reaction occurs. Generally, the thermal-explosion mode is used in the production of intermetallic compounds with relatively low exothermic properties.

SHS reactions have been used to produce many compounds, intermetallics and composites and can be classified into three categories: (1) elemental systems, where the reactants are in elemental form; (2) compound reaction systems, where at least one of the reactants is a compound; (3) thermite systems, where the reaction involves a reduction stage which is usually the metallothermic reduction of an oxide.

Over the past 10-15 years, more than 500 compounds have been produced via the SHS method [Munir,1989; Yi,1990] for numerous applications. Details of some of the compounds produced, and their applications are shown in shown in Tables 2.1 and 2.2 respectively.

2.1.1 Advantages

The SHS process provides many advantages over conventional methods of producing advanced materials. These advantages include:

Simple and inexpensive equipment

Only simple and inexpensive equipment is required in order to carry out SHS reactions. Scaling up of the reaction is not a problem as it has been found that a more complete reaction, thus higher product yield [Subrahmanyam,1992], is achieved when using larger quantities due to the smaller heat losses involved. This is because the product is held at a higher temperature for longer and thus the reaction is more complete.

Production efficiency

The energy required to initiate an SHS reaction is minimal as only a small region of the sample needs to be heated for the reaction to proceed. As mentioned previously, once the reaction is initiated it becomes self-sustaining thus there is no need for further heating. Due to the high combustion wave velocities experienced, from 1 to 250 mm/s [Dunmead,1989], a reaction time of a few minutes, if not seconds is not uncommon. The process, therefore, offers high productivity.

Pure products

The high combustion temperatures achieved during the reaction (1200-6000K) helps to remove any volatile impurities. Matirosyan et al. [1977] studied the impurity levels in the reactants and products using different adiabatic temperatures. They found that product purity increased with increasing adiabatic temperatures, if volatile impurities were present. These high temperatures may also improve hard phase/matrix bonding when producing cermets, as any volatile impurities at the grain/phase boundaries are removed. This in turn, can improve the wear resistance of the material, as it can, for example, prevent carbide pullout from the matrix during wear due to the improved carbide/matrix bonding (Section 5).

Metastable products

Non-equilibrium structures can be produced due to the high thermal gradients and fast cooling rates encountered. The non-equilibrium nature of the process can be used to produce non-stoichiometric, intermediate or metastable phases [Munir,1988].

Formation of porous products

A porous product is produced after reaction. This porosity, and other structural imperfections such as lamination and cracking are due to three main causes. These are, the rapid evolution of impurity gases or volatile reactants and/or products during the reaction; the volume change that occurs between the reactants and product; and the porosity present in the green reactant mixture [Moore,1995]. These structural defects can be an advantage during the crushing stage as the friable nature of the material produced aids the size reduction of the powders. For other applications, where the product density must be low, these defects are a big drawback. The poor density can be partially overcome by the application of an external pressure during reaction [Grebe,1992; Kecskes,1990].

2.1.2 Disadvantages

Process control

It is very difficult to control the reaction and the final microstructure and composition. This is due to the extremely fast reaction rate and high thermal gradients, which produce non-equilibrium conditions. A degree of control can be

achieved however, by the addition of diluents, or powders with large particle sizes (Section 2.4).

Production of porous products

Whilst this can be seen as an advantage during the crushing stage, it can also have adverse effects if the cermet produced were to be used for thermal spraying of coatings.

2.2 Thermodynamics

As mentioned in Section 2.1, the adiabatic temperature is the maximum combustion temperature that is achieved under adiabatic conditions, i.e. no effects from outside influences. A typical combustion reaction can be represented by Equation 2.1, where reactants A and B combine via an exothermic reaction to form product AB.

$$A_{(S)} + B_{(S)} = AB_{(S)} \text{ ----Equation 2.1}$$

The adiabatic temperature of this reaction, or any other, can be calculated from the thermodynamic functions of heat capacities and enthalpies of formation and transformation, the latter where applicable. According to Munir [1988], calculations of the adiabatic temperature depend on the following criteria:

$$\text{(a) If } \Delta H^\circ_{f298} < \int_{298}^{Tm} Cp_s dT$$

then $T_{ad} < T_m$ and can be calculated from,

$$\Delta H^\circ_{f298} = \int_{298}^{Tad} Cp_s dT \text{ ----Equation 2.2}$$

Where, ΔH°_{f298} is the enthalpy of formation of the compound AB at 298 K, Cp is the heat capacity of AB in the solid state, and T_m is the melting temperature on the absolute scale. If,

$$(b) \qquad \int_{298}^{Tm} Cp_s dT + \Delta H_m > \Delta H^\circ_{f298} > \int_{298}^{Tm} Cp_s dT$$

then, partial melting occurs and T_{ad} is the melting point of the product and the relationship is represented by

$$\Delta H^\circ_{f298} = \int_{298}^{Tm} Cp_s dT + v\Delta H_m \text{ ----Equation 2.3}$$

where ΔH_m is the enthalpy of fusion of solid AB and v is the fraction of the product that is in the molten state. In order for complete melting to occur,

$$(c)\ \Delta H^\circ_{f298} > \int_{298}^{Tad} Cp_s dT + \Delta H_m$$

and the appropriate relationship can be calculated from

$$\Delta H°_{f298} = \int_{298}^{Tm} Cp_s dT + \Delta H_m + \int_{298}^{Tad} Cp_l dT \text{ ----Equation 2.4}$$

where Cp_l is the heat capacity of liquid AB.

Adiabatic temperatures can also be used in a semi-quantitative manner to calculate whether or not a compound can be produced in a self-propagating manner. From experimental evidence, Munir [1988] suggests that an adiabatic temperature of 1800 K must be exceeded in order for the reaction to become self-sustaining.

2.3 Reaction mechanisms

2.3.1 Solid-Solid reactions

In such systems, all of the components are in the solid state and only a diffusion mechanism is possible. Once a product layer has formed between the reactants, the reaction can only proceed by the diffusion of the reactant atoms through the product layer which leads to slow reaction kinetics. A typical material which is formed through solid-solid reaction is TaC [Subrahmanyam,1992].

2.3.2 Solid-Liquid reactions

Solid-liquid reactions are the most common mechanism in combustion synthesis. Several carbides and borides are formed in this manner and it is the metallic element that is in the molten condition at T_{ad}, usually between 3000-4000 K. The mechanism of the SHS of TiC is a typical solid-liquid reaction and it has been

established that melting of titanium precedes the combustion reaction. The mechanism of the formation of TiC is discussed in more depth in Section 2.5.1.

2.4 Reaction parameters

The following section discusses the reaction parameters that can affect SHS reactions. These parameters include the effect of reactant particle size, stoichiometry (including the use of diluents or inert reactants), green density, thermal conductivity and ignition temperature.

2.4.1 Reactant particle size

The effect of particle size has an effect on the adiabatic temperature of a system. Subrahmanyan et al. [1992] have suggested that the adiabatic temperature of carbides and borides decreases with an increase in metal particle size. They explain this effect in terms of the high thermal mass of larger particles. However, Brown [2000] suggest that the decrease in adiabatic temperature with increasing particle size is due infact to a significant reduction in the reaction kinetics with decreasing surface area for reaction, and thus a decrease in the measured combustion temperature. In the synthesis of TiC, the titanium is said to melt prior to combustion (Section 2.5). If the titanium is large, the melting is confined only to a limited thickness on the particle surface, and hence a reduction in the adiabatic temperature results. This can also have an effect on the degree of conversion of the reactants [Subrahmanyan,1992]. Table 2.3 shows the

dependence of adiabatic temperature on the particle size of titanium [Azatyan,1977].

2.4.2 Diluent

The velocity of the combustion wave and the adiabatic temperature can be controlled to a certain degree by the addition of a diluent. Munir et al. [1989] have shown the effects of the addition of pre-reacted TiC as a diluent in the SHS formation of TiC. The results illustrated that the adiabatic temperature decreases with an increase in pre-reacted TiC content. Figure 2.3 shows the effect of addition of a diluent (TiC) on the adiabatic temperature of the formation of TiC. Azatyan et al. [1977] conducted experiments which also showed the same trend as Munir et al. [1989]. This effect can be explained in terms of the exothermic reaction which occurs when titanium and carbon combine. If an "inert" substance, such as pre-reacted TiC, is added, this will increase the heat capacity of the product with no commensurate increase in exothermic energy available. Hence the speed and temperature of the combustion wave will be reduced. If too much is added, the exothermicity of the reaction may be so greatly reduced that the reaction will not self-propagate.

In the SHS-production of a cermet, where a ceramic hard phase and metallic binder phase are synthesized, it is the binder that acts as the diluent. This will be further discussed in Section 2.7.

2.4.3 Green density

Powders used for SHS reactions are usually pressed into a green compact. The thermal conductivity and heat capacity of the green compact changes with the density of the compact [Subrahmanyam,1992]. At low densities, the heat transfer in the combustion zone may not be sufficient as to allow the reaction to self-propagate. In contrast, at higher densities, the thermal conductivity may be too high to allow a build-up of heat at a discrete region of the compact, which is required for the initiation of the reaction, and instead the heat will be dissipated throughout the compact.

2.4.4 Sample diameter

According to Munir et al. [1989], the combustion temperature increases with an increase in the compact diameter and remains constant after reaching a threshold value, which is dependent upon the combustion system. This is explained in terms of heat loss, where a small diameter sample will exhibit more radial heat loss during the reaction. This effect therefore poses no problems when scaling up from laboratory scale to industrial scale (Section 2.1.1).

2.5 Synthesis of titanium carbide

The Ti-C system has been extensively studied [Munir,1988; Munir1989; Azatyan,1977] and is commonly considered to be a model system for combustion synthesis processes [Dunmead,1989]. The titanium-carbon SHS reaction is highly exothermic, and Holt has stated an adiabatic temperature of 2930°C. TiC

exists over a wide carbon-titanium ratio, $TiC_{0.47}$ to $TiC_{0.97}$, (Section 4.2.1) and the effects of differing from $TiC_{0.97}$ on the adiabatic temperature have been shown to decrease with a deviation from this ratio [Advani,1992; Moore,1995]. This reduction in adiabatic temperature was rationalized in terms of the smaller amount of reacting powders present.

2.5.1 Mechanisms of formation

There have been numerous investigations on the mechanism of formation of TiC [Dunmead,1989;Lee,1995;Fan,1996;Vadchenko,1976;Rogachev,1996], however, there are significant differences in these proposals. The proposals are discussed below.

Vadchenko et al. [1976] performed a study of the mechanism of formation of TiC using carbon-coated titanium wires. They concluded that the combustion process was preceeded by melting of titanium and that the carbide formed by precipitation from the molten phase. They also stated that no reaction occurred at a temperature lower than the melting point of titanium and when the titanium did melt, it flowed outwardly, filling the pores between the particles of the carbon coating. This theory is complemented by work performed by Rogachev et al. [1996], where a mixture of titanium powder and carbon black was placed into a wedge-shaped notch in a copper block and ignited. The combustion reaction was then quenched due to heat transfer to the copper block. They then studied the resultant microstructure and observed that the onset of the reaction coincided with

the melting of the titanium, which subsequently spread over the carbon forming rounded titanium carbide particles.

Dunmead et al. [1989] have studied the mechanism of formation of TiC using activation energies for the combustion reaction between Ti and C and conclude that two different combustion regimes were found. They propose that at high combustion temperatures (>2400°C) TiC formation occurs via the dissolution of C into liquid Ti with subsequent precipitation from the melt, while at low temperatures (<2400°C) the TiC formation occurs via a carburization process where a TiC layer forms around the carbon particles, and TiC formation continues via diffusion of C through the TiC layer.

Fan et al.[1996] suggest a 'TiC shell' mechanism where a thin TiC layer is formed around the solid titanium particles, by solid-state diffusion of carbon. TiC particles then form by diffusion of the C through the TiC layer. They conclude that the mechanism is dependent upon the titanium particle size. If the titanium is coarse, the combustion temperature will be lower and it will be harder to melt the titanium and the TiC shell mechanism will be predominant. If, on the other hand, the titanium is smaller, the combustion temperature will be higher, allowing the titanium to melt and the reaction to proceed by other mechanisms.

Lee et al. [1995] studied the mechanism of formation of TiC when using carbon black (~0.01μm). They reported that ignition occurs due to surface reaction leading to formation of TiC layers. The reaction proceeds when titanium melts and the initial TiC layer dissolves into the liquid titanium. The liquid titanium

then infiltrates into the pores of the carbon black, forming TiC, and carbon diffuses through the TiC layer to react with the liquid titanium. Reaction occurs both in the bulk titanium phase and in the carbon black matrix.

2.6 Synthesis of titanium diboride

The synthesis of titanium diboride has been widely researched [Holt,1985; Roy,1993; Kogan,1996; Bhaumik,2000] and is thought to be the first SHS experiment to be conducted by Merzhanov et al. in the 1970's [Subrahmanyam,1992]. The reaction is highly exothermic and Cutler [1991] reports an adiabatic temperature of 3225°C.

2.6.1 Mechanism of formation

There have been very few attempts to study the mechanism of formation of titanium diboride. It has been reported that the mechanism of the formation of titanium diboride is of the solid-liquid type where melting of titanium occurs [Subrahmanyam,1992].

2.7 Synthesis of iron-titanium carbide cermets

There have been limited studies on the Fe-TiC system produced by SHS. Saidi et al. [1997] studied the effect of changing the C/Ti ratio when producing Fe-TiC cermets by the thermal explosion method. They found that when producing a cermet with equimolar quantities of Ti and C, XRD analysis showed peaks for Fe and TiC. When substoichiometric TiC (i.e. containing less carbon) was produced,

intermetallics such as FeTi and Fe_2Ti were also observed. Fan et al. [1997] also showed that when a Fe-TiC cermet was produced, the phases present were Fe and TiC, although in a previous study by the author, a small amount of FeTi was also present. Experiments produced by Capaldi et al. [1996, 1997] showed that only Fe and TiC phases were present

2.7.1 Mechanism of formation

The mechanisms of formation of Fe-TiC production via SHS have been studied by two authors, namely Saidi [1994] and Fan [1997]. Saidi et al. [1994] believe that the mechanism involves the formation of a $FeTi_2$ phase by solid-state reaction between the titanium and iron powders. $FeTi_2$ is a eutectic compound with a melting point of 1085°C and Saidi found that this temperature was close to the ignition temperature of the reaction. The reaction was then said to proceed with the melting of the $FeTi_2$ phase followed by solution of C into the molten droplets and subsequent precipitation of TiC particles from the melt. A contrasting explanation was given by Fan et al. [1997] who believe that the mechanism suggested by Saidi et al. to be inaccurate. They believe that it is more likely for C to diffuse into Fe than for Fe and Ti to react, as solid-state diffusion of C into Fe is faster than Ti into Fe, making $FeTi_2$ formation improbable. They propose a mechanism which begins with the interstitial diffusion of C into the Ti. Carbon is also said to diffuse into the Fe which subsequently lowers the melting point of the Fe-C alloy. Melting of the Fe then accelerates the solution of Ti into the molten

iron droplets. When the concentrations of C and Ti are saturated in the iron droplets, TiC particles precipitate out.

2.8 Synthesis of iron-titanium diboride

There has been very limited work performed on iron-titanium diboride cermet production by SHS [Maksimov,1984; Maksimov,1985]. Maksimov et al. [1984, 1985] have studied the synthesis of the Fe-Ti-B system and found that the main products formed were TiB_2 and Fe, although small amounts of FeB, TiB and Fe_2B were occasionally found.

2.8.1 Mechanism of formation

Maksimov et al. [1984, 1985] also formulated a basic mechanism of formation for the production of Fe-TiB_2. They suggested that the initial reaction begins with the formation of two eutectics by solid-phase diffusion, B in Fe (1200°C), followed by diffusion of Ti in Fe (1085°C). This was followed by the subsequent formation of a TiB_2-Fe eutectic (1340°C) from which TiB_2 grains precipitated out of the melt.

2.9 Powder production for thermal spraying

The following section compares the properties of coatings sprayed from cermet powders, produced from various manufacturing techniques. A variety of cermet powders are used for thermal spraying and the production route of these powders very much effects the properties of the coatings.

2.9.1 Cermet powder production routes

There are numerous commercial production methods for thermal spray powders, namely, mechanical blending, sintered (or fused) and crushed, cladding, agglomerated and plasma densified.

Mechanical blending involves the mixing of the powders desired for cermet coating production, e.g. NiCr-Cr_3C_2. The metallic powders are usually produced by atomization. Mechanical blending has been found to produce poor coatings as there is no intimate mixing of the hard phase and matrix phase before spraying. This can result in the powders travelling independently of one another producing poor adhesion between matrix and hard phase. Poor coating microstructure, hardness, deposition efficiency and wear abrasion can result [Wirojanupatump,1999].

Sintering and crushing has been employed in the production of WC-Co cermets and involves intimate contact between hard phase and liquid matrix during the sintering process. The powders produced have a blocky and irregular morphology, which results in lower flowability. A subsequent spherodisation technique can be employed to improve the powder morphology. Cladding involves coating a core of one material with a porous or dense layer of another. Powders produced from this method are also known as composite powders.

Agglomeration (or spray drying) is a very versatile production route as it permits the agglomeration of any kinds of materials together. This process involves introducing a slurry of finely dispersed materials, in an organic binder and water,

into a centrifugal atomizer where the atomized slurry is dried and the solid particles collected. Agglomerated powders are often highly porous and a subsequent densifying process is required. Plasma densification is often used and as the name suggests, plasma is implemented to produce a denser powder.

2.9.2 Comparison of coating properties

The following section compares the coating microstructures, spray efficiencies and wear properties of sprayed coatings produced from powders from different processing routes.

Smith et al. [1995] studied the properties of various coatings produced from SHS, agglomerated and plasma densified (APD), and fused and crushed powders (FC). They concluded that when comparing NiCr-TiC coatings sprayed from SHS and APD powders, the SHS-produced coating showed a more uniform microstructure with well-bonded and distributed carbides, while the APD-produced coating exhibited coarser, more poorly bonded and irregularly distributed carbides, due to the variability in the agglomeration process. When comparing $MoSi_2$ coatings, they found that the SHS coating exhibited a more uniform distribution of structural features than the fused and crushed powders. They also found the SHS coatings, in most cases, to have lower material losses during sliding wear, when compared with other coatings of similar compositions. They attributed this to a more homogeneous distribution of hard phases, a bi-modal distribution of the TiC phase, and improved carbide/matrix bonding due to the SHS reactions.

Bartuli et al. [1997] also found that NiCr-TiC coatings produced from SHS powders had superior sliding wear properties to coatings produced from plasma densified powders. This has been attributed to the strong carbide/matrix bonding which reduces TiC pullout during wear, and the rounded morphology of the TiC in the SHS coating, which is said to reduce damage to the surface.

Mohanty and Smith [1995] studied the properties of coatings sprayed from SHS-produced powders and mechanically mixed powders. They found that the coating produced from the mechanically mixed powders resulted in segregation during spraying leading to lower deposition efficiencies and coating uniformity. The SHS TiC/Ti coating exhibited a higher hardness and improved sliding wear properties by a factor of three over the mechanically blended TiC/Ti coating. This was attributed to the good carbide/matrix bonding which exists in SHS-produced coatings.

Smith and Mutasim [1991] studied the effects of spraying NiCr-TiC coatings from mechanically blended and agglomerated and plasma densified powders. They stated that spraying of mechanically blended powders resulted in a non-homogeneous coating with much segregation, while the agglomerated and plasma densified coating exhibited a much higher degree of homogeneity.

Wirojanupatump [1999] studied the effects of spraying NiCr-Cr_3C_2 mechanically blended, sintered and crushed, and composite cermet powders. In this study, the

author found that the mechanically mixed powder coating exhibited a poor coating microstructure with the lowest deposition efficiency, hardness and wear performance. The composite coating was the best coating overall in terms of microstructure, deposition efficiency and wear performance.

Borides	CrB, HfB_2, NbB, NbB_2, TaB_2, TiB_2, MoB, MoB_2, MoB_4, Mo_2B, WB, WB_4, VB, V_3B_2, VB_2
Carbides	TiC, ZrC, HfC, NbC, Cr_3C_2, B_4C, WC, TaC, Ta_2C, VC, Al_4C, Mo_2C
Nitrides	Mg_3N_2, BN, AlN, SiN, Si_3N_4, TiN, ZrN, HfN, VN, NbN, Ta_2N, TaN (hexagonal and cubic)
Silicides	$TiSi_3$, Ti_5Si_3, ZrSi, Zr_5Si_3, $MoSi_2$, $TaSi_2$, Nb_5Si_3, $NbSi_2$, WSi_2, V_5Si_3
Aluminides	NiAl, CoAl, $NbAl_3$
Hydrides	TiH_2, ZrH_2, NbH_2, CsH_2, PrH_2, IH_2
Intermetallics	NiAl, FeAl, NbGe, $NbGe_2$, TiNi, CoTi, CuAl
Carbonitrides	TiC-TiN, NbC-NbN, TaC-TaN, ZrC-ZrN
Cemented carbides	TiC-Ni, TiC-(Ni, Mo), WC-Co, Cr_3C_2-(Ni, Mo)
Binary compounds	TiB_2-MoB_2, TiB_2-CrB_2, ZrB_2-CrB_2, TiC-WC, TiN-ZrN, MoS_2-NbS_2, WS_2-NbS_2
Chalcogenides	MgS, $NbSe_2$, $TaSe_2$, MoS_2, $MoSe_2$, WS_2, WSe_2
Composites	TiB_2-Al_2O_3, TiC-Al_2O_3, B_4C-Al_2O_3, TiN-Al_2O_3, TiC-TiB_2, $MoSi_2$-Al_2O_3

Table 2.1 : Materials produced by the SHS process [Moore,1995]

1	Abrasives, cutting tools and polishing powders, e.g. cemented carbides
2	Shape memory alloys (SMA), e.g. TiNi
3	Composite materials, e.g. TiC + Al_2O_3, TiC + Al_2O_3 + Al
4	Resistive heating elements, e.g. $MoSi_2$
5	High temperature intermetallic compounds, e.g. nickel aluminides
6	Thin films and coatings, e.g. $MoSi_2$, TiB_2
7	Functionally-graded materials (FGM), e.g. TiC + Ni
8	Powders for further ceramic processing, e.g. Si_3N_4
9	Steel processing additives, e.g. nitrided ferroalloys
10	Electrodes for electrolysis of corrosive media, e.g. TiN, TiB_2
11	Coatings for containment of liquid metals and corrosive media, e.g. products of aluminium and iron oxide thermite reactions
12	Materials with specific magnetic, electrical or physical properties, e.g. $BaTiO_3$, $YBa_2Cu_3O_{7-x}$

Table 2.2 : Typical applications of SHS produced products [Moore,1995]

Particle size of titanium (μm)	T_{ad} (±80 K)
≤ 45	3070
125 - 160	2800
250 - 280	2660

Table 2.3: Dependence of the particle size of titanium on the adiabatic temperature of titanium carbide [Azatyan,1977]

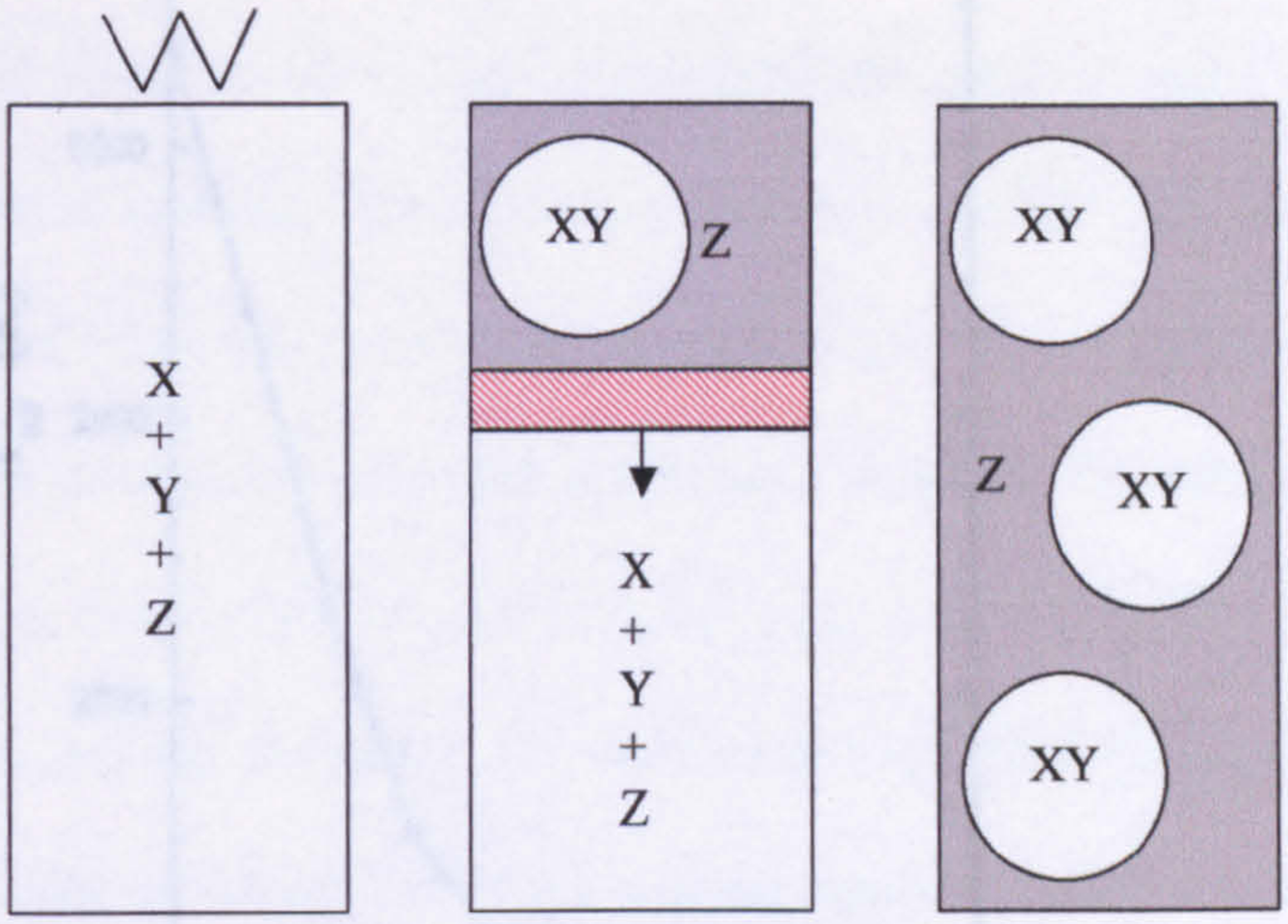

Figure 2.1 : Schematic representation of a typical SHS reaction. Rectants X, Y and Z are ignited and react to form ceramic phase, XY, and binder phase, Z.

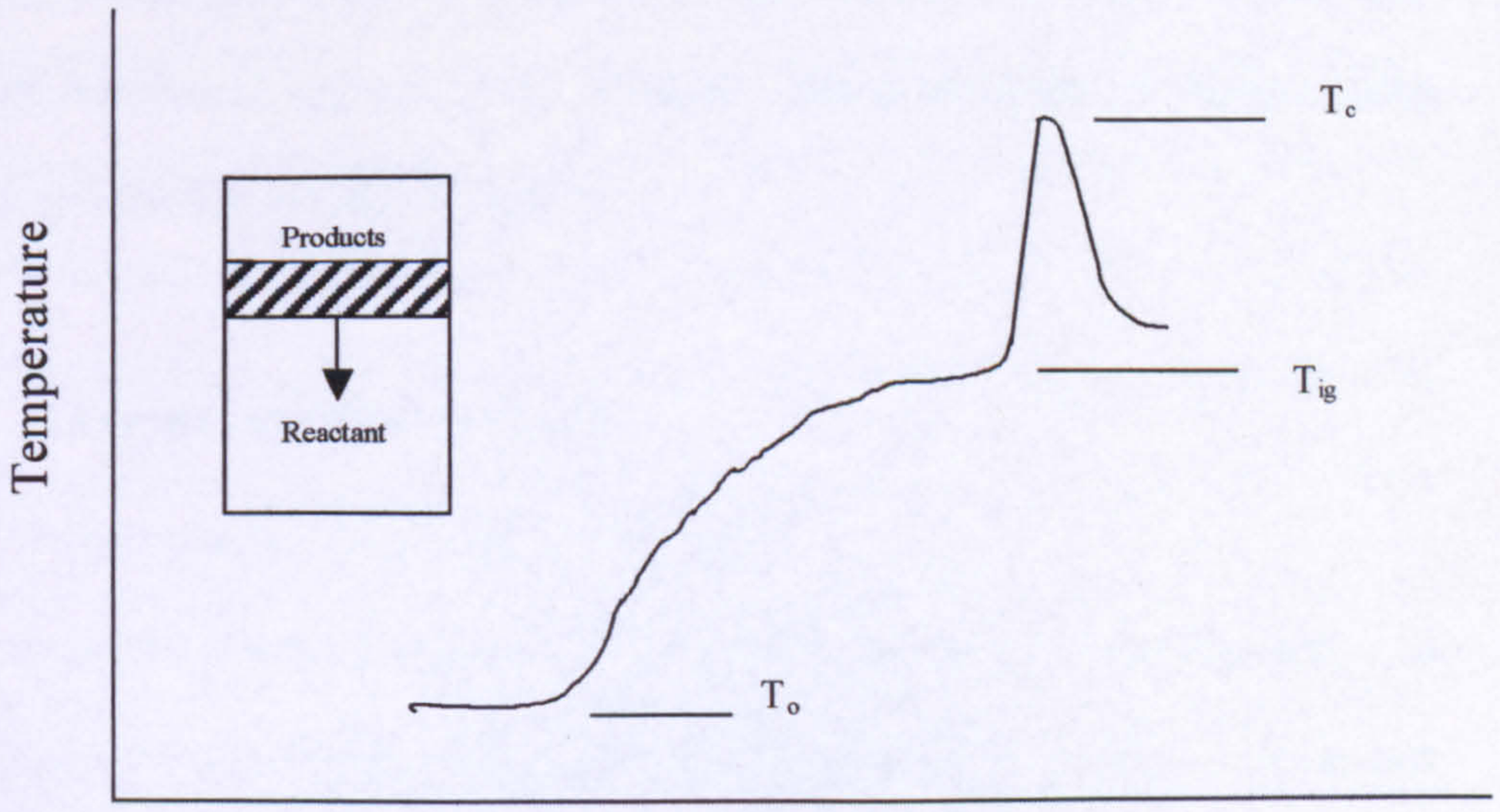

Figure 2.2 : Schematic representation of a typical time-temperature plot for an SHS reaction

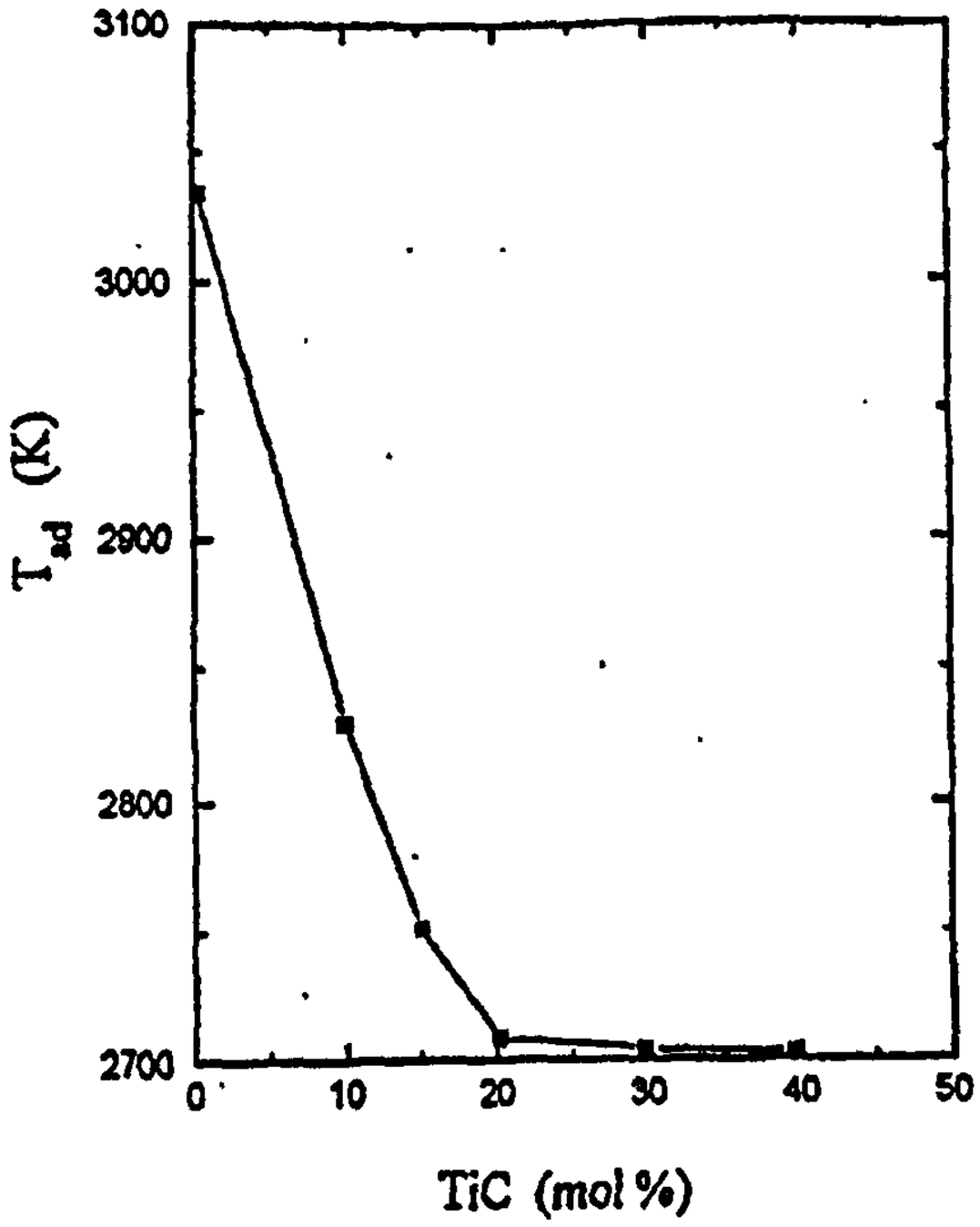

Figure 2.3: Effect of addition of a diluent (TiC) on the adiabatic temperature of the reaction Ti + C = TiC [Moore,1995]

3 Thermal spraying

Thermal spraying consists of a group of processes where metals or non-metallic materials (in the form of wire, rod or powder) are sprayed onto a prepared substrate to form a coating. The coating materials are fed into the spraying system and heated (via oxygen-fuel gas combustion, an electric arc or a plasma) to a molten or semi-molten state and accelerated towards the substrate, where upon impact, thin, lenticular splats are formed. Figure 3.1 [Krepski,1993] shows a schematic of a coating formed by thermal spraying. This diagram illustrates other common phases which can form during spraying, such as oxides and unmelted particles. Porosity may also be present.

The following chapter outlines the various common thermal spraying techniques available for the production of cermet coatings, and previous studies of thermally sprayed iron-based TiC and TiB_2 coatings. Some methods of thermal spray powder production are also included.

3.1 Thermal spray processes

3.1.1 Atmospheric plasma spraying (APS)

In atmospheric plasma spraying, a flowing inert gas stream, normally argon, is heated by a DC arc formed between a water-cooled tungsten alloy cathode and copper nozzle. The gas is partially ionized forming a plasma. The plasma gas then expands to the atmosphere and becomes very hot; temperatures can be as high as 12000°C [Nicoll,1985]. The powder, which is suspended in a carrier gas,

is then injected into the plasma where melting occurs and the molten particles are then propelled towards the substrate. Particle velocities can range from 100-300 m s^{-1} [Herman,1996]. A typical feedstock throughput can range from 3 kg/hr to 9 kg/hr. Plasma spraying is used in a wide range of applications, such as, corrosion and wear resistant coatings, thermal barrier coatings. Typical materials include nickel-based alloys, hard-facings (WC-Co and ferrous alloys), ceramic refractory oxides (alumina) and a range of other cermets. A schematic diagram of the atmospheric plasma spraying process is shown in Figure 3.2 [Nicoll,1985].

3.1.2 Vacuum plasma spraying (VPS)

Vacuum plasma spraying (VPS), also known as Low-Pressure Plasma Deposition (LPPD) or Low-Pressure Plasma Spraying (LPPS), is used when spraying materials which contain elements that are susceptible to reaction with air, (e.g. aluminium). A range of cermet coatings can also be deposited using this method. In-situ reaction with air is reduced or totally eliminated by using an inert atmosphere and operating under a low pressure. When a low pressure is used, the length of the plasma jet increases (Figure 3.3) [Nicoll,1985] and the particle velocity increases due to the absence of gas molecules (as encountered in APS). Another advantage of VPS is the use of the reversed transferred arc between the torch and the workpiece which cleans and preheats the component before spraying. This allows coating adherence on smooth surfaces, in contrast to APS where a rough surface is required. A major drawback with VPS is the high cost associated with the equipment required to produce the necessary environment

(vacuum systems, etc). Another derivative of the plasma spray system is Underwater Plasma Spraying (UPS) where rapid quenching occurs which can be advantageous for some coatings. This method also controls noise, eliminates airborne dust and facilitates collection of overspray.

3.1.3 Detonation gun spraying (D-Gun)

The detonation gun spraying process is shown in Figure 3.4, and consists of a water cooled barrel about 1m in length and an inside diameter of 25mm. Oxy-acetylene gas and powder are injected into the barrel and ignited with a spark plug. A detonation wave then accelerates the semi-molten or molten powder towards the substrate at approximately 800 m s^{-1} [Nicol,1985] producing a very dense (less than 2% porosity), well-bonded coating. The combustion chamber is then flushed out with nitrogen, and a new cycle begins. The cycles are repeated around 4-8 times per second giving a relatively low spray rate of 0.3 to 0.9 kg/h. Temperatures exceeding 4200°C can be achieved with this process. Materials such as tungsten carbide-cobalt (WC-Co) and chromium carbide nickel chromium (NiCr-Cr_3C_2) are deposited using this process for applications such as gas turbine components.

3.1.4 High velocity oxy-fuel spraying (HVOF)

HVOF is one of the most recent developments in thermal spraying techniques and was developed as an alternative to the D-Gun. This process differs from conventional flame spraying as the combustion process is internal and the gas

flow rates and delivery pressures are much higher than those in the atmospheric burning, flame-spraying processes. The HVOF system uses oxygen and a fuel gas which are delivered at high pressures and flow rates to a mixing chamber where combustion occurs. Powder is then injected via a carrier gas (nitrogen, argon, helium) into the chamber and is subsequently heated until molten or semi-molten. The gases exit the nozzle at supersonic velocities and produce characteristic shock diamonds. Gas velocities have been measured to be approximately 1800 m s^{-1} [Chawla,1993] and powder velocities within the range of 550 to 800 m s^{-1} [Dorfman,1988]. The maximum flame temperature in the gun can reach up to 3000 °C, although the temperature of the flame depends upon the fuel type and the fuel to oxygen ratio. A photograph of a coating being deposited by the Top Gun system is shown in Figure 3.5.

A wide variety of materials, with different melting points, can be sprayed by selecting the necessary powder size and combustion chamber length. Higher temperatures can be achieved with longer barrels which extends the particle's residence time in the flame and with smaller particle sizes which increases the heat transfer rate to the particles. High melting point ceramics would usually have a fine powder size (5-15 μm) and a long chamber. Materials with lower melting points would have a coarser powder size (15-45 μm) and a shorter chamber size. HVOF-sprayed coatings exhibit high bond strength, low porosity and low oxide content and are compared with other conventional spraying processes in Table 3.1. This spray system has been used to produce many cermet coatings such as NiCr-Cr_3C_2 and WC-Co.

The original HVOF system (Jet Kote) was developed by Browning Engineering for the production of carbide cermet coatings for wear resistance in gas turbine applications. The success of the Jet Kote prompted development of other HVOF systems such as, Diamond Jet, Top Gun, HV2000, and JP5000 systems. There are numerous variations of the HVOF system and all differ in terms of nozzle design, combustion fuel, and coating feed injection. The JP5000 system differs from the other processes as it permits use of a liquid fuel (kerosene) which is said to provide the highest combustion pressures and particle velocities of any HVOF system [Krepski,1993]. The Top Gun and HV2000 systems differ from the Jet Kote and Diamond Jet systems (powder fed into exhaust barrel), as they are designed so that the powder is fed into a combustion chamber, which maximizes heat transfer into the particles and allows the spraying of high melting point materials, e.g. Al_2O_3. The Top Gun is also capable of utilizing acetylene as the fuel gas which produces the highest flame temperature of any HVOF gun. A schematic diagram of the Top Gun system, which is the system used in this study, is shown in Figure 3.6.

Other variations of the HVOF system exist, namely High Velocity Air Fuel (HVAF) system which uses compressed air as opposed to oxygen [Jarosinski,1993], and Hyper Velocity Impact Fusion (HVIF) which is used for wire spraying [Steffens,1993].

3.2 Other methods of cermet coating production

Cermet coatings have also been deposited by other methods ranging from the use of lasers to the in-flight production of a cermet during APS, known as Plasma Spray Synthesis (PSS). Figure 3.7 shows a schematic diagram of the PSS process. Also known as Reactive Plasma Spray Synthesis, the process involves the simultaneous synthesis and deposition of a cermet coating by plasma spraying. Gilles et al. [1990] used this method in the production of a Fe-TiC coating by injecting pellets comprising of ferrotitanium and graphite into the plasma of a spray gun. Whilst in the plasma, the powders reacted to form a Fe-TiC cermet and were accelerated towards the substrate. XRD analysis showed that the synthesized pellets consisted of TiC, Fe, free Ti and a FeTi intermetallic. The coating produced was reported to have a homogeneous thickness, consisting of titanium and iron-rich layers and oxide stringers. The authors have also previously used this technique in the production of TiB_2-based coatings [Gilles, 1990].

Ananthapadmanabhan et al. [1999] have studied the production of Fe-TiC composite coatings by reactive plasma spraying of ilmenite ($FeTiO_3$). They found that complete conversion of ilmenite to Fe and TiC phases was possible, depending upon the spraying parameters used. The average coating thickness was reported to be 4 μm.

Agarwal et al. [1999] studied the use of Pulsed Electrode Surfacing (PES) (Fig. 3.8) and Laser Surface Engineering (LSE) (Fig. 3.9) techniques to produce TiB_2-based coatings. It is reported that the PES process utilizes a high current, short

duration pulse to melt an electrode (Sintered Ni-TiB_2) which is then deposited onto the substrate and can be compared with arc-welding, but with a much lower heat input. Air, nitrogen and argon can all be used to form the plasma. The main advantage of this process is said to be the fact that a coating can be produced with little heat input to the substrate at ambient temperature, and can minimize changes in the metallurgical properties of the substrate and also reduce distortion caused by thermal stresses. Characterization of the coating highlighted a rough and irregular surface with a splash-like appearance. Cross-sections showed a homogeneous, dense, structure with a non-uniform coating thickness (35-40 μm max.) and an average hardness of 1124 ± 94 kg mm^{-2}. The phases present were reported to be Fe and TiB_2.

In contrast to the PES technique, LSE is reported to use a laser beam to melt a precursor material (TiB_2) pre-deposited using a spray gun. Interaction between the laser and substrate then results in plume/plasma formation. Heating of the TiB_2 and the substrate then forms a "melt zone" which encourages mixing of the coating and substrate resulting in a composite region. Characterization of the coating highlighted a relatively smooth and flat surface when compared with PES. Cross-sections indicated a continuous, adherent, Fe-TiB_2 composite coating (200 μm) with an average hardness of 1742 ± 306 kg mm^{-2}. The phases present were reported to be Fe, TiB_2, TiB and numerous Fe_xB_y metastable phases.

Tondu et al. [Tondu, 2000] studied a process called Laser Glazing which can be described more of a fabrication technique rather than a coating technique. The

authors utilized atmospheric plasma spraying to produce FeCr-TiC composite coatings from feedstock powders (45wt.% Fe-13Cr + 55 wt.% TiC) produced by the SHS method (Chapter 2). The coatings were found to be very porous (16-20%) and Laser Glazing was applied to reduce the porosity. An experimental set-up of the process is shown in Figure 3.10. It was reported, that during laser glazing, the matrix melted while the TiC particles remained solid (surface temperature of 2000°C) but some dissolution of TiC in the melt occurred where the carbon from the TiC formed Fe_2C. The melting zone ranged from 40 – 100 μm depending upon the scan speed of the laser. XRD analysis indicated a composition that contained TiC, Fe_2C and Cr phases. It was reported that the Cr phase was prominent due to the "selective evaporation" of the iron phase that resulted in a chromium-rich alloy. The chromium was then said to solidify first due to its higher melting point (1830°C c.f. 1539°C). The suggestion that iron "selectively evaporates" leaving a prominent Cr phase seems implausible as the boiling points of Fe and Cr are 2860°C and 2680°C respectively, indicating that Fe is not likely to evaporate preferentially to chromium. Also, as Fe-Cr is an alloy system, it is difficult to understand how Cr solidifies as a separate entity.

3.3 Comparison of the thermal spray methods of cermets

The aim of this section is to compare the microstructures and phases of cermet coatings produced by the various spraying techniques.

Smith et al. [Smith and Mutasim, 1991] studied the wear properties, effects of powder manufacture on the coating properties and microstructures of three NiCr-

TiC based coatings deposited by APS, LPPS and HVOF spraying techniques. The wear properties will be discussed in Section 5 whilst the effects of feedstock powder on the coating properties were discussed in Section 2. In terms of coating microstructures, the authors found that APS produced the least dense coatings with large carbides and oxides present. VPS was found to produce the densest coatings with few oxides and best retained the original carbide structure. HVOF produced coating microstructures with a very fine carbide distribution and the finest lamellar structures with a relatively high, but well-dispersed oxide content. Verstak et al. [1996] found that dense FeCr-TiC coatings were produced when using HVOF thermal spraying. The hardness of a FeCr-TiC coating with 50% TiC was 650 ± 160 HV_{300}. They reported a drop in deposition efficiency (70% to 25%) and an increase in porosity (2% to 10%) of APS-deposited FeCr-TiC coatings, when the TiC content in the powder feedstock was increased from 50% to 80%. There was also a subsequent increase in the microhardness of the coatings (800 HV_{300} to 1040 HV_{300}) due to the higher fraction of TiC. However, the deposition efficiency and porosity levels indicate the difficulty of producing FeCr-TiC coatings with a high content of ceramic phase when using APS.

Mohanty et al. [Mohanty & Smith,1995] studied the effects of APS and VPS of coatings from SHS-produced FeCr-TiC powders. They found that spraying these powders by air plasma spraying was unsuccessful due to the poor microstructures obtained, 10-15 % porosity. However, a coating exhibiting fine and uniform distributions of carbides was obtained when depositing the powder using VPS. They claim that only FeCr and TiC phases were present in the coating after XRD

analysis, but it is evident from the trace that other phases are also present. They report a microhardness for the VPS deposited 80/20 TiC/Fe30Cr coating as 991 ± 161 HV_{300}.

Tan et al. [Tan,1999] found that when comparing plasma sprayed coatings to those produced by HVOF, the latter had superior hardness and bond strength along with lower porosity and oxide content. Vitiaz et al. [Vitiaz,1996] found that when spraying titanium carbide, underwater plasma spraying (UPS) produced the best coating when compared with APS, which produced a porous (15-20%) and oxidised coating, and LPPS which had almost no deposition. This effect was reported to be due to the oxidation or partial thermal decomposition of titanium carbides in coatings produced using APS and LPPS. When spraying Al(Si)/TiC powders, the authors also found that the HVOF sprayed coatings had a higher hardness than the APS coatings. Smith et al. [1990] state that HVOF deposited coatings have a higher hardness than air plasma sprayed coatings due to the higher amount of retained titanium carbide after spraying.

The majority of the studies suggest that HVOF spraying is a good method of coating production mainly because of the hard and dense coatings, which are formed due to the high velocity and low temperatures of the spraying process.

3.4 Key process variables

The following section discusses some of the key variables that have to be controlled in order to produce a high quality coating.

3.4.1 Chemical uniformity of feedstock powder

It is imperative to have reasonable control over the chemical uniformity of the feedstock. For example, oxides present in the powders, due to manufacturing method, may form in the sprayed coating and can be deleterious to the properties of the coating such as hardness, wear resistance, cohesion/adhesion, etc [Bartuli,1997].

3.4.2 Particle morphology

The particle morphology can affect parameters such as, powder packing in the powder feeder, powder feed rate, effective dwell time in the flame and atmospheric interaction during time of flight. Rounded particles are reported to have better flowability within the flame.

3.4.3 Particle size distribution

Interactions between the spray particle, heat source, atmosphere and substrate depend on the size of the given particle. When powder feeds are used during spraying, the size distribution is essentially the same as that which impacts onto the substrate. Therefore a tight particle range is desired so that the spraying parameters can be adjusted to optimize particle heating. It is also important to select the particle size range in terms of the operating temperature of the spraying process being employed. If a small particle size range is used in a process with a high combustion temperature, then the smaller particles may vaporize or be expelled from the jet. Smaller powder particles are also more prone to in-flight

oxidation as was shown by Sobolev et al. [Sobolev,1998]. If a large particle size range is used in a lower temperature spraying process, the particles may bounce off the substrate or remain as unmelted particles in the sprayed coating. Smith et al. [Smith, 1990] also studied the effect of powder size with relation to the type of fuel used when using HVOF. They concluded that when using the higher combustion temperature, with a propylene fuel, powder with a particle size range of 15-45 μm tended to excessively heat up and oxidize, whereas, the powder fraction 45-75 μm was preferable. When using hydrogen, which resulted in a lower flame temperature, they stated that the 15-45 μm powder size was more suitable as the 45-75 μm powder tended to form porosity and unmelted particles in the coating.

As HVOF is a high velocity spraying process and the powders have a short residence time in the combustion zone (1-2 milliseconds) [Krepski,1993], a finer particle size range is usually employed, 15-45 μm (Section 4.2.4).

3.4.4 Particle velocity

A high particle velocity tends to promote a denser, more adherent coating. This is a key aspect of the D-Gun and HVOF processes. Typical particle velocities produced when using these processes can be found in Table 3.1.

3.4.5 Substrate conditions

It is imperative to have a properly prepared substrate surface, as this is the key to effective bonding of the coating. Before spraying it is usual practice to grit blast

the substrate to produce a mechanical interlock and increase the surface area for chemical and physical bonding.

	Flame Temp. (°C)	Particle velocity ($m\ s^{-1}$)	Typical Spray Rate (kg/h)	Coating Porosity (Vol.%)	Bond Strength (MPa)
D-Gun Spraying	4200	800	0.3-0.9	<2	-
Air Plasma Spraying	12000	100-300	3-9	2-8	20->70
Vacuum Plasma Spraying	12000	400	3-9	<5	-
HVOF Spraying	3000	550-800	2-4	<2	>70

Table 3.1: Characteristics of thermal spray processes [Krepski] [Nicol,1985] [Harvey,1996] [Jarosinski,1993] [Steffens,1993]

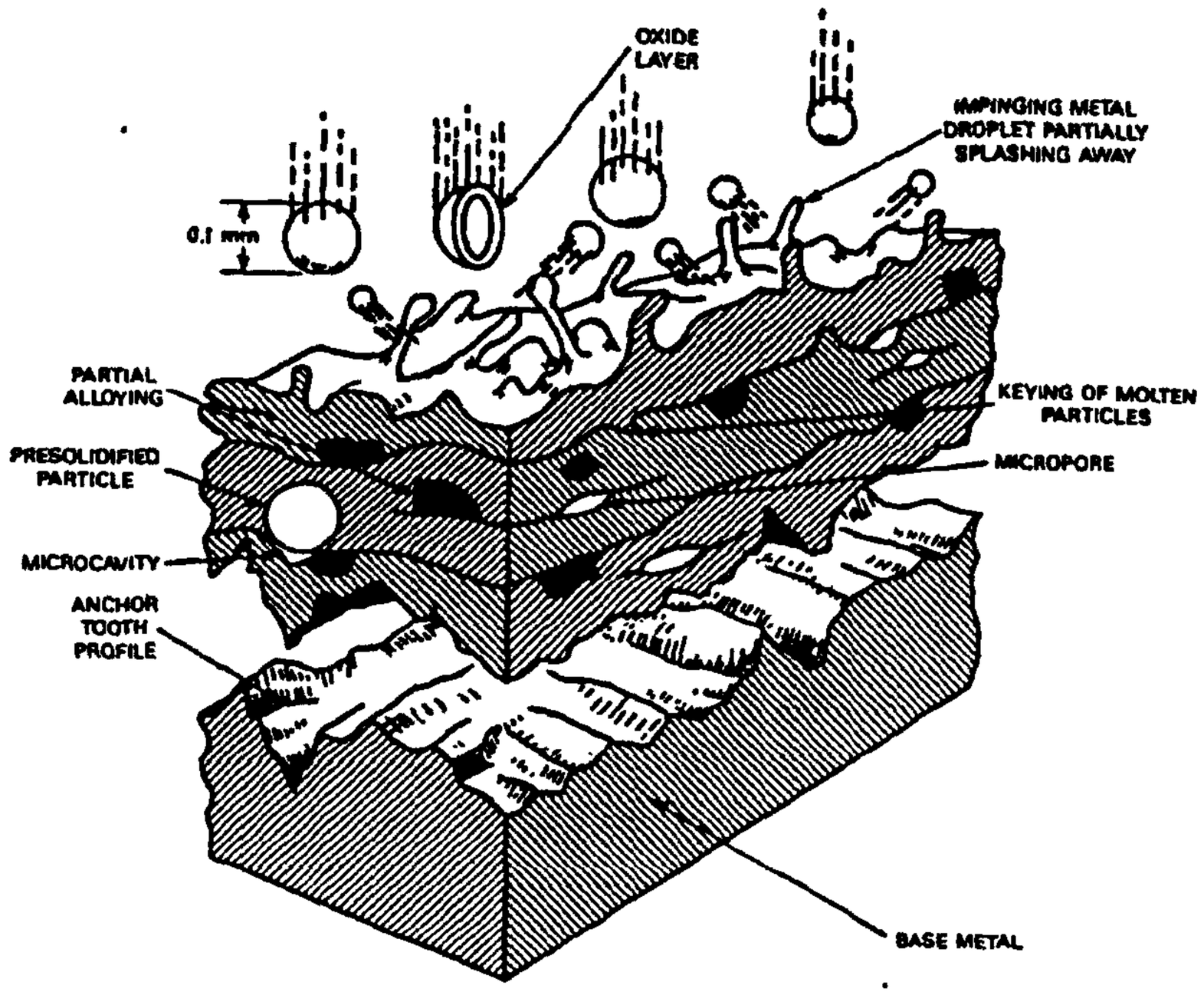

Figure 3.1 Schematic of a generic coating formed by thermal spraying [Krepski,1993]

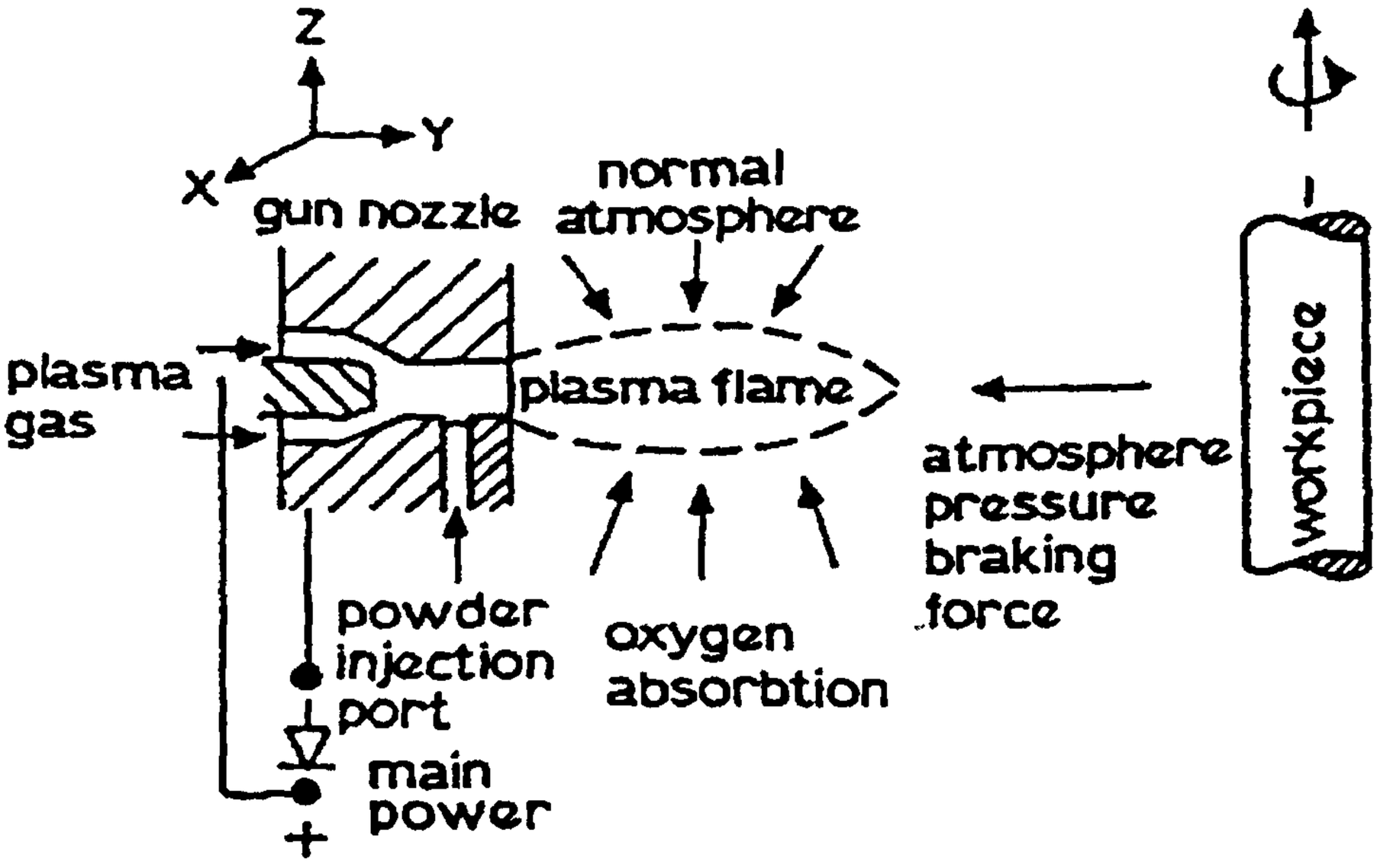

Figure 3.2: Atmospheric Plasma Spraying (APS) process [Nicoll,1985]

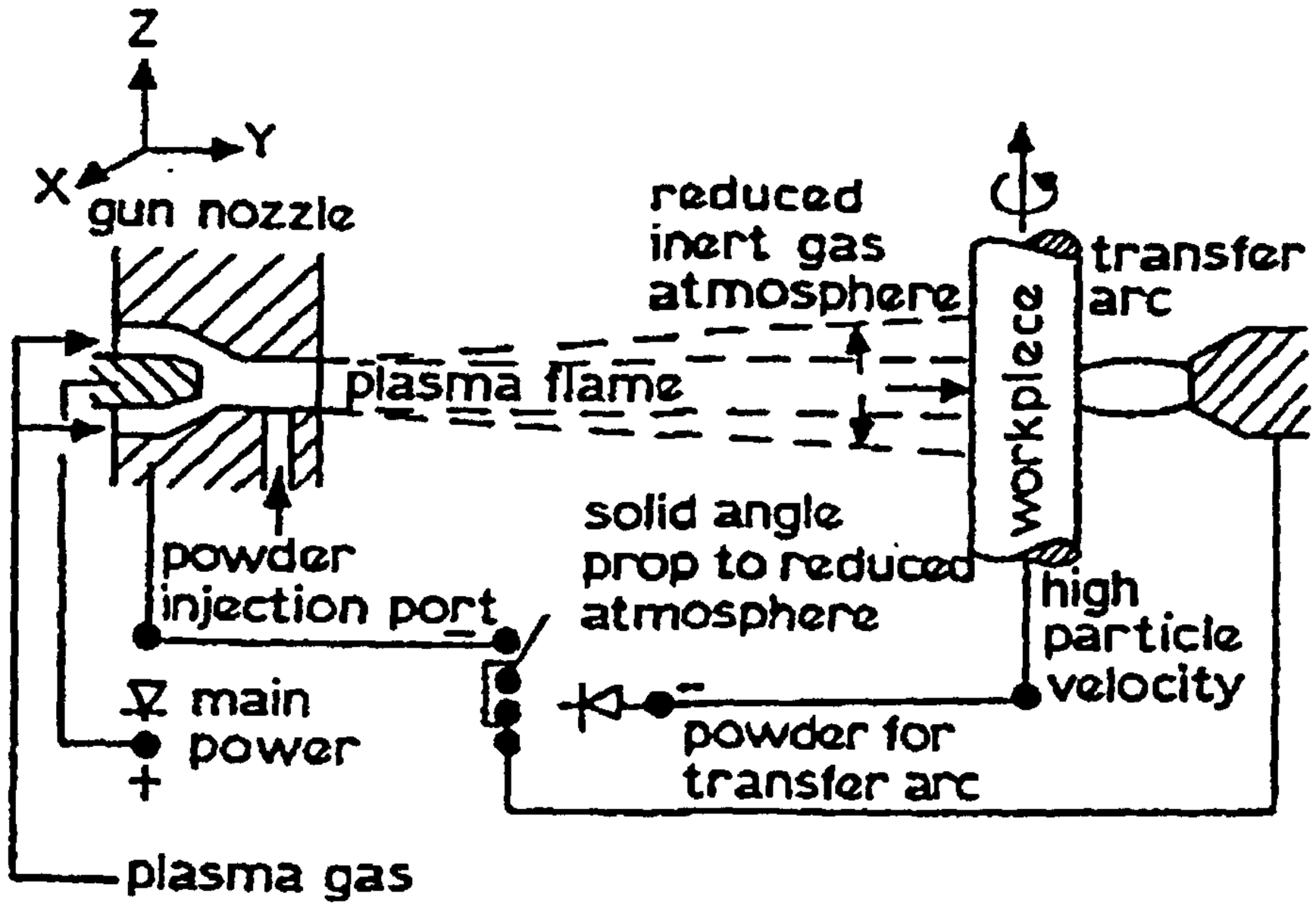

Figure 3.3: Vacuum Plasma Spraying (VPS) process [Nicoll,1985]

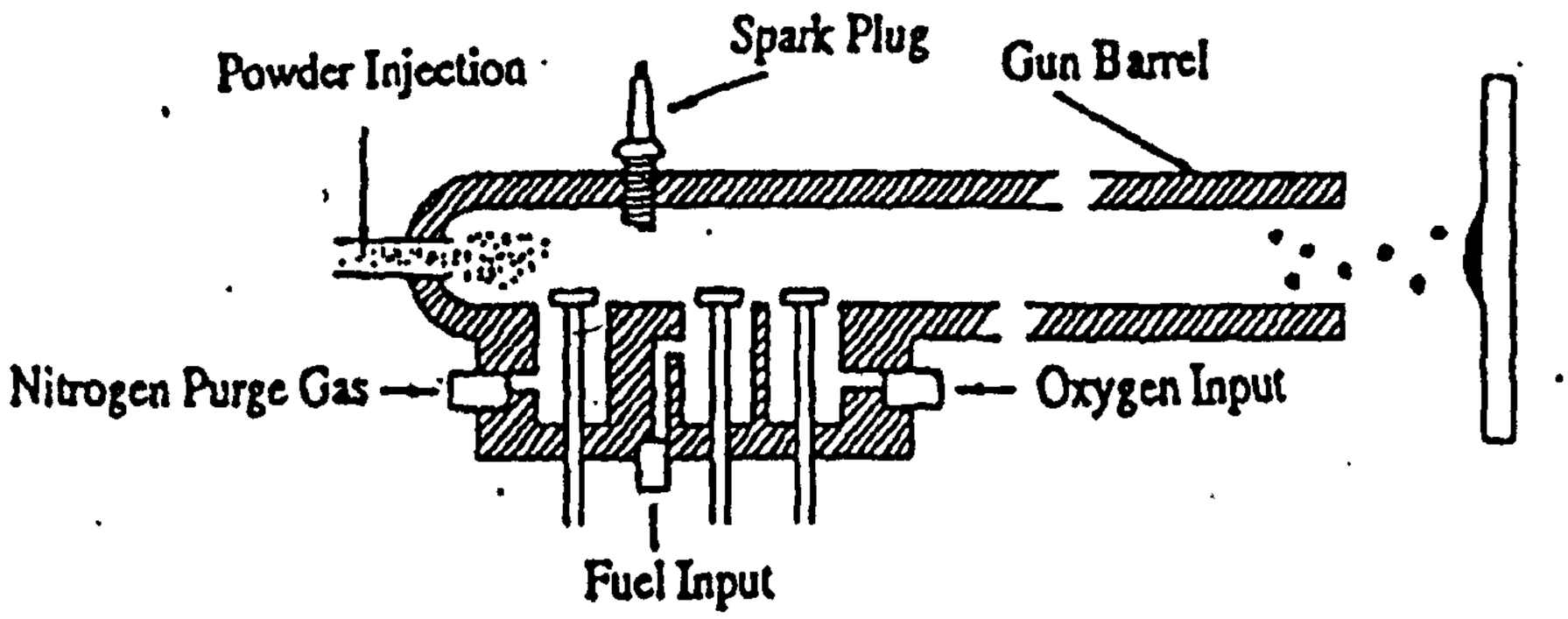

Figure 3.4: Detonation Gun (D-Gun) spraying process

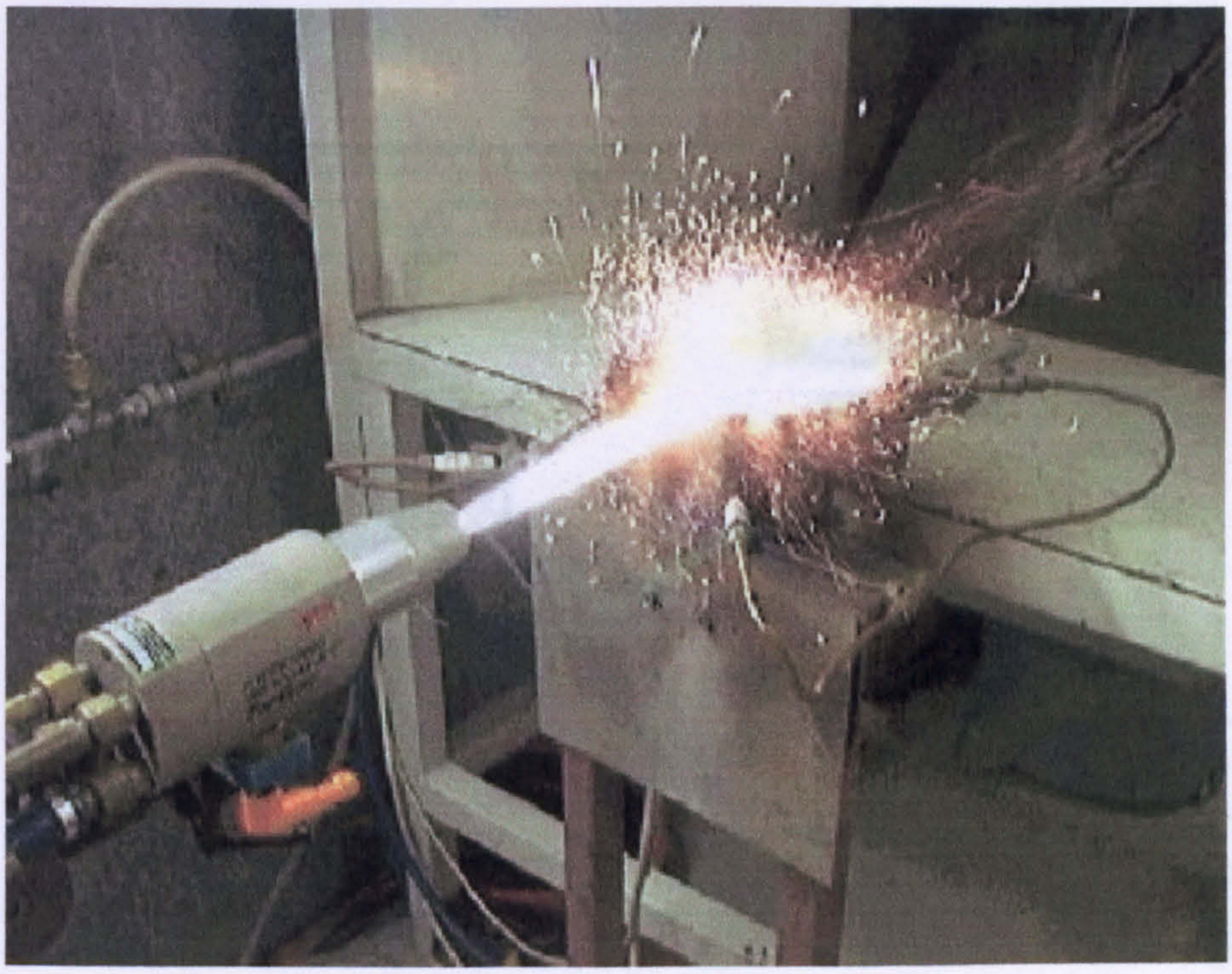

Figure 3.5: Photograph of Top Gun system

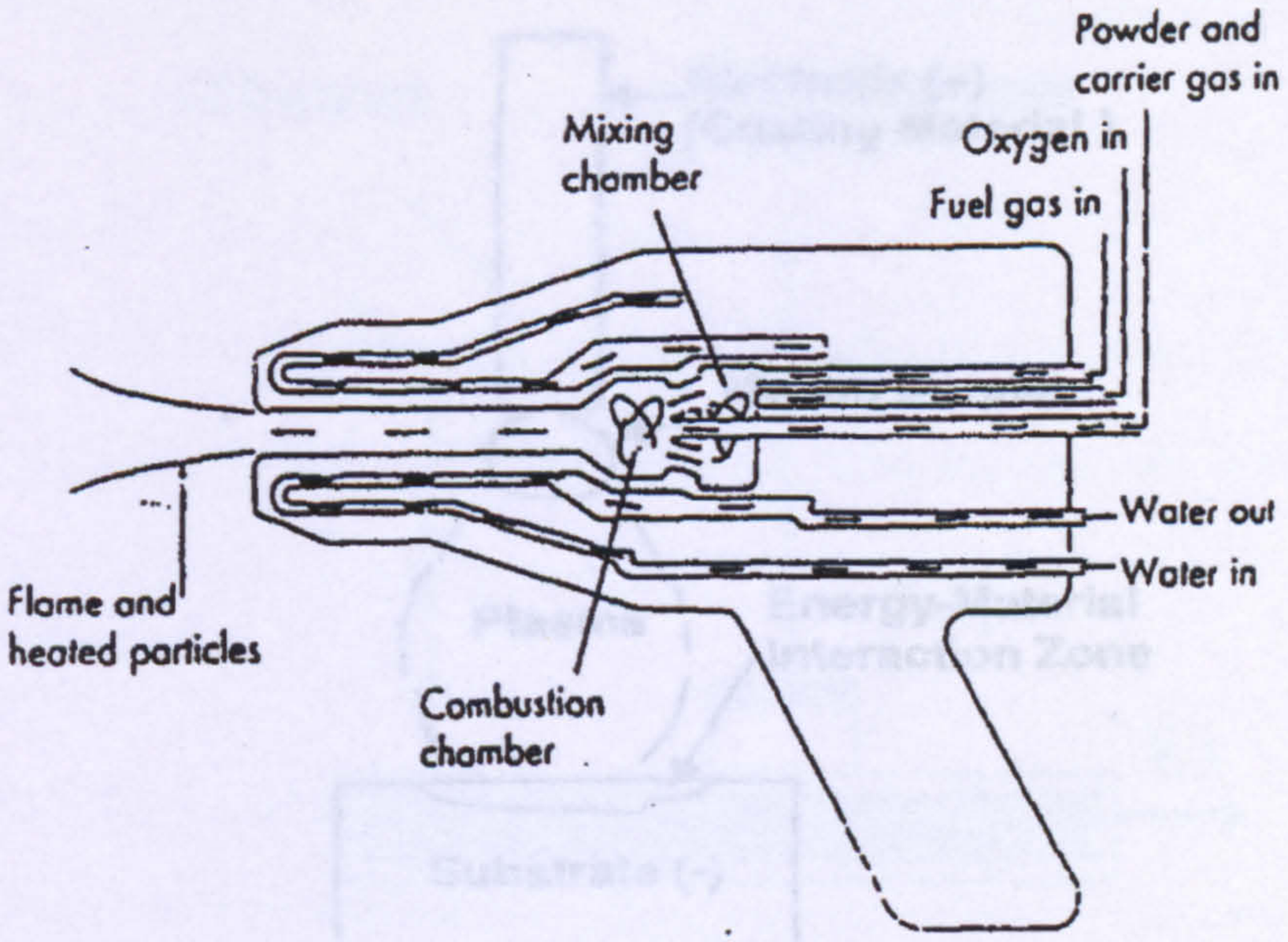

Figure 3.6: Top Gun HVOF system [Sturgeon,1994]

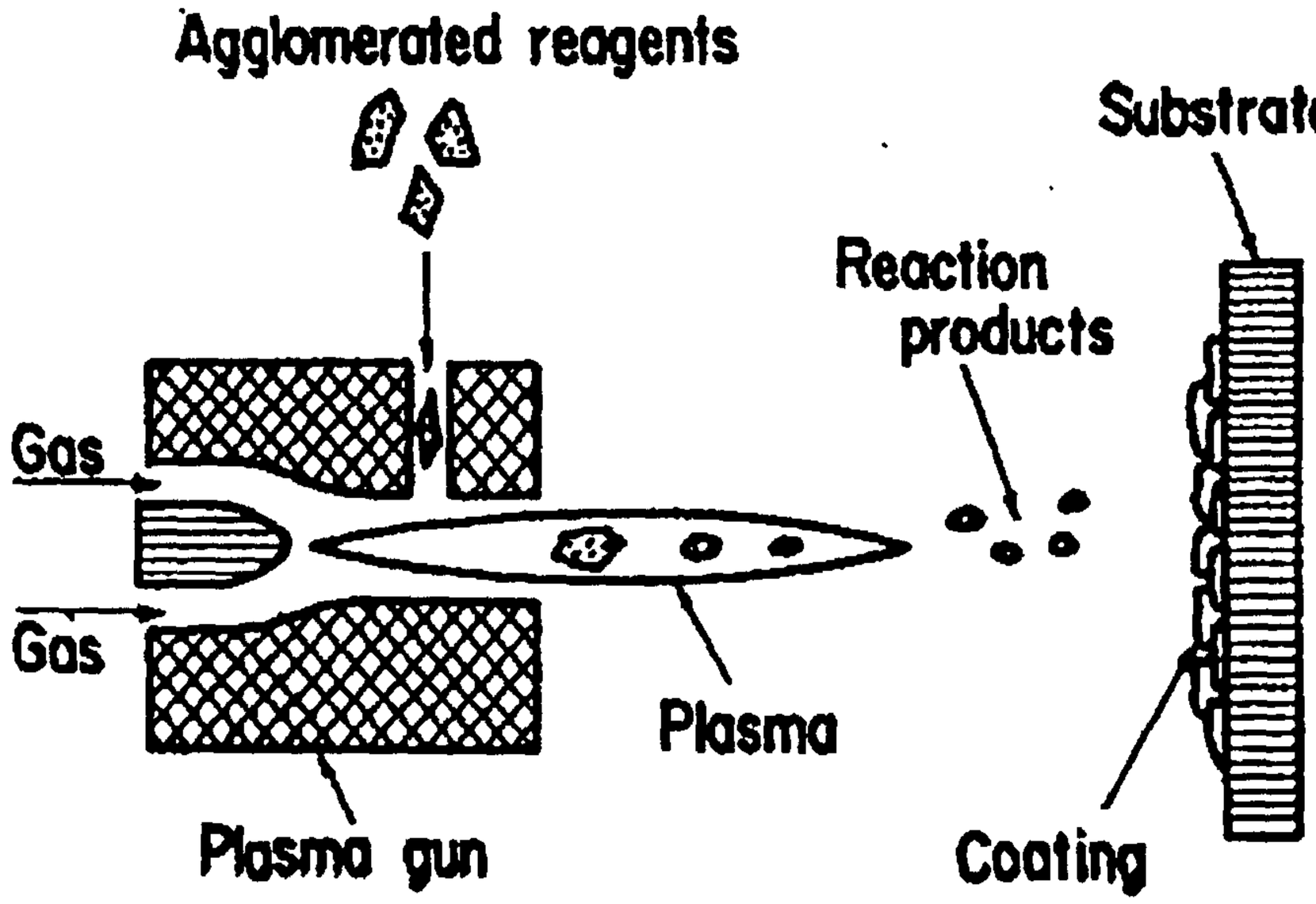

Figure 3.7: Plasma Spray Synthesis (PSS) [Gilles,1990]

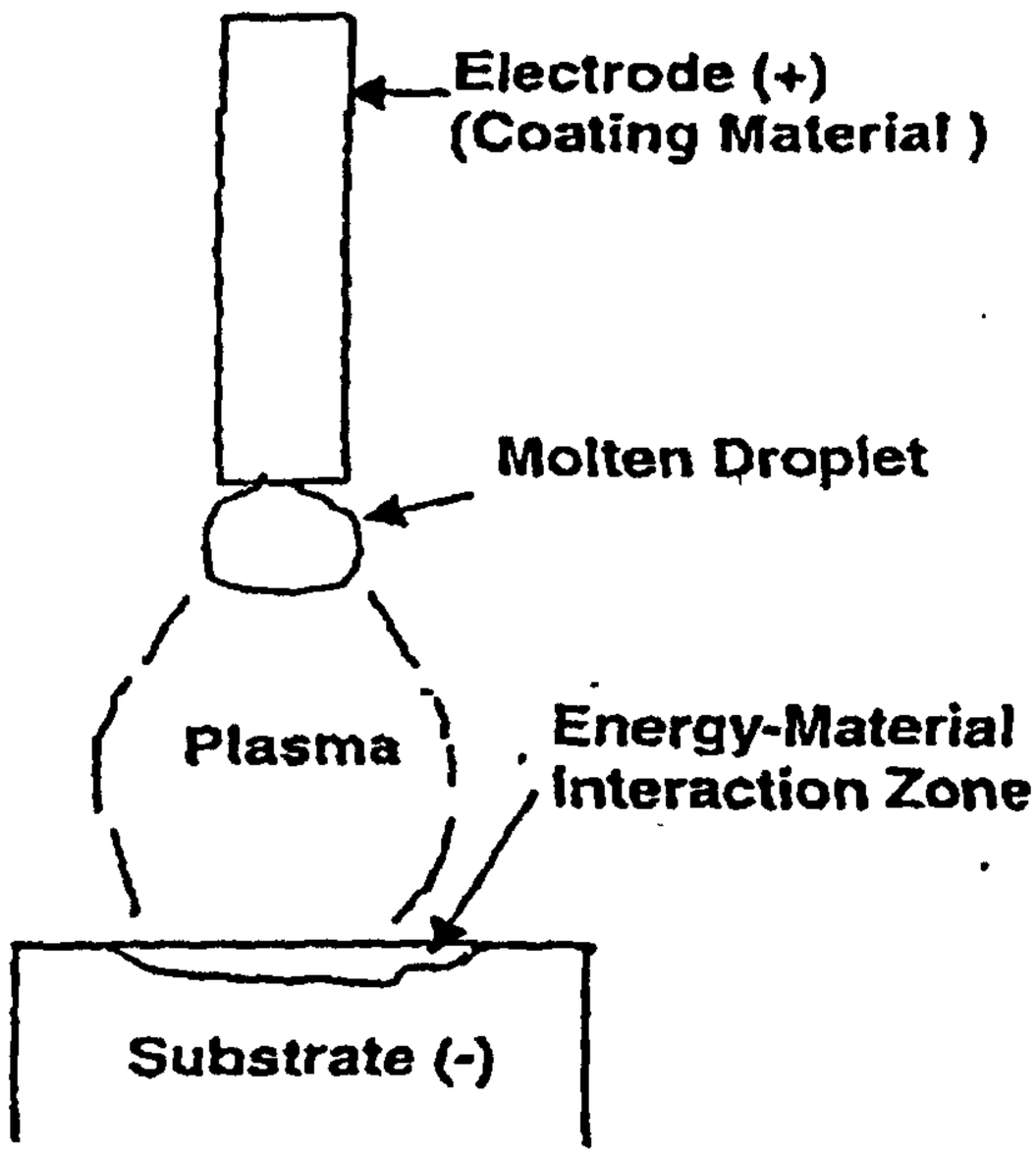

Figure 3.8: Pulsed Electrode Surfacing (PES) [Agarwal,1999]

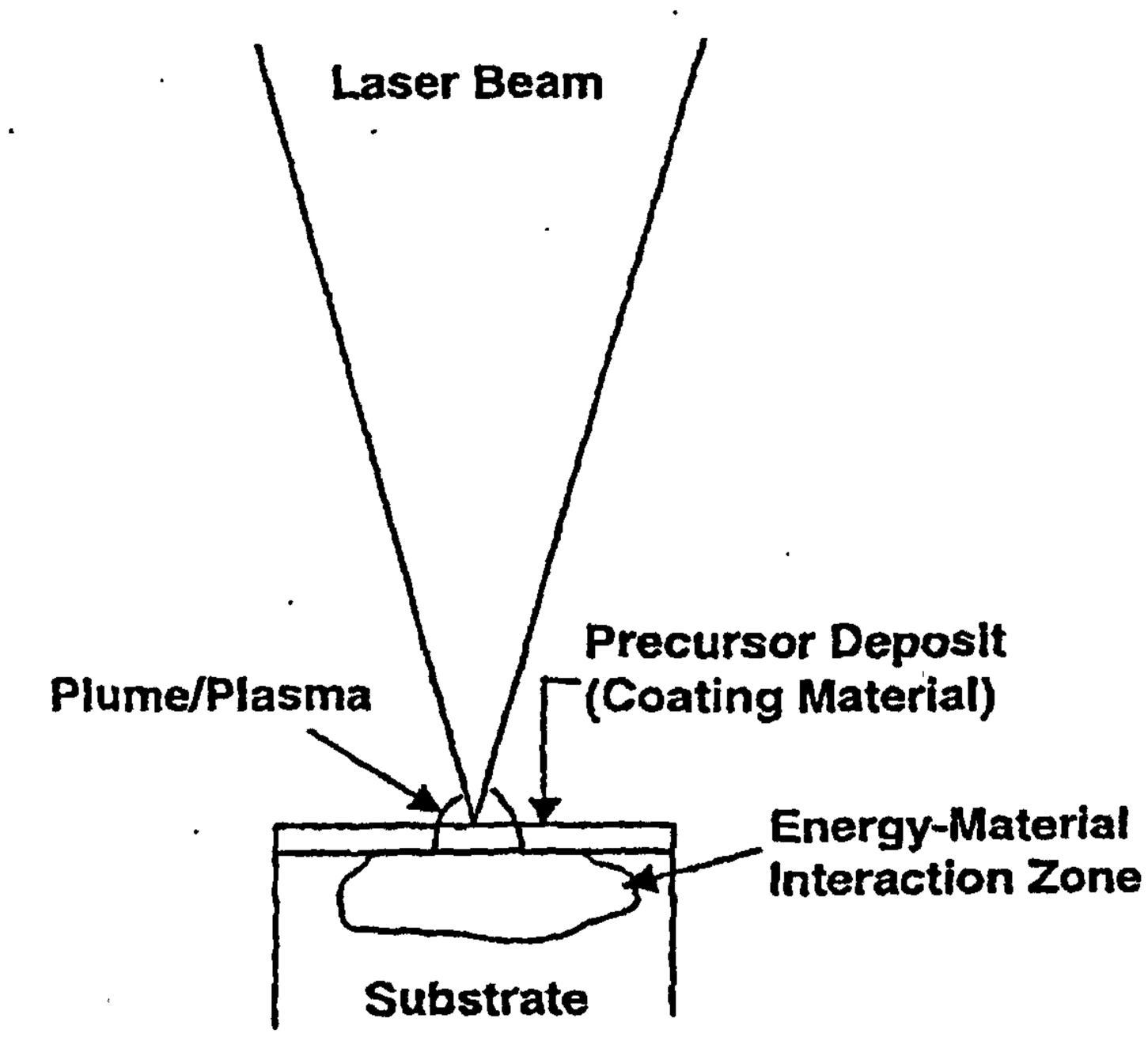

Figure 3.9: Laser Surface Engineering (LSE) [Agarwal,1999]

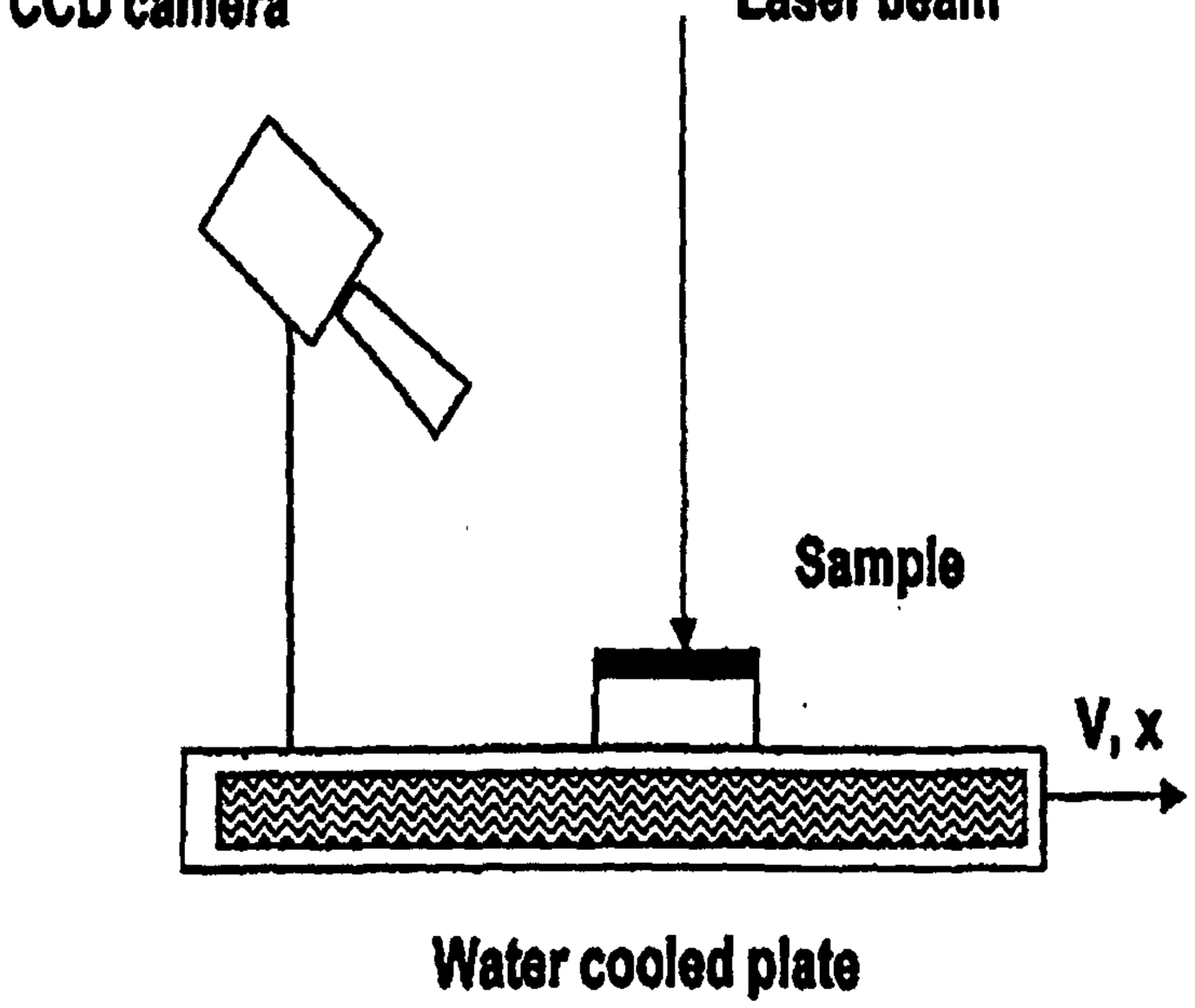

Figure 3.10: Laser Glazing [Tondu,2000]

4 Materials

4.1 Iron

Pure iron exists in two crystal forms, body-centred cubic (bcc) (α-iron, ferrite) which remains stable up to 910°C and face-centred cubic (fcc) (γ-iron, austenite) which is stable between 910°C and 1390°C. Above this temperature, it reverts back to the bcc form (now δ-iron) which remains stable up to the melting point, 1536°C. Due to the fact that both α- and γ-iron have different crystal structures, the properties will be different, e.g. the solubility of non-metallic elements such as carbon, the diffusivity of alloying elements at elevated temperatures, and the general mechanical behaviour.

4.1.1 Carbon in solution in α- and γ-iron

When carbon is added to α- or γ-iron it enters the lattice as interstitial solute atoms. The fcc structure of γ-iron is more closely packed than α-iron but the largest interstices exists in the fcc γ-iron. The solubility of C is therefore considerably greater in austenite than in ferrite due to the larger interstices available. The solubility of carbon in γ-iron can be as high as 9 at% compared with only 0.1 at% for the α-iron [Honeycombe,1995].

4.1.2 Fe-C binary phase diagram

Figure 4.1 shows the iron-carbon equilibrium diagram. The main constituents are γ-iron (austenite), α-iron (ferrite), δ-iron and Fe_3C (cementite). It can be seen that

austenite has a much larger phase field than ferrite and is due to the higher solubility of carbon in austenite, with a maximum of just over 2 wt% at 1147°C (Point E). The ferrite phase field is much more restricted, with a maximum carbon solubility of 0.02 wt% at 723°C (Point P) so for steels with carbon contents of 0.05 to 1.5 wt%, the excess carbon usually forms iron carbide in one form or another. The δ-phase is also restricted between 1390 and 1534°C and disappears completely when carbon contents reaching 0.5 wt% are used.

There are numerous important temperatures and points in the iron-carbon diagram. The A_1 temperature (Line PSK) is where the eutectoid reaction occurs at 723°C. The temperature where ferrite transforms to austenite is known as the A_3 temperature. For pure iron this occurs at 910°C but lowers along the line GS by the addition of carbon. The final point is A_4 (Point N) and this is where austenite transforms to δ-iron at 1390°C for pure iron, which progressively increases with the addition of carbon.

4.1.3 Effects of alloying elements

With relation to the effect of alloying elements, iron binary equilibrium diagrams fall into four categories (Figure 4.2): open and closed γ-field systems and expanded and contracted γ-field systems. This suggests that alloying elements will either, expand the γ-field and encourage the formation of austenite, i.e. γ-stabilizers, or contract the γ-field and encourage the formation of ferrite, ferrite stabilizers.

Figure 4.2a shows an open γ-field phase diagram where austenite formation is encouraged. The main alloying elements which cause an open γ-field are nickel and manganese and if added in sufficient quantities will completely eliminate the bcc ferritic phase and replace it with austenite down to room temperature. Figure 4.2b shows an expanded γ-field phase diagram where carbon and nitrogen are the most prominent elements in this group. The γ-phase is expanded, but its range of existence is cut short by compound formation. Figure 4.2c shows the closed γ-field phase diagram where the formation of austenite is restricted and the γ-field is contracted to a small area called the γ-loop, therefore encouraging the formation of ferrite. Elements that cause this effect include titanium and chromium. Finally, the contracted γ-field phase diagram is shown in Figure 4.2d and shows that the γ-loop is contracted strongly. The most significant element that causes this effect is boron.

A convenient method of illustrating the effects of an alloying element on the γ-phase field of the Fe-C system is to show the γ-phase field boundaries for differing concentrations of a particular element. Figure 4.3 shows the effect of titanium and chromium on the γ-phase field. It can be seen that just over 1% Ti will eliminate the γ-loop, while 20% Cr is required to reach this point.

4.1.4 Martensite formation

As mentioned earlier (Section 4.1) a transformation from austenite (fcc) to ferrite (bcc) iron between 723 and 910°C. If the austenite is rapidly cooled to room

temperature the driving force tending to cause the austenite-ferrite transformation is so great that it occurs before carbon has an opportunity to form the equilibrium Fe_3C phase. What results is a bcc structure supersaturated with carbon, which causes considerable distortion of the structure and makes slip virtually impossible. As such, this phase exhibits a high hardness and low fracture toughness. This structure is known as martensite and is single-phased as all of the carbon has been retained in solid solution. If the degree of cooling is less severe and transformation is allowed at some temperature between 250 and 550°C then carbide will be allowed to precipitate and a structure known as bainite is formed.

4.1.5 Stainless steels

Stainless steels are known for their excellent corrosion resistance and must contain at least 12% Cr, which permits a thin, protective layer of chromium oxide to form when exposed to oxygen. As previously reported, chromium restricts the γ-loop, but with the addition of carbon the γ-loop can be extended to allow higher chromium contents. Figure 4.4 and 4.5 show the effect of carbon on the Fe-Cr diagram and it is evident that increasing the C content opens the γ-loop, encouraging austenite formation. Figure 4.4 shows that when 0.05 wt% carbon is added to a 20 wt% Cr steel, both $\alpha+\gamma$ and α-phases can be obtained. At 0.4 wt% C the steel can consist of $\alpha+\gamma$ phases (Figure 4.5). It is therefore evident that the C content opens the γ-loop. There are several categories of stainless steels based on crystal structure and alloying elements. Typical properties are shown in Table 4.1.

4.1.5.1 Austenitic stainless steels

Nickel is a major alloying element in austenitic stainless steels as this is an austenite-stabilising element and thus inhibits ferrite formation. The fcc austenitic stainless steels have excellent ductility, corrosion resistance and low-temperature impact properties. High strengths are obtained by extensive solid solution strengthening and the austenitic stainless steels may be cold-worked to higher strengths than the ferritic stainless steels. The high nickel and chromium contents make the alloys expensive.

4.1.5.2 Martensitic stainless steels

Martensitic stainless steels are limited to chromium contents of 13 wt% but this can be increased with increasing carbon content. They are more economical to produce, but are less corrosion resistant than austenitic and ferritic stainless steels.

4.1.5.3 Ferritic stainless steels

Ferritic stainless steels can contain between 17 and 30 wt% Cr and less than 0.12 wt% C. They possess a bcc structure and have good strength and moderate ductility due to solid solution strengthening and strain hardening. They have excellent corrosion properties and are relatively inexpensive. There are two phenomena which may affect the properties of ferritic stainless steels. Firstly, what is known as '475°C embrittlement', which occurs when ferritic stainless steels heated between 400 and 500°C, and becomes more prominent with increasing chromium content. The origins of this problem are still in doubt.

Secondly, 'sigma phase' is a phenomenon which occurs in both ferritic and austenitic stainless steels, but more pronounced in the former, which is detected below 600°C and causes embrittlement.

4.2 Titanium carbide and titanium diboride

The following section discusses the crystallography, thermal, mechanical and chemical properties of both titanium carbide and titanium diboride.

4.2.1 Titanium carbide

Titanium carbide is a transition metal carbide and is reported to exist over a wide range of carbon-titanium ratio, $TiC_{0.97}$ to $TiC_{0.47}$ [Choi,1994]. The mechanical properties of TiC are highly dependent upon the stoichiometry and will be outlined in later sections. Table 4.2 shows typical properties of titanium carbide. The crystal structure is said to be similar to that of NaCl where the carbon atoms exist in octahedral interstices of the face-centred cubic Ti (Figure 4.6).

4.2.1.1 C/Ti ratio

As mentioned previously, TiC exists over a wide range (Section 4.2.1) which results in a range of properties of TiC. The adjustment of the carbon-titanium ratio therefore allows the possibility of controlling these properties. Holleck [1986] has shown (Figure 4.7) that as the C content increases in TiC, the hardness also increases. This is also evident for other carbides such as ZrC and HfC.

A change in carbon-titanium ratio also has an effect on the carbide/matrix bond in cermets. This effect has been studied by Ramqvist [1965] who has demonstrated that a change in C/Ti ratio from 1 to 0.49 can decrease the wetting angle between TiC_x and copper from 108° to zero (i.e. complete wetting is achieved by $TiC_{0.49}$). This is reported to be due to the stability of the carbides, where carbides with strong inter-atomic bonds will have a lower tendency to interact with the liquid metal. Morozova et al. [1962] also studied this relationship and concluded that the wettability of TiC_x with varying carbon contents follows a trend identical with that for the heat of formation. Both studies used the enthalpy of formation ($\Delta H°$) to compare thermal stability. The relationship between wettability of TiC by liquid Cu and the C/Ti ratio is shown in Figure 4.8. The effect of contact angle (θ) and work of adhesion (W) (i.e. the bonding force between the liquid and solid phase) of copper and TiC_x are shown in Table 4.3. Eustathopoulos et al. [1991] suggest that the contact angle decreases and work of adhesion increases with a decrease in C content due to the TiC becoming increasingly more metallic in character and thus bonding is more ionic in nature. Ramqvist [1986] also studied the wetting of equimolar TiC (i.e. C/Ti ratio is 1:1) by iron at 1490°C, and measured a low angle of 28°, indicating good wetting behaviour. The change of lattice parameter with changing C/Ti ratio is shown in Table 4.4. It can be seen that the lattice parameter decreases with decreasing carbon content.

4.2.1.2 Thermal properties

Table 4.5 shows the specific heat capacity (Cp), enthalpy of formation (ΔH_f) and Gibbs free energy of formation for TiC.

4.2.1.3 Mechanical properties

Equimolar titanium carbide has a reported hardness of 3200 kgf mm^{-2} (Figure 4.7). Ramalingam [1977] investigated the effects of temperature on the hardness of TiC and they reported that the hardness of TiC cutting tool material decreased with increasing temperature. This relationship is shown in Figure 4.9. The hot yield strength of equimolar TiC has been reported to be approx. 33 kg/mm^2. This value is reported to change with changing C/Ti ratio. This effect is shown in Figure 4.10.

4.2.2 Titanium diboride

Titanium diboride (TiB_2) is a transition metal-based refractory ceramic that has a low density, high hardness, high melting point, wear resistance and corrosion resistance, and makes it a suitable material for use in high temperature, high wear conditions [Agarwal,1999]. Some typical applications include nuclear, fossil and geothermal energy environments, industrial cutting tools, agricultural and textile components requiring wear resistance and high temperature sensors [Agarwal,1999]. Some properties of titanium diboride are shown in Table 4.6. The hexagonal crystal structure of TiB_2 is shown in Figure 4.11.

4.2.2.1 Thermal properties

Table 4.7 shows the specific heat capacity, enthalpy of formation, and Gibbs free energy of formation (from the elements) for TiB_2.

4.2.2.2 Mechanical properties

Titanium diboride has a typical hardness value reported of 3650 kgf mm^2 [Champagne,1985]. Figure 4.12 shows the hardness of TiB_2 as a function of temperature and it can be seen that the hardness decreases as the temperature increases. Figure 4.13 shows the strength of TiB_2 and other borides as a function of temperature and shows that bend strength of TiB_2 increases with increasing temperature up to 1400 °C.

Ramberg et al. [1987] investigated the high-temperature deformation of TiB_2 under vacuum. They concluded that with the exception of high-purity SiC, the yield strength of TiB_2 was greater than any other ceramic compound for which data existed.

4.2.3 Comparisons with other hard phases

This section compares the properties of TiC and TiB_2 mainly with two hard phases commonly used in cermets, these being Cr_3C_2 and WC. Table 4.8 shows the physical properties of the mentioned hard phases. WC is the densest hard phase followed by Cr_3C_2, TiC and finally TiB_2. It can also be seen that TiB_2 has the highest melting point followed by TiC, WC and Cr_3C_2.

4.2.3.1 Thermal properties

Table 4.9 shows the heat capacity, enthalpy of formation and Gibbs free energy of formation of TiC, TiB_2, Cr_3C_2 and WC. Cr_3C_2 exhibits the highest heat capacity followed by TiB_2, WC and finally TiC. TiB_2 exhibits the highest enthalpy of formation and will produce the highest adiabatic temperature during SHS reaction. The TiB_2 hard phase also exhibits the most negative Gibbs free energy value and will thus be the most stable.

4.2.3.2 Mechanical properties

Table 4.10 shows the hardness of the ceramic phases. TiB_2 has the highest, followed by TiC, WC and finally, Cr_3C_2. The hardness of the ceramic phases can determine whether hard or soft abrasion occurs during wear (Section 5.2.5). Table 4.11 shows the abrasive wear and hardness properties of different single-phase hard materials. The table shows that B_4C is the most abrasive wear resistant, followed by SiC, TiB_2 and finally, TiC. It is important to note that the abrasive wear resistance of TiB_2, when subjected to alumina, is twice that of TiC. Holleck [1986] studied certain properties of transition metal carbides from group IV, V and VI of the periodic table. He concluded that the amount of metallic bonding increases going from group IV to group VI. TiC and WC represent the limits of this changing bond character of refractory carbides (TiC-highest, WC-lowest amount of directed M-C bonding). Also, from group IV to group VI there is a decrease in room-temperature hardness and wetting angle with Fe, Co, Ni, and an increase in hot hardness, fracture toughness and solubility in Fe, Co, and

Ni. Therefore, the greatest advantage of coating materials from group IV carbides are high room-temperature hardness and the small interaction tendency with common binder phases. The main disadvantage is the high brittleness. Coatings from group VI carbides have a higher fracture toughness.

4.3 Iron-titanium carbide cermets

Whilst, titanium carbide-based cermets have received much attention within the family of metal-ceramic materials, information on the iron-based system is very limited. Goetzel [1991] has collated properties from various studies of iron-titanium-carbide based cermets. For a 45% TiC, 55% steel matrix (containing 17% Cr), the hardness was 85.5 HRA and the Young's Modulus was 303 GPa.

4.4 Iron–titanium diboride cermets

In the last ten years, titanium diboride-based cermets are increasingly becoming more popular as wear resistant materials because they retain high hardness, strength and wear resistance. The function of the Fe-based binder phase in this research is to improve the strength properties of the coating. This was demonstrated in work performed by Yen et al. [1978] who showed that an addition of up to 10 vol.% Fe to pure TiB_2 improved its strength properties twofold.

Andrievski [1992] performed mechanical tests on a range of iron (18-28 vol%) and titanium diboride-based composites, which were produced by a combination of SHS and hot pressing. The conclusions of his study are shown in Figure 4.14.

From the results Andrievski concluded that, at room temperature, the bending strength of WC-24vol%Co was much greater than that of the iron-boride based composites, but between 500-600 °C, the strength values became comparable. Both the iron-titanium boride based composites and WC-24vol%Co generally had higher strength values than those for the sintered TiB_2-Fe-Mo composite over a range of temperatures. Also, TiB_2-28vol%Fe composite had a higher hardness than that of WC-24vol%Co, up to approximately 750°C.

Andrievski concluded that iron-boride based composites obtained by SHS compaction had promising physical-mechanical properties in a wide temperature range. He also stated that these materials were characterized by brittle fracture up to 600-700 °C before plastic deformation occurred. Another important feature, which TiB_2 possesses is that it is stable in pure iron [Andrievski,1992] (Refer to Figures 4.20 and 4.21).

4.5 Phase equilibria of the composite systems

4.5.1 Titanium-carbon phase diagram

Figure 4.15 shows the binary phase diagram of titanium and carbon. The phase diagram consists of three terminal solids, bcc (body-centred cubic) β-Ti, cph (close-packed hexagonal) α-Ti and carbon; and a refractory monocarbide, TiC, which has a wide homogeneity range, 32 to 48.8 at.% C (approx. 10 to 19.25 wt.% C). Other phases present are liquid (L) and graphite. One peritectoid and two eutectic reactions appear in the system at 920, 1646 and 2776°C respectively.

4.5.2 Iron-titanium phase diagram

Figure 4.16 shows the iron-titanium binary phase diagram. The equilibrium solid phases present in the system are: (i) pure α-Ti (cph) solid solution which begins to form below 882°C; (ii) pure β-Ti and α-Fe (both bcc) where the Ti remains in the bcc form above 882°C while the Fe remains bcc below 912°C and above 1394°C; (iii) pure γ-Fe (fcc) between 912 and 1394°C; (iv) TiFe compound (CsCl structure) formed from the melt by a peritectic reaction, $L + TiFe_2 \rightarrow TiFe$ at 1317°C; and (v) $TiFe_2$ ($MgZn_2$-type Laves phase) which melts congruently at 1427°C.

4.5.3 Iron-titanium-carbon phase diagram

Figure 4.17 shows a liquidus projection of the iron-titanium-carbon ternary phase diagram. It can be seen that TiC is the first phase to precipitate out from the melt (approx. 3000°C). Other phases present are α-iron (bcc) (Fe(HT1)), γ-iron (fcc) (Fe(HT2)), Fe_2Ti, FeTi, Ti, and C.

4.5.4 Titanium-boron phase diagram

Figure 4.18 shows the binary phase diagram of titanium and boron [Murray]. The terminal solid solutions present are high-temperature bcc (β-Ti), a low-temperature cph (α-Ti), and a rhombohedral (β--B). Also present are two intermetallic compounds, TiB and TiB_2. Another phase present is Ti_3B_4. From the figure, it can be determined that TiB_2 is the first phase to precipitate from

melts (3225 ± 25 °C max. temp.) containing ~40-95at% boron. If <40at% boron was present, TiB would form.

4.5.5 Iron-boron phase diagram

Figure 4.19 shows the binary phase diagram of iron and boron [Liao]. The terminal solid solutions present are high-temperature bcc (δFe), medium-temperature fcc (γFe), low-temperature bcc (αFe) and rhombohedral (βB). Two boride-based compounds are also present, these being Fe_2B and FeB.

4.5.6 Iron-titanium-boron phase diagram

Figure 4.20 shows a pseudobinary diagram taken from an isothermal section at 1273 K [Tanaka,1999]. The author is aware that this diagram is not ideal as it does not account for the mole fraction of boron within the sprayed FeCr-TiB_2 powder composition, but it is intended to be used as a rough guide of the phases that may be attained. Figure 4.21 shows a pseudobinary phase diagram of Fe-Ti-B and the effects of impurities such as C, O, Al, Si and Mn present in the FeTi and FeB starting powders and it shows that Fe_2B is present. Again, this phase diagram is used as a rough guide.

AISI-SAE Grade	BS Grade	%C	%Cr	%Ni	% Others	Tensile Strength ($MN.m^{-2}$)	Yield Strength ($MN.m^{-2}$)	% Elong.
Austenitic:								
201	-	0.15	17	5	6.5 Mn	650	310	40
304	304S15	0.08	19	10	-	520	205	30
304L	304S12	0.03	19	10	-	520	205	30
316	316S16	0.08	17	12	2.5 Mo	520	205	30
321	321S12	0.08	18	10	0.4 Ti	585	240	55
347	347S17	0.08	18	11	0.8 Nb	620	240	50
Ferritic:								
430	430S15	0.12	17	-	-	450	205	22
442	442S19	0.12	20	-	-	520	275	20
Martensitic:								
416	416S21	0.15	13	-	0.6 Mo	1240	965	18
431	431S29	0.20	16	2	-	1380	1035	16
440C	-	1.10	17	-	0.7 Mo	1965	1895	2

Table 4.1: Typical compositions and properties of stainless steels [Askeland,1996]

Crystal structure	Space Group	Lattice parameter, a (Å)	Theoretical density (g/cm^3)	Melting point (°C)
Cubic	$Fm3m\ (O^5_h)$	4.327	4.91	3067

Table 4.2: Properties of titanium carbide [Holleck,1986; Storms,1967]

	θ (°)	W ($mJ\ m^{-2}$)
$TiC_{0.98}$	120	650
$TiC_{0.60}$	50	2100
$TiC_{0.50}$	0	2600

Table 4.3: Contact angle (θ) and work of adhesion (W) of copper at T ≈ 1371 K on TiC_x [Eustathopoulos,1991]

TiC_x	Lattice parameter, a
$TiC_{0.98}$	4.326
$TiC_{0.85}$	4.319
$TiC_{0.66}$	4.307
$TiC_{0.49}$	4.297

Table 4.4: Effects of changing C/Ti ratio on the lattice parameter of TiC_x [Ramqvist,1986]

Specific heat capacity, C_p (J / deg mole) at 298K	Enthalpy of formation, ΔH_f (kJ / mol) at 298K	Gibbs free energy of formation, ΔG_f (kJ / mol) at 298K
33.6	-183	-181

Table 4.5:Thermal properties of TiC [Storms,1967 ; Kubaschewski, 1983]

Crystal structure	Lattice parameters		Theoretical density (g/cm^3)	Melting point
	a (Å)	c (Å)		°C
Hexagonal	3.0303	3.230	4.52	3225

Table 4.6: Properties of titanium diboride [Cutler,1991]

Specific Heat capacity, C_p (J / deg mole) at 298K	Enthalpy of formation, ΔH_f (kJ / mol) at 298K	Gibbs free energy of formation, ΔG_f (kJ / mol) at 298K
44.5	-323	-319

Table 4.7: Thermodynamic data for TiB_2 [Cutler,1991]

Carbide phase	Crystal structure	Lattice parameters			Theoretical density (g/cm^3)	Melting point (°C)
		a (Å)	b (Å)	c (Å)		
Titanium carbide (TiC)	Cubic (fcc)	4.327	-	-	4.93	3067
Titanium diboride (TiB_2)	Hexagonal	3.030	-	3.230	4.52	3225
Tungsten carbide (WC)	Hexagonal	2.51	-	2.84	15.72	2776
Chromium carbide (Cr_3C_2)	Orthorhombic	11.46	5.52	2.821	6.68	1810

Table 4.8: Properties of TiC, TiB_2, Cr_3C_2 and WC [Holleck,1986; Storms,1967; Berger,1996]

	Specific heat capacity, Cp (J / deg mole) at 298K	Enthalpy of formation, ΔH_f (kJ / mol) at 298K	Gibbs free energy of formation, ΔG_f (kJ / mol) at 298K
TiC	33.6	-183	-181
TiB_2	44.5	-323	-319
WC	35.5	-38	-37
Cr_3C_2	97.5	-109	-13.5

Table 4.9: Thermal properties of selected hard phases [Kubaschewski, 1983; Cutler,1991]

Hard Phase	Hardness (kgf mm^2)
TiC	3200
TiB_2	3650
Cr_3C_2	1400
WC	2200

Table 4.10: Hardness values of selected ceramic phases [Berger,1996; Cutler,1991]

	TiC (km/cm^3)	TiB_2 (km/cm^3)	SiC (km/cm^3)	B_4C (km/cm^3)
SiC	2	3	4	10
Al_2O_3	5	10	19	23
Hardness (kgf mm^2)	2700	2800	3500	4050

Table 4.11: Abrasive wear resistance of different single-phase hard materials using both silica and alumina abrasives [Holleck,1986]

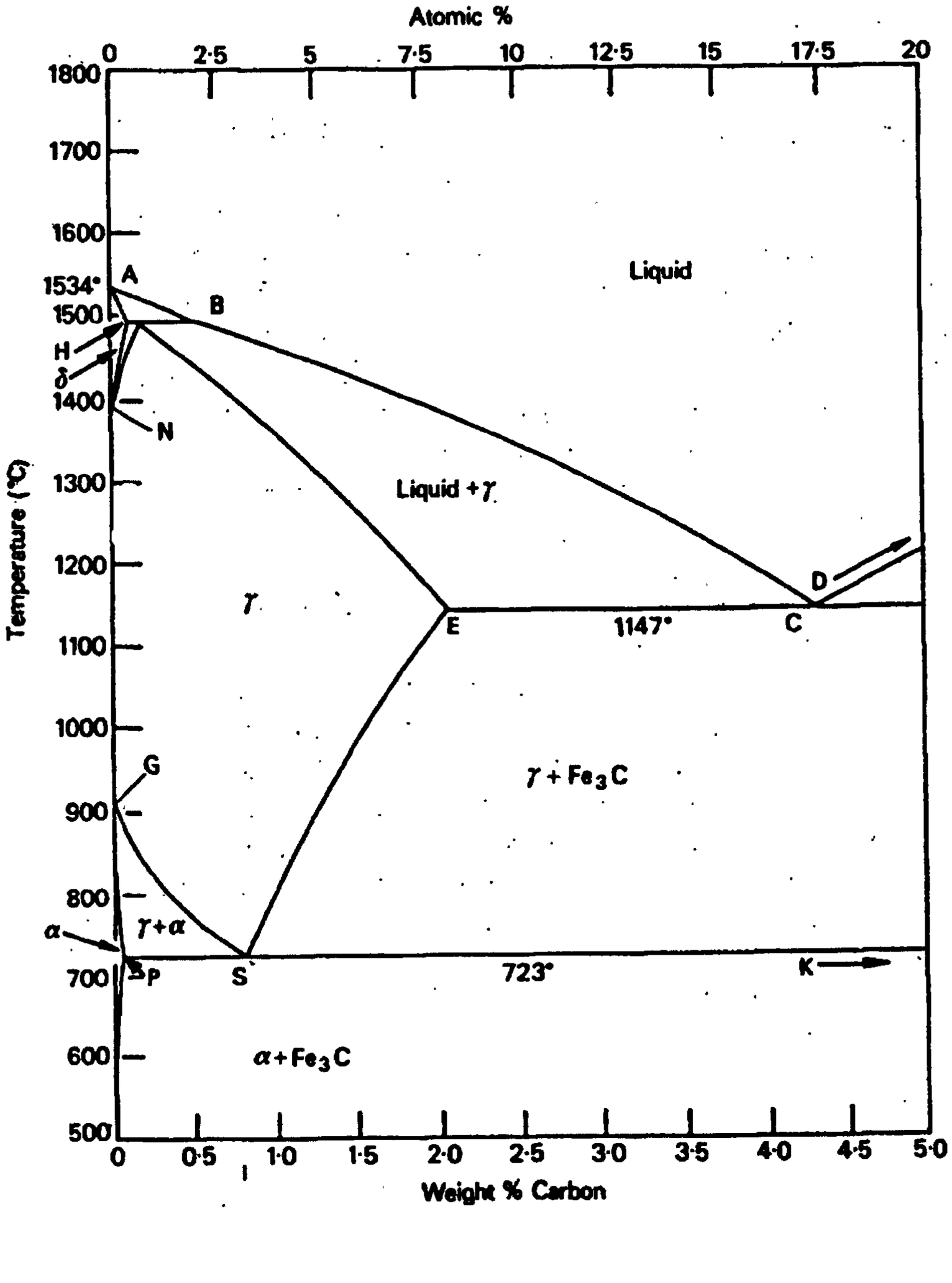

Figure 4.1: Iron-carbon equilibrium diagram [Honeycombe,1995]

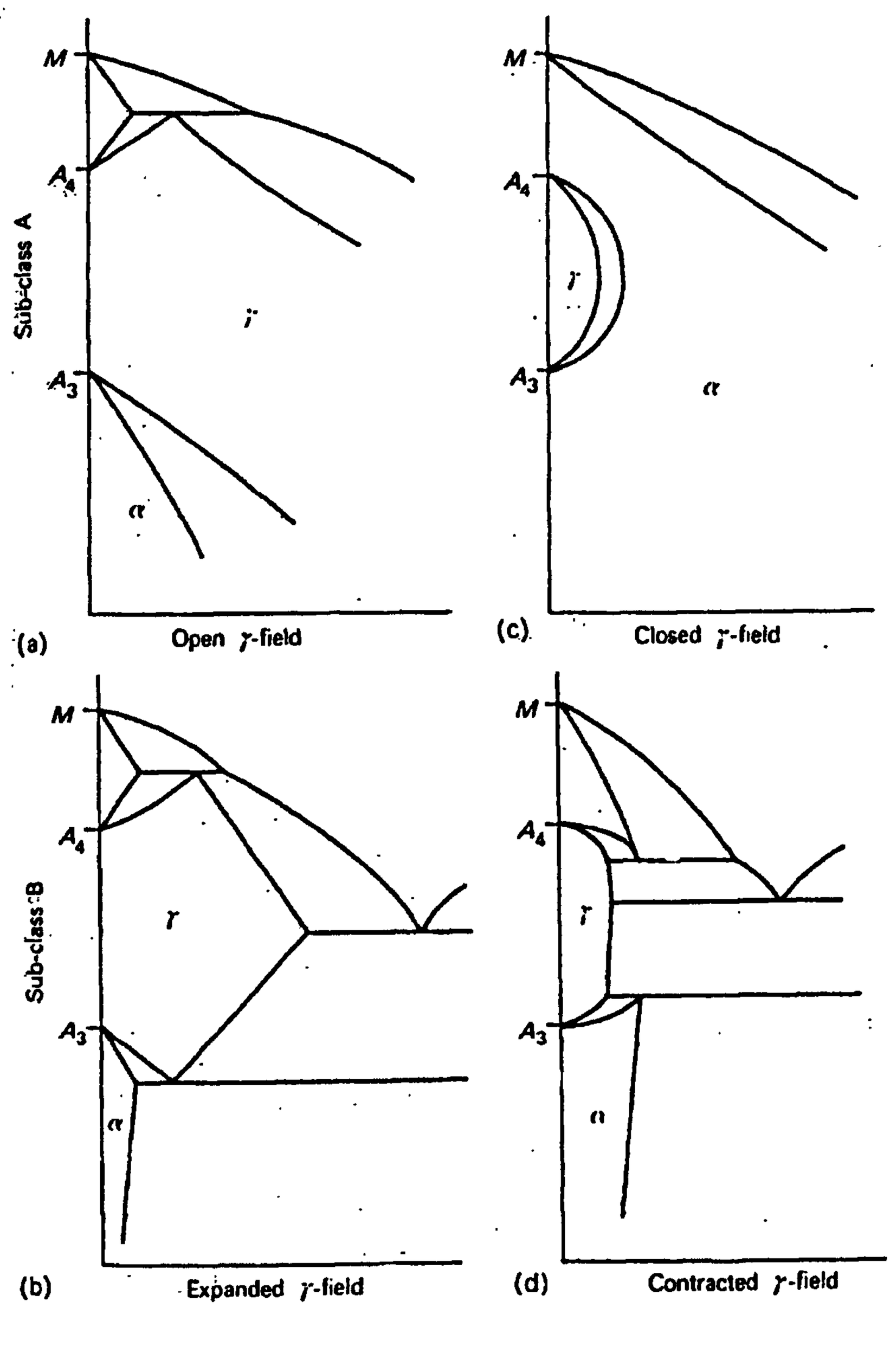

Figure 4.2: Classification of iron alloy phase diagrams. (a) open γ-field; (b) expanded γ-field; (c) closed γ-field; (d) contracted γ-field [Honeycombe,1995]

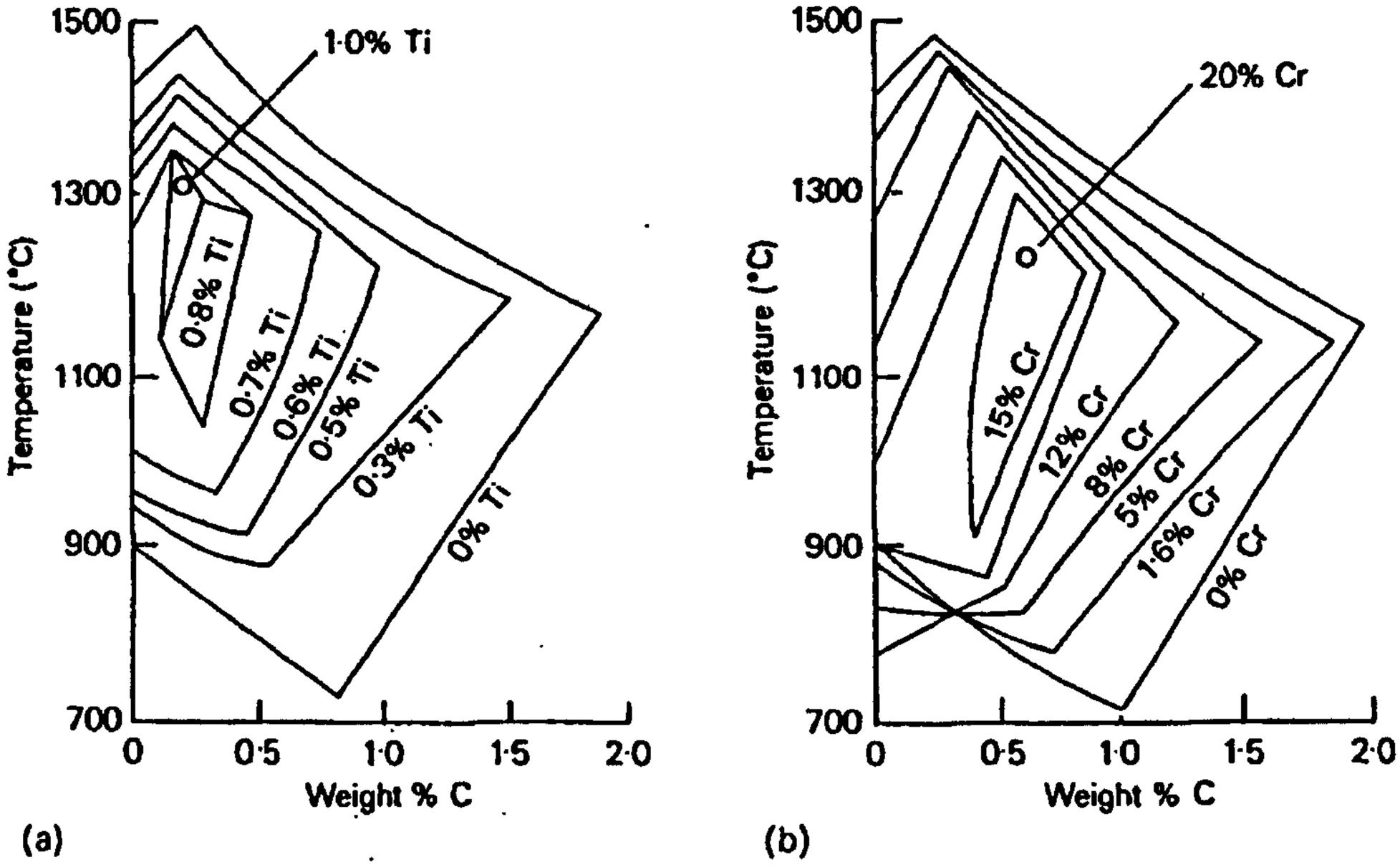

Figure 4.3: Effect of alloying elements on the γ-phase field. (a) titanium; (b) chromium [Honeycombe,1995]

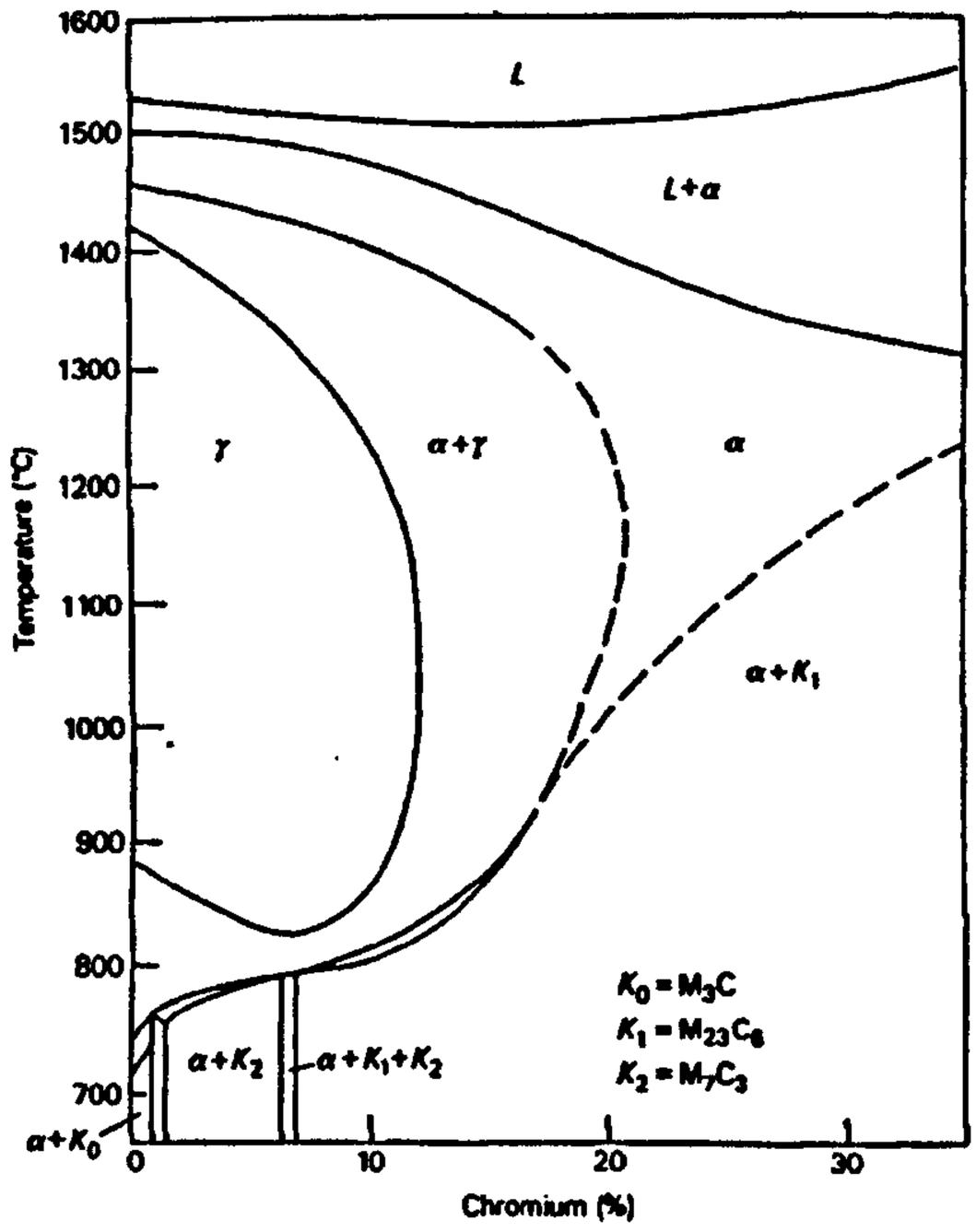

Figure 4.4: Effect of 0.05 wt% C on the Fe-Cr phase diagram [Honeycombe,1995]

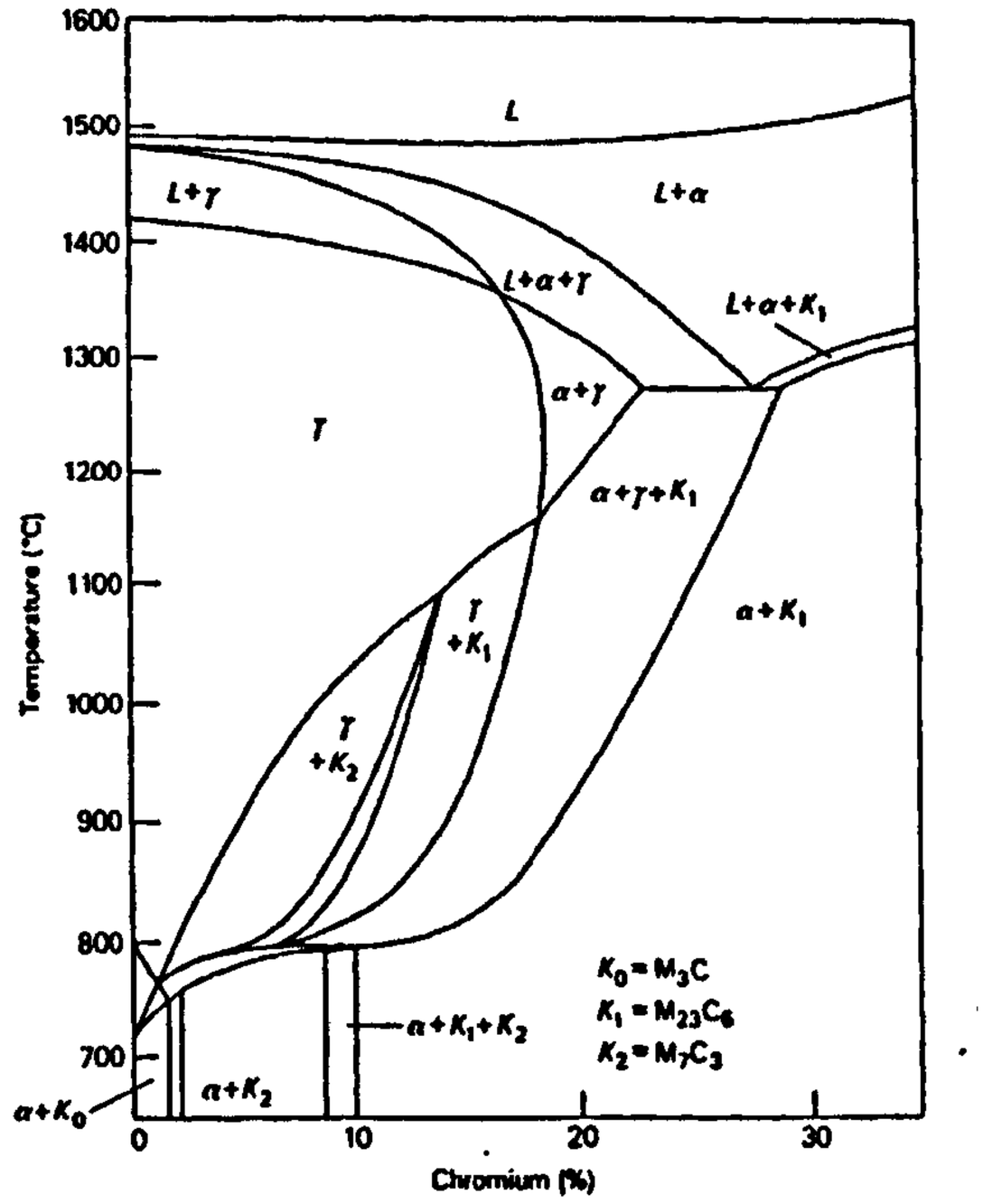

Figure 4.5: Effect of 0.4 wt% C on the Fe-Cr phase diagram [Honeycombe,1995]

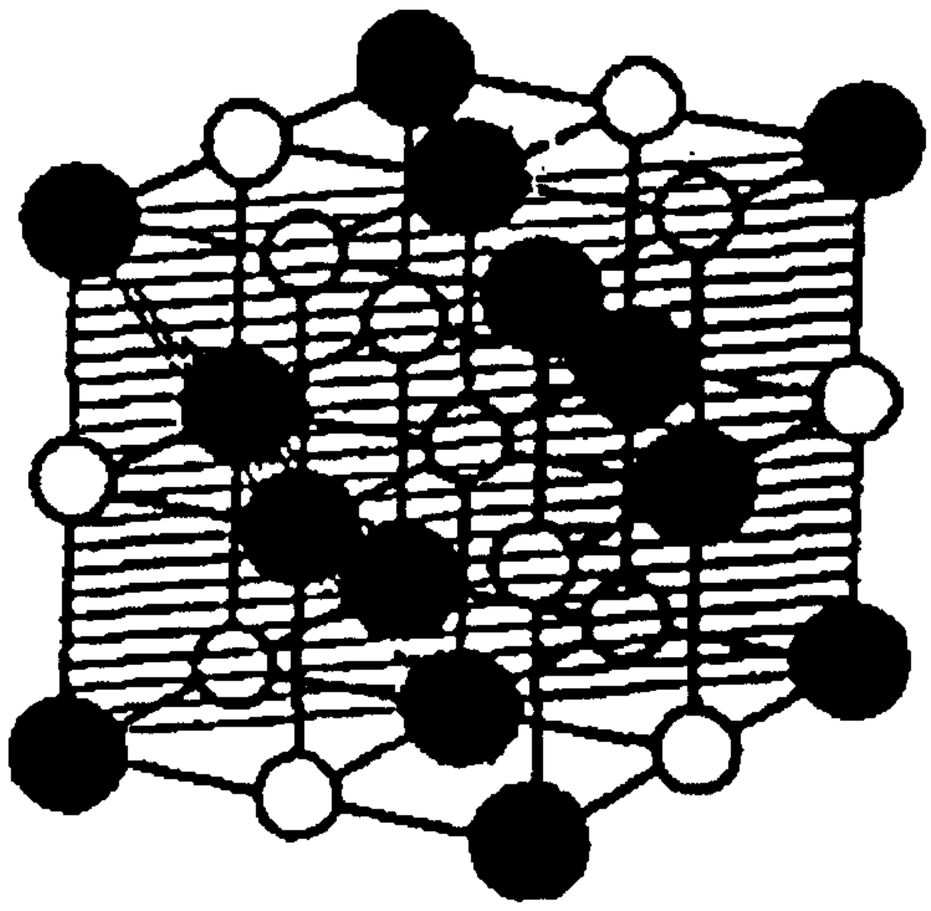

Figure 4.6: Crystal structure of titanium carbide [Holleck, 1986]

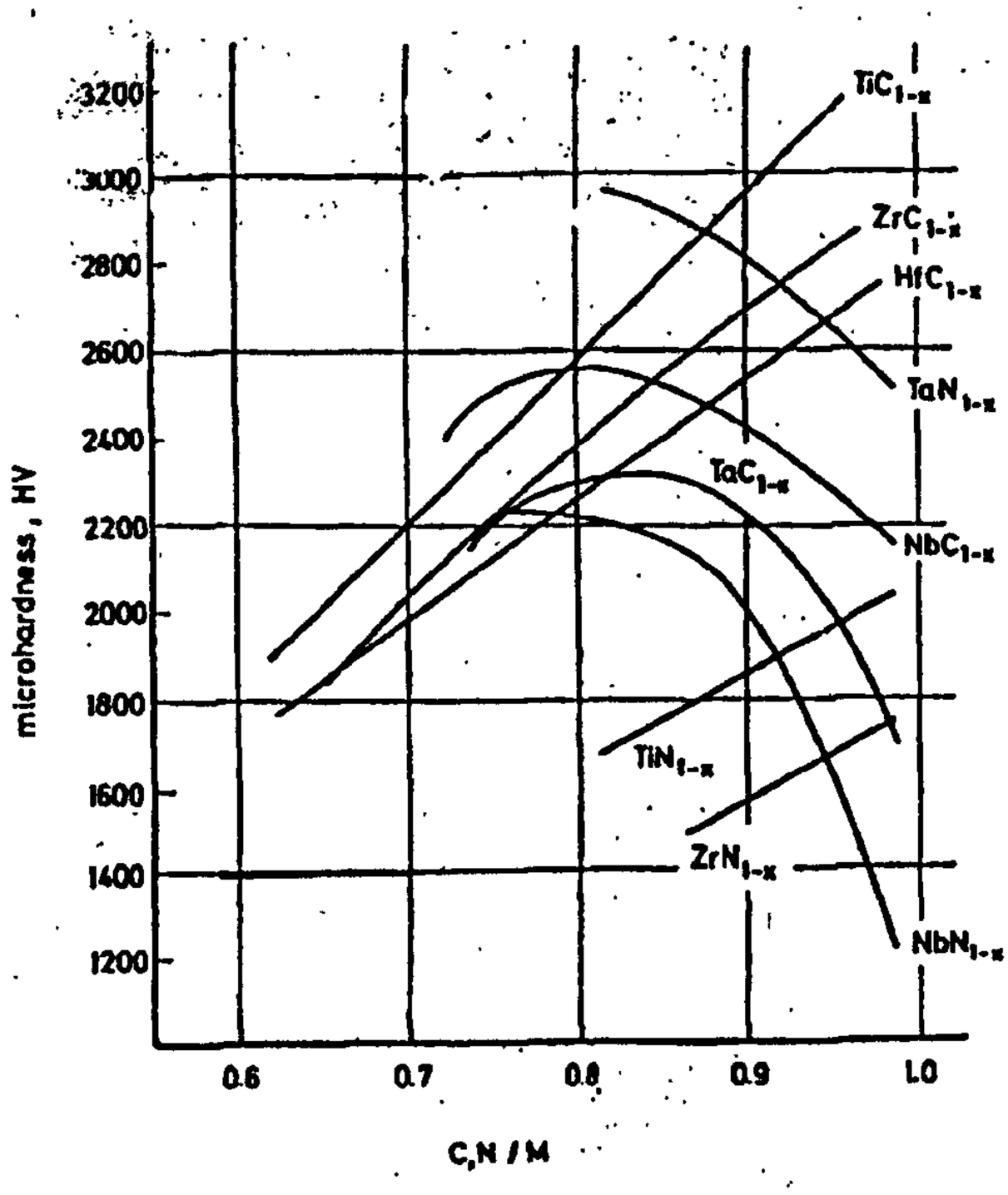

Figure 4.7: Effect of nonmetal-metal ratio on hardness [Holleck,1986]

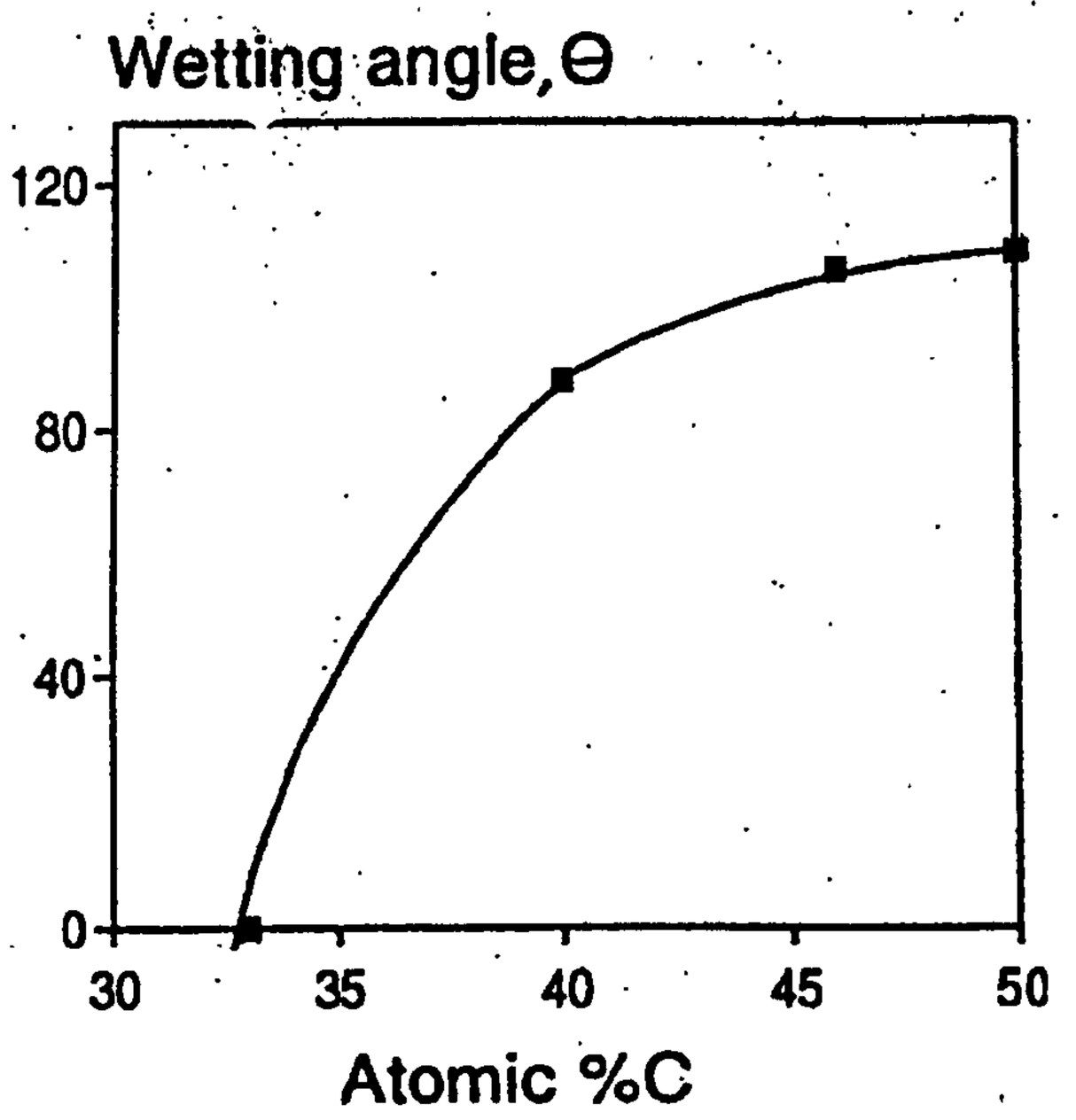

Figure 4.8: Wettability of TiC by liquid Cu at 1100°C versus carbon composition [Morozova,1962]

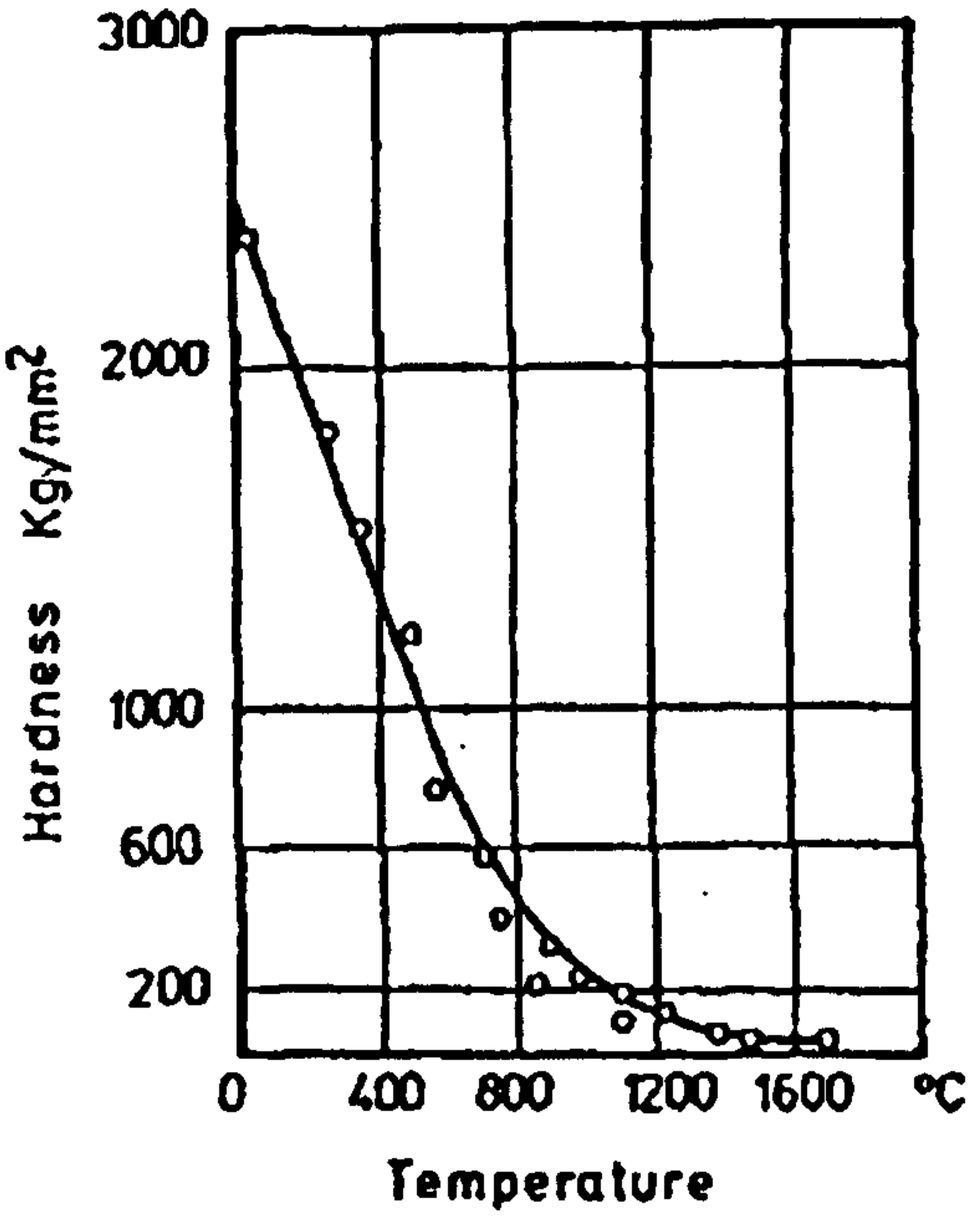

Figure 4.9: Elevated temperature hardness of TiC cutting tool material [Ramalingam,1977]

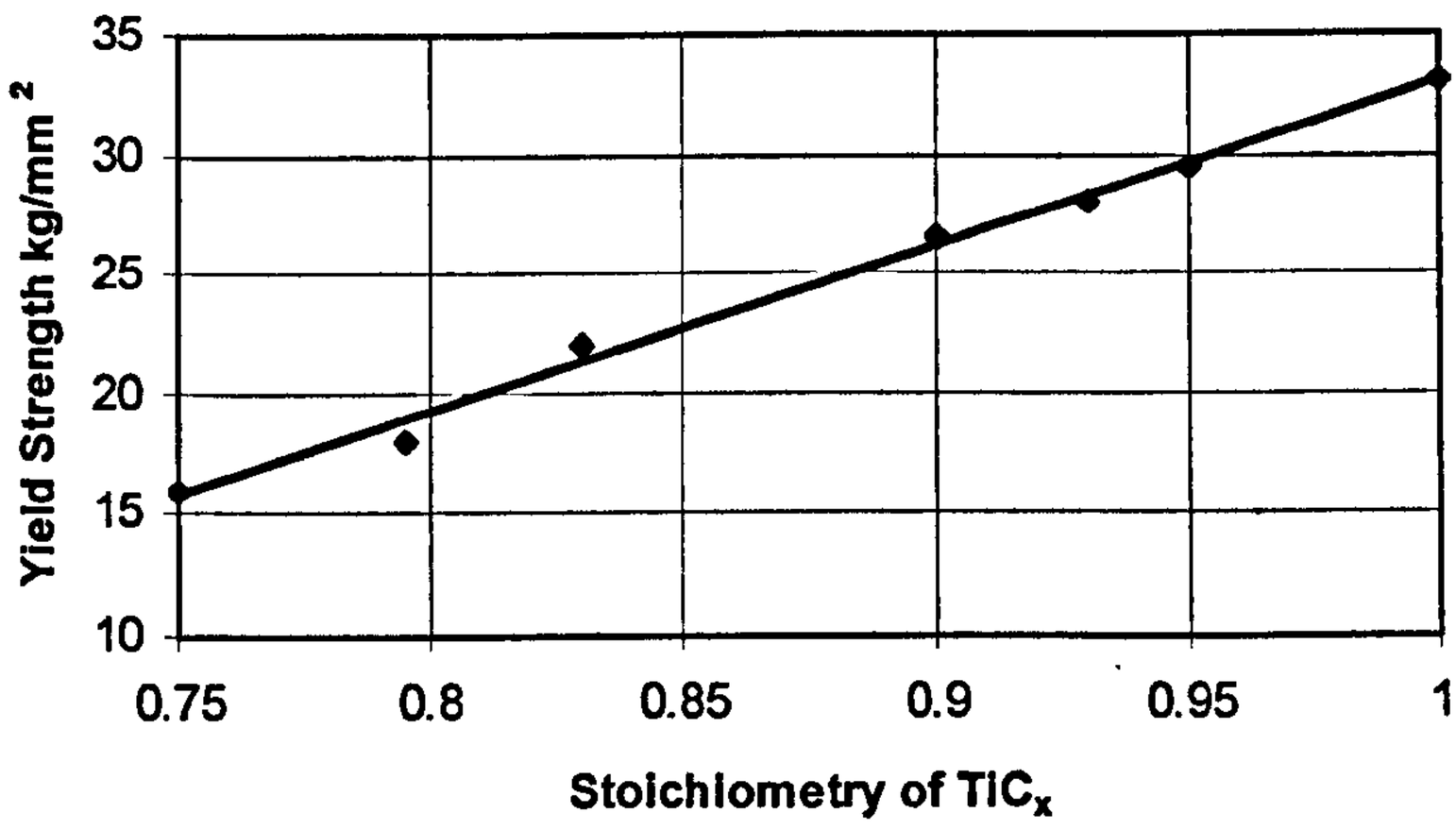

Figure 4.10: Yield strength as a function of TiC stoichiometry at 800°C [Ramalingam,1977]

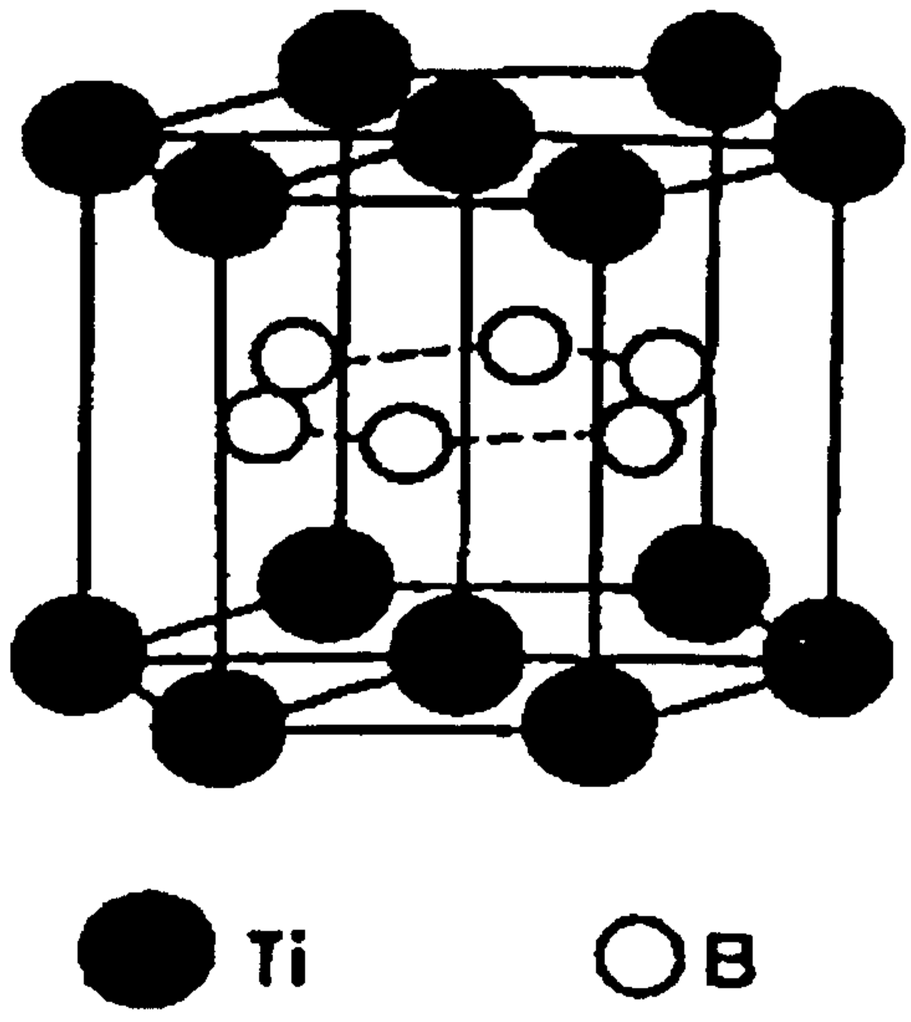

Figure 4.11: Crystal structure of titanium diboride [Holleck,1986]

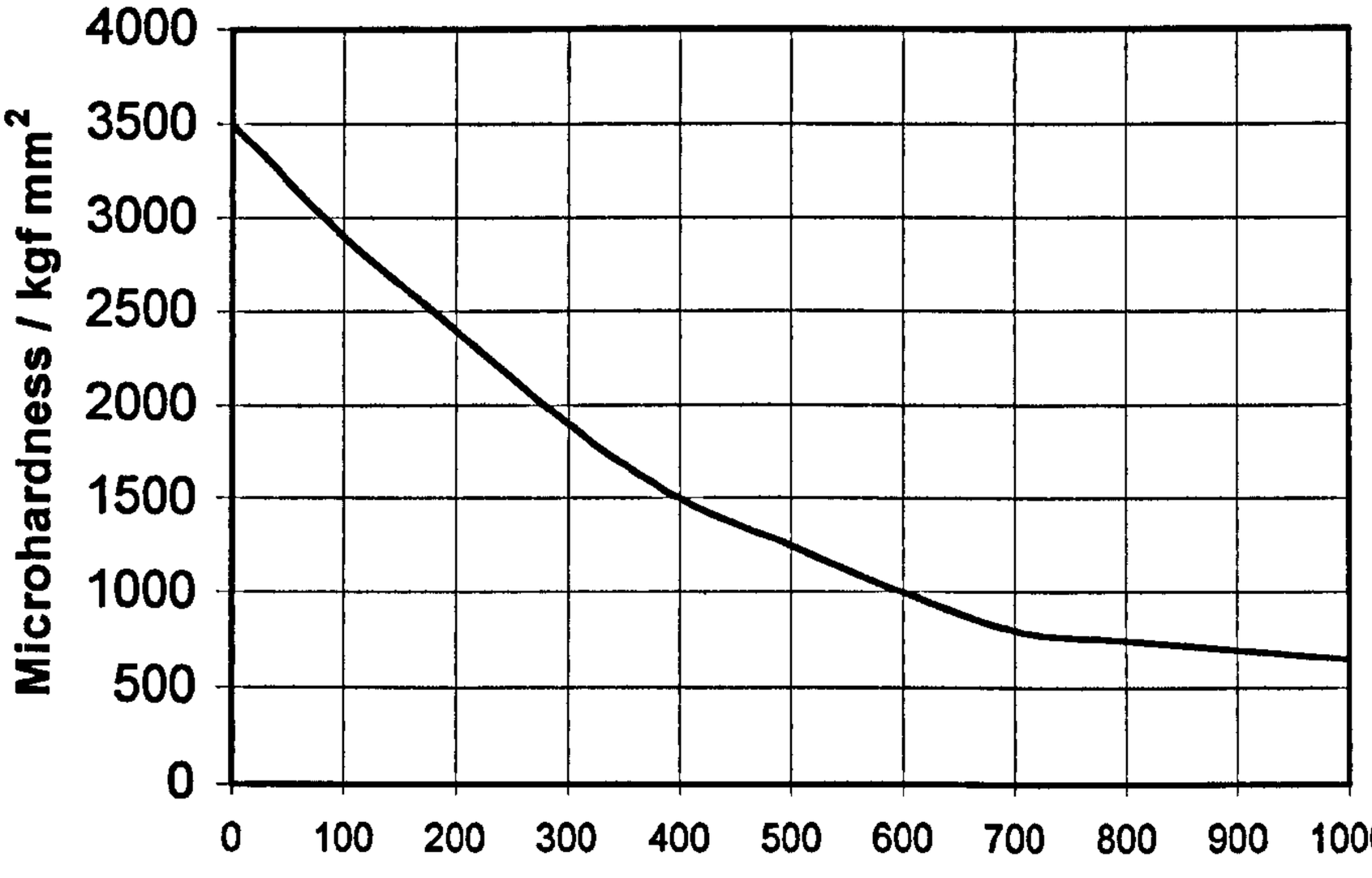

Figure 4.12: Hardness of TiB_2 as a function of temperature [Cutler,1991]

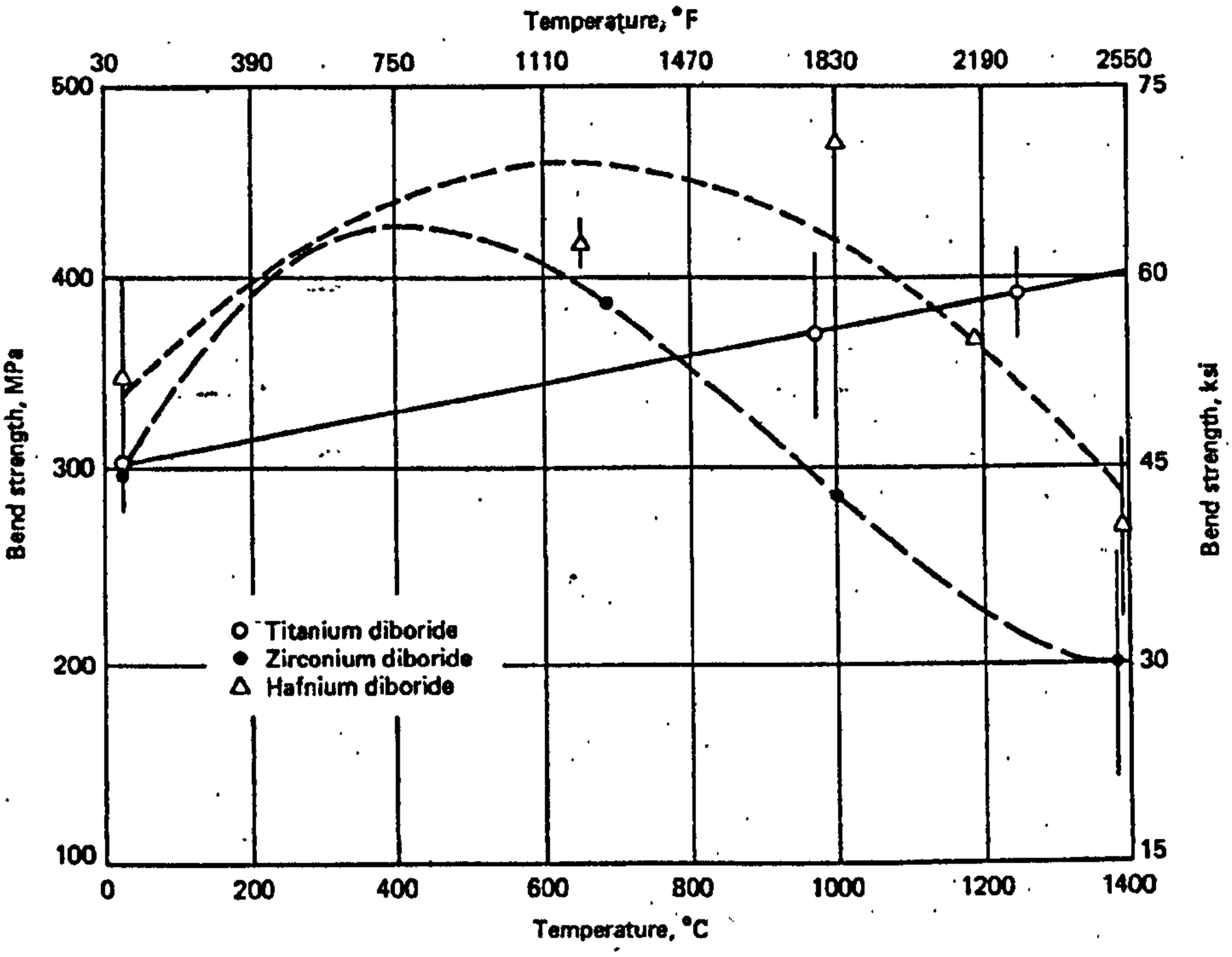

Figure 4.13: Strength of TiB_2 as a function of temperature [Cutler,1991]

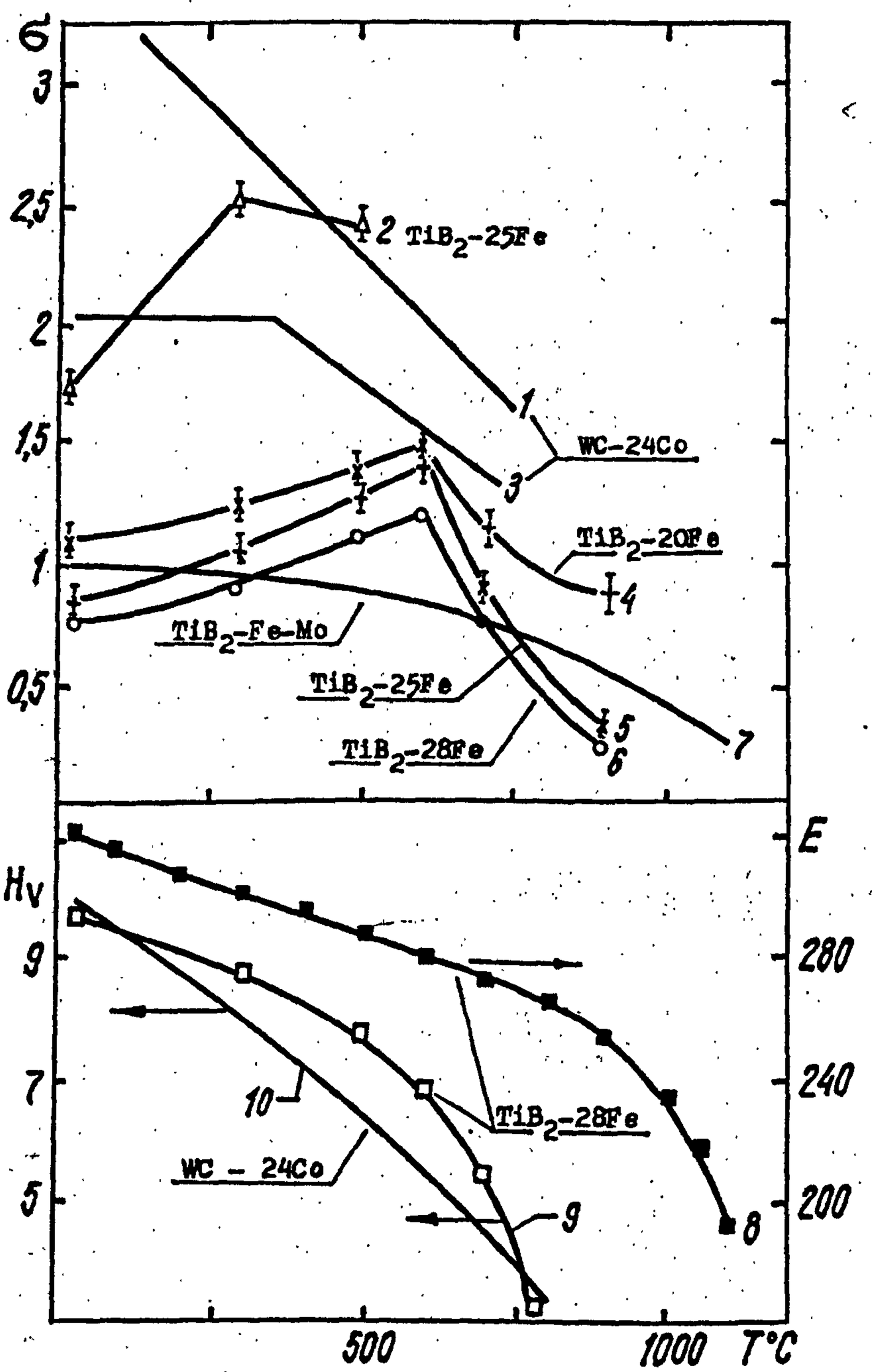

Figure 4.14: Effect of temperature on mechanical properties of Fe-TiB_2 (2,4-6,8,9) Fe-Mo-TiB_2 (7) and WC-Co (1,3,10) cermets. Temperature dependence of Compression (1,2) and Bending Strength (σ) (3-7), Young's Modulus(E) (8), Hardness (Hv) (9,10) [Andrievski,1992]

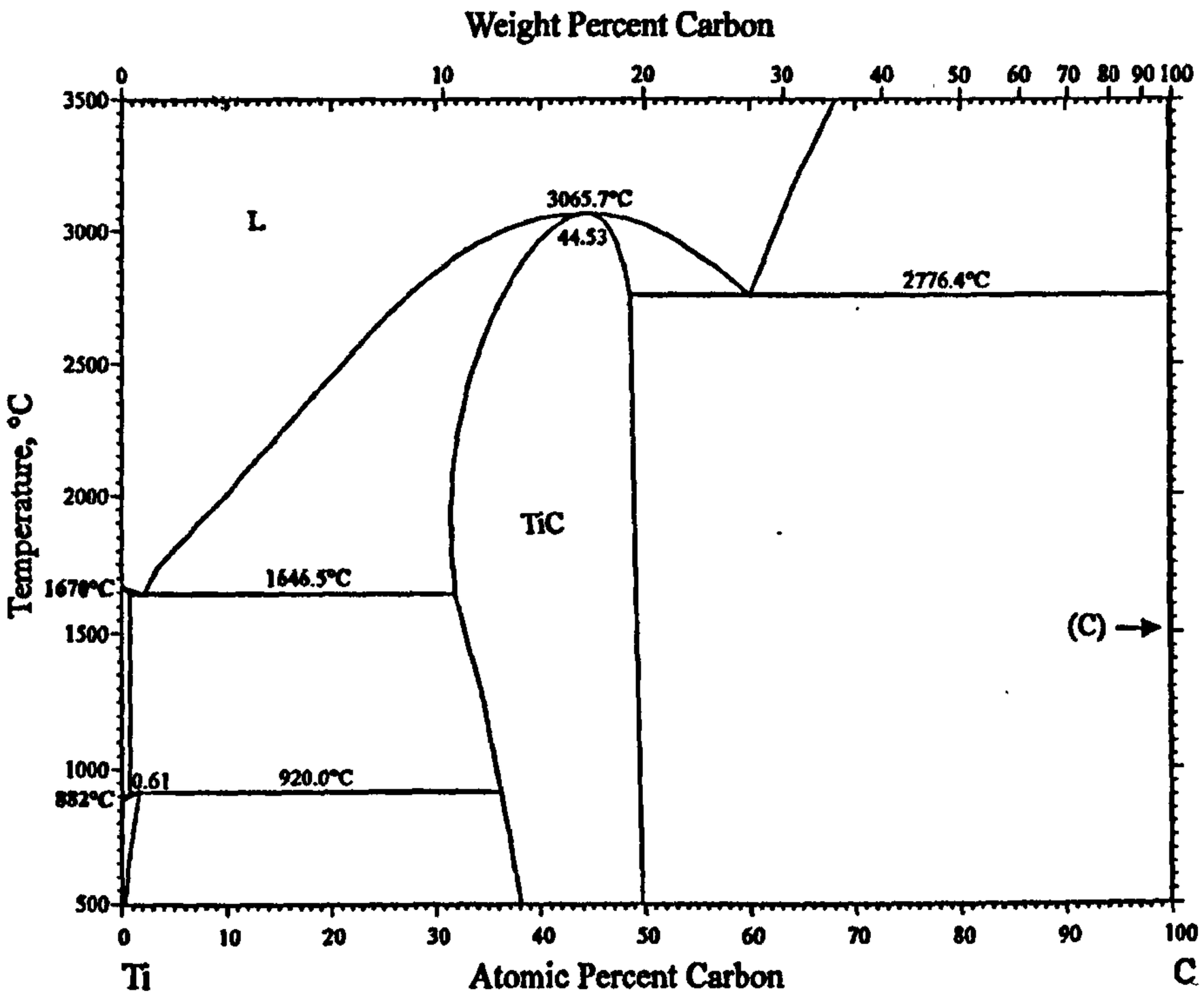

Figure 4.15: Ti-C binary phase diagram [Bandyopadhyay,1999]

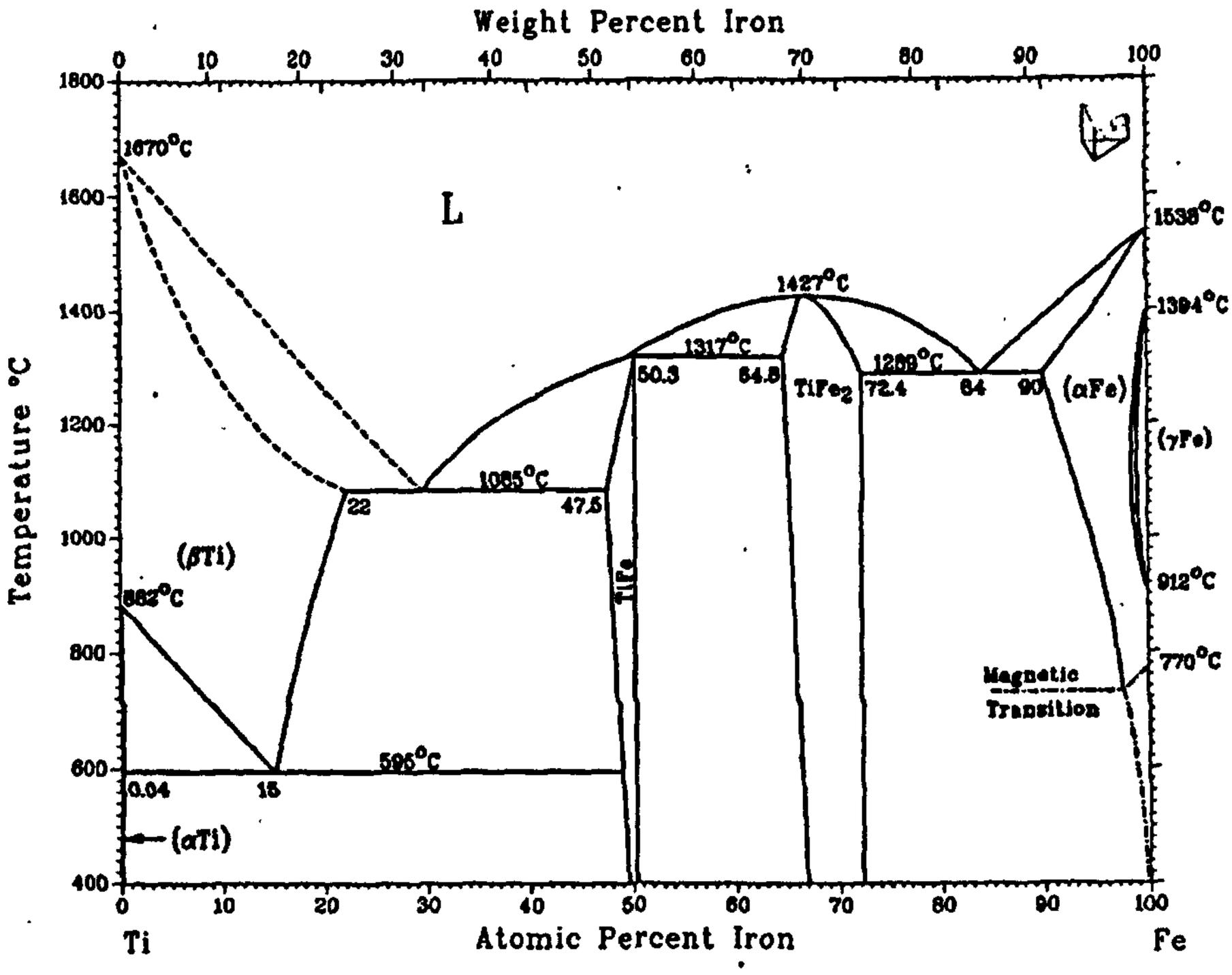

Figure 4.16: Fe-Ti binary phase diagram [Murray]

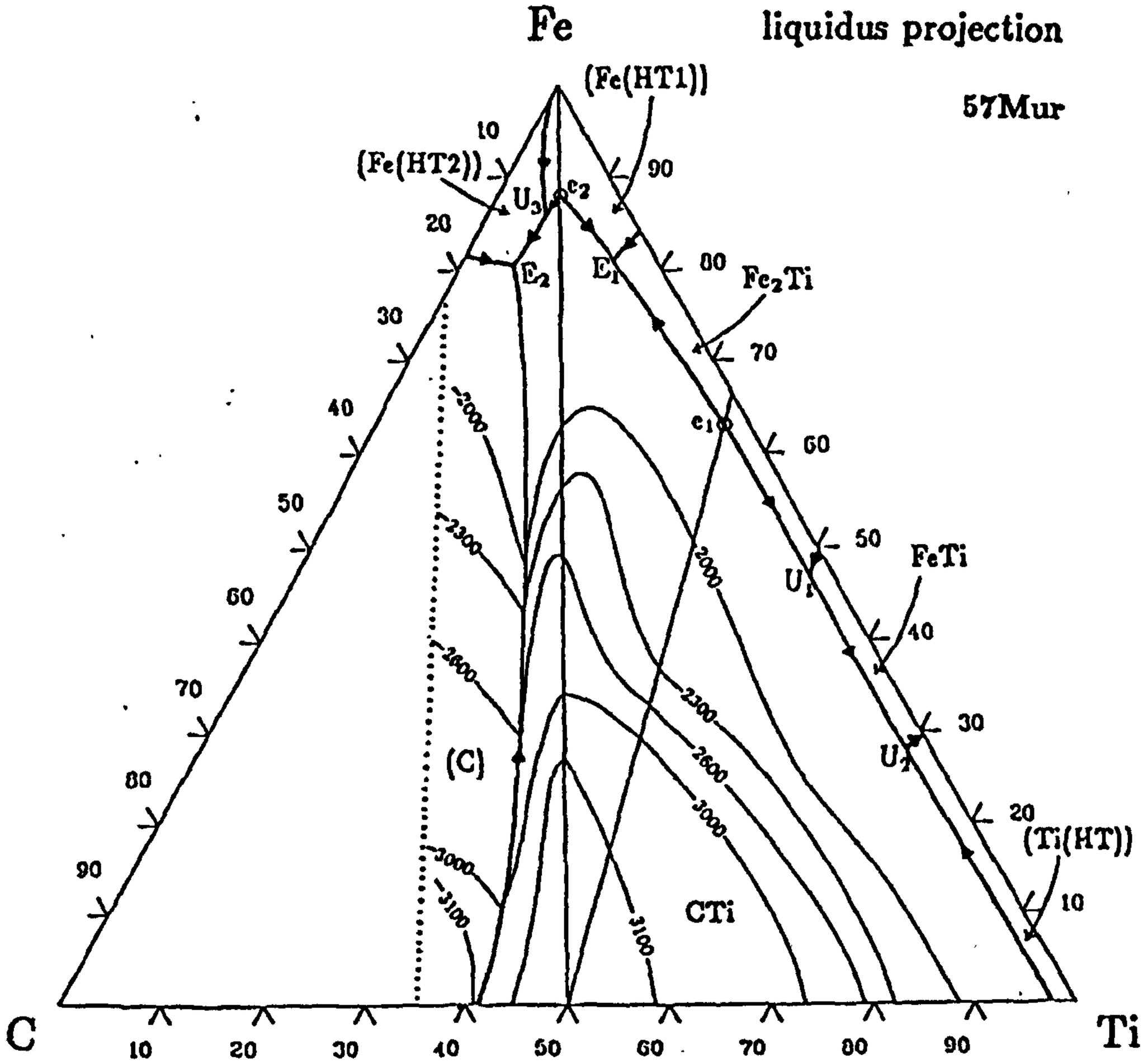

Reaction Scheme

e_1 :	$l \leftrightarrow TiC + Fe_2Ti$	1520°C
e_2 :	$l \leftrightarrow TiC + (Fe(HT1))$	~1350°C
E_1 :	$L \leftrightarrow TiC + (Fe(HT1)) + Fe_2Ti$	1340°C
E_2 :	$L \leftrightarrow (C) + TiC + (Fe(HT2))$	~1130°C
U_1 :	$L + Fe_2Ti \leftrightarrow TiC + FeTi$	1300°C
U_2 :	$L + TiC \leftrightarrow FeTi + (Ti(HT))$	1100°C
U_3 :	$L + (Fe(HT1)) \leftrightarrow TiC + (Fe(HT2))$	1320°C

*NB - (Fe(HT1)) is bcc
- (Fe(HT2)) is fcc

Figure 4.17: Fe-Ti-C ternary phase diagram [Murakami,1957]

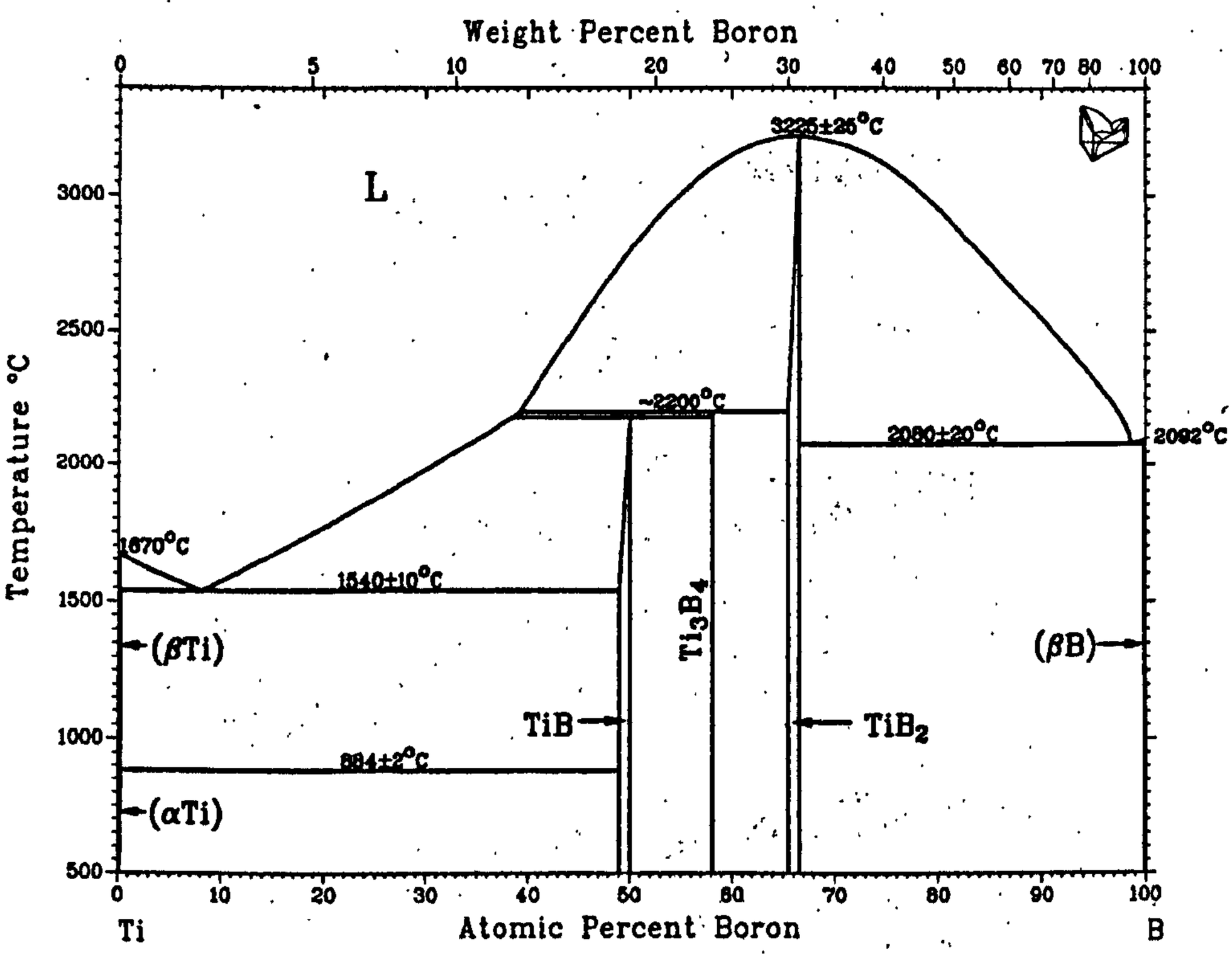

Figure 4.18: Ti-B binary phase diagram [Murray]

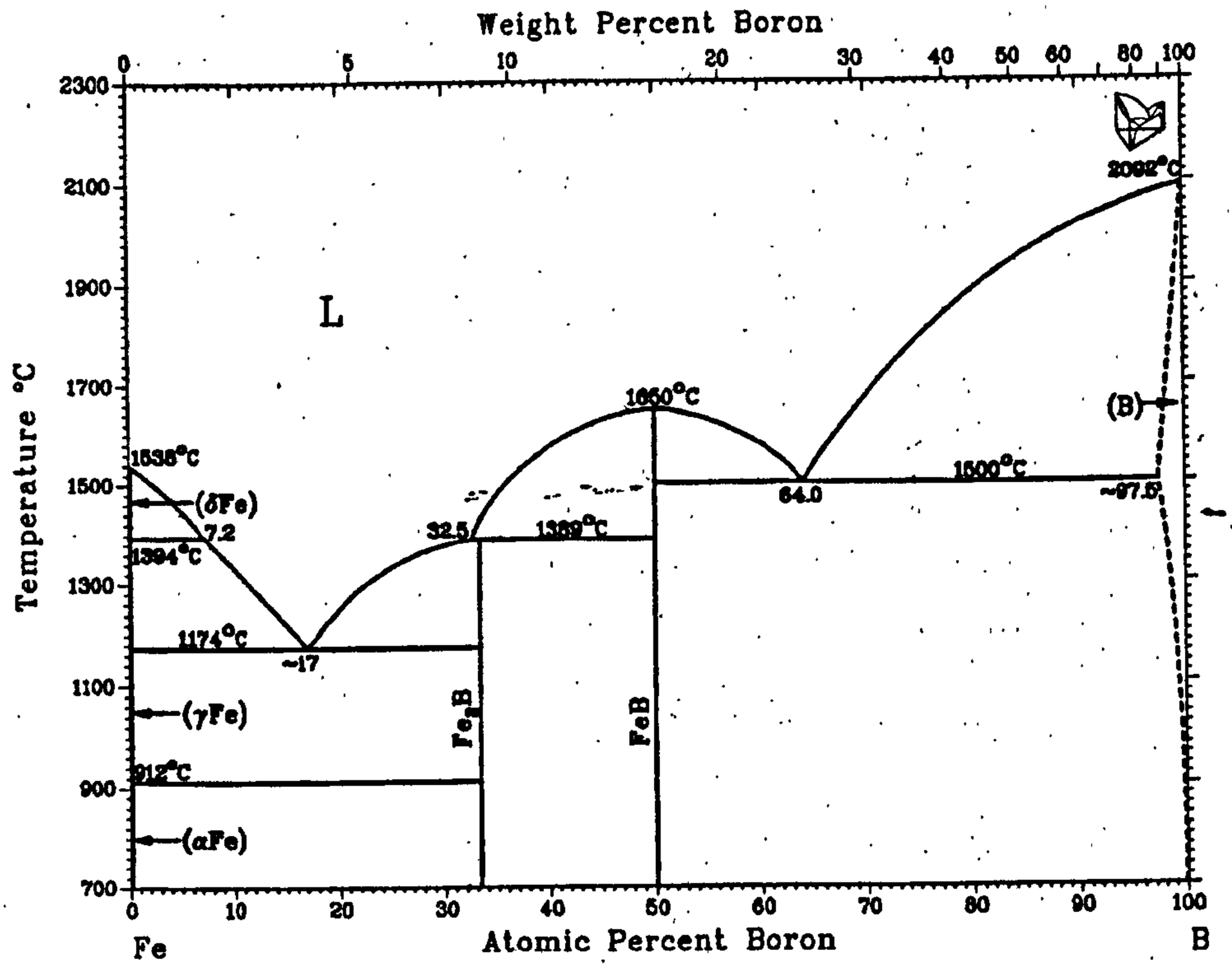

Figure 4.19: Fe-B binary phase diagram [Liao]

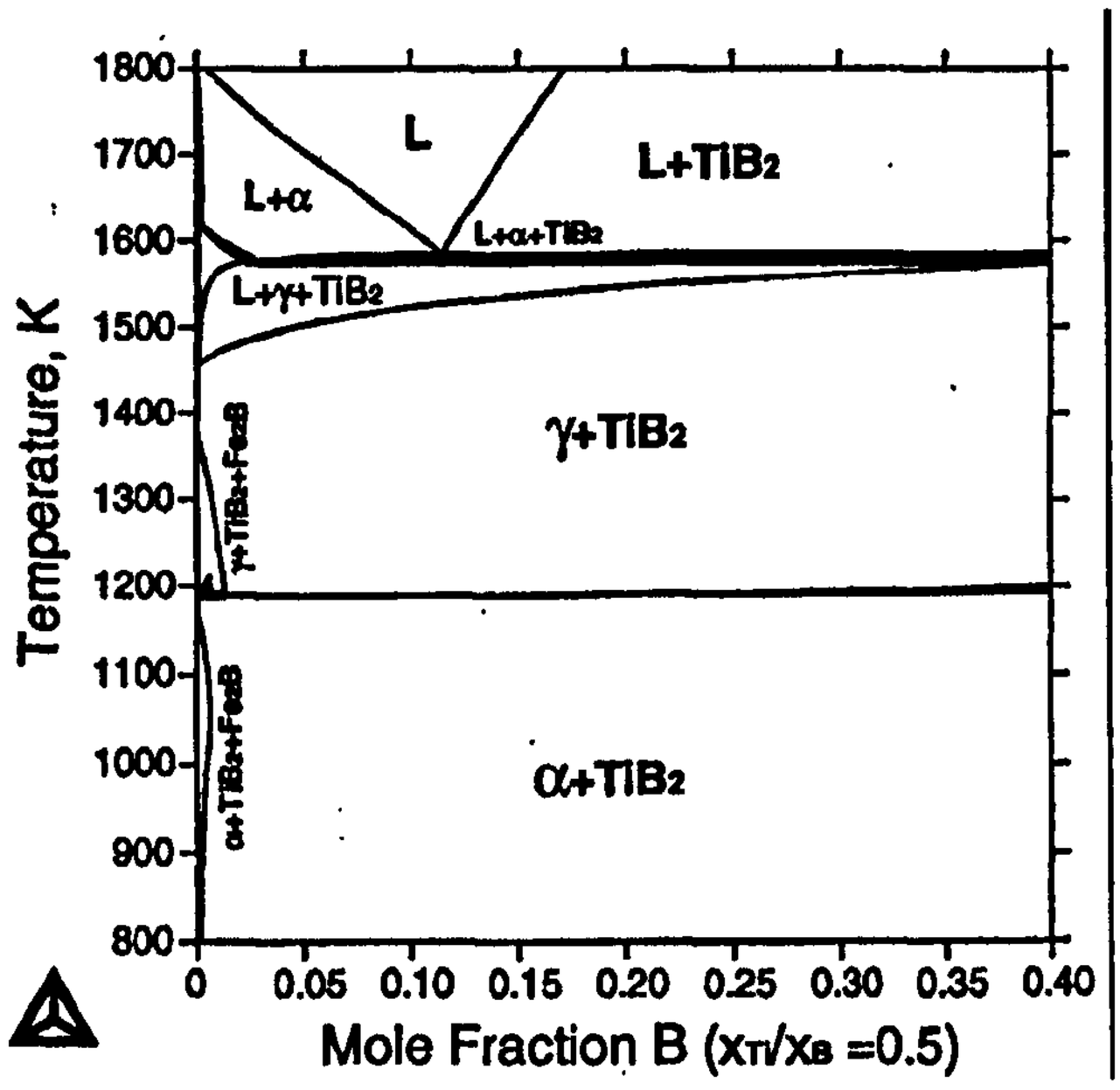

Figure 4.20: Pseudobinary phase diagram from an isothermal section at 1273 K [Tanaka,1999]

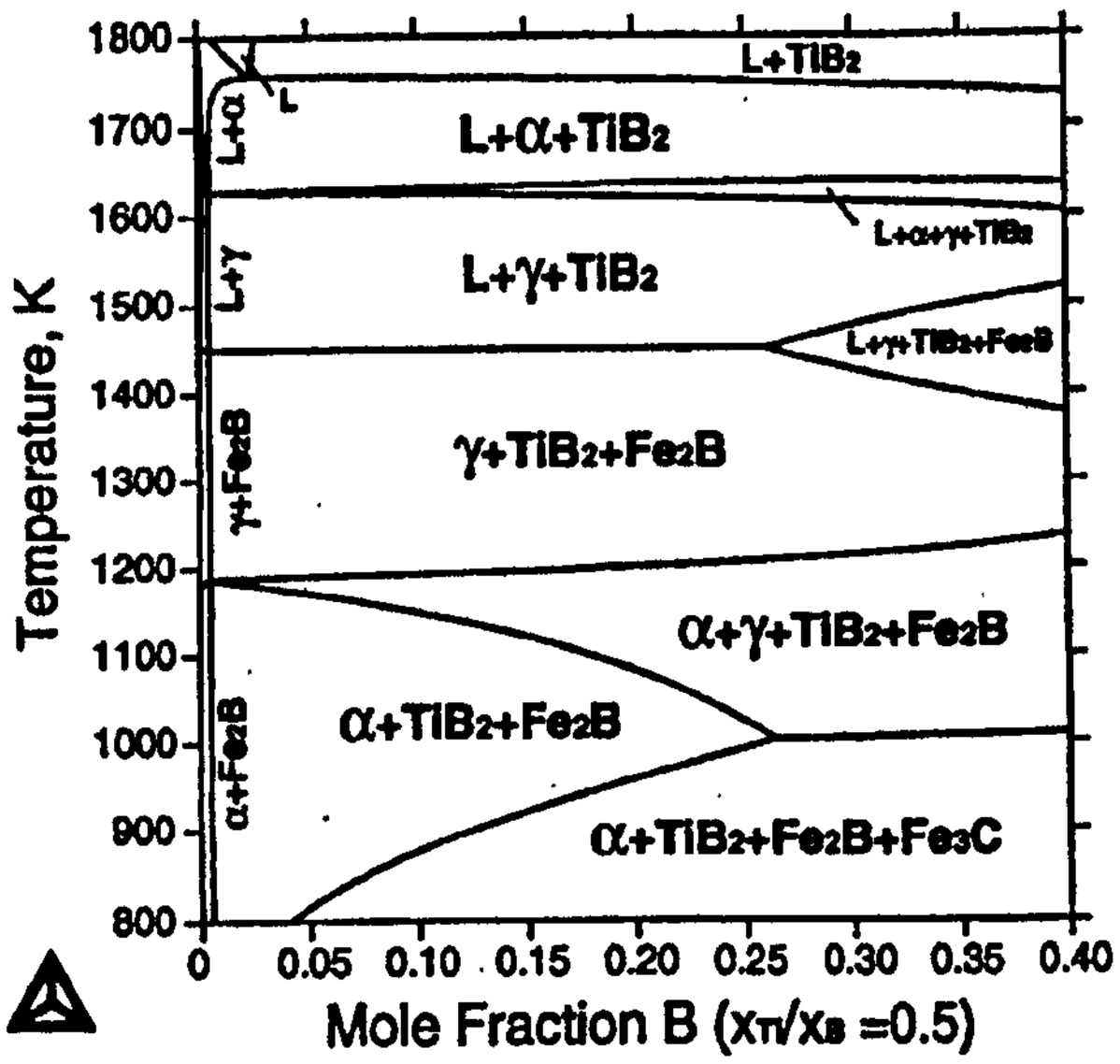

Figure 4.21: $FeTiB_2$ pseudobinary phase diagram [Tanaka,1999]

5 Wear

According to Tylczak [1992] wear is defined as damage to a solid surface that generally involves progressive loss of material and is due to relative motion between that surface and a contacting body. Wear processes can be divided into two categories. Single-phase wear and multiple-phase wear [Bhushan and Gupta,1997]. In single-phase wear, a solid, liquid or gas moving relative to a surface causes material to be removed from the surface. The relative motion may be sliding (unidirectional or reciprocating) or rolling. In multi-phase wear, the solid, liquid or gas moving relative to a sliding surface acts as a carrier for a second phase (particle, asperity, liquid drop, and gas bubble) that actually produces the wear. Some of the different types of wear phenomena are discussed, along with their mechanisms, in section 5.1.

5.1 Types of wear

Wear can occur by many processes, namely, adhesive wear, abrasive wear, fatigue wear, corrosive wear, fretting wear, erosive wear and cavitation wear. Adhesive wear occurs when two solid surfaces slide over one another under an applied load. Surface projections or asperities are plastically deformed and eventually welded together by the high local pressures. Corrosive wear occurs when wear is taking place in a corrosive environment and the wear debris is often highly corroded. Fretting wear takes place when components are subjected to very small vibratory movements at high frequency. This process is initiated by adhesion followed by abrasion. This effect can also be increased by corrosion.

Erosive wear is the removal of material by impingement of solid particles onto the surface. Finally, cavitation wear arises when a fluid is in relative motion with a surface and bubbles formed in the fluid become unstable and implode against the surface of the material causing erosion

Abrasive wear is the predominant wear mechanism which is most likely to occur in the dry-sand rubber-wheel abrasive wear testing of cermet coatings (Section 4.6.1), although, fatigue wear may also contribute to material loss. A brief description of both wear mechanisms is shown below.

5.1.1 Fatigue wear

Fatigue wear occurs by the cyclic loading and unloading of a surface as a result of sliding, rolling or impacting motions. The repeated movements initiate cracks which in time link up and cause the material to spall away. Fragments are then free to move between the contacting surfaces. This type of failure can occur after a large number of loading cycles even where the applied load is below that expected to produce failure in a single loading application.

5.1.2 Abrasive wear

Abrasive wear can occur due to hard particles or protuberances that are forced against and moved along a solid surface forming scratches and grooves. The main mechanisms of abrasive wear are plastic deformation and brittle fracture.

5.2 Abrasive wear

Wear by abrasion is very common and it has been estimated by Eyre [1976] that 50% of all wear problems in industry are due to abrasion. This has a significant cost and Tylczak [1992] has estimated that the cost of abrasion in an industrialised nation can range from 1 to 4% of the gross national product (GNP) of that nation.

Abrasion is classified according to the types of contact, namely two-body and three-body abrasion. Two-body abrasion occurs when an abrasive slides along a surface and is not free to rotate, and three-body abrasion occurs when an abrasive is caught between two surfaces and is free to rotate between them. It can be further classified in terms of the amount of abrasive fragmentation occurring in the system. Low–stress abrasion occurs when there is little fragmentation of the abrasive, whereas high-stress abrasion, or gouging abrasion, exists when abrasive fragmentation is more prominent.

5.2.1 Two-body abrasion

As mentioned earlier, two-body abrasion occurs when an abrasive slides along a surface, e.g. when sanding down wood with abrasive paper (Figure 5.1a). Tylczak [1992] quotes that a two-body system experiences from 10 to 1000 times as much loss as three-body systems for a given load and path length of wear. This is because in three-body abrasion, the abrasive is free to roll between the surfaces, and indentation and ploughing will occur more often, and cutting less often, than

if the abrasive was fixed to the counterface as in two-body wear. The volume of material removed by two-body abrasion is directly proportional to the sliding distance and the normal load and inversely proportional to the hardness of annealed pure metals [Hutchings,1992].

5.2.2 Three-body abrasion

Three-body abrasion occurs when an abrasive is free to roll and slide between two surfaces (Figure 5.1b). The rate of three-body abrasion, as with two-body abrasion, is dependent upon a number of factors, namely, hardness, fracture strength and size of the abrasive particles, the hardness and roughness of the surfaces and the type of motion [Dept. of Trade and Industry,1986]. The types of mechanisms which can occur when a single abrasive tip traverses a surface are discussed in section 5.2.4.

5.2.3 Archard equation

Equation 5.1 is commonly known as the Archard equation, which was originally derived for adhesive wear but is widely used for abrasive wear also. The Archard equation is based upon the concept of a single abrasive particle acting as a scratch indenter sliding along the surface of a counterface material. Figure 5.2 shows an abrasive particle, idealized as a cone of semiangle α, being dragged across a ductile counterface which deforms under an indentation pressure, P. A groove is formed in the counterface and it assumed that wear occurs by some removal of the counterface material being displaced by the particle. The normal load, w, which

is carried by the particle, is supported by the plastic flow beneath the particle and in turn causes a pressure, P, to act over the area of contact between the particle and the counterface. As the cone is sliding across the surface, then only the front of the cone is in contact. Therefore,

$$w = P\frac{\pi a^2}{2} = \frac{1}{2}P\pi x^2 \tan^2\alpha \text{ ---- Equation 5.1}$$

where x and a are shown in Figure 5.2.

The volume of material displaced from the groove by the cone over a sliding distance l is lax or $lx^2\tan\alpha$. If the actual fraction of material displaced from the groove is η, then the volume of wear debris produced by this one particle per unit sliding distance, q, is given by,

$$q = \eta\pi x^2 \tan\alpha \text{ ---- Equation 5.2}$$

If x^2 is substituted into Equation 5.2,

$$q = \frac{2\eta w}{\pi P \tan\alpha} \text{ ---- Equation 5.3}$$

If this effect by a single abrasive is assumed to occur over many abrasive particles, and also assuming that P ≈ H, where H is the indentation hardness of the counterface, the total volume removed per unit sliding distance, Q, is given by,

$$Q = \frac{KW}{H}$$ ---- Equation 5.4

where, W is the total applied normal load and the constant K is a material constant and is dependent upon the fraction η of displaced material actually removed.

The dimensionless wear coefficient, K, may be used as a measure of the severity of wear. Hutchings [1992] found that typical values of K in two-body abrasion of metals was within the range of $5x10^{-3}$ and $50x10^{-3}$, whereas, the less aggressive three-body abrasion within $0.5x10^{-3}$ and $5x10^{-3}$.

The dimensional wear coefficient k can also be used and is usually quoted in units of $mm^3\ m^{-1}\ N^{-1}$ and this represents the volume of material removed by wear (mm^3), per unit distance slid (m), per unit normal load of contact (N). This is particularly useful when comparing the wear rates of different materials and is given by,

$$k = \frac{K}{H}$$ ---- Equation 5.5

If wear is measured in mass loss instead of volume loss, the wear coefficient can also be quoted in units of mg m^{-1} N^{-1}.

5.2.4 Abrasive wear mechanisms

Figure 5.3 shows some of the mechanisms which can occur when a single abrasive tip is traversed across a surface [Tylczak,1992]. Ploughing is a wear mechanism which occurs under low loads where little material is lost and is the process of displacing material from a groove to the sides. Wedge formation is another mild form of wear and occurs when the total amount of material removed from the groove is greater than the material which is displaced to the sides, resulting in a buildup of material at the front of the abrasive tip. The most severe form of abrasive wear for ductile materials is cutting, where the material is removed in the form of a chip, much like a machine tool in a metal-working operation. This results in material removal with little displaced material compared to the size of the groove.

5.2.5 Effect of abrasive properties

5.2.5.1 Abrasive hardness

The hardness of the particles in abrasion influences the rate of wear of cermets. Abrasives with a lower hardness than the counterface will produce a low wear loss (soft abrasion), whereas abrasives with a higher hardness will subject the counterface to a higher wear loss (hard abrasion). Hutchings [1992] suggests that if wear resistance is studied in terms of the hardness ratio of the abrasive and

metal counterface, the wear of the metal will decrease dramatically if its hardness approaches that of the abrasive. Under "hard abrasion" conditions, the abrasive particles may cause plastic deformation in both the hard phase and matrix and wear occurs mainly by plastic ploughing and cutting, with some fracture occurring in the more brittle cermets. During "soft abrasion" the abrasives cannot produce plastic grooves in the hard phase and instead material removal is caused by carbide pullout or micro-crack formation due to a fatigue-type mechanism, where the hard phase cyclically moves due to normal and tangential forces applied by the abrasive.

A critical value of 1.2 has been suggested [Moore,1978] for the ratio of the abrasive hardness, H_a, to that of the metal surface, H_s; "Hard" abrasion is said to occur when $H_s / H_a < 0.83$ and "soft" abrasion when $H_s / H_a > 0.83$ Figure 5.4 shows the effects of the H_s / H_a ratio on the volume wear rate, for a range of metals and ceramics and abrasive particles for two-body abrasion. From the graph it can be concluded that the wear rate is much more sensitive to the H_s / H_a ratio when the ratio is less than ~1 [Moore,1978].

5.2.5.2 Abrasive toughness

The toughness of the abrasive is important under high loads where abrasive fracture may occur. A rounded abrasive may result in a low wear rate due to its morphology. However, if this abrasive fractures, it results in smaller, angular particles which result in higher rates of wear (Section 5.2.5.3) [Halling,1975].

5.2.5.3 Abrasive morphology

Wear rates depend strongly on the shapes of the abrasives [Stachowiak,2000], with angular particles causing greater wear than rounded particles. Hutchings [1992] states that differences in angularity of rounded and angular quartz abrasives can affect the wear rate by a factor of ten or more. This difference can be explained in terms of the critical angles of the abrasives. Tylczak [1992] states, for a sharp abrasive particle, a critical "attack angle" exists where there is a transition from ploughing to cutting. This is dependent upon the material being abraded and is different for each material, e.g. 45° for copper, 85° for aluminium. Angular particles tend to have higher attack angles, leading to a greater proportion of particles which cut and lead to a higher wear rate than rounded particles.

5.2.5.4 Abrasive size

Hutchings [1992] and Wirojanupatump [1999] state that abrasive wear rates of metals are nearly independent of the particle sizes of abrasives greater than about 100 μm. Below this value, a marked decrease in wear rate is observed.

5.2.6 Counterface material properties

5.2.6.1 Crystal structure

Abrasive wear has been found to be dependent upon crystal structure. Alison [1964] showed that cubic metals wear at approximately twice the rate of hexagonal metals due to the limited deformation characteristics of the hexagonal metals as slip usually only occurs along the basal plane in an hexagonal structure.

As wear is commonly associated with plastic deformation, h.c.p. metals, such as cobalt, exhibit good wear resistance. A disadvantage of h.c.p. metals is that they have limited stability and may be allotropic. For example, Halling [1976] concluded that cobalt has good wear properties below 417°C as it retains its h.c.p. crystal structure. Above this temperature, cobalt can transform to f.c.c which may increase the wear rate one hundred-fold.

5.2.6.2 Material

When selecting a wear resistant material, it is important to understand that microstructure as well as the more easily measurable properties, such as hardness, has a strong influence on wear behaviour. Tylczak [1992] states that austenitic and bainitic carbon steels of equal hardness are more abrasion resistant than ferritic, pearlitic, or martensitic steels, due to the higher strain-hardening capacity and ductility of austenite. This is also shown in work performed by Moore [1981] where austenitic steels show greater abrasive wear resistance, at the same hardness, than pearlitic or bainitic steels (Figure 5.5). This is attributed to the ductility and strain-hardening rates of the various microstructures. It can also be seen that the wear resistance for all four types of steel increases with increasing carbon content. Martensitic steels exhibit the highest wear resistance with an increase in alloy content and hardness.

Lansdown and Price [1986] suggest that high carbon, martensitic alloy steels have superior wear resistance to alloyed pearlitic, bainitic and ferritic steels, when subjected to three-body abrasion. Table 5.1 shows the relative resistance of some

groups of metals to three-body abrasion and illustrates that wear-resistance is not always directly related to hardness. This trend is shown in Table 5.1 where the three classes of martensitic chromium-molybdenum steels show a closer relationship with carbon content. This is also emulated in Figure 5.6, which illustrates the effect of carbon content on the abrasion resistance for a series of martensitic cast steels. Table 5.2 also shows the effects of microstructure of steels on the abrasion resistance. Lansdown and Price [1986] also conclude that the best structure for carbon steels appears to be lower bainite.

5.2.6.3 Abrasive wear of ductile materials

The abrasive wear of ductile materials usually involves plastic deformation and the predominant wear mechanism is ploughing or cutting depending upon the wear conditions. The dominant requirement for abrasion resistance of a ductile metal is hardness (Section 5.2.5.1). Kato [1990] conducted an experiment where the effect of a rounded tip pushing through a surface was analyzed. For ductile materials, ploughing, wedge formation and cutting were observed. He concluded that the degree of penetration was critical to the transition from ploughing and wedge formation to cutting. He stated that when the degree of penetration divided by the contact area exceeded approximately 0.2, cutting was the predominant mechanism. Scanning electron microscope images of the three mechanisms are shown in Figure 5.7. A simple model for the abrasive wear of ductile materials is called the Archard equation as previously discussed in Section 5.2.3.

5.2.6.4 Abrasive wear of brittle materials

The dominant abrasive wear mechanism of brittle metals is brittle fracture; therefore an essential requirement for abrasion resistance is fracture toughness. Hutchings [1992] has studied the effects of a hard, angular abrasive particle indenting a brittle material. He concluded that local plastic deformation and lateral cracking can occur at the point of contact which can lead to wear. Lateral cracks only form when the normal load of the indenter exceeds a critical value, w^*. This relationship is shown below.

$$w^* = A\left(\frac{K_c}{H}\right)^3 K_c \quad \text{---- Equation 5.6}$$

This value is dependent upon the fracture toughness of the material, K_c and its hardness, H. The ratio H/K_c provides a useful measurement of the brittleness of the material. A low value of this ratio corresponds to a high w^* value which indicates that the material is less likely to fracture on indentation. Figure 5.8 illustrates the crack formation in a brittle material due to point indentation. High stresses are formed at the point of contact between the indenter and the material, and are relieved by local plastic flow or densification around the tip of the indenter; this deformation zone is indicated in Figure 5.8 [Lawn and Swain,1975] by the letter D. As the load is increased, to a critical value, tensile stresses across the mid-plane of the sample form a median vent crack, M, which extends as the load is increased. The median crack closes when the load is reduced and eventually, lateral vent cracks, L, initiate and propagate due to the residual elastic

stresses within the material caused by the relaxation of the deformed material around the region of contact. When the load is removed, the lateral cracks curve upwards to the surface and material is removed. When a hard, angular particle slides over a brittle surface, a plastic groove is formed and lateral cracking grows upwards to the surface resulting in material removal. This effect is shown in Figure 5.9 [Evans,1979].

It is important to note that if the abrasive particles used are small and numerous in the contact region, the load carried by each particle may be less than w^* resulting in wear occurring by the plastic processes mentioned in Section 5.2.6.3.

If a brittle material is indented by a blunt body and if the contact stresses remain elastic, then a Hertzian cone crack may form. If the body then slides over the surface, a series of incomplete conical cracks form, which intersect the surface in a row of circular arcs and are not directly responsible for material removal. If on the other hand, this process were repeated numerous times, material removal would occur.

5.3 Abrasive wear of cermets

Cermets are composite materials containing one or more ceramic phases and a metal or alloy, which are intimately bonded together. Generally, cermets are much harder than metals and alloys and exhibit good abrasion resistance. There are three main wear mechanisms in cermets, namely, (i) hard phase pullout, (ii) binder extrusion followed by hard phase pullout, and (iii) hard phase fracture.

The following section attempts to address the key parameters involved in cermets when desiring a wear-resistant cermet.

5.3.1 Hard phase grain size

The size of the hard phase is an important factor in the wear resistance of cermet materials. Hutchings [1992] states that the response of the cermet materials depends upon the size of the deformation zone formed by the abrasive particle in comparison to the size of the hard phase. If the hard phase in the cermet is smaller than the abrasive particles, the material is said to be removed in a homogeneous manner and the hard phase could be completely removed or pushed into the matrix. A small hard phase size also produces a matrix with a small mean free path, which is desirable, as it increases the apparent yield strength of the matrix (due to constraint effects) and reduces the ease of extrusion of the binder phase by the abrasive. If, on the other hand, the hard phase is comparable in size with the abrasive, then, the hard phase will offer more resistance to the abrasive, and may blunt the abrasive reducing its severity, and the wear rate will depend upon the strength of the hard phase / matrix interface. The strength of the hard phase / matrix interface in terms of abrasion resistance was discussed by Liao et al. [2000]. They concluded that when the abrasive particle size was larger than the hard phase within a cermet coating, the strength of the hard phase / matrix interface was of paramount importance. It must also be remembered that having larger hard phase particles will produce a matrix with a larger mean free path, which will increase the chance of extrusion of the matrix. Extrusion of the matrix

could eventually result in the undercutting of the hard phase and subsequent pullout. Also, it is important that the hard phase has sufficient toughness because a large material loss would occur if a large carbide fractured.

Rohatgi et al. [1991] displayed results which indicated that under abrasive wear, dispersions of coarser carbides (chromium-enriched M_7C_3 carbide) reduced the wear rate of cobalt-based metal matrix composites. Other researchers [Mantyla,1991; Champagne,1985; Scussel,1991] believe that a fine carbide grain size is desired when selecting a cermet coating with high abrasion resistance. This can be explained in terms of the strengthening effects on the matrix which the fine hard phase provides [Smith,1995]. It has also been suggested that for sliding wear, a bi-modal distribution of carbide was preferred, where larger particles would act as a bearing surface whilst the smaller carbides would strengthen the matrix [Smith,1995]. This may also be the case for abrasive wear. A fine carbide grain size also tends to yield a high strength and hardness [Goetzel,1991; Mantyla,1991], where hardness is important for a wear resistant material [Kubarsepp,2001; Scussel].

5.3.2 Hard phase volume fraction

It is widely reported that the abrasive wear resistance of a cermet increases with increasing volume fraction of the hard phase [Hutchings,1992; Scussel,1991; Kubarsepp,2001; Tjong, 2000a; Tjong,2000b; Vuoristo,1996]. This is due to a number of factors, firstly, the hardness of the cermet increases with increasing

volume fraction of the hard phase, [Goetzel,1991; Tjong,2000a] and the hardness of the cermet dictates whether hard or soft abrasion will occur (Section 5.2.5.1). Secondly, the dimension of the mean free path of the matrix decreases with increasing volume fraction of hard phase (Section 5.3.1).

5.3.3 Matrix material

The main parameters required for a wear resistant matrix are microstructure, hardness, fracture toughness and a strong matrix/hard phase interface. The matrix must provide sufficient hardness and fracture toughness which can be achieved by controlling the grain size and phases within the material. Hardness of the matrix is important as this can determine whether or not 'soft' or 'hard' abrasion is occurring (Section 5.2.5.1). A high fracture toughness of the matrix is imperative as the matrix provides the ductility in the cermet and relieves the stress when under load, and provides a level of safety against catastrophic failure in service. Finally, a good carbide/matrix bond is vital as it is the hard phase which protects and reinforces the matrix and acts as a bearing surface during abrasive wear. A good bond also prevents hard phase pullout during abrasive wear which can lead to high wear rates.

5.4 Comparison of thermal spray methods for deposition of wear resistant cermet coatings

In order to produce a thermally sprayed cermet coating with good wear properties, generally, there should be a low level of porosity, oxides and unmelted particles.

The following section compares the abrasive wear properties of cermet coatings produced using different spraying techniques.

Vuoristo et al. [1996] compared the abrasive wear resistance of a (Ti,Mo)C-28.4%NiCo coating deposited by APS, D-Gun and HVOF spray systems. They found that DGS had the lowest volume loss with 13.9 mm^3, followed by HVOF with 15.7 mm^3, and finally APS with 16.7 mm^3. They compared these values with those obtained from HVOF and APS-sprayed Cr_3C_2-25%NiCr coatings, and found them to be comparable. As such, they concluded that all the methods were suitable for deposition of these coating materials.

Berger et al. [1996] studied the effects of thermal spray technique on the rubber wheel abrasive wear resistance of a range of cermet materials. They concluded that for WC-12%Co coatings deposited by HVOF and DGS spraying systems, both exhibited similar wear properties, although DGS was slightly better, and were superior to the APS deposited coating. This may be due to the higher velocities at which both HVOF and DGS operate which may produce a more coherent coating. Steinhauser et al. [2000] produced a study on the abrasive wear resistance of Fe-TiC coatings deposited by APS and LPPS. They found the LPPS deposited coating had superior wear properties to the APS coating due to the lower porosity and the higher hardness of the LPPS coating. They also state that the abrasion resistance of the LPPS deposited coatings was comparable to WC-Co coatings deposited by HVOF.

Mantyla et al. [1991] studied the abrasive wear properties of WC-Co based coatings deposited by various thermal spray techniques. They concluded that the

coatings deposited by DGS and CDS (Continuous Deposition Spraying) produced the best abrasion resistance. This was explained in terms of the more uniform microstructure and finer carbide distribution produced by these techniques. The APS and VPS coatings had inferior wear properties, with the VPS deposited coatings exhibiting the worst abrasion resistance. Pawlowski [1995] also states that the harder and less porous HVOF and D-Gun deposited WC-Co coatings had superior abrasive wear resistance, when compared with coatings deposited by APS and VPS.

5.5 Dry Sand Rubber Wheel (DSRW) Abrasive Wear Testing

The most common laboratory configuration for three-body abrasion testing is that of a specimen loaded against a rotating wheel with abrasive particles being entrained into the contact zone. This is the principle behind the ASTM Standard G65, dry sand-rubber wheel abrasion test. A schematic diagram of a modified DSRW abrasion tester that is used in this investigation is shown in Figure 7.14, and details of this equipment are shown in Section 7.6.

When performing rotating abrasion tests, the behaviour of the material not only depends upon its properties but also upon the conditions of the test. These conditions include the type, size and shape of the abrasive (Section 5.2.5), and also the hardness and stiffness of the rubber wheel. The rubber wheel abrasion test produces low stress abrasion where the abrasive particles generally remain intact following the abrasion process [Wirojanupatump,2000].

Increasing wear resistance ↑

Group	Material	Hardness VPN 30kg	Relative wear rate
1	High chromium white cast irons	865	89
2	Martensitic 1% carbon Cr-Mo steel	595	100 (std)
3	"Martensitic" Ni-Cr-Mo white iron, chill cast	674	107
4	Martensitic 0.7% carbon Cr-Mo steel	653	111
5	Nickel-chromium alloyed martensitic white cast irons	595	116
6	Martensitic 0.4% carbon Cr-Mo steel	595	120
7	Pearlitic 0.8% carbon Cr-Mo steel	382	127
8	Austenitic manganese steel	484	195
9	Pearlitic low Cr white iron	484	195
10	Unalloyed steels	120	225

Table 5.1: Relative resistance of some groups of metals to three-body abrasion. [Lansdown and Price,1986]

Increasing wear resistance ↓

Metals	VPN 30 kg	Influence of microstructure
SG iron	270	Free graphite has deleterious effects
SAE 1020 steel	137	Wear-resistance dependent upon pearlite content in untreated state
Pearlite white cast iron	425	Hard, brittle carbides in soft matrix, broken up by grinding action
Austenitic manganese steel	212	Austenitic grains, mechanical properties impaired if some cementite precipitation occurs at grain boundaries
Chrome steel C.R.O.	283	Increasing abrasion resistance with increase in pearlite with %C
Low alloy martensitic steel	510	Martensitic structure gives better abrasion resistance
Low C chrome moly steel	358	Abrasion resistance results from production of fully martensitic structure
Eutectic Ni-hard	640	Normally contain some retained austenite in matrix, thus slightly inferior to high-chromium martensitic white irons
Regular Ni-hard	570	
High Cr martensitic white iron	740	Very hard carbides in predominantly martensitic matrix beneficial

Table 5.2: Effect of microstructure of three-body abrasion resistance [Lansdown and Price,1986]

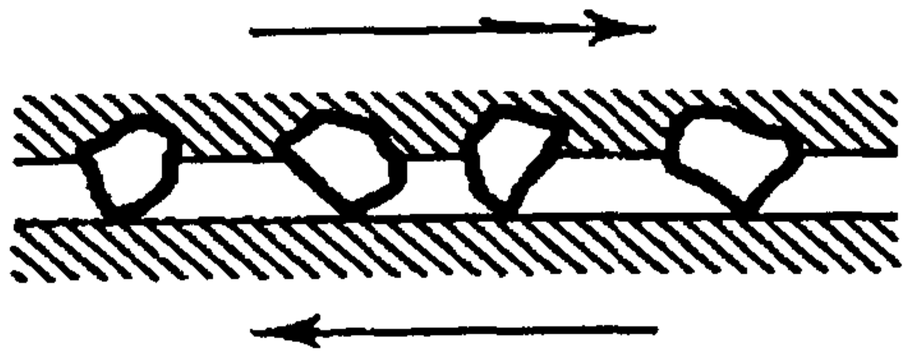

(a) Two-body abrasion

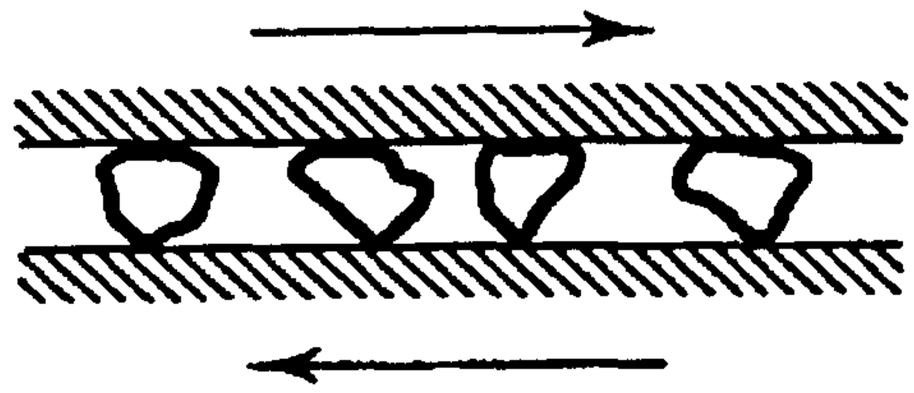

(b) Three-body abrasion

Figure 5.1: Schematic diagrams of (a) two-body abrasion, and (b) three-body abrasion [Hutchings,1992]

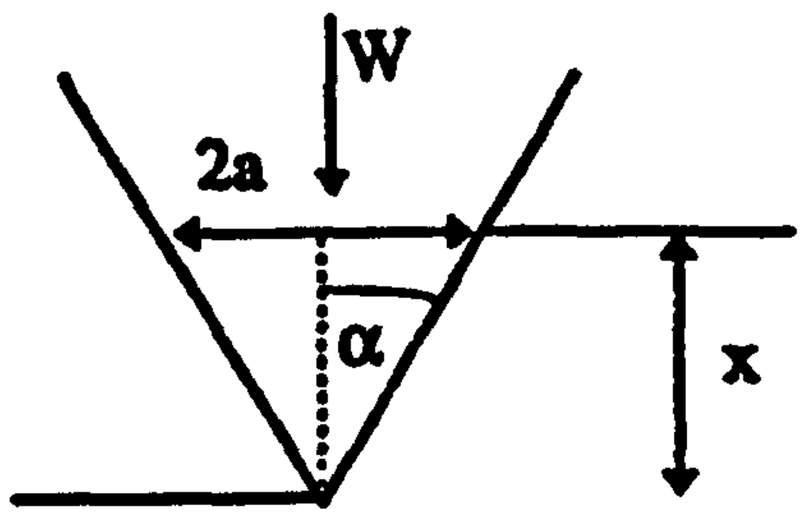

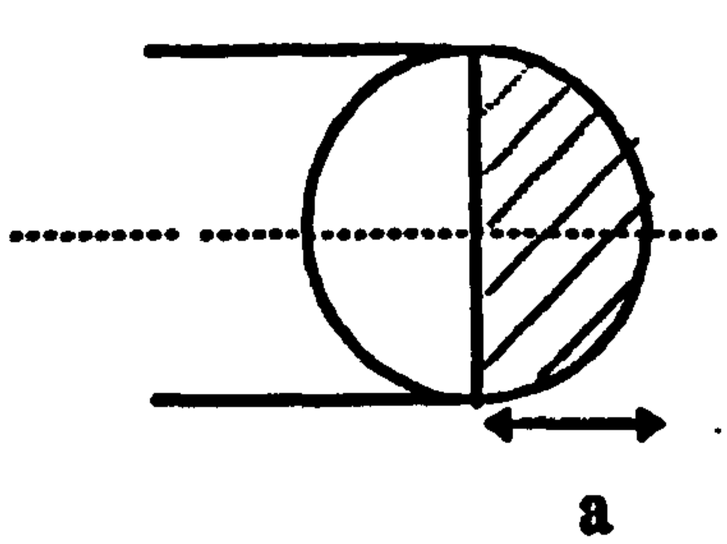

Figure 5.2: Schematic diagrams showing a scratch indenter sliding along a counterface material and forming a groove [Hutchings,1992]

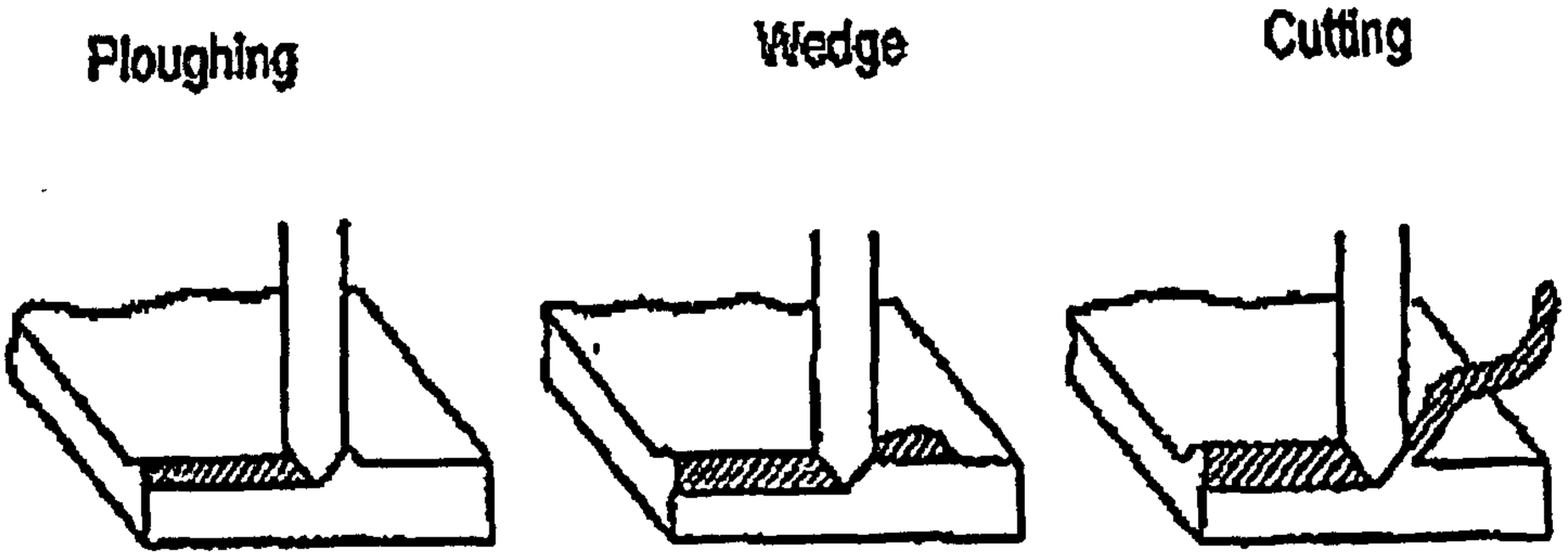

Figure 5.3: Abrasive wear mechanisms [Tylczak,1992]

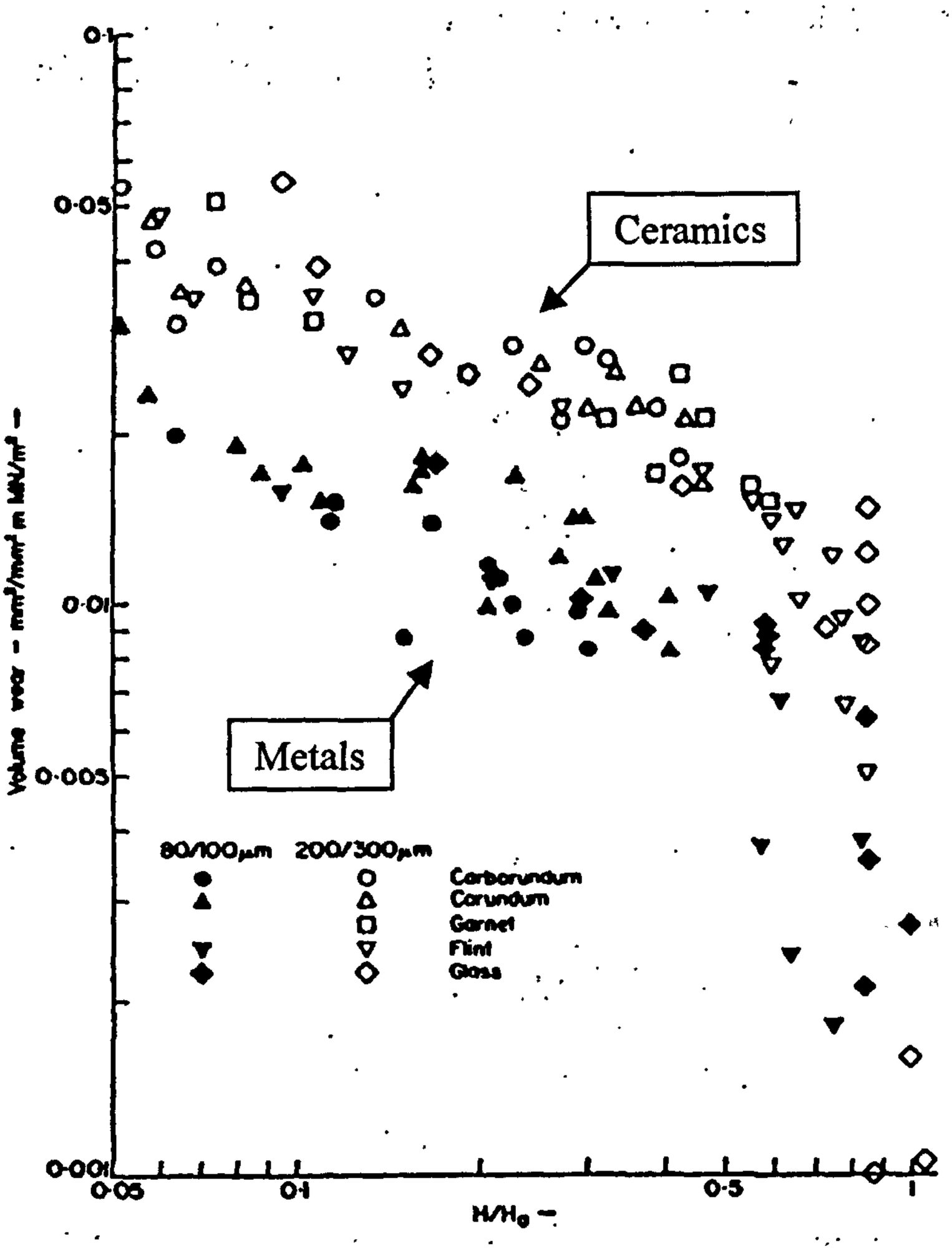

Figure 5.4: Plot showing effects of the H_s / H_a ratio on the volume wear rate [Moore,1978]

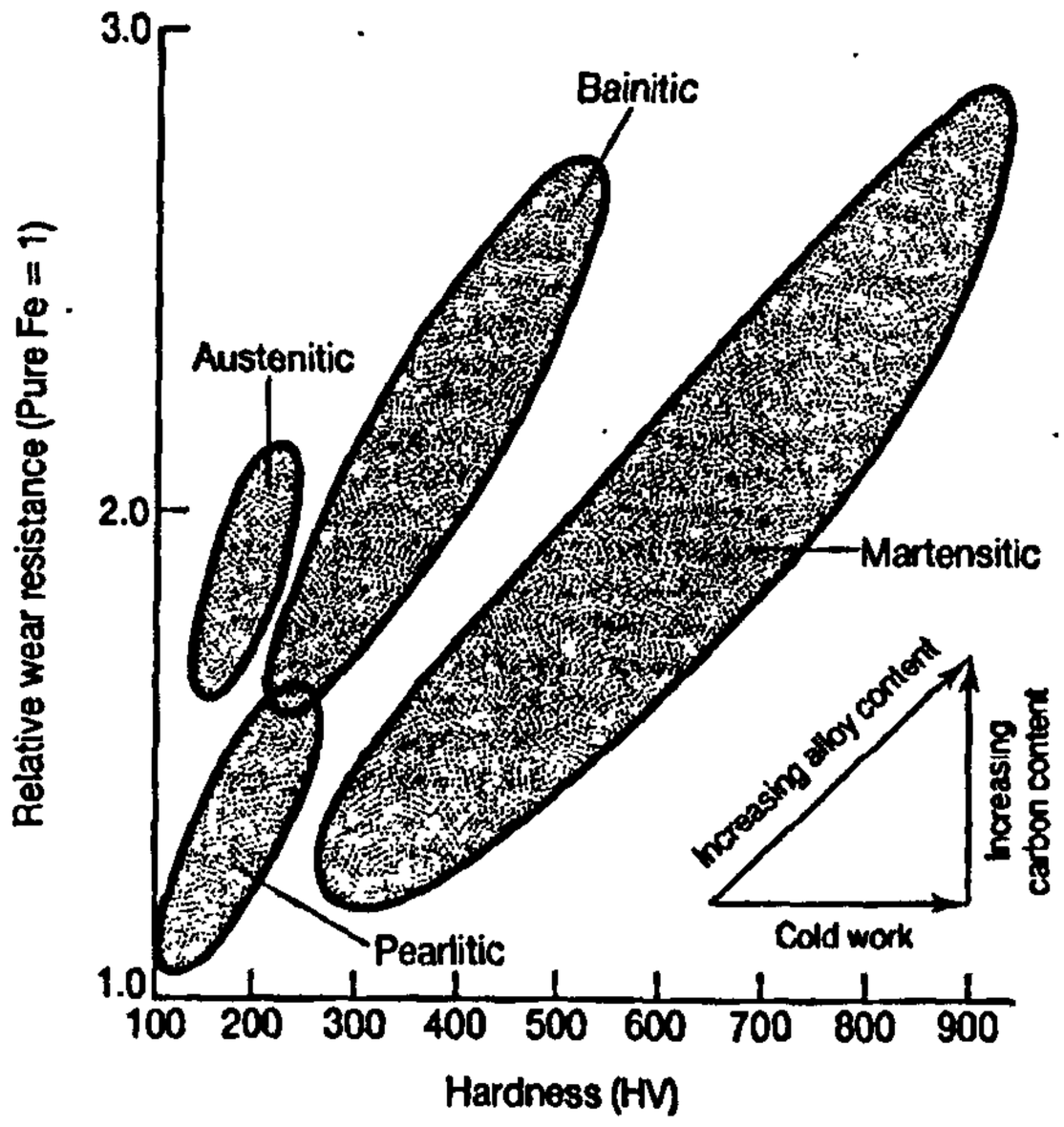

Figure 5.5: Effect of structure, heat treatment and alloy content on the relative two-body abrasive wear resistance of steels against 90μm alumina abrasives [Moore,1981]

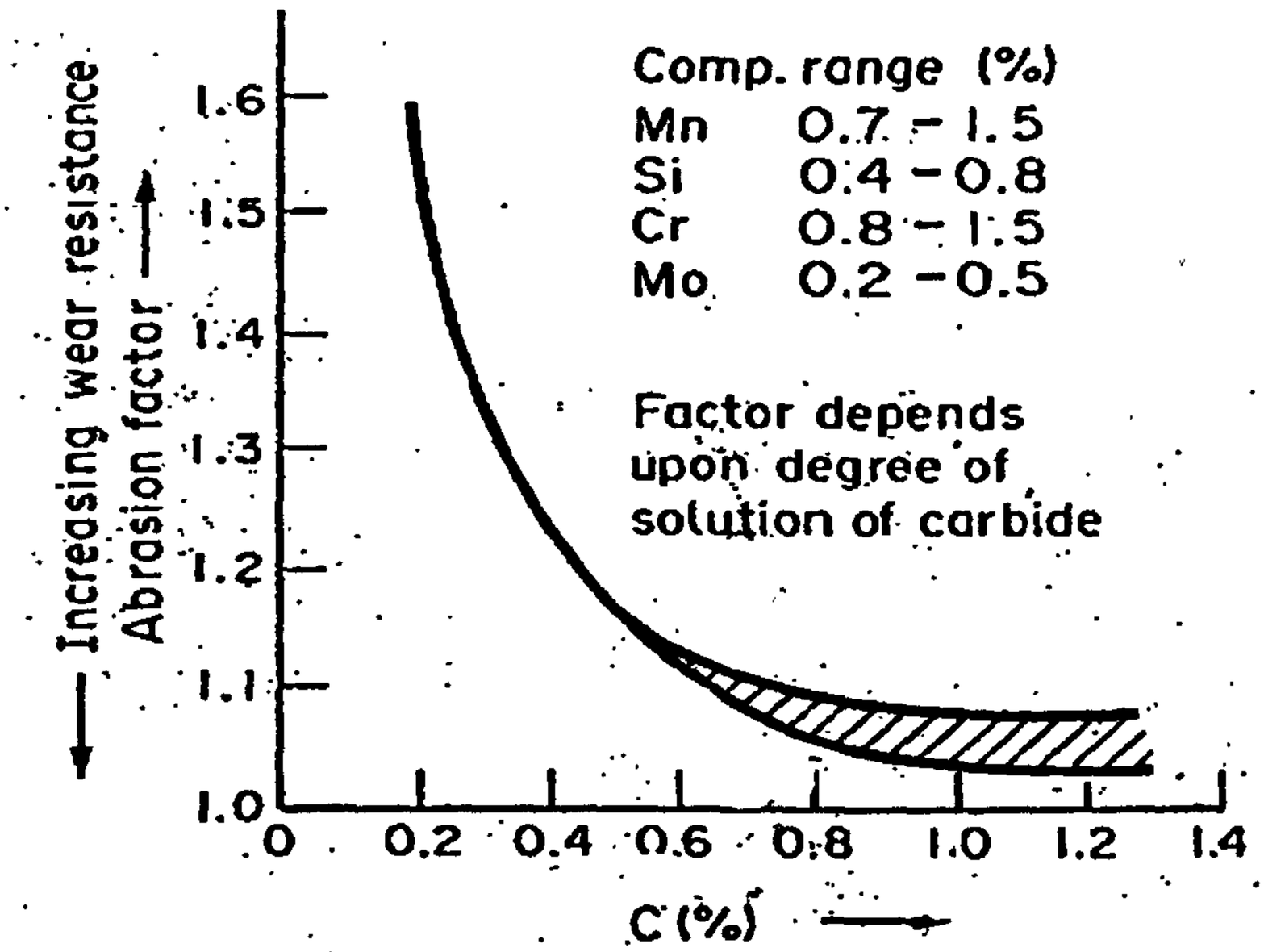

Figure 5.6: Effect of carbon content on wear-resistance of martensitic cast steels (Tested in grinding siliceous ore) [Lansdown and Price,1986]

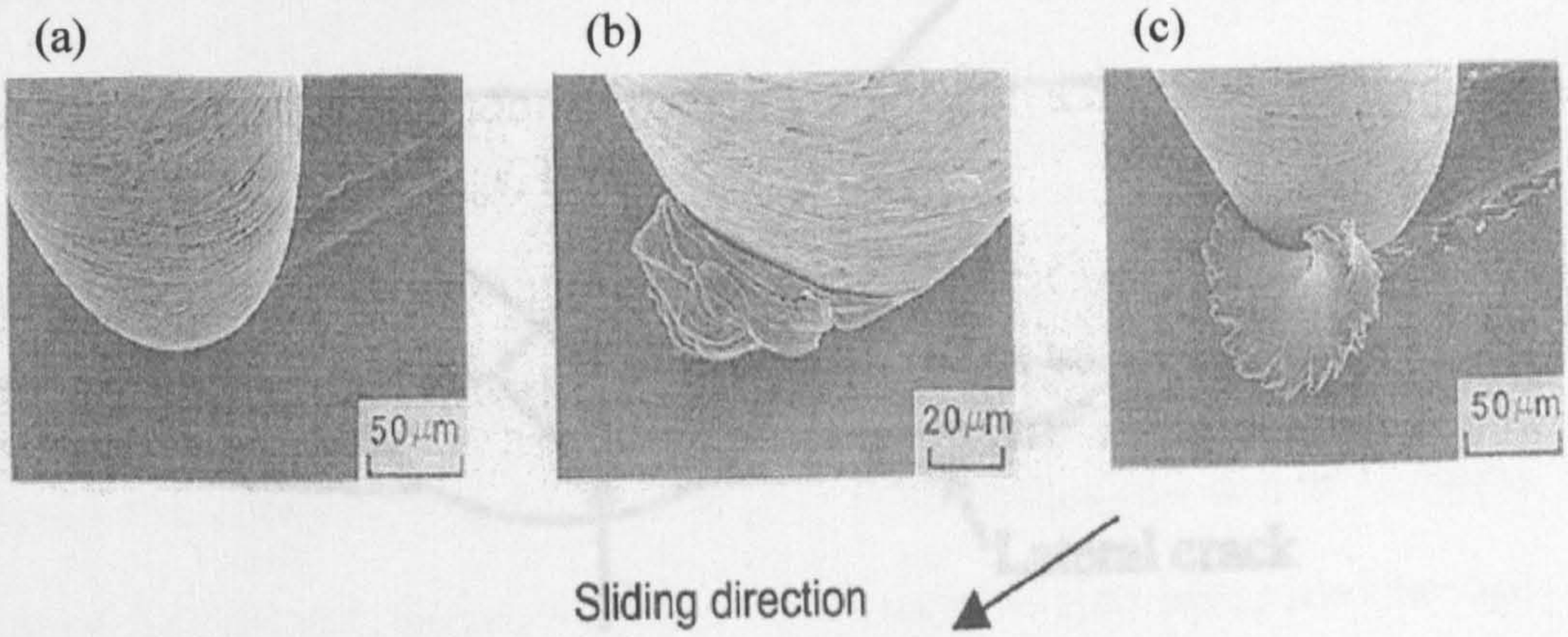

Figure 5.7: Scanning Electron Microscope images of the three processes of abrasive wear; (a) ploughing, (b) wedge, and (c) cutting [Kato,1990]

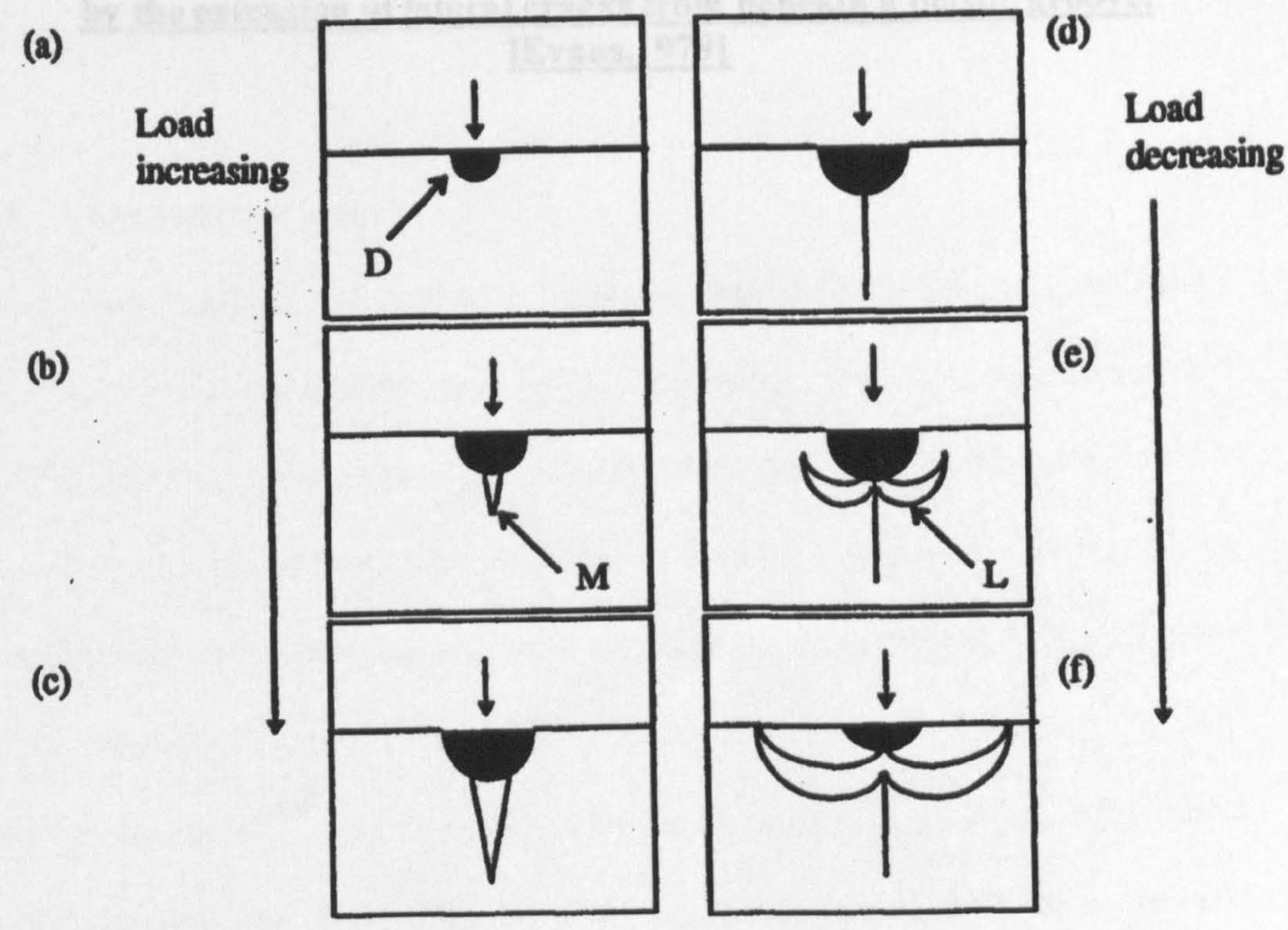

Figure 5.8: Crack formation in a brittle material due to point indentation. Load increases (a) to (c) and decreases (d) to (f). D = deformation zone, M = median vent crack and L = lateral vent crack [Lawn and Swain,1975]

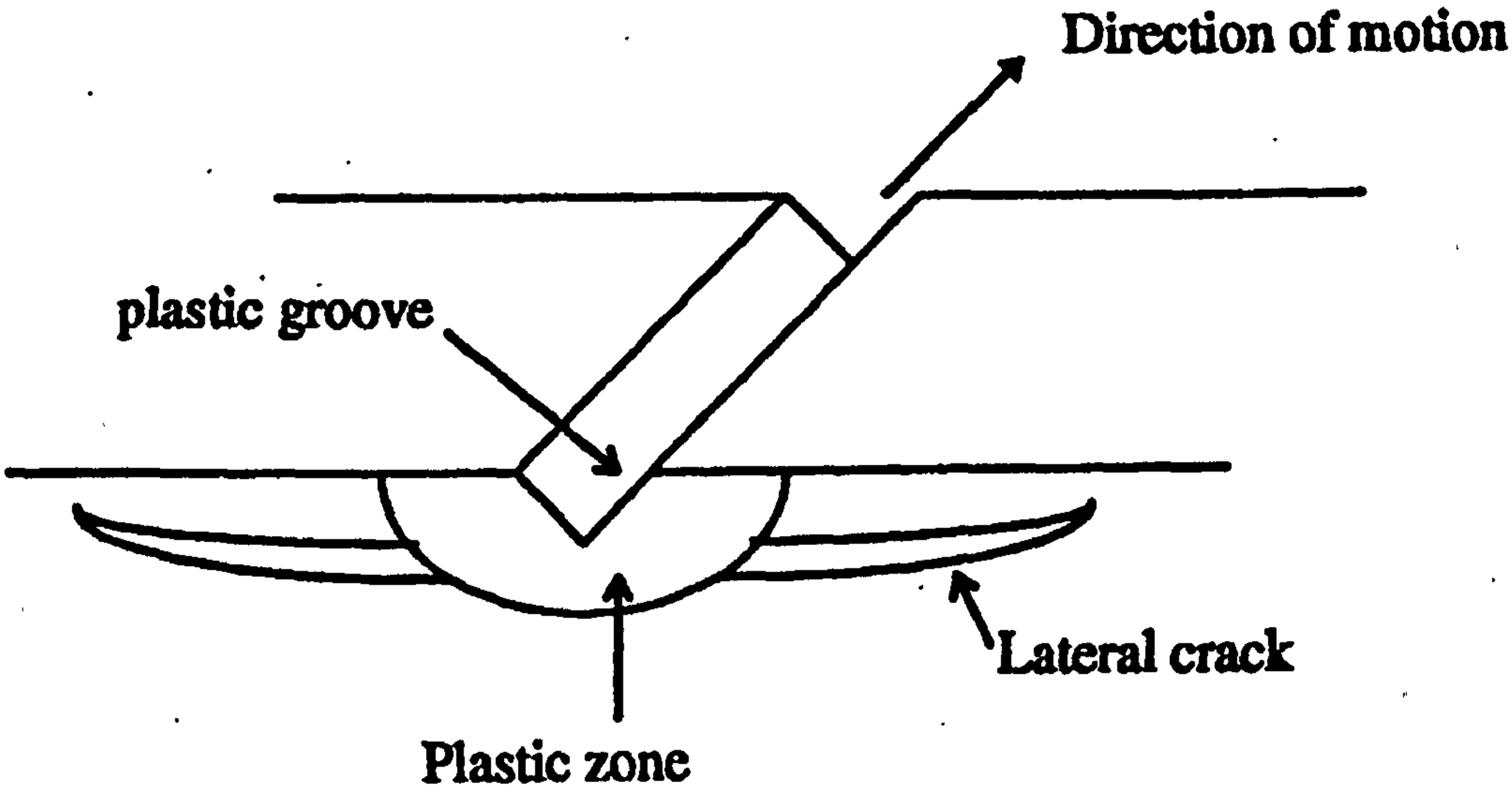

Figure 5.9: Schematic diagram of material removal in a brittle material by the extension of lateral cracks from beneath a plastic groove. [Evans,1979]

6 Oxidation

When metals are oxidized, the following reaction occurs.

$$yM_{(s)} + {}^{x}/_{2}\,O_{2(g)} \rightarrow MyOx_{(s)} \text{ ---- Equation 6.1}$$

It is seen that the solid reaction product, MO, will separate the two reactants as shown in Figure 6.1. For the reaction to proceed further, one or both reactants must diffuse through the oxide layer, i.e. either metal must be transported through the oxide to the oxide-gas interface where reaction takes place or oxygen must be transported to the oxide-metal interface for reaction to occur. This transportation occurs by the movement of ions and electrons within the materials.

6.1 Oxidation of iron

When iron oxidizes, the formation of multi-layered scales occur, namely, FeO (wustite), Fe_3O_4 (magnetite), and Fe_2O_3 (haematite). FeO does not form below 570°C; therefore, iron which is oxidized below this temperature would form a two-layered scale of Fe_3O_4 and Fe_2O_3, with the Fe_3O_4 next to the metal. Above this temperature, a three-layered scale would form, consisting of FeO, Fe_3O_4 and Fe_2O_3, with the FeO next to the metal (Figure 6.2).

Due to the much greater mobility of ions in wustite, due to its high defect concentration, this layer will be very thick compared with magnetite and haematite. At 1000°C, the relative thickness' of Fe:Fe_3O_4:Fe_2O_3 are in the ratio of 95:4:1.

6.2 Oxidation of chromium and titanium

Oxidation of chromium is more likely to occur when compared with iron and a minimum of 12% chromium is used in steels to provide oxidation resistance. Oxidation of chromium produces a single oxide, namely Cr_2O_3. This oxide has a low vacancy concentration and is thus protective. The oxidation of titanium is quite complex as it can produce a number of stable oxides and has high oxygen solubility (approx. 14wt%). The various oxides formed are TiO, Ti_2O_3 and Ti_3O_5.

6.3 Oxidation of alloys

Oxidation of alloys can occur internally or externally. Internal oxidation occurs when oxygen diffuses into an alloy and causes sub-surface precipitation of the oxides of one or more alloying elements. The necessary conditions for internal oxidation are (i) ΔG^{θ} of formation (per mole O_2) for the solute metal oxide, BO_v, must be more negative than ΔG^{θ} of formation (per mole O_2) for the base metal oxide; (ii) base metal must have a solubility and diffusivity for oxygen; (iii) solute concentration of the alloy must be lower than that required for the transition from internal to external oxidation; and, (iv) a surface layer must not prevent the dissolution of oxygen into the alloy at the start of oxidation.

External oxidation takes place when the amount of solute metal is large enough to form a continuous layer of oxide and prevent internal oxidation. This transition to external oxidation is the basis for the design of Fe-, Ni- and Co- base engineering alloys which contain a sufficient amount of solute metal (e.g. Cr, Al or Si) to

produce an external layer of oxide (e.g. Cr_2O_3, Al_2O_3 and SiO_2) which prevents oxidation of the parent metal. This is known as 'selective oxidation'.

6.3.1 Fe-Cr alloys

Figure 6.3 shows the Fe-Cr-O phase diagram. It can be seen that both Fe_2O_3 and Cr_2O_3 are present along with Fe_3O_4. At low Cr levels, no internal oxidation is present as the rate of external scale formation is so rapid. Both chromium-rich and iron oxides form on the surface. At high Cr levels, i.e. greater than 18 at% (Figure 6.3), a permanent protective Cr_2O_3 scale is formed, and most Fe-Cr systems designed for heat resistance have at least 20% Cr. The use of Cr contents higher than 20-25% cannot be produced without other alloying additions to avoid sigma phase formation (Section 4.1.5.3).

6.4 Oxidation of TiC

Macdonald and Ransley [1959] investigated the oxidation of TiC in air between 300 and 1000°C for periods up to 200 hours. At temperatures between 300 and 450°C, the oxidation product was a loose, non-adherent TiO_2 (anatase) powder, which was non-protective. A maximum oxidation rate was observed at approximately 450°C. Between 500 and 700°, a slower oxidation rate was observed which indicated that a protective film had formed in this intermediate temperature range. The actual composition of the oxidation product was not investigated but it was postulated to be rutile (TiO_2). Above 700°C, the oxidation rate increased and rutile was formed.

Voitovich [1997] studied the oxidation of TiC between 600 and 1200°C in air for up to 5 hours. He found that for temperatures up to 800°C, the TiC samples were oxidized slightly and no weight gain was recorded. When temperatures approached 1000°C, the oxidation rate increased sharply. XRD analysis showed that 5 hours at 700°C produced a scale that consisted of Ti, TiO (monoclinic), TiO (cubic), TiO_2 (rutile) and TiO_2 (anatase). For exposure at 900°C for 5 hours, the phases present in the scale were Ti, TiO (monoclinic), TiO (cubic) and TiO_2 (rutile). According to Storms [1965], observations by Webb et al. [1956] indicated that $TiC_{0.63}$ was oxidized more rapidly than $TiC_{1.0}$ although this was not confirmed.

Berger et al. [1998] described Cr_3C_2 and TiC as having the highest oxidation resistance of all transition metal carbides, while WC had the lowest. They also found that dense, hot-pressed samples of nearly stoichiometric TiC have shown a high stability against oxidation up to 1000°C.

Berger et al. [1998] studied the oxidation properties, in air, of WC, Cr_3C_2 and TiC hard phases. They found that Cr_3C_2 exhibited the best oxidation resistance, followed by TiC , and finally WC. They stated that the oxidation of WC began at 400°C and rapidly oxidised up to 600°C, where complete oxidation had taken place. Similar to TiC, the oxidation rate of Cr_3C_2 was more continuous as the temperature increased. The reasons for the different oxidation resistances of the hard phases were postulated to be due to the degree of protection from the initial oxide layers formed.

6.5 Oxidation of TiB_2

Macdonald and Ransley [1959] also conducted oxidation tests on TiB_2 in the same series of experiments as TiC. They observed a maximum oxidation rate at approximately 450°C, followed by a fall to a minimum and then an increase at higher temperatures again. The composition of the oxides were not investigated, but they were postulated to be TiO_2 and B_2O_3 based. They concluded that TiB_2 exhibited a greater oxidation resistance than TiC, particularly between 400-500°C, and is thought to be due to the formation of a glassy oxidation product, i.e. B_2O_3.

Barandika et al. [1998] state that the general understanding involving the oxidation of TiB_2 is that TiO_2 is the main oxidation product formed by the following reaction.

$$TiB_2 + \tfrac{5}{2}O_2 \rightarrow TiO_2 + B_2O_3 \text{ ---- Equation 6.3}$$

6.6 Oxidation of TiC-based cermets

Berger et al [1998] studied the oxidation behaviour, in air, of Co-WC, NiCr-Cr_3C_2 and Ni-TiC spray powders. It was again found that WC-Co oxidised rapidly between 400-600°C. NiCr-Cr_3C_2 showed the highest oxidation resistance as it began to oxidize intensively only at temperatures higher than 800°C. The Ni-TiC powder showed poorer oxidation resistance than NiCr-Cr_3C_2, but was not fully oxidised at 1000°C. It was proposed that the low oxidation resistance of the WC-Co was due to low adhesive properties of the oxide scale, WO_3 and $CoWO_4$.

6.7 Oxidation of TiB_2-based cermets

Agarwal et al. [2000] performed oxidation tests on TiB_2-based cermet coatings formed by the deposition of TiB_2 onto AISI 1010 steel substrates using a laser. All oxidation tests were carried out in commercial grade bottled air at 600°C, 700°C, 800°C and 1000°C for periods of 10, 30 or 50 hours. Samples tested at 600°C showed no signs of oxide build-up, although, the sample tested for 50 hours showed signs of coating cracking. The phases present were TiB_2, Fe and TiO_2. Samples tested at 800°C exhibited oxide layers of thickness 25μm (10 hours) and 48μm (30 hours). When oxidized for 50 hours, the oxide coating was >50μm thick and spallation from several locations was observed, and coating cracking by propagation through the TiB_2 particles was also observed. The phases present in the oxide layers were TiO_2, $Fe_xTi_yO_z$ and Fe_3BO_6. TiB_2 peaks were not observed. The samples tested at 1000°C showed extensive porosity at the coating/steel substrate interface. Samples oxidized for 30 or 50 hours exhibited three distinct layers, namely, an oxidized boride coating, an intermediate iron oxide phase and the steel substrate. In both cases, the iron oxide layer has separated from the steel substrate. The major phases present in the oxide layers were Ti_2O_3, Fe_2O_3 and $Fe_xTi_yO_z$.

The oxidation rate at 600 and 700°C was very slow and increases at 800°C until reaching a high value at 1000°C which is three orders of magnitude higher than that at 600°C. This effect was partly thought to be due to the evaporation of B_2O_3 phase which formed at 450°C and acted as a protective coating. Evaporation took place at 750°C which caused an increase in oxidation rate at 800°C. The sharp

increase in oxidation rate at 1000°C was due to the increased evaporation of the B_2O_3 layer at temperatures higher than 950°C.

Barandika et al. [1999] performed a study of the oxidation in air of two sintered TiB_2 cermets containing Fe-Ni-Ti-Al-ferritic and 316L-type stainless steel binders within the temperature range 700-1000°C for up to 70 hours. They found that up to 775°C the phases present in the oxide scale were TiO_2 and $Fe_2Ti_2O_7$, which was thought to be the product of the reaction of TiO_2 and Fe_2O_3. For temperatures above 800°C, the main phases present were TiO_2 and $Fe_3Ti_3O_{10}$, which is a product of the reduction of $Fe_2Ti_2O_7$.

6.8 Oxidation of WC-Co and NiCr-Cr_3C_2 coatings

WC-Co coatings have excellent wear and erosion resistance but are limited to maximum service temperatures of 500°C [Laul,2000;Somaraju,2000]. This is due to the resultant oxide coatings having no protective properties against further corrosion.

NiCr-Cr_3C_2 coatings have been reported to have excellent oxidation resistance and can be used up to 900°C [Wirojanupatump,2001; Valente,2001; Zimmermann,1996]. This is due to the formation of a dense and highly adhesive layer of Cr_2O_3 on its surface and its low oxidation rate [Zimmermann,1996]. However, a disadvantage of sprayed NiCr-Cr_3C_2 coatings is that decarburisation takes place during spraying from Cr_3C_2 into carbides with a lower carbon content,

namely, Cr_7C_3 and $Cr_{23}C_6$ which affects the hardness and wear resistance of the coatings [Zimmermann,1996].

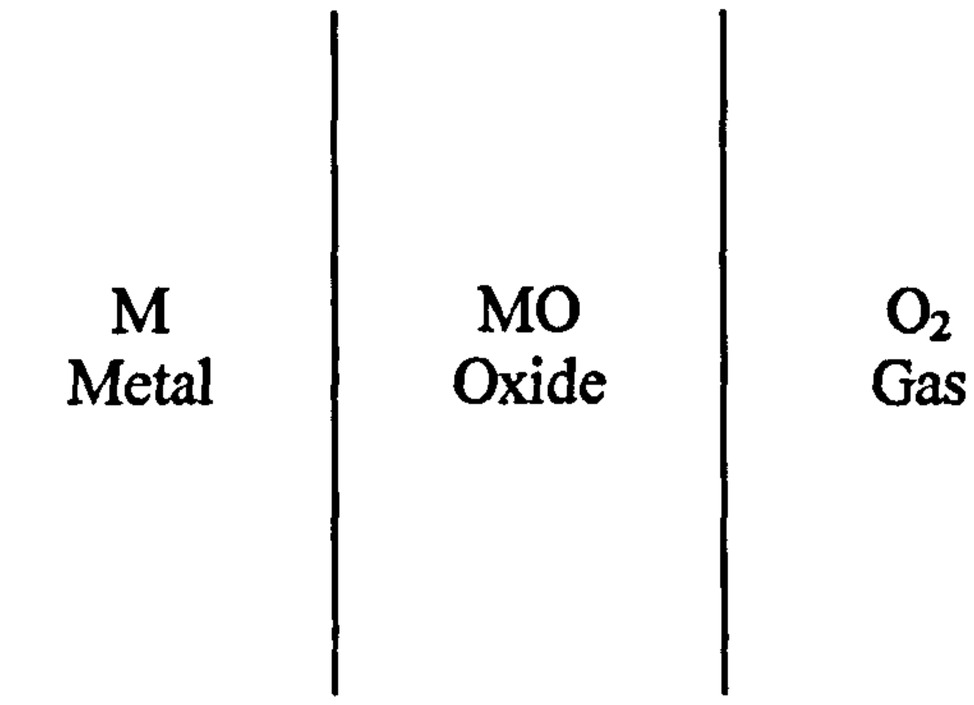

Figure 6.1: Reaction product of oxidation of metals [Birks and Meier,1983]

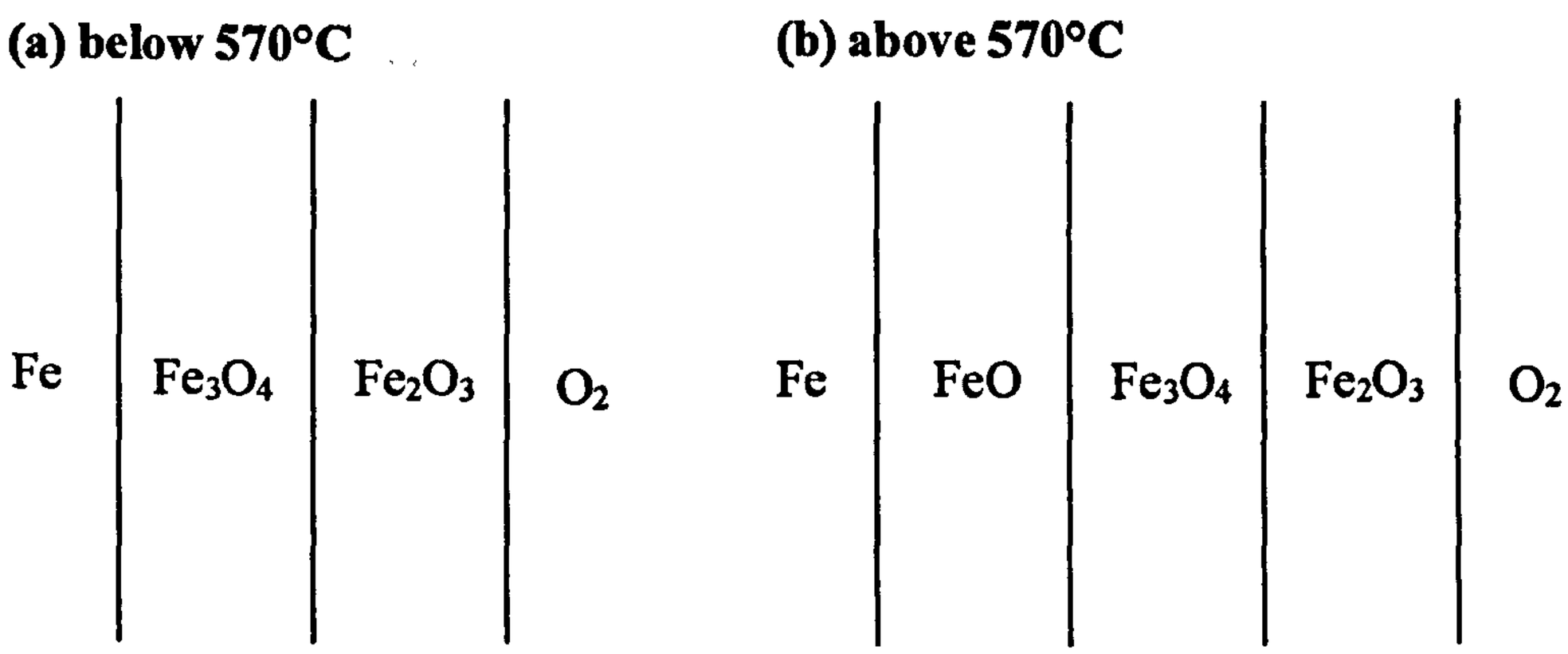

Figure 6.2: Oxidation products of Fe (a) below 570°C and (b) above 570°C [Berks and Meier,1983]

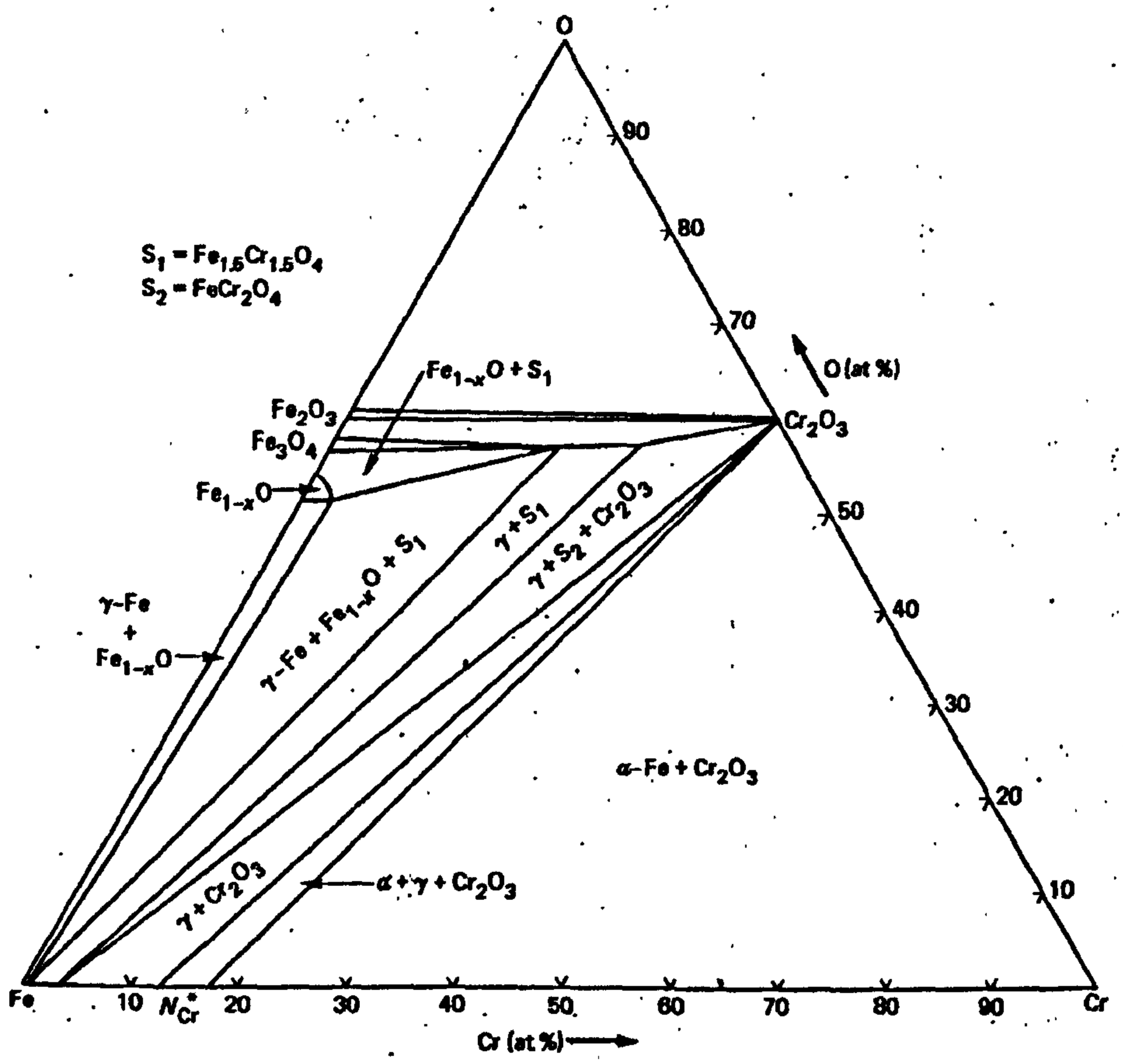

Figure 6.3: Isothermal section of the Fe-Cr-O phase diagram at 1200°C [Birks and Meier [1983]

7 Experimental details

The following chapter outlines the manufacturing route of the sprayed coatings including the production of the cermet compact via the SHS method, grinding, sieving air classification and finally thermal spraying. Figure 7.1 shows a flow chart of the various stages in the production of the coatings.

7.1 Raw materials

The powders used for this research, were iron, titanium, chromium, carbon and boron. The majority of the powders were supplied by London and Scandinavian Metallurgical Company Limited (LSM). Morphologies of all powders are shown in Figures 7.2 to 7.6.

7.1.1 Iron powder

The iron powder had a purity of 98+%, (impurities included Si<1400 ppm, C<200 ppm, P<150ppm). The mean particle size of the iron powder was 60μm. The iron powder was purchased from Goodfellows.

7.1.2 Titanium powder

The titanium powder was supplied by LSM. The powder was 95% pure with impurities of Fe, Cr, C, Si and Al. The particle size range of the titanium powder was 100-500μm.

7.1.3 Chromium powder

The chromium powder was supplied by LSM and impurities included 0.04%

Al, 0.3% Fe, 0.114% O and 0.062% Si. The particle size of the chromium powder was <180μm.

7.1.4 Carbon powder

The non-dusting carbon powder was supplied by LSM. The impurities included small amounts of oxides, such as <0.05% Al_2O_3, <0.05% TiO_2. The particle size range of the agglomerated particles is 100-1000μm.

7.1.5 Boron powder

The boron powder was supplied by Alfa (Karlsruhe, Germany) and had a purity of 95%. The particle size of the boron was <45 μm.

7.2 Feedstock powder production

The four powder compositions contained elemental Fe, Cr, Ti and either C or B each based upon an iron-chromium binder of 30 wt.%, with a chromium to iron ratio of 1:4 by weight, and 70 wt.% of hard phase based upon Ti and C or B, except for the excess C sample where the 70wt% combined of titanium and carbon powders will not produce 70wt% TiC due to the proportions of the elements in the reactants. Three powder compositions contained titanium and carbon, each having a different molar proportion of titanium to carbon, while the fourth powder contained titanium and boron. Table 7.1 shows the compositions of the mixes of the elemental powders prior to SHS reaction, and the desired hard phases in each composition.

7.2.1 Elemental powder preparation

For each sample, the powders were accurately weighed and mixed dry in a plastic bottle containing ball bearings to assist mixing. The powders were mixed for a period of 20 minutes in the *Glen Creston Turbula mixer* to ensure that each of the elemental powders were sufficiently distributed throughout the mix as concentrations of a single element in the mix may hinder the combustion process and also effect the final microstructure.

7.2.2 Methods of containment of powders

Three methods of containment were used for SHS firing (see Section 7.2.3). The pressed compact was used initially and the reaction observed. The reaction was then scaled-up to the glass vial and finally to the graphite tube.

7.2.2.1 Pressed compact

Previously mixed powders were poured into a steel mould and were subjected to a load of 2 tonnes. The dimensions of the cylindrical compact formed were 12 mm in diameter and approximately 25 mm in length. The compacts weighed approximately 25g. Figure 7.7 shows the dimensions of the compact.

7.2.2.2 Glass vial

Powders were hand-pressed into a glass vial, which contained around 60g of powder. A pressed compact was produced under the same conditions and to the same dimensions as mentioned above. The compact was placed on top of the vial to ensure that the powders were in close vicinity to the tungsten filament. A diagram of the arrangement is shown in figure 7.8.

7.2.2.3 Graphite tube lined with porous ceramic paper

The graphite tube was lined with ceramic paper. As it was porous, the paper allowed the gases, which are evolved during the SHS reaction, to escape. The lined graphite tube was filled with powder and hand-pressed. A pressed compact (see Section 7.2.2.1) was placed on top to ensure that the tungsten filament did not come into contact with graphite tube.

The tube contained approximately 640g of powder and the dimensions are shown in Figure 7.9.

7.2.3 Combustion procedure

The SHS reaction was performed in an evacuable glove box with a quartz window fitted to allow the combustion temperature to be measured. The chamber was evacuated for approximately 1.5 hours to ~10^{-1} – 10^{-2} atm. and back-filled with argon to provide an inert atmosphere in order to minimise oxidation.

The samples were placed on a moveable stage and positioned so that the top surface was approximately 1-2 mm below a tungsten filament. In order to produce the heat required to initiate the reaction, a current between 100-120 amps was applied through the filament. Once initiation occurred, the sample was allowed to react until completion. A schematic diagram of the equipment is shown in Figure 7.10.

7.2.3.1 Temperature measurement

The temperature of the pressed compacts were measured using a *Raytek*

Thermalert Marathon (MR1S series) 2-colour infrared pyrometer. In 2-colour mode, temperatures are determined from the ratio of two separate and overlapping bands. The 2-colour mode is best for measuring the temperature of targets that are partially obscured (either intermittently or permanently) by other objects or openings that reduce energy, or in terms of this project, smoke generated from the SHS reaction. The pyrometer has a temperature range of 1000-3000°C and an accuracy to within 1% of the full scale. The pyrometer was placed approximately 30-40 cm from the sample. The diameter of the measured spot on the sample was approximately 4 mm. The sample being analysed had the same dimensions as mentioned in section 7.2.2.1. A computerised data acquisition system was also used to monitor the voltage output of the pyrometer which was converted to temperature via a calibration. The combustion temperatures for both the TiC-based and TiB_2-based cermets are shown in Table 8.1.

7.2.4 Grinding of SHS compacts for HVOF powder production

The particle size range of the powders used for HVOF spraying was 15-45μm as this particle size range is supplied by many HVOF powder suppliers such as Praxair Surface Technologies (Indianapolis, USA). Other researchers have also used this size range [Smith,1995]. Also, if the powder fraction is too small, during spraying, it may vaporise or severely oxidise affecting the integrity of the coating. If the powder is too large it may not sufficiently melt and may bounce off the substrate or form unmelted particles in the coating, again affecting its integrity. To obtain this desired particle size range, a *Glen Creston Gyro-Mill* was used. The compacts were initially reduced to <15mm

using a fly press. The powders were then crushed in the gyromill in 100g batches. After each grind, the powders were weighed and then sieved for 10 minutes using an *Endecotts Octagon Digital* sieving machine (Endecotts, London, UK). Ball bearings, placed on the screens, were also used to aid the sieving process. The screen sizes used to classify the powders were between 38 and 710μm. Air classification of the powders then followed to remove any sub-15μm powder particles. This was performed at LSM.

7.3 Coating production

7.3.1 Substrates

The substrates used were mild steel (BS080A15, 0.13%C, 0.7%Mn). The dimensions of the substrates used for the wear samples were 55 x 12 x 5 mm while the dimensions of the substrates used for characterisation were 57 x 25 x 2 mm. Stainless steel substrates (304) were also used for the oxidation tests and had dimensions 57 x 25 x 2 mm.

7.3.2 Spraying procedure

The HVOF (High-Velocity Oxy-Fuel) spraying equipment used was a *Miller Thermal / UTP Top Gun* system. Prior to spraying, the substrates were sand-blasted and degreased. The fuel gas used was hydrogen, while the powder carrier gas was nitrogen. The spray parameters were identical for all coatings and are shown in Table 7.2. The substrates were mounted on a turntable and rotated while the spray gun traversed vertically. Compressed air jets were used to cool the samples during and after spraying. A schematic diagram of

the thermal spraying set-up is shown in Figure 7.11. The spraying parameters used by Wirojanupatump [1999] and Stewart [1999] to deposit NiCr-Cr_3C_2 and WC-Co respectively, are shown in Table 7.3.

7.4 Oxidation tests

Oxidation tests were performed in a muffle furnace at three temperatures, 500°C, 700°C and 900°C. The coatings were placed in alumina dishes, in a pre-heated furnace, at these temperatures for 100 hours. The samples were then furnace cooled to alleviate thermal shock and any subsequent weight gain was measured. The coatings were also sectioned to observe the coating microstructure and any oxidation which may have occurred.

7.5 Characterisation of powders and coatings

Numerous examination techniques were used to analyse the SHS-produced compacts, sprayable powders and as-sprayed coatings. These techniques are discussed.

7.5.1 Particle size analysis

Particle size analyses of the powders were conducted using a *Malvern Instruments laser particle size analyser* which employs, (i) light scattering size measurement and (ii) SEM imaging of powder samples.

7.5.2 Scanning Electron Microscopy (SEM)

The powder and coating samples were observed using the *JEOL 6400 SEM.*

The parameters used on the *JEOL 6400*, which were predominantly used, were an acceleration voltage of 20 kV and a working distance of 17 mm. Back-scattered imaging was mainly used as it provided atomic contrast between the matrix, hard phase and other features in the microstructure. Energy Dispersive X-ray analysis (EDX) was performed to determine the chemical composition of different phases in the samples, where a working distance of 39 mm was used. A *Noran* EDX system with Be window for heavy elements (Fe, Cr and Ti) and ultra thin Al window for light element (C, B and O) analysis was used.

7.5.2.1 Cermet compact preparation

After SHS reaction, the samples were prepared for SEM examination. Compacts were sectioned using a *Struers Accutom-5* wheel saw (Struers, Copenhagen, Denmark) to ensure that a reasonably flat surface was achieved prior to polishing. The samples were then mounted in conductive bakelite (MetPrep, Coventry, UK) and polished using silicon carbide abrasive papers from 240 to 1200 grit, and finally polished on 6μm and 1μm diamond pads. The polished samples did not require etching for SEM examination.

7.5.2.2 Feedstock powder preparation

The feedstock powders were prepared for SEM examination, EDX analysis and particle size analysis. Powders used for SEM examination and EDX analysis of the cross-sections, were mounted in conductive bakelite and polished using the same procedure as that used for the preparation of the compact cross-sections. The morphologies of the powders were obtained by mounting the powders onto carbon tabs.

7.5.2.3 Coating preparation

The as-sprayed coatings were prepared for SEM examination and EDX analysis. The cross-sections of the coatings for SEM examination and EDX analysis were sectioned using *Struers Accutom-5* wheel saw. The coating samples were then mounted in conductive bakelite and polished using silicon carbide abrasive papers from 240 to 1200 grit, and finally polished on 6μm and 1μm diamond pads. The polished samples did not require etching for SEM examination. The coating samples subjected to oxidation tests were cold-mounted in polyester resin (Kleer Set, MetPrep, Coventry, UK) and polished using the afore mentioned procedure. These coatings were gold coated prior to SEM and EDX examination.

7.5.3 X-ray Diffraction analysis (XRD)

X-ray diffraction analysis was performed on both powders and coatings using a *Siemens Kristalloflex Diffractometer unit* combined with a computer running *Diffrac-AT* analytical software for peak identification. The machine was operated at 40kV and 20mA using Cu K_α radiation with wavelength 0.15406 nm. Samples were analysed from 2θ values of 20° to 140° using a step size of 0.02° and a step time of 2 seconds. When determining the lattice parameters of the titanium carbide for both powder and coating, a step size of 0.02° and a step time of 9 seconds was used. Powder samples were investigated by sprinkling onto an adhesive tab. Coating samples were examined by adhesion to a glass slide.

7.5.3.1 Lattice parameter measurements

As mentioned in the literature survey, titanium carbide exists over a wide stoichiometry range, $TiC_{0.47}$ to $TiC_{0.97}$. In order to calculate the stoichiometry of the titanium carbide in the powders and coatings it was necessary to calculate the lattice parameters from the XRD data. This was performed by using the 2-theta values and their subsequent d-spacings from each of the relevant peaks on the XRD traces. The lattice parameter values were then calculated using equation 7.1 below.

$$d = \frac{a}{\sqrt{N}} \quad \text{----- Equation 7.1}$$

The equation $\cos^2\theta$ / $\sin\theta$ was used as this was recommended by Cullity [1978] as this compensates for displacement of the specimen from the diffractometer axis, which is usually the largest single source of error.

The calculated lattice parameters were then plotted against $\cos^2\theta$ / $\sin\theta$ in order to extrapolate the true lattice parameter value, a_o. An example of a typical plot is shown in Figure 7.12. The lattice parameter values of TiC for the powders and coatings were then compared with a graph comparing data from numerous investigations (Figure 7.13) to obtain C/Ti atomic ratios for each. Cullity [1978] collated this data and explains that a good trend is achieved at low ratio values but the scatter is more prominent at higher ratio values. This difference is explained in terms of the difficulties in producing pure titanium carbide, as oxygen and nitrogen impurities tend to lower the lattice parameters. The trendline was therefore drawn for the experiments

which produced the highest lattice parameter values as it was thought that these would be the purest.

7.5.4 Transmission Electron Microscopy (TEM)

A *JEOL 2000 FXII TEM* machine with an Al thin window EDX system was used to investigate the morphology, composition and structure of the phases present in the coatings. An operating voltage of 200 kV was used.

Disks of 3mm diameter were cut from the bulk coating using a wire spark cutter. These disks were then ground to 150 μm thickness from the substrate side using silicon carbide abrasive pads. The sample thickness was further reduced to approximately 20 μm using a dimpler (Model 2000, Fischione Instruments, USA). The samples were dimpled and polished using 6 μm and 1μm diamond slurries. Ion beam thinning was then carried out using a *Low Angle Milling and Polishing System* (Fischione Instruments, USA) until a thin electron transparent region was formed. The ion mill was operated at 6 kV and 8mA at a temperature of –90°C and a milling angle of 15°. Each sample was demagnetised prior to being placed into the TEM.

7.5.5 Chemical analysis

Chemical analyses of the powder fines, feedstock powders and as-sprayed coatings were performed by London & Scandinavian Metallurgical Co. (LSM). XRF was used for Fe, Cr and Ti elemental analysis, where a typical tolerance of ±0.4% for 100% of an element was obtained. For total carbon analysis, a *LECO CS-444 C & S* analyser was used where a tolerance of ±

0.5% of the total C present can be obtained. Oxygen content was measured using the *LECO TC-436AR* nitrogen and oxygen determinator with a tolerance of 1% of the total oxygen present. Finally, boron content was determined using a boron monitor, which is based upon neutron absorption of boron. The analytical error is dependent upon the material type.

7.5.6 Microhardness Tests

Microhardness testing of the coatings was performed using a *Leco M-400* microhardness tester with a 300g load and a dwell time of 15 seconds. Each coating was tested at 10 random points along the centre of the sample.

The coatings used for microhardness testing of the coating cross-sections were sectioned and polished using the same cutting and mounting techniques mentioned in section 7.5.2.3.

7.5.7 Grain size and volume fraction of hard phases

Estimates of the grain size of both the TiC-based and TiB_2-based powders and coatings were determined using the *JEOL 6400 SEM.*

The volume fractions of the hard phases were determined using the manual line measurement method. This involved superimposing random lines of known length and measuring the length of the hard phase that the line intersects. All measurements were performed using more than 100 second phase intersections. Due to the small scale of the hard phase particles (especially in the coatings) along with the presence of oxides etc., identification of the hard phase was not easy and may have resulted in

significant errors. The difficulties associated with this method of measurement resulted in estimated errors of ± 10%.

7.5.8 Profilometry and roughness measurements

Profilometry and roughness measurements of the coatings were performed using a *Surfcom Surface Texture Measuring Instrument* (Advanced Metrology Systems, Leicester, UK) with a traversing length of 5 mm and a cutoff of 0.08 mm.

7.5.9 Coating thickness measurements

The thickness of the coatings was measured by examination of a coating cross-section using the *JEOL 6400 SEM.* Ten random areas were selected and the coating thickness measured in order to obtain an average.

7.6 Abrasive wear testing

Abrasive wear testing of the coatings were performed using a *dry sand rubber wheel (DSRW)* abrasive wear-testing rig. All four coatings were tested along with coatings sprayed from commercially available cermet powders, namely, WC-Co and NiCr-Cr_3C_2 as a comparison [Wirojanupatump,1999; Stewart,1998].

7.6.1 Dry Sand Rubber Wheel (DSRW) abrasive wear test rig

A schematic diagram of the wear testing apparatus is shown in Figure 7.14. In this design, both the specimen and rubber wheel sat in a trough (width 12.9

mm) so that the abrasive particles were constrained to pass through the wear zone. The abrasive particles were passed through the contact zone once only to minimise any particle degradation effects which may occur during testing. Both the specimen holder and wheel, which the rubber tyre was fixed around, were made of a reinforced epoxy resin (Tufnol). The Tufnol wheel had a diameter of 130 mm and an overall diameter including the rubber tyre of 150 mm. The rubber tyre was a cast polyurethane elastomer (Just Rubber, Cwmbran, UK) with an International Rubber Hardness of 63. The wheel was driven by a d.c. motor mounted on the pivot arm and was rotated at a speed of 75 r.p.m. Loads were applied to the specimen by placing weights on the pivot arm. The abrasive was fed into the chute by a rotating nylon drum, containing a groove, at a constant speed of approximately 80 g min^{-1} for alumina and approximately 70 g min^{-1} for silica (the difference being due to the packing densities of the two abrasives).

7.6.2 Abrasives

Two types of abrasive were used during testing, angular alumina (Abrasive Developments Ltd., Henley-in-Arden, UK) and rounded silica (David Ball Group, Cambridge, UK). Both of the abrasives were sieved to obtain a desired particle size fraction of 500-600 μm using an *Endecotts Octagon Digital* sieving machine (Endecotts, London, UK).

Hardness measurements of the abrasives were determined using the *Leco M-400* microhardness testing machine with an applied load of 200g and a dwell time of 15 seconds. The morphologies of these abrasives are shown in Figure 7.15.

7.6.3 Test parameters

All abrasive wear tests were performed under a load of 54 N. Each test consisted of a set number of revolutions, which were selected dependent upon the abrasive used. An extended wear run at the beginning of the test was performed to remove any surface asperities from the coatings, which may affect the wear results. The samples were cleaned and weighed before and after each wear test so that an accurate mass loss could be recorded. The tests were continued until steady state conditions were obtained. Figure 7.16 shows an example of the raw mass-loss data for one of the abrasive wear tests performed. The volumetric wear losses of the coatings were calculated using the volume fractions of the hard phase and matrix for each coating from Table 8.6. The average densities were then calculated and the resultant volume losses were obtained using the initial mass losses of the coatings.

7.6.4 Wear scar characterisation

When examining the wear scars, top-surface and cross-sectional images were obtained. The cross-sectional samples were sectioned along the direction of abrasive flow and cold mounted in polyester resin, followed by gold coating. EDX analysis was also used for qualitative analysis.

Composition	Fe / wt.%	Cr / wt.%	Ti / wt.%	C / wt.%	B / wt.%	Desired Hard Phase
FeCr-TiC (Equi.)	Balance	6	56	14	-	$TiC_{0.96}$
FeCr-TiC (Excess C)	Balance	6	47	23	-	$TiC_{0.96}$
FeCr-TiC (Excess Ti)	Balance	6	62	8	-	$TiC_{0.48}$
FeCr-TiB_2	Balance	6	48	-	22	TiB_2

Table 7.1: Elemental powder compositions

Spray parameter	Parameter value
Oxygen flow rate	236 l min^{-1}
Fuel gas (hydrogen) flow rate	599 l min^{-1}
Carrier gas (nitrogen) flow rate	21 l min^{-1}
Combustion chamber length	22 mm
Spray distance	203 mm
Substrate velocity (horizontal plane)	1 m s^{-1}
Gun traverse speed (vertical plane)	5 mm s^{-1}
Powder feed rate	~1.2 kg / hr
Number of passes	20

Table 7.2: HVOF spraying parameters

Spray parameter	Parameter value WC-Co	Parameter value $NiCr-Cr_3C_2$
Oxygen flow rate	240 l min^{-1}	130 l min^{-1}
Fuel gas (hydrogen) flow rate	640 l min^{-1}	400 l min^{-1}
Carrier gas (nitrogen) flow rate	16.5 l min^{-1}	18 l min^{-1}
Combustion chamber length	-	12
Spray distance	300 mm	250 mm
Substrate velocity (horizontal plane)	1 m s^{-1}	1 m s^{-1}
Gun traverse speed (vertical plane)	5 mm s^{-1}	5 mm s^{-1}
Powder feed rate	~3.3 kg / hr	~1.14g / hr
Number of passes	30	40

Table 7.3: HVOF spraying parameters to deposit WC-Co and $NiCr-Cr_3C_2$

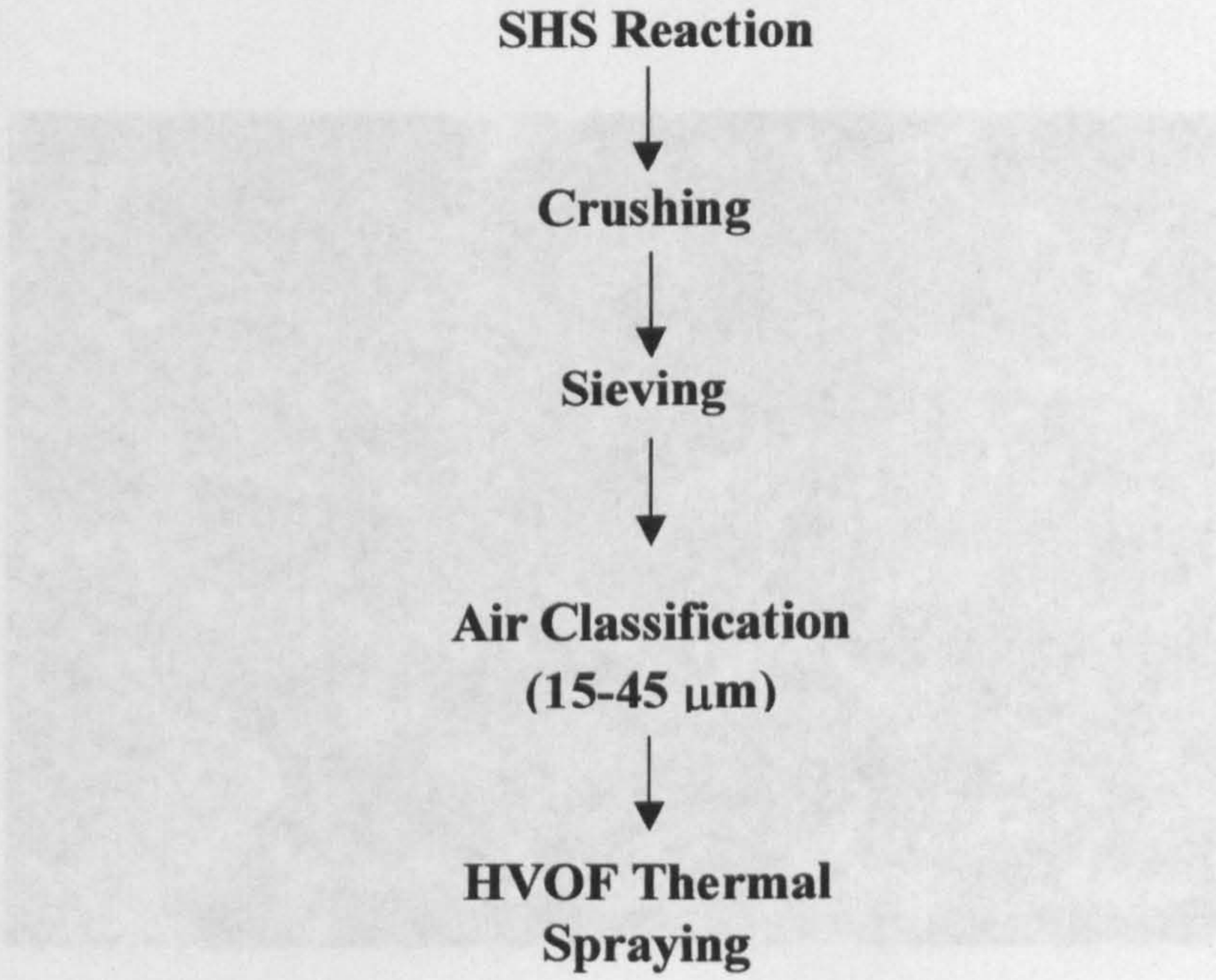

Figure 7.1: Flow-chart of the various stages of coating production

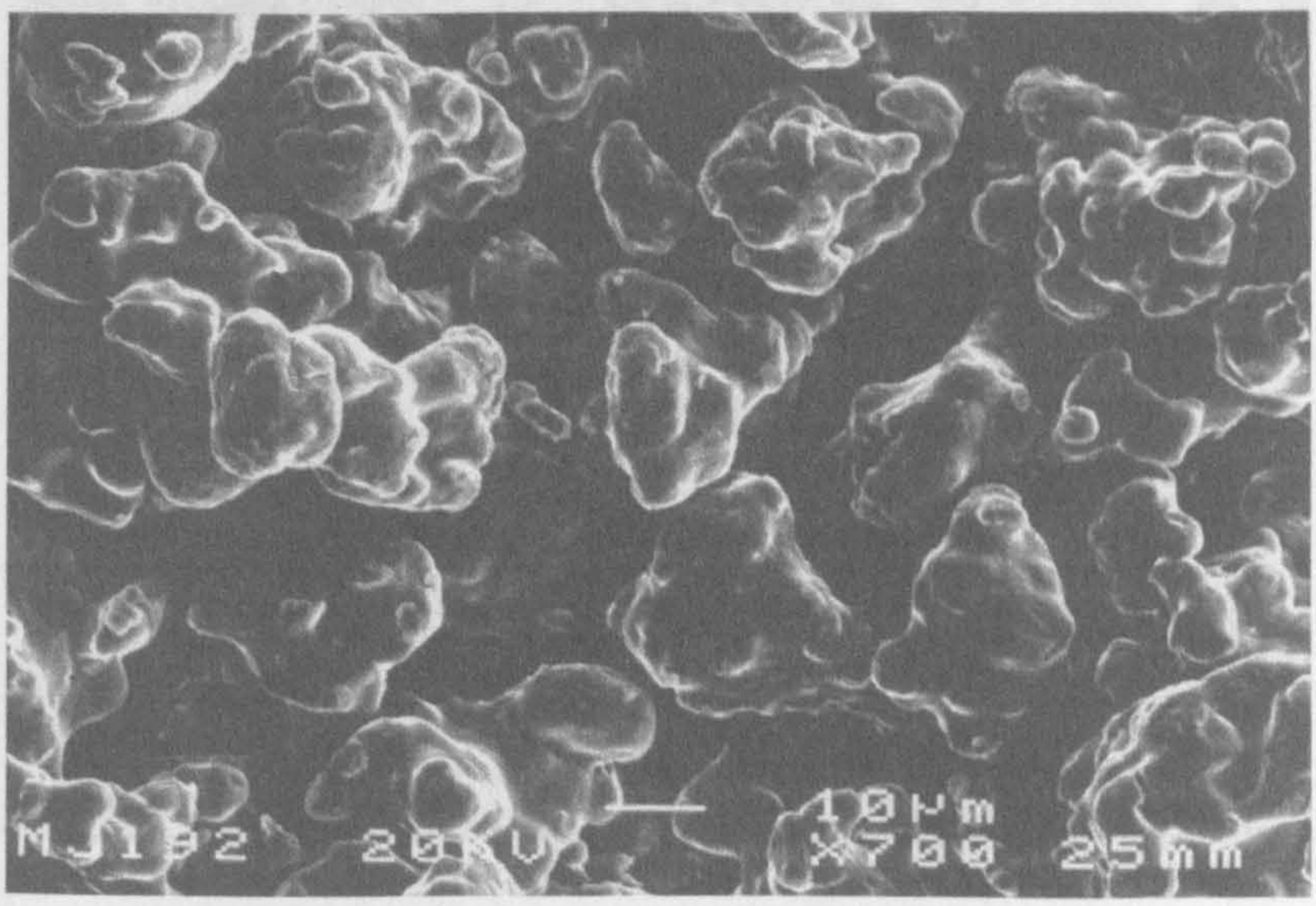

Figure 7.2: Morphology of iron powder

Figure 7.3: Morphology of titanium powder

Figure 7.4:Morphology of chromium powder

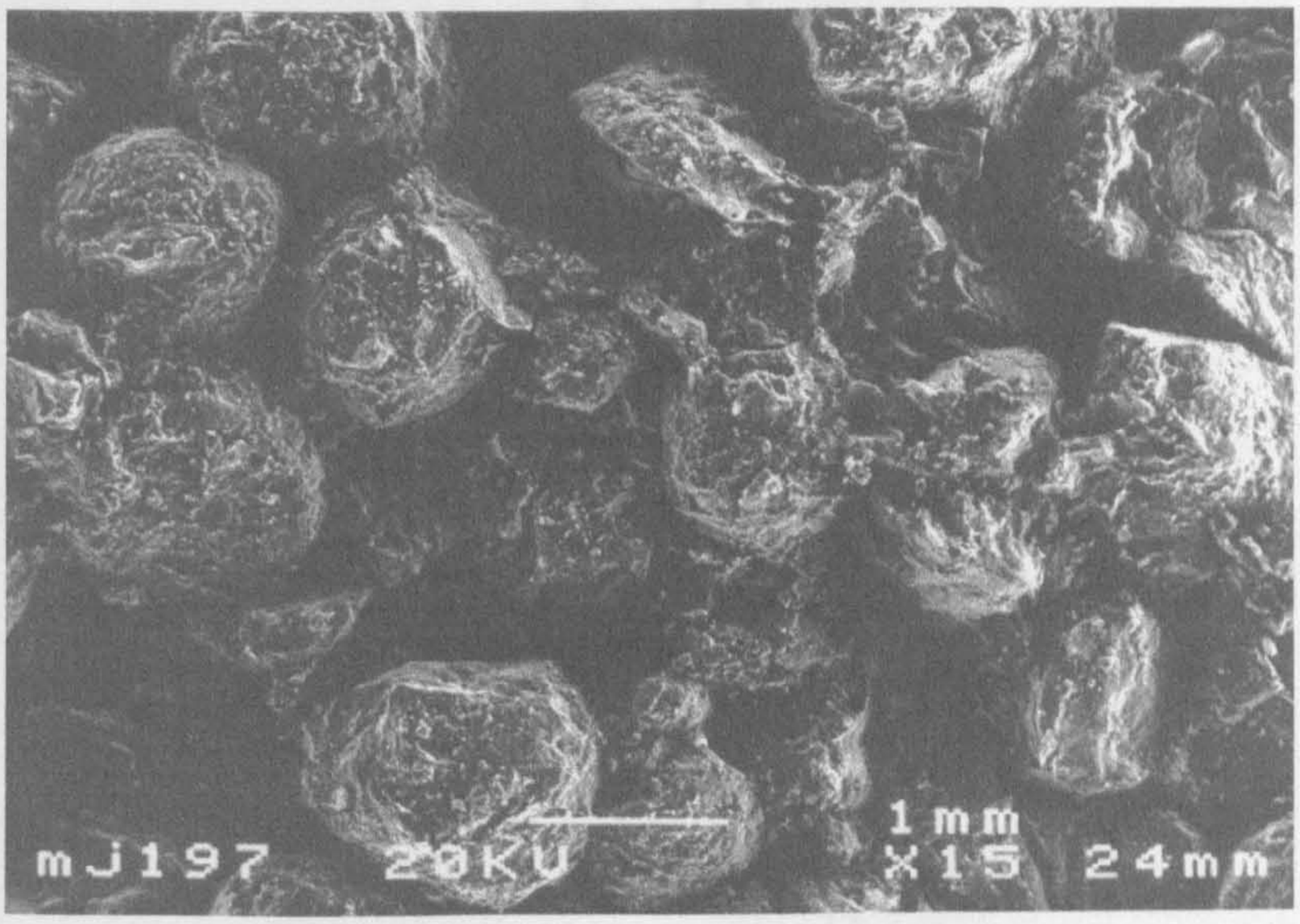

Figure 7.5: Morphology of carbon powder

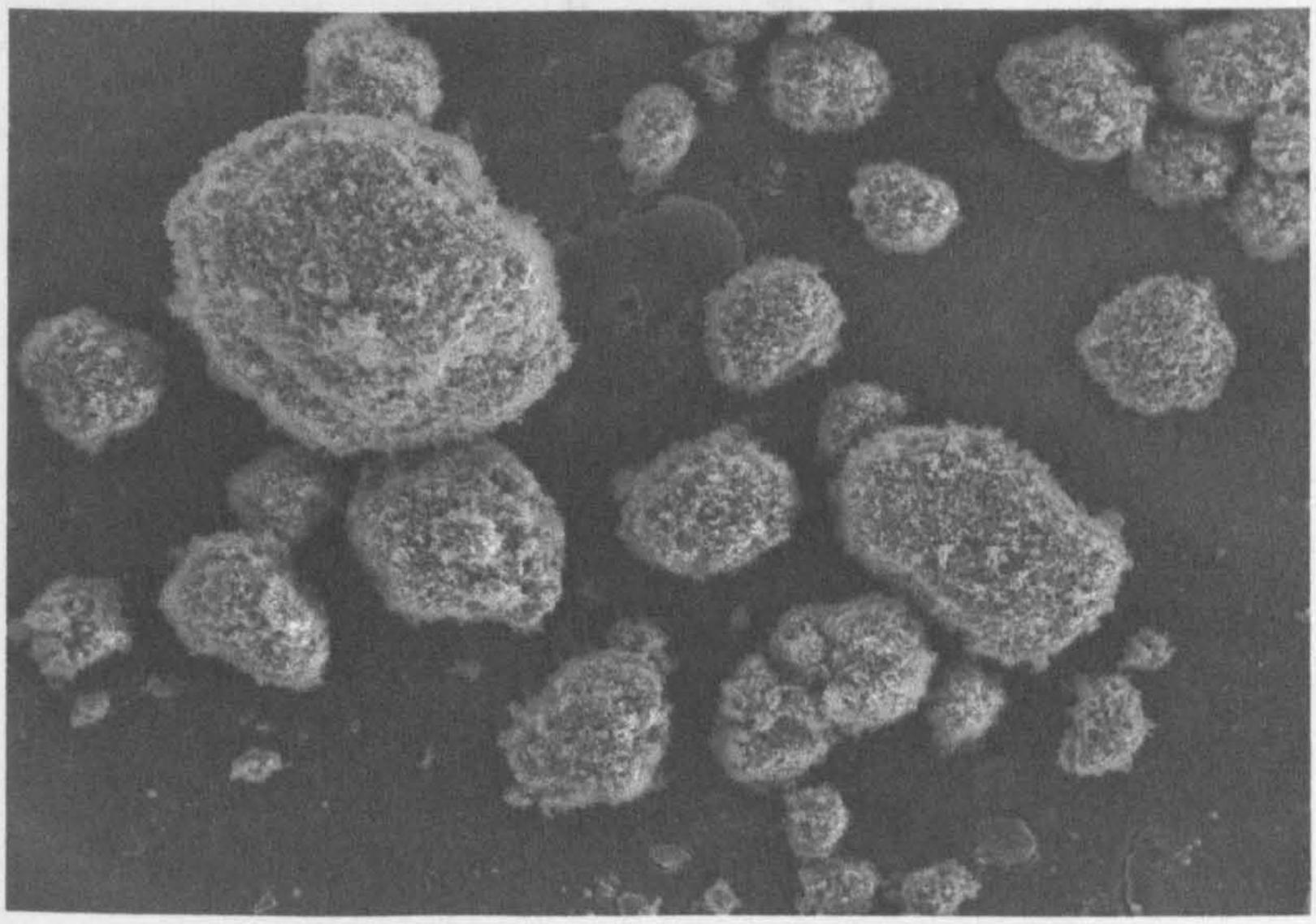

Figure 7.6: Morphology of boron powder

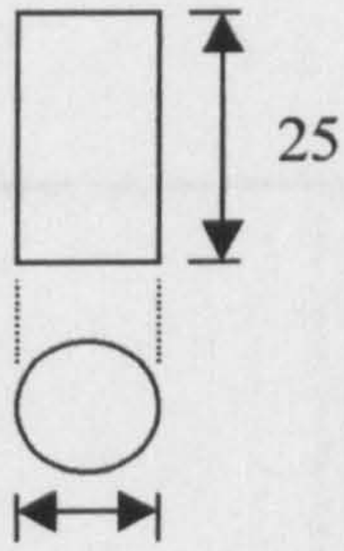

12

Figure 7.7: Dimensions of pressed compact (mm)
(Not to scale)

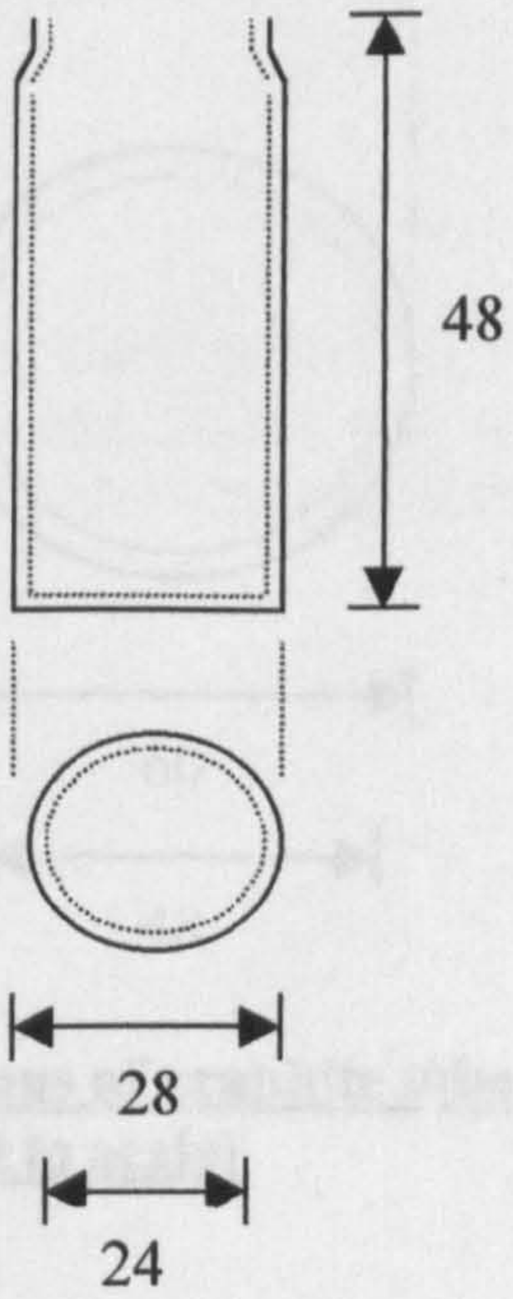

Figure 7.8: Dimensions of glass vial (mm)
(Not to scale)

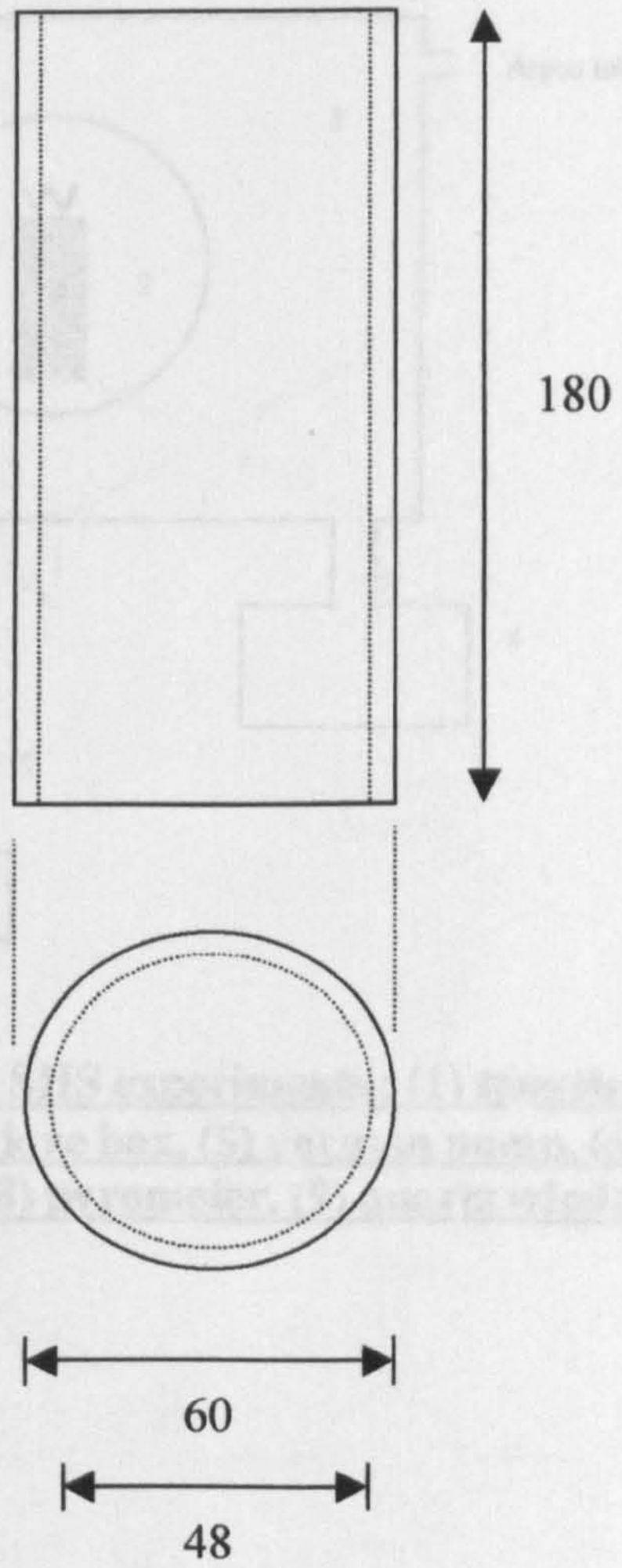

Figure 7.9: Dimensions of graphite tube (mm)
(Not to scale)

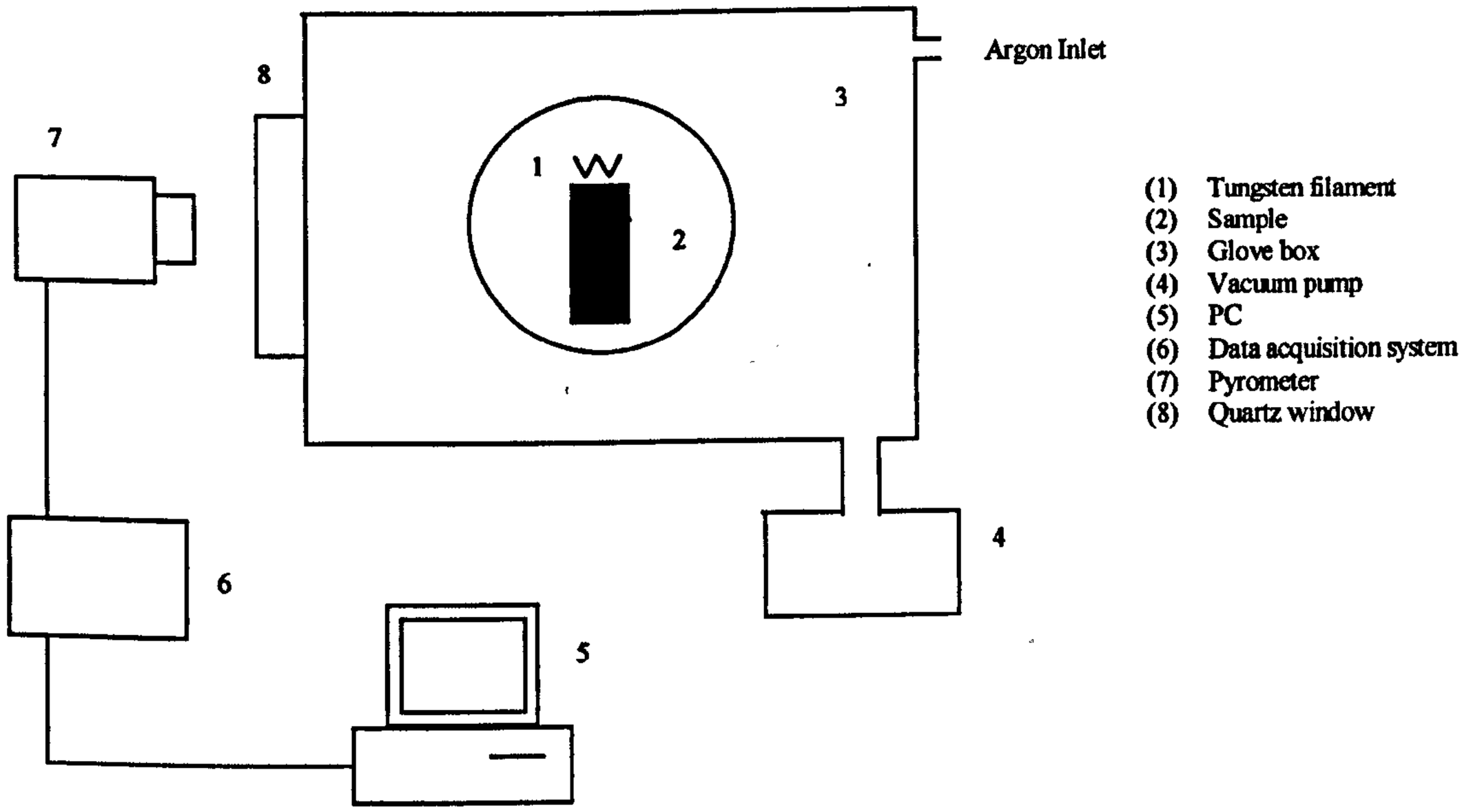

Figure 7.10: Apparatus used for SHS experiments : (1) tungsten filament, (2) sample, (3) graphite stage, (4) glove box, (5) vacuum pump, (6) PC, (7) data acquisition system, (8) pyrometer, (9) quartz window

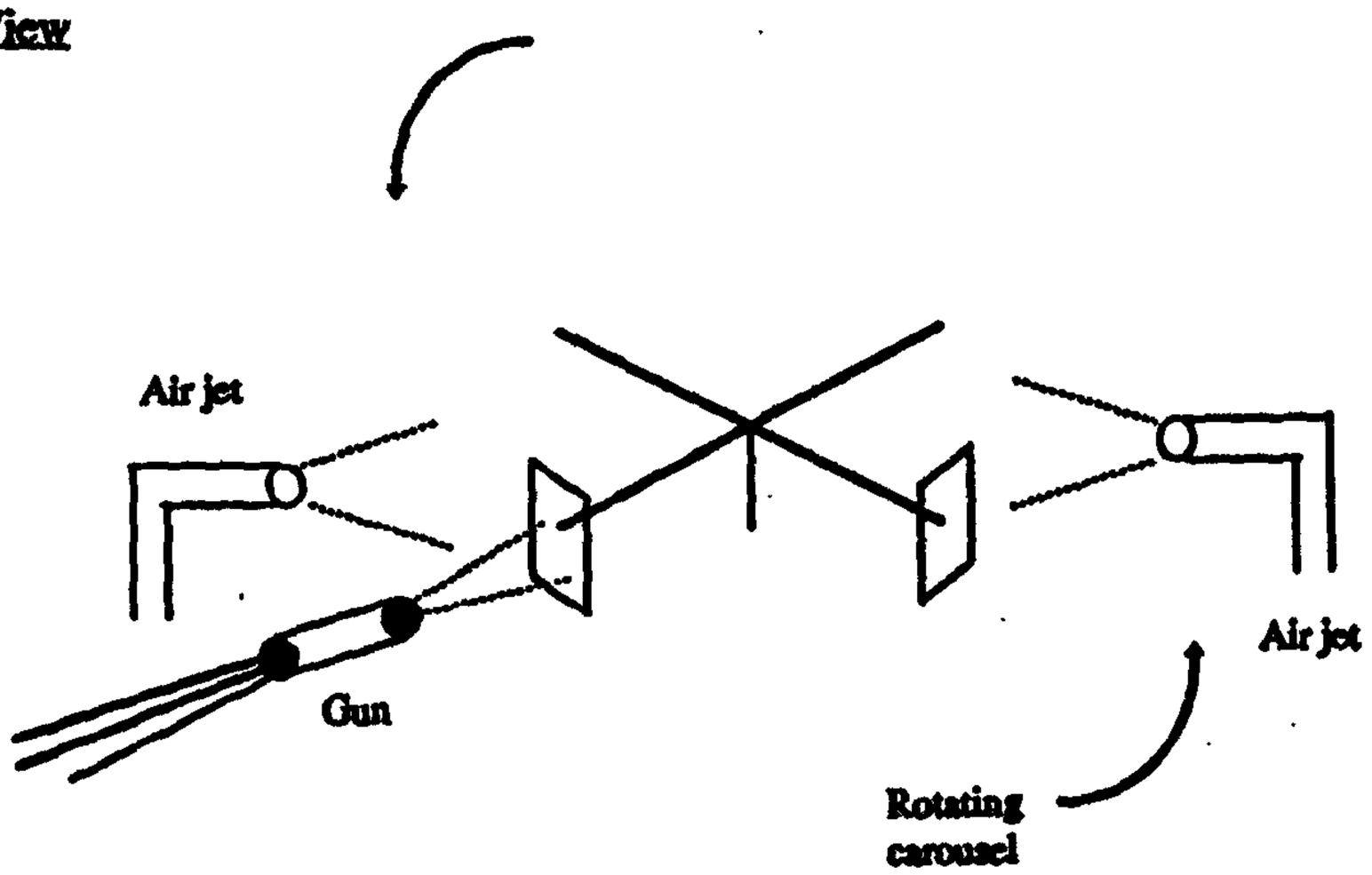

Figure 7.11: Schematic of thermal spray set up

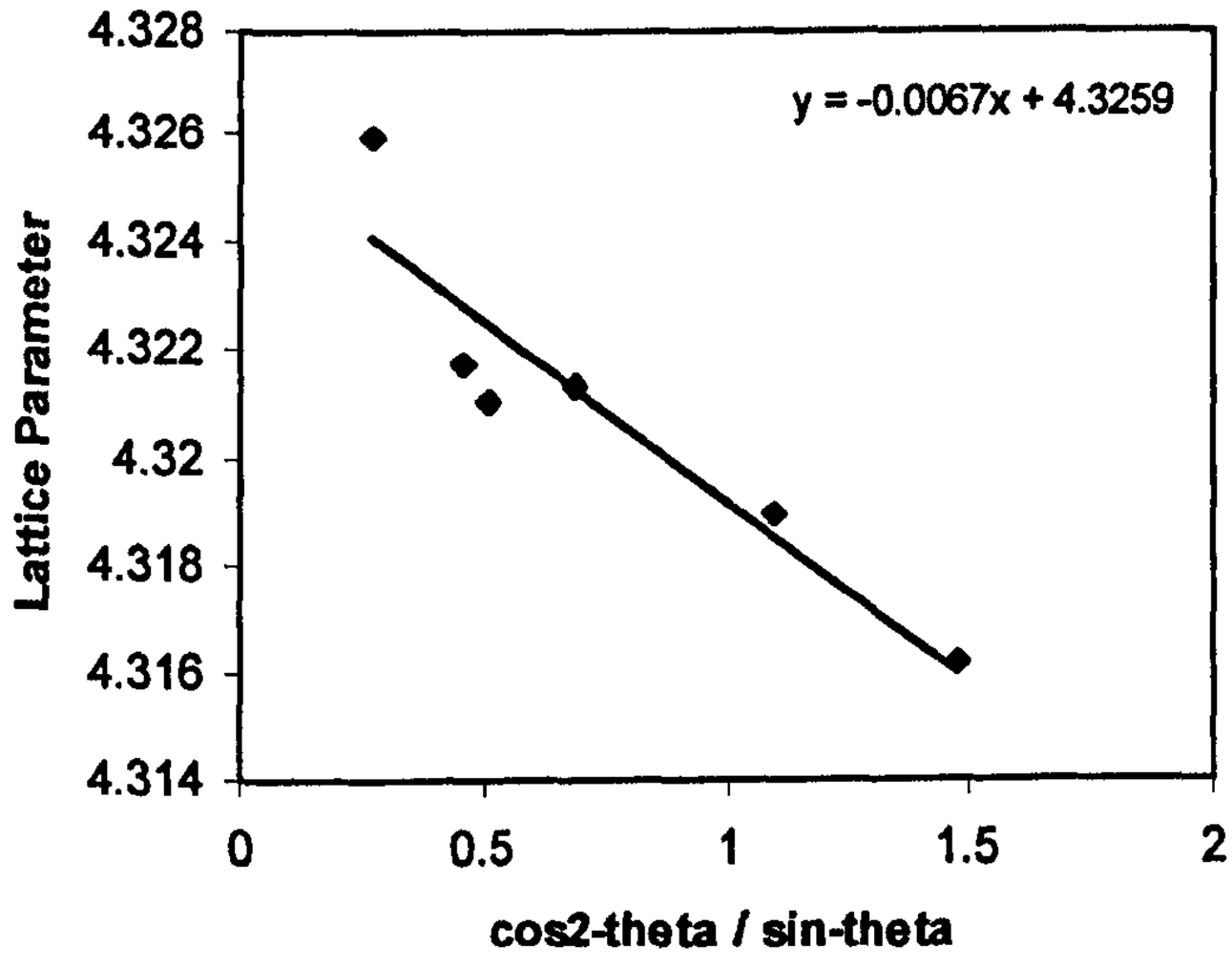

Figure 7.12: Plot of calculated lattice parameter against $\cos^2\theta$ / $\sin\theta$

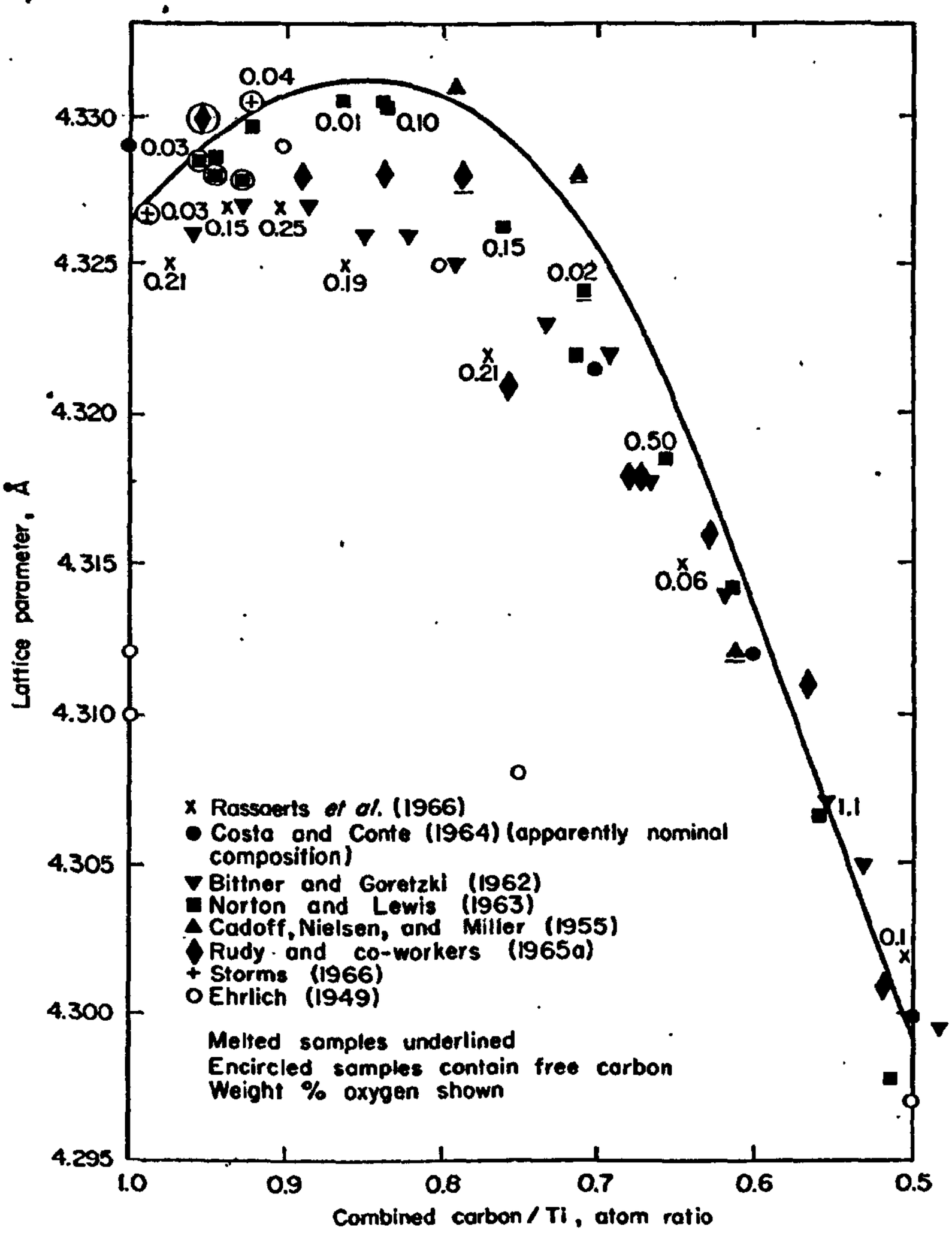

Figure 7.13: Lattice parameter of TiC as a function of composition [Storms,1967]

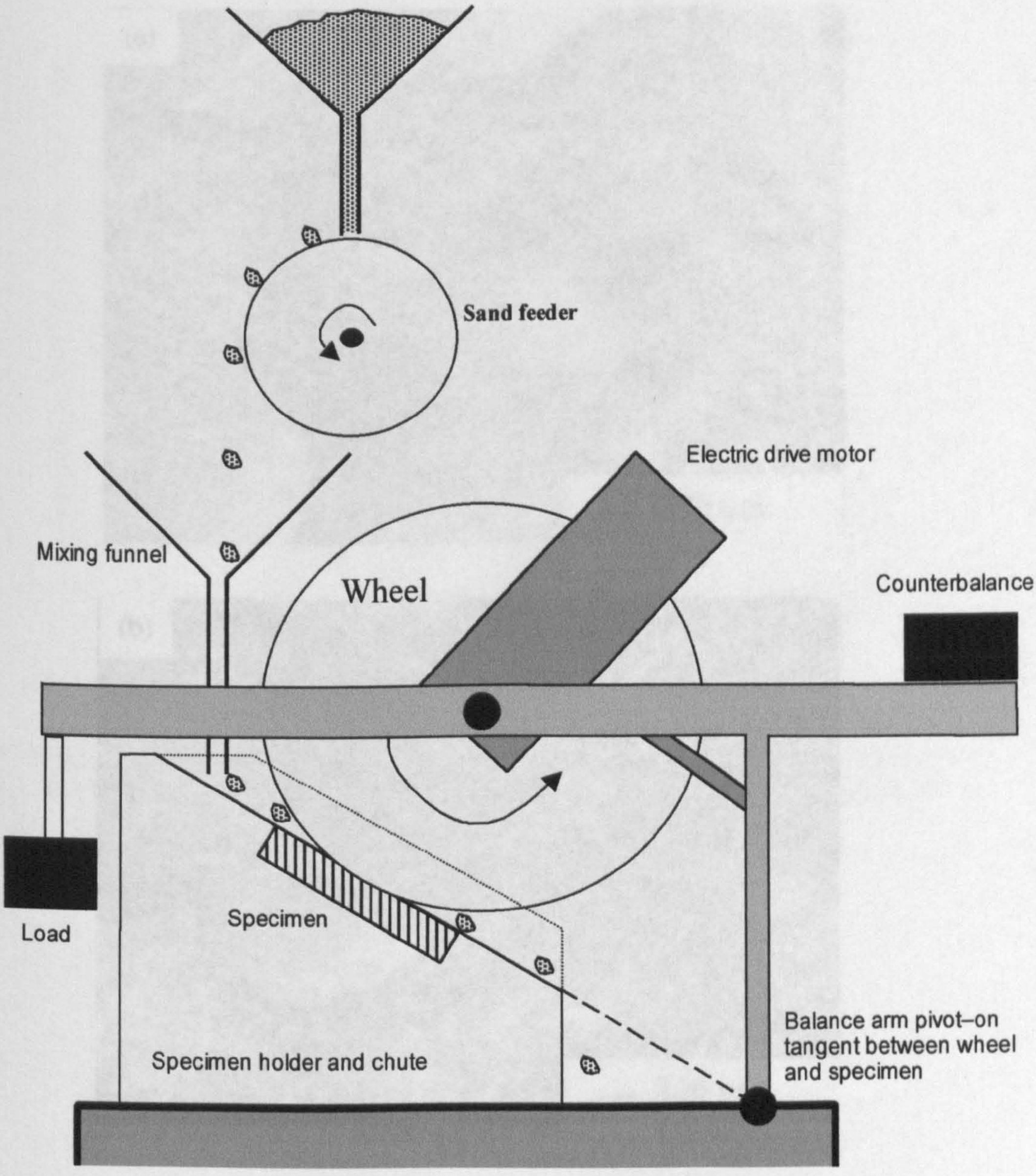

Figure 7.14: Schematic diagram of the dry sand rubber wheel (DSRW) abrasive wear test rig

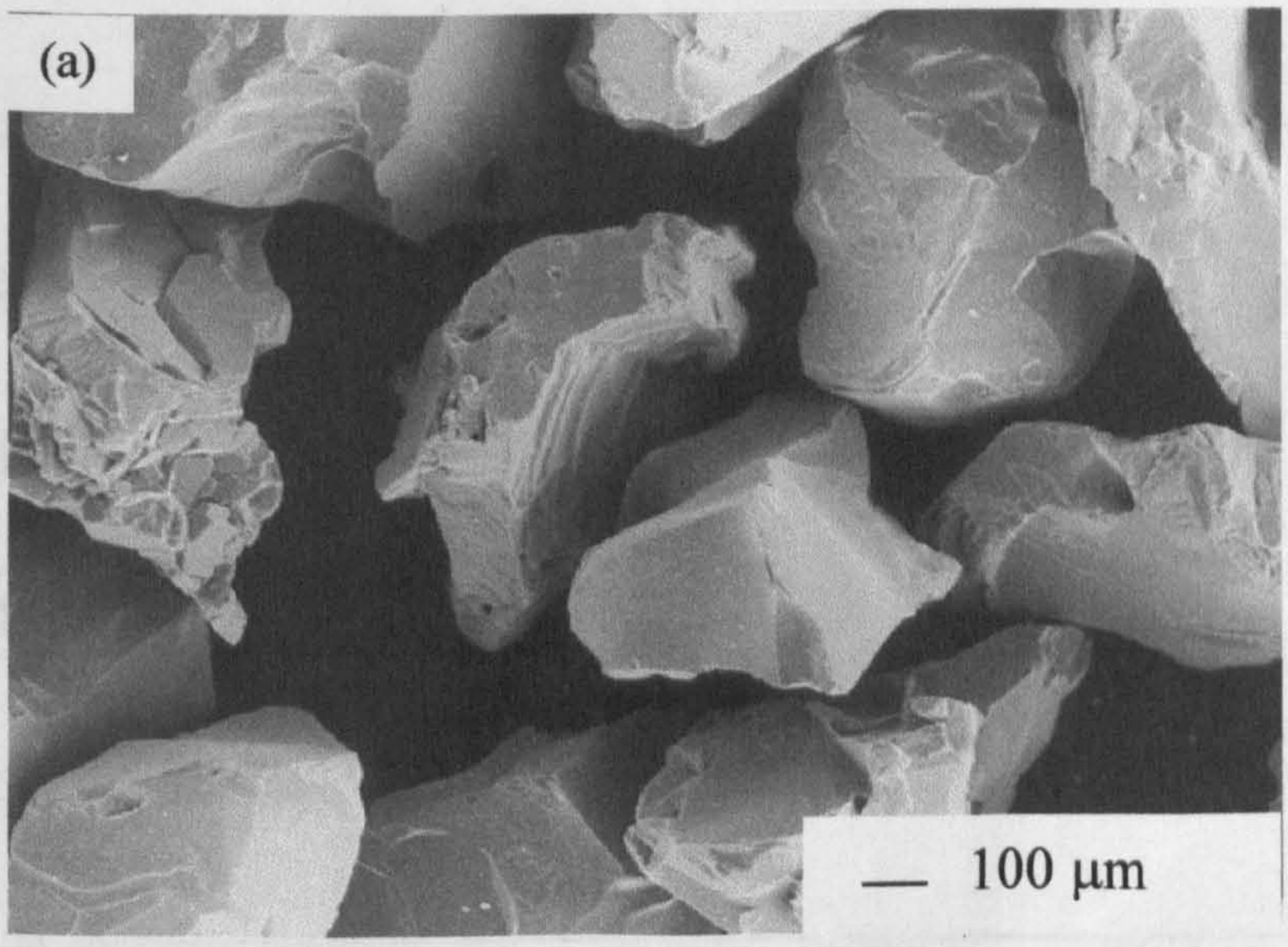

Figure 7.15: Morphologies of (a) alumina abrasive, and (b) silica abrasive.

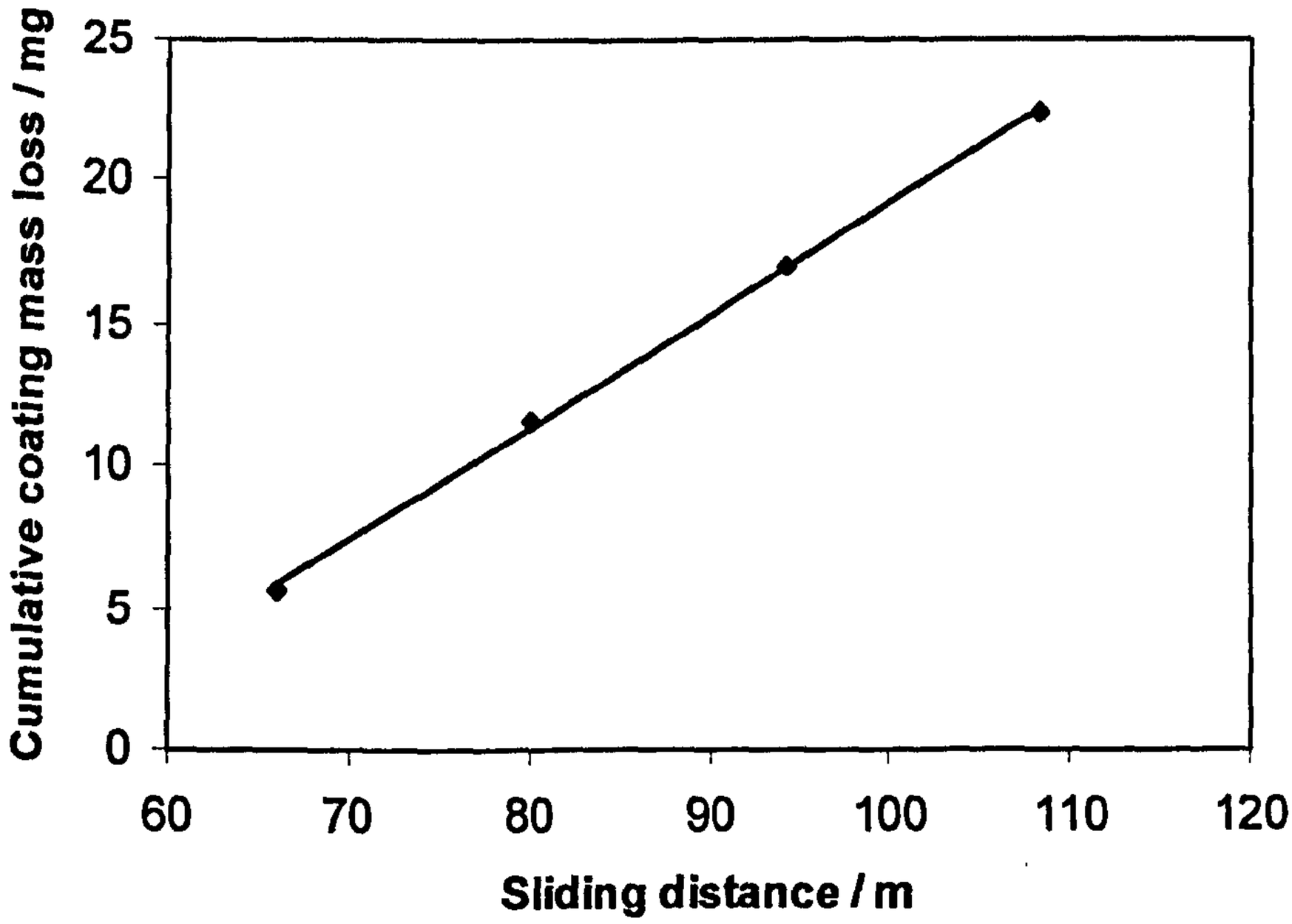

Figure 7.16: Example of raw mass-loss data as a function of sliding distance for dry sand rubber wheel abrasion with alumina abrasive under a load of 54N.

8 Results

8.1 Feedstock powder production

This section briefly outlines the combustion temperatures achieved during SHS reaction of each composition, and the morphology, microstructure, chemical analysis and XRD analysis of the powders after crushing and air classification.

8.1.1 Combustion temperatures

Table 8.1 shows the combustion temperatures which were recorded for the synthesis of the four cermets. It can be seen that for the TiC-based cermets, the equimolar had the highest combustion temperature, followed by the excess C and excess Ti cermets. The TiB_2-based cermet attained the highest combustion temperature overall.

8.1.2 Chemical analysis of powders

Tables 8.2 to 8.5 show the compositions of the elemental powders prior to SHS reaction, the powder fines and feedstock powders. Tables 8.2, 8.3 and 8.4 show the compositions of the equimolar TiC, excess C and excess Ti powders respectively. For both the equimolar and excess Ti powders it can be seen that the compositions of the feedstock powders and the initial SHS reactant mixtures are similar, apart from a loss of titanium carbide particles from the matrix during grinding. The excess C sample shows a significant loss of C which is not commensurate with the loss of Ti. In all cases, the powder fines contain a larger proportion of Ti and C than in the powder feedstock. Table 8.5 shows the

composition of the TiB_2-based elemental powder mix prior to reaction, powder fines and the feedstock powders. The compositions of the feedstock powders and the initial SHS reactant mixtures are similar, although there appears to be a preferential loss of titanium. All compositions show an increase in the weight percentages of Fe and Cr, when comparing the SHS reactant powders with the feedstock powders.

8.1.3 Feedstock powder morphology and size

Figure 8.1 shows the morphologies of the crushed powders after air-classification. It can be seen that each of the cermet powders have an angular morphology with both large particles and smaller particles within the ranges of 15-45μm. Figure 8.2 shows the Malvern particle size distributions of the feedstock powders and all show similar size distributions. It can be seen that in both Figure 8.1 and 8.2 there is a significant fraction of particles below the nominal 15μm cutoff.

8.1.4 Powder microstructure

Figure 8.3a-d shows the powder cross-sections of equimolar, excess C, excess Ti and TiB_2-based powders respectively. XRD and EDX analysis shows that the equimolar and excess C samples contain dark, spherical regions which are the TiC particles and the lighter, surrounding regions are a ferritic, iron-based matrix. The excess Ti sample again shows dark, spherical regions which are TiC particles and a lighter, surrounding matrix. XRD analysis (Figure 8.6b) shows that the iron peak, at approximately 45.5°, which is clearly present in the equimolar and excess

C coatings, is missing (or very small) in this coating. However, the presence of FeTi and Fe_2Ti is indicated in the XRD trace (Figure 8.6b) and EDX analysis shows that these phases make up the matrix. SEM, XRD and EDX analysis indicate that the TiB_2-based powder consists of dark, angular regions which are TiB_2 and a lighter ferritic, iron-based matrix. The volume fraction of the hard phase for each composition was measured by the line counting method (Section 7.5.7) and is shown in Table 8.6. It shows that the TiC-based powders have, in general, a higher volume fraction of hard phase than the TiB_2-based powder. The coatings however, show a different trend where the TiB_2-based coating has retained a higher volume fraction of hard phase than the TiC-based coatings. In terms of the TiC-based powders and coatings, the equimolar sample exhibits a higher volume fraction of hard phase, followed by the excess C and sample and finally the excess Ti sample. Table 8.6 also shows the sizes of the hard phases in both the powders and coatings. It shows that the TiC-based feedstock powders all have very similar hard phase sizes of approximately 1-5μm (predominantly greater than 2.5μm), while the TiB_2-based powder has a hard phase size range of sub-μm to 6μm (predominantly less than 3μm). The hard phase size ranges for all coatings are the same as their subsequent feedstock powders, but perhaps in different proportions.

8.1.5 XRD analysis of powders

The XRD analyses of the fines (after air classification) and feedstock powders can be seen in Figures 8.4 to 8.7. The XRD traces show the phases that are present in

the powders and coatings. Figure 8.4a shows the XRD trace of the equimolar powder fines and when compared with the feedstock powders (Fig. 8.4b) it can be seen that they both contain predominantly TiC and Fe(Cr), with trace amounts of an FeTi intermetallic and Cr_7C_3. Free C is also thought to be present in the system but is not evident in the XRD trace as it is amorphous. Figure 8.5a and b show the XRD traces of the excess C fines and feedstock powder. The phases present in the fines are predominantly TiC and Fe(Cr), with trace amounts of FeTi intermetallic and Cr_7C_3, Fe_3C and free C, which is not present in the XRD trace as it is amorphous. The feedstock powder contains predominantly TiC and Fe(Cr), with trace amounts of FeTi and Cr_7C_3.

Figures 8.6a and b show the XRD traces of the excess Ti powder fines and feedstock powder respectively. It can be seen that the phases present in the feedstock powder are TiC, and three intermetallic phases, namely, Fe_2Ti, FeTi, and a small amount of Cr_2Ti. The powder fines contain the same phases, apart from Cr_2Ti. It must also be noted that there is switch in intensities of the two main TiC peaks between 35 and 42°, when compared with the equimolar and excess C powders. Figures 8.7a and b show the XRD traces of the TiB_2-based powder fines and feedstock powders respectively. The phases present in both traces are TiB_2, Fe(Cr), an FeTi intermetallic, and small amounts of FeB, Fe_2B and Cr_2Ti. For the benefit of the reader, Figures 8.4 to 8.7 are reproduced in Figures 8.8 to 8.11 respectively, with the three states (fines, powder feedstock and coating) overlayed so that differences can be easily discovered.

The lattice parameters of the TiC in the powders were calculated from the XRD data, using the 2-theta values and their subsequent d-spacings (Section 7.5.3.1), and are shown, along with the C/Ti ratios, in Table 8.7. It can be seen that the difference in the C:Ti ratios is small, indicating that the carbide stoichiometry is very similar despite the differences in reactant makeup. The main differences in the powder feedstock appear to be in the matrix.

8.2 Coating properties

This section outlines the characteristics of the coatings produced by thermal spraying, including microstructure and physical properties.

8.2.1 Coating properties

The thickness, hardness and roughness properties of the four cermet coatings are shown in Table 8.8. The average thickness of the equimolar coating is 100μm compared with approximately 120μm for the remaining coatings. The TiB_2-based coating exhibits the highest hardness, followed by excess C and equimolar, which are of similar hardness, and finally, the excess Ti coating. In terms of coating roughness, the TiB_2-based coating exhibits the highest average roughness, followed by the TiC-based coatings where the roughness values are comparable. The calculated average densities of the four coatings and NiCr-Cr_3C_2 and WC-Co are also shown in Table 8.8. These values were obtained in order to calculate the volumetric wear losses from the mass wear coefficients of the coatings. The calculations and assumptions are shown in Appendix A.

8.2.2 Coating microstructure

8.2.2.1 SEM images

The microstructures of the sprayed coatings are shown in Figure 8.12. The TiC-based coatings show that a significant loss of the TiC phase (approximately 50%) has occurred when compared with the feedstock powder (Table 8.6). The hard phase can be seen as spherical-like dark regions. The lighter regions in the coating are a ferritic-based iron matrix while the stringer-like features are oxides. The excess C coating exhibits a finer carbide distribution than the other TiC-based coatings and the excess Ti coating appears to have the largest volume fraction of oxide stringers. The TiB_2-based coating contains angular TiB_2 particles, a lighter ferritic iron-based matrix, and a small proportion of oxide stringers. The coating contains a higher volume fraction, and finer size range, of hard phase when compared with the TiC-based coatings. There also appear to be fewer oxide stringers. Table 8.6 shows the volume fraction and size range of the hard phases in the coatings.

8.2.2.2 TEM images

The images obtained from TEM analysis of the four cermet coatings are shown in Figures 8.13 To 8.27. It must be noted that the circles, which are superimposed onto some of the images, are not the actual sizes of the apertures used, but a indicator of the region being investigated. Figure 8.13 shows images obtained from the equimolar coating. Figure 8.13a shows a general view of the coating where numerous rounded TiC particles are bonded to the matrix. A higher

magnification view of a TiC particle and its corresponding diffraction pattern can be seen in Figures 8.13b and d respectively. Figure 8.14 shows a high magnification image of a TiC particle and matrix with the subsequent EDX analyses. The EDX analysis of the TiC particle indicates only the presence of titanium, while the EDX of the matrix phase indicates a predominantly FeCr-based phase with a small amount of Ti. There is no C in the EDX trace of the TiC particle, as EDX analysis has difficulty in analysing low atomic mass elements such as carbon. Figure 8.15 shows images of the matrix phase with corresponding EDX and diffraction pattern. The matrix phase has a granular appearance and it can be seen from the EDX trace that this consists of an FeCr-rich phase along with a small amount of Ti. Analysis of the diffraction pattern reveals a phase believed to be FeCr-based although the d-spacings of 2.155 and 1.868Å do not match perfectly. Figures 8.16 to 8.20 shows images obtained from the TEM analysis of the excess C coating. Figure 8.16a shows a low magnification image of the rounded TiC particles bonded to the matrix over an approximate area of 12 μm^2. Figure 8.16b shows a higher magnification image of a TiC particle which exhibits a large dislocation network within the particle, whilst Figure 16c shows three TiC particles in the matrix. Figure 8.17 shows an image of a TiC particle containing a high density of dislocations. EDX of the TiC particle indicates that it is titanium rich, with no Cr or Fe contents, while EDX of the matrix shows an FeCr-rich phase with a small amount of Ti. Copper is also regarded as being present, but this is due to the sample holder used. Bright-field and dark-field images of both TiC particle and matrix are shown in Figure 8.18

with a diffraction pattern and EDX trace of the particle. The bright-field image shows the grains of the matrix more clearly which are very similar to those found in the equimolar sample (Figure 8.15). Higher magnification images of the granular matrix are shown in Figure 8.19. Two diffraction patterns of the grains, taken from different zone axes, can be seen in Figure 8.19 where diffraction pattern, (a), exhibits both a spot pattern and streaking between the spots. Indexing of the spots of diffraction pattern (a) reveals the three largest d-spacings of 3.5085, 2.5369 and 2.0577Å. Diffraction pattern (b) has the three largest d-spacings of 6.0857, 3.6506 and 3.6383Å (Figure 8.19b). Although EDX analysis of the grains reveal a predominantly FeCr-based phase, the d-spacings obtained from the diffraction patterns do not match any published PDF card perfectly. The higher magnification image of the grains reveals a lamellar-type structure in the grains and also a second phase between the grains. Extinction contours are also visible in Figure 8.19c and indicates that each cell is in the same orientation as the next, which suggests that it is not a random, polycrystalline material. Figures 8.20a and b show high magnification BF and DF images of the grains and both indicate that a second phase is present between the grains.

Figures 8.21 to 8.24 show the images obtained from the excess Ti sample. Figure 8.21 shows images of TiC particles within the matrix. Figure 8.22 shows a region of the matrix which consists of a mixture of phases that are rich in Ti, Fe and O. Indexing of the diffraction pattern revealed a mixture of Fe_2Ti, Ti_2O_3 and $FeTiO_3$, which is complemented by the fact that the rings are not well defined and this

indicates that a mixture of phases are present. As the EDX trace consists predominantly of titanium, it is proposed that mainly Ti_2O_3 is present. Figure 8.23 shows a phase present in the matrix, which appears to have substantiated proportions of Fe and Ti, with a small amount of Cr. Indexing of the diffraction pattern reveals that both FeTi and Fe_2Ti intermetallics are present which is again complemented by the fact that the ring patterns are not clearly defined and indicates a mixture of phases. Figure 8.24a shows an image which contains dark, globular precipitates which are rich in Fe and Cr. The diffuse ring in the diffraction pattern of this phase indicates that the iron is amorphous. The phase surrounding the precipitate is Ti and O rich and the diffraction pattern reveals that this phase is a mixture of Ti_2O_3 and $FeTiO_3$ phases (Figure 8.24b).

Figures 8.25 shows a general view of a TEM foil obtained from a TiB_2-based coating. The sample shows areas containing TiB_2, matrix and oxide. Figure 8.26 shows low magnification images of angular TiB_2 particles and a matrix phase. A spot diffraction pattern of the TiB_2 particle is shown in Figure 8.26 with a zone axis [-1,-2,2]. The region at the bottom of the TiB_2 particle in Figure 8.26c is the matrix, containing a mixture of amorphous and crystalline phases and can be seen in Figure 8.27a. The crystalline phase is Ti-rich and is accompanied by a ring diffraction pattern and indexing reveals that it consists of Ti_2O_3 and $FeTiO_3$ (Figure 8.27g). The darker regions are amorphous, as indicated by the diffuse rings in the diffraction patterns, and EDX analysis indicates that they consist of

FeCr with a small amount of Ti. However, the titanium content in the trace may be contributed by the crystalline, oxide phase.

8.2.3 XRD analysis of coatings

Figures 8.4c to 8.7c show the XRD traces of the equimolar, excess C, excess Ti and TiB_2-based coatings respectively. The equimolar and excess C coatings contain TiC, a ferritic iron-based phase, two oxides, $FeTiO_3$ and Ti_2O_3, and trace amounts of FeTi and Cr_2Ti intermetallics, and Cr_7C_3. The excess Ti coating contains TiC, Fe_2Ti, FeTi, trace amounts of Cr_2Ti, two oxides, $FeTiO_3$ and Ti_2O_3 and also a ferrtic iron-based phase. The TiB_2-based coating contains TiB_2, a ferritic iron-based phase, two oxides, $FeTiO_3$ and Ti_2O_3, and trace amounts of FeB, Fe_2B, FeTi and Cr_2Ti intermetallics. A comparison of the various phases present in the powder fines, feedstock powders and coatings are shown in Figures 8.8 to 8.11. The more obvious changes in the equimolar material appear when comparing the powders to the coating. New phases appear at approximately, 32°, 41°, 43°, 51° and 53°, which are mainly a result of the oxides present in the coating. This is the same for the excess C coating. The excess Ti traces (Figure 8.10) illustrate that the new phases appear in the coating at 32°, 44°, 53° and 63°, which correspond with the oxides and iron. It is also evident that the Fe_2Ti peaks appear to have decreased at 37°, 43.5°, 44.5°, 46° and 49°. The TiB_2-based coating exhibits new peaks at 32°, 35°, 41°, 49°, 53° and 63°, which all correspond with oxide. The lattice parameters of the TiC in the coatings are shown along with the corresponding C:Ti ratios in Table 8.7.

8.2.4 Chemical analysis of coatings

The chemical analyses of the coatings along with those for the initial elemental mixtures, powder fines and feedstock powders are shown in Tables 8.2 to 8.5. The TiC-based coatings all show a general increase in the iron and chromium weight percentages as a result of the reduction in titanium and carbon contents. An increase in the oxygen contents is also evident. The TiB_2-based coating also shows an increase in the iron and chromium weight percentages, with a subsequent reduction in the titanium and boron contents. An increase in the oxygen content is also evident. These changes will be discussed in further detail in Chapter 9.

8.3 Abrasive wear of coatings

The following section shows the wear results and characteristics of the coatings which were subjected to abrasion by alumina and silica abrasives of particle size 500-600μm under a load of 54N.

8.3.1 Abrasive wear results

Figure 8.28 shows the wear coefficients, in terms of mass losses, of the equimolar, excess C, excess Ti and TIB_2-based coatings, along with three coatings sprayed from commercially available cermet powders, namely sintered and crushed 17% WC-Co, sintered and crushed 25%NiCr-Cr_3C_2, and blended 25%NiCr-Cr_3C_2 (Spraying parameters are shown in Table 7.3). The results show that when using an alumina abrasive, the TiB_2-based coating had the superior

wear properties, in terms of mass loss, followed by the NiCr-Cr_3C_2 coating produced from sintered and crushed powder, and then the equimolar TiC coating. When using silica abrasive, the TiB_2-based coating again had the superior wear properties, followed by WC-Co and then NiCr-Cr_3C_2 produced from the sintered and crushed cermet powder.

When the wear results are displayed in terms of volumetric wear (Figure 8.29), WC-Co has the superior wear properties when subjected to alumina abrasive and is followed by sintered and crushed NiCr-Cr_3C_2 and then FeCr-TiB_2. When the coatings were subjected to abrasion by silica, again, the WC-Co coatings exhibited the best wear properties, followed by FeCr-TiB_2 and then sintered and crushed NiCr-Cr_3C_2. The wear results are also displayed in a tabular form in Table 8.9.

8.3.2 Wear characteristics

The following section outlines the wear characteristics of the four coatings when abrasion tested with alumina and silica abrasives.

8.3.2.1 Top-surface wear scars

The top-surface wear scars of the equimolar, excess C, excess Ti and TiB_2-based coatings after abrasion with alumina are shown in Figures 8.30 to 8.33 respectively. The equimolar coating shows signs of ploughing and also pitting and delamination. This is also the case for the excess C coating which appears to

show more surface damage than the equimolar coating. The excess Ti sample shows signs of pitting and delamination, and also increased levels of ploughing than the other coatings. Pitting can also be seen at the edges of the grooves caused by the ploughing mechanism. The TiB_2-based coating shows signs of both ploughing and, pitting and delamination, with the latter appearing more prominent when compared with the surface of the equimolar coating.

The top-surface wear scars of the equimolar, excess C, excess Ti and TiB_2-based coatings after abrasion with silica are shown in Figures 8.34 to 8.37 respectively. All four coatings show signs of pitting and delamination on the surfaces. Each coating also contains black deposits, confirmed by EDX to be silica, on the surfaces which appears in close proximity to where surface damage has occurred. Regions of the surface coatings appear to have undergone a polishing effect, which is especially evident in the high magnification image of the TiB_2-based coating (Figure 8.37).

8.3.2.2 Cross-sectional wear scars

The cross-sectional wear scars of the equimolar, excess C, excess Ti and TiB_2-based coatings after abrasion with alumina are shown in Figures 8.38a to 8.38d respectively. Each coating exhibits a relatively smooth surface with no evidence of large-scale sub-surface cracking, although some sub-surface delamination is evident.

The cross-sectional wear scars of the equimolar, excess C, excess Ti and TiB_2-based coatings after abrasion with silica are shown in Figures 8.39a to 8.39d respectively. All four coatings exhibit a rougher surface than the coatings subjected to abrasion with alumina. The equimolar coating exhibits a small amount of carbide pullout while the excess C coatings shows signs of carbide pullout and extensive sub-surface cracking. The excess Ti coating exhibits some sub-surface cracking and also some exposed carbides can be observed which have not be easily removed from the matrix by the abrasive action. Figure 8.39d shows that the TiB_2-based coating has 2-5μm sized diboride particles at the surface that appear to be standing proud at the surface, which is not evident in the equimolar and excess C coatings. The diboride particles appear to be well bonded to the matrix; indeed the borides appear to be chipping at their edges resulting in a relatively rough surface with micropits between the diboride particles at the surface. One larger pit can be observed to the left of the image.

It is important to note that the silica deposits that were evident in the top-surface images of the coatings do not appear in the cross-sectional images.

8.4 Oxidation of coatings

The following section outlines the oxidation properties of the four coatings that were subjected to temperatures of 500°C, 700°C and 900°C for 100 hours. Table 8.10 shows the weight gain per area for the four coatings when subjected to the range of test temperatures. It can be seen that at all three temperatures, the excess Ti coating has the lowest weight gain, followed by the TiB_2-based coating, the

equimolar coating and finally the excess C coating. Figures 8.40 to 8.43 show images of the surfaces subjected to 500°C of equimolar, excess C, excess Ti and TiB_2-based coatings respectively. All four coatings show few signs of oxide build-up at the surface and there are no signs of changes in the microstructure. The phases present in the four coatings are shown in Table 8.11.

The coatings subjected to 700°C are shown in Figures 8.44 to 8.47 for equimolar, excess C, excess Ti and TiB_2-based coatings respectively. Each coating exhibits an oxide layer at the surface but show no signs of microstructure change. The phases present in the four coatings are shown in Table 8.12.

The equimolar and TiB_2-based coatings subjected to 900°C are shown in Figures 8.48 and 8.49 respectively. The equimolar coating shows no signs of any significant oxide buildup at the surface, but it is believed that oxide layer spallation may have occurred. The coating microstructure appeared to have undergone some sort of transformation at this temperature and will be addressed in the Discussion section. The TiB_2-based coating again shows no signs of oxide build-up at the surface of the coating as the oxide layer was completely detached from the coating and is shown in the second image. No microstructure change appears to have occurred in this coating. The phases present in the coating after XRD analysis have not been presented as most of the oxide layer had become detached from the coatings and therefore may not be representative.

Composition	Combustion Temperature (°C)
30% FeCr-TiC (Equimolar)	1844
30% FeCr-TiC (Excess C)	1730
30% FeCr-TiC (Excess Ti)	1636
30% FeCr-TiB_2	1996

Table 8.1 : Combustion temperatures of SHS-produced powders

	Weight %					Atomic %				
	Fe	Cr	Ti	C	O	Fe	Cr	Ti	C	O
SHS reactants	Balance	6	56	14	0	Balance	4	40.6	40.5	0
Powder fines	Balance	6	54	15	2	Balance	3.8	37.2	41.2	4.1
Feedstock powder	Balance	6	50	13	1	Balance	4.1	36.7	38.1	2.2
Coating	Balance	7	44	9	6	Balance	4.8	33	27	13.4

Table 8.2 : Chemical analysis of 30% FeCr-TiC (Equimolar) feedstock powders and coating

	Weight %					Atomic %				
	Fe	Cr	Ti	C	O	Fe	Cr	Ti	C	O
SHS reactants	Balance	6	47	23	0	Balance	3.4	28.5	55.6	0
Powder fines	Balance	6	52	18	1	Balance	3.6	34.2	47.2	2
Feedstock powder	Balance	7	47	15	1	Balance	4.5	33.1	42.1	2.1
Coating	Balance	9	39	11	3	Balance	5.5	28.9	32.5	8.9

Table 8.3 : Chemical analysis of 30% FeCr-TiC (Excess C) feedstock powders and coating

	Weight %					Atomic %				
	Fe	Cr	Ti	C	O	Fe	Cr	Ti	C	O
SHS reactants	Balance	6	62	8	-	Balance	4.6	51.7	26.6	-
Powder fines	Balance	6	58	9	2	Balance	4.4	45.7	28.3	4.7
Feedstock powder	Balance	6	57	7	1	Balance	4.7	48.2	23.6	2.5
Coating	Balance	9	36	4	12	Balance	5.7	27.8	12.3	27.7

Table 8.4 : Chemical analysis of 30% FeCr-TiC (Excess Ti) feedstock powders and coating

	Weight %					Atomic %				
	Fe	Cr	Ti	B	O	Fe	Cr	Ti	B	O
SHS reactants	Balance	6	48	22	-	Balance	3.2	28	56.8	-
Powder fines	Balance	5	47	20	1	Balance	2.8	28.3	53.3	1.8
Feedstock powder	Balance	7	41	22	1	Balance	3.7	23.7	56.4	1.7
Coating	Balance	8	38	16	4	Balance	4.7	24.1	45.0	7.6

Table 8.5 : Chemical analysis of 30% FeCr-TiB_2 feedstock powders and coating

	Feedstock Powder		Coating	
	Size (μm)	Vol. Fraction (%)	Size (μm)	Vol. Fraction (%)
30% FeCr-TiC (Equimolar)	1-5	72	1-5	36
30% FeCr-TiC (Excess C)	1-5	69	1-5	32
30% FeCr-TiC (Excess Ti)	1-5	63	1-5	26
30% FeCr-TiB_2	sub-6	64	sub-6	52

Table 8.6 : Size and volume fraction of hard phase for both feedstock powders and coatings

	Feedstock Powder		Coating	
	Lattice parameter (Å)	C/Ti ratio	Lattice parameter (Å)	C/Ti ratio
Equimolar	4.326	0.710	4.326	0.711
Excess C	4.3261	0.711	4.3261	0.717
Excess Ti	4.3258	0.709	4.317	0.62

Table 8.7 : Lattice parameters and C/Ti ratios of TiC for TiC-based feedstock powders and coatings

	Thickness (μm)	Hardness (Hv_{300})	Average Roughness (Ra)	Average densities (kg/mm^3)
30% FeCr-TiC (Equimolar)	100	964	3.76	6577
30% FeCr-TiC (Excess C)	125	968	3.90	6706
30% FeCr-TiC (Excess Ti)	125	840	3.89	6898
30% FeCr-TiB_2	120	1013	4.54	6063
25% NiCr-Cr_3C_2	-	-	-	7058
17% Co-WC	-	-	-	13888

Table 8.8 : Sprayed coating properties

	Mass loss wear coefficients ($mg\ m^{-1}\ N^{-1}$)		Volumetric wear coefficients ($mm^3\ m^{-1}\ N^{-1}$)	
	Alumina	Silica	Alumina	Silica
30% FeCr-TiC (Equimolar)	0.00906	0.00024	0.00135	$3.58*10^{-5}$
30% FeCr-TiC (Excess C)	0.01275	0.00029	0.00184	$4.19*10^{-5}$
30% FeCr-TiC (Excess Ti)	0.02041	0.0002	0.00287	$2.82*10^{-5}$
30% FeCr-TiB_2	0.00724	0.00012	0.00118	$1.95*10^{-5}$
25% NiCr-Cr_3C_2 (Blended)	0.01907	0.00037	0.00264	$5.12*10^{-5}$
25% NiCr-Cr_3C_2 (S+C)	0.00744	0.00014	0.00104	$1.97*10^{-5}$
17% Co-WC (S+C)	0.01071	0.00012	0.00073	$9.09*10^{-6}$

Table 8.9 : Wear coefficients of coatings following abrasive wear testing using alumina and silica abradents

Composition	Temperature (°C)	Weight gain ($g\ m^{-2}$)
30% FeCr-TiC (Equimolar)	500	10.3
	700	37.6
	900	352.8
30% FeCr-TiC (Excess C)	500	16.3
	700	43.2
	900	445.2
30% FeCr-TiC (Excess Ti)	500	8.28
	700	22.8
	900	236
30% FeCr-TiB_2	500	14.28
	700	22.8
	900	300.4

Table 8.10: Weight gains of oxidised coatings

Equimolar	Excess C	Excess Ti	TiB_2-based
Fe	Fe	Fe	Fe
FeTi	FeTi	FeTi	FeTi
TiC	TiC	TiC	TiB_2
TiO_2 (Rutile)	TiO_2 (Rutile)	TiO_2 (Rutile)	TiO_2 (Rutile)
Fe_2O_3 (Haematite)	Fe_2O_3 (Haematite)	Fe_2O_3 (Haematite)	Fe_2O_3 (Haematite)
Cr_2O_3 (Eskolaite)	Cr_2O_3 (Eskolaite)	Cr_2O_3 (Eskolaite)	Cr_2O_3 (Eskolaite)
		Fe_2Ti	B_2O_3

Table 8.11 : XRD analysis of oxidised coatings @ 500°C

Equimolar	Excess C	Excess Ti	TiB_2-based
Fe	Fe	Fe	Fe
FeTi	FeTi	FeTi	FeTi
TiC	TiC	TiC	TiB_2
TiO_2 (Rutile)	TiO_2 (Rutile)	TiO_2 (Rutile)	TiO_2 (Rutile)
Cr_2O_3 (Eskolaite)	Cr_2O_3 (Eskolaite)	Cr_2O_3 (Eskolaite)	Cr_2O_3 (Eskolaite)
$Fe_2Ti_3O_9$ (Pseudorutile)	$Fe_2Ti_3O_9$ (Pseudorutile)	$Fe_2Ti_3O_9$ (Pseudorutile)	$Fe_2Ti_3O_9$ (Pseudorutile)
		Fe_2O_3 (Hematite)	B_2O_3
		Fe_2Ti	

Table 8.12 : XRD analysis of oxidised coatings @ 700°C

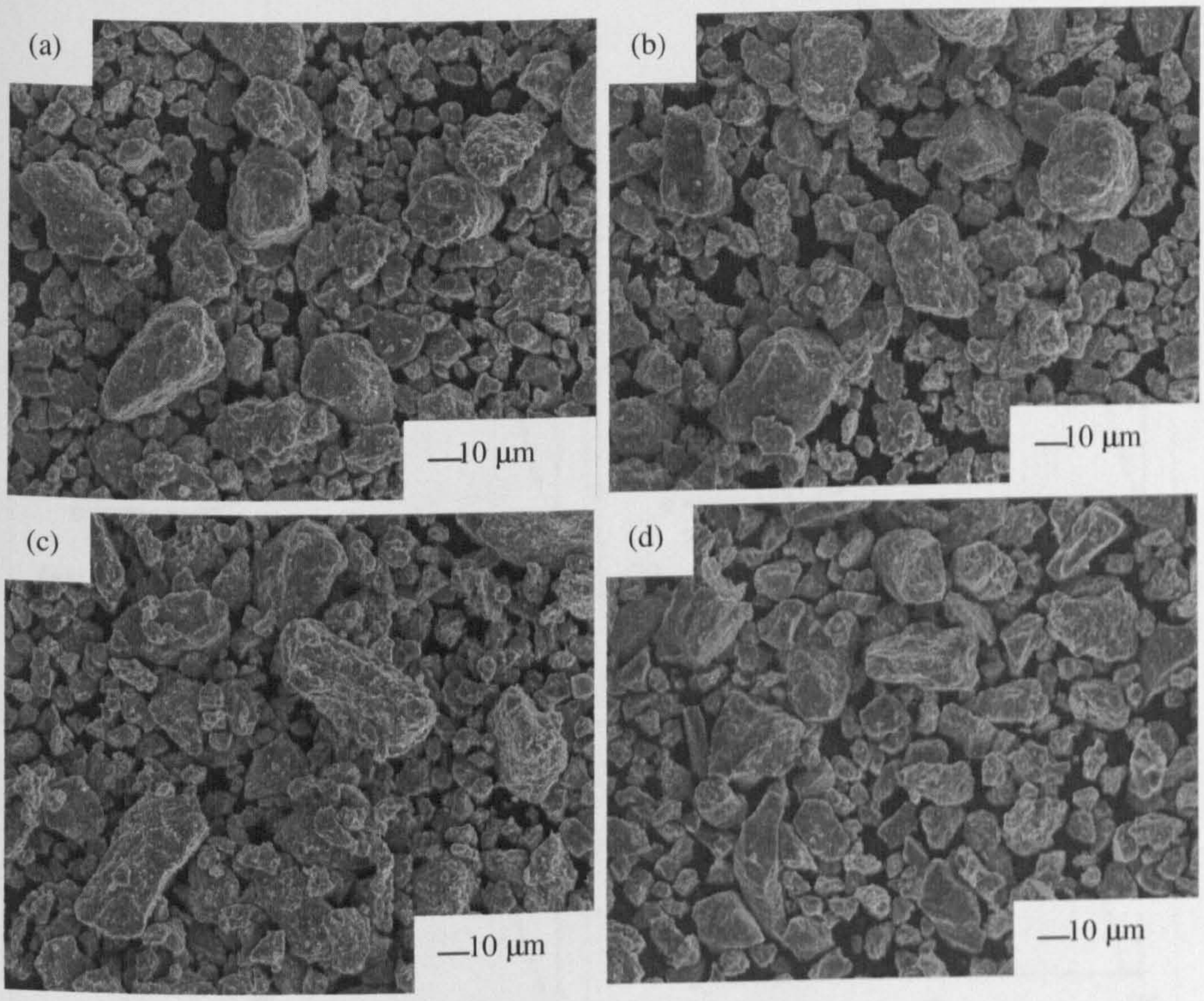

Figure 8.1 : Morphologies of (a) 30% FeCr-TiC (Equimolar), (b) 30% FeCr-TiC (Excess C), (c) 30% FeCr-TiC (Excess Ti) and (d) 30% FeCr-TiB_2 feedstock powders

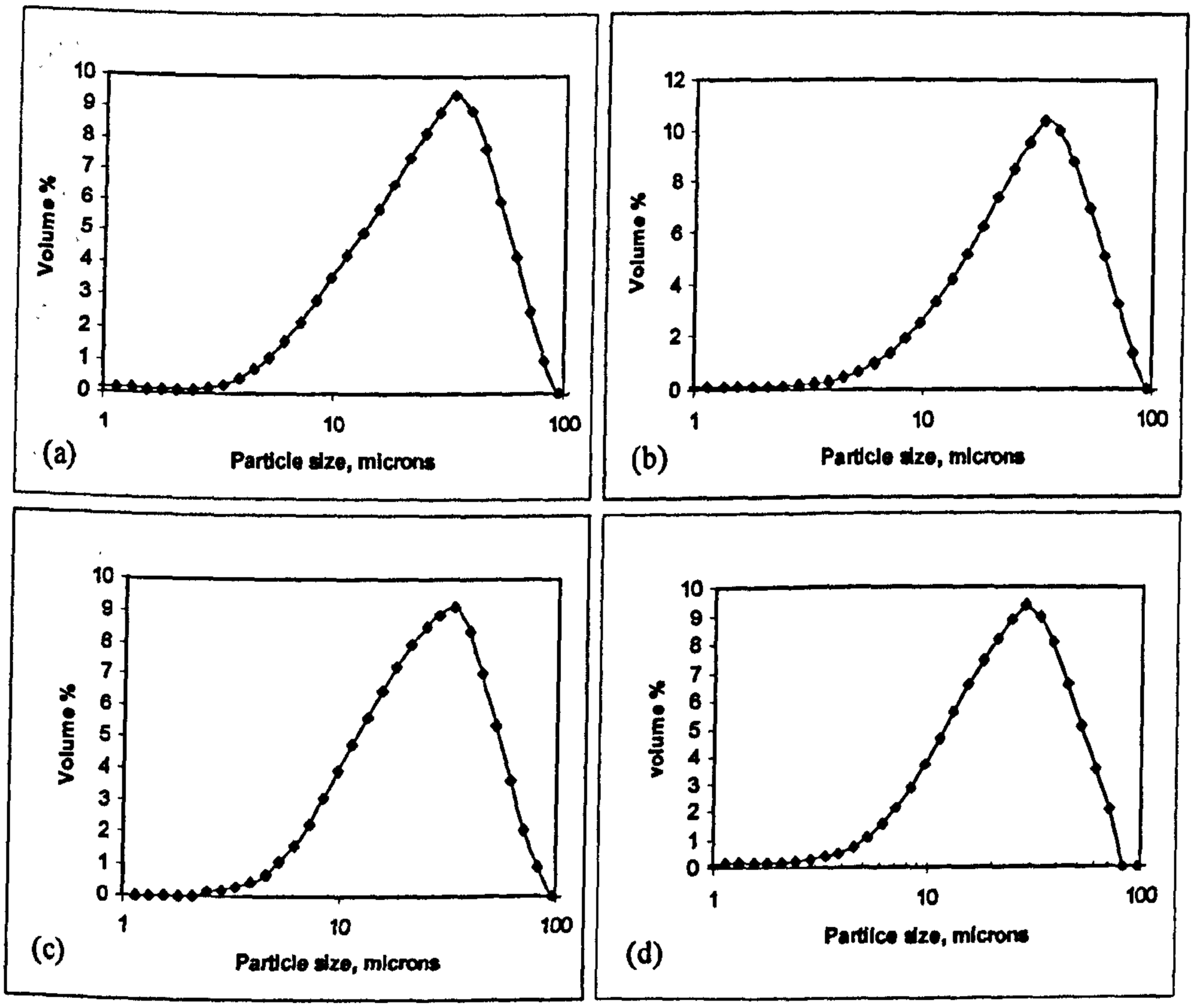

Figure 8.2 : Particle size distribution of (a) 30% FeCr-TiC (Equimolar), (b) 30% FeCr-TiC (Excess C), (c) 30% FeCr-TiC (Excess Ti) and (d) 30% FeCr-TiB_2 feedstock powders

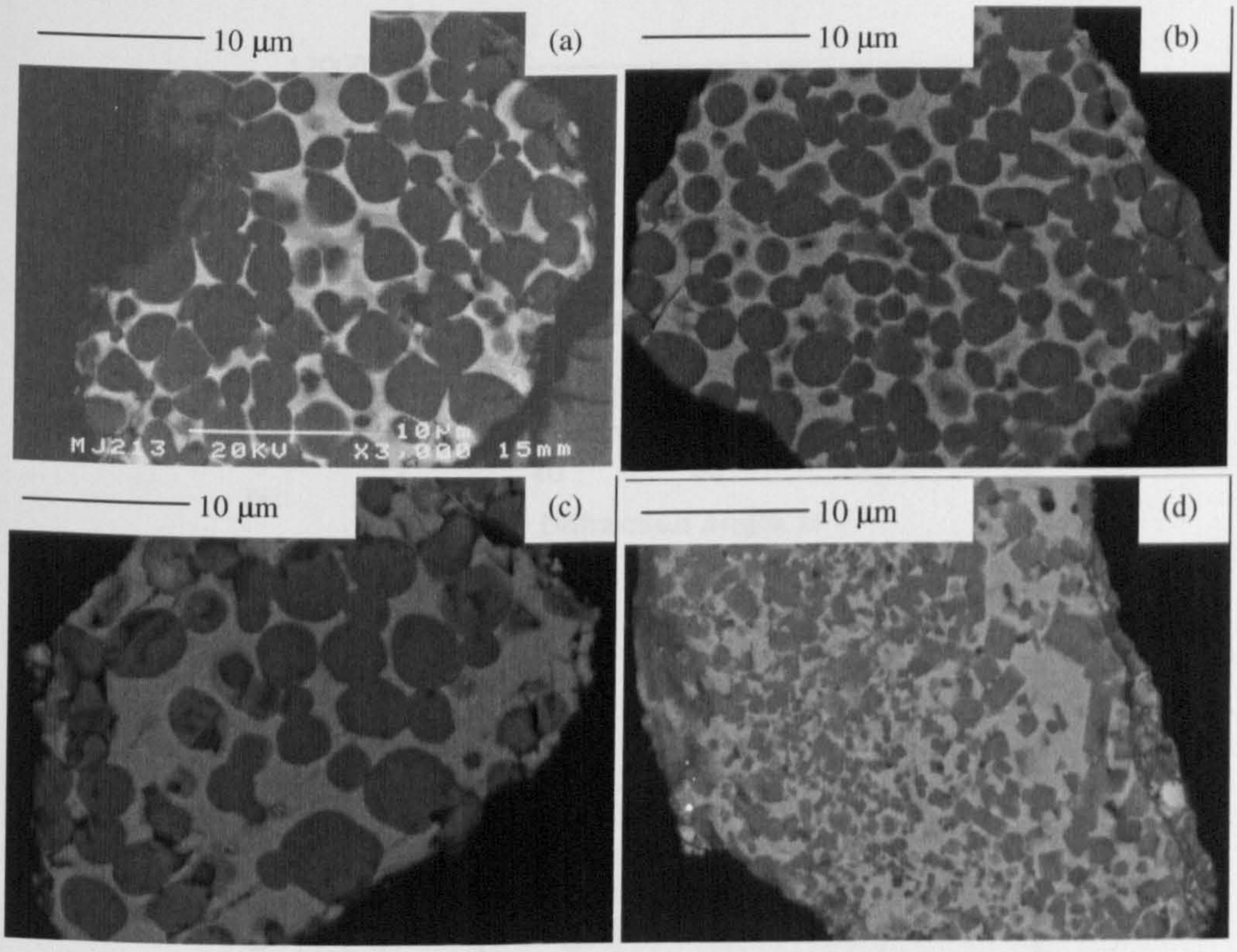

Figure 8.3 : BSE images of cross-sections of (a) 30% FeCr-TiC (Equimolar), (b) 30% FeCr-TiC (Excess C), (c) 30% FeCr-TiC (Excess Ti) and (d) 30% FeCr-TiB_2 feedstock powders

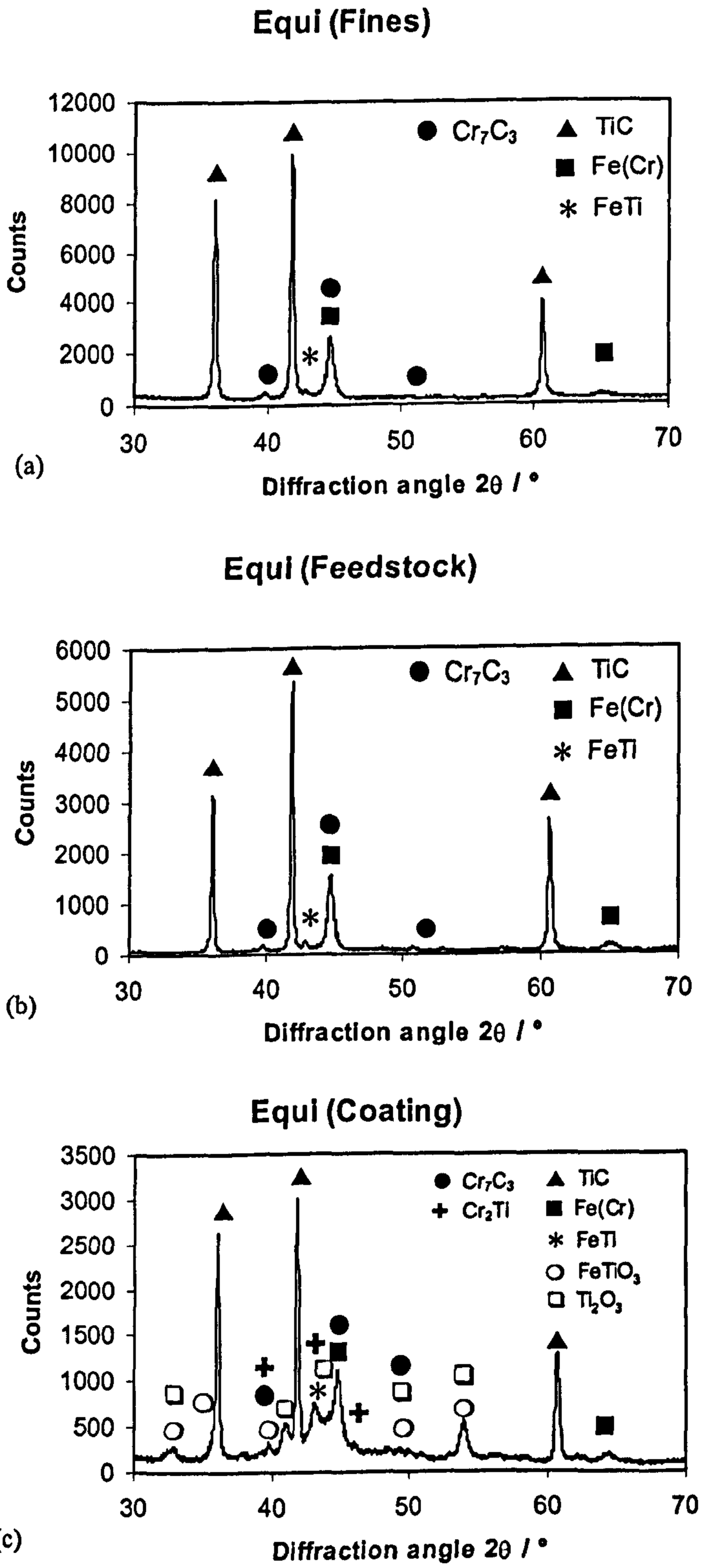

Figure 8.4 : XRD patterns of 30% FeCr-TiC (Equimolar) (a) powder fines, (b) feedstock powder and (c) coating

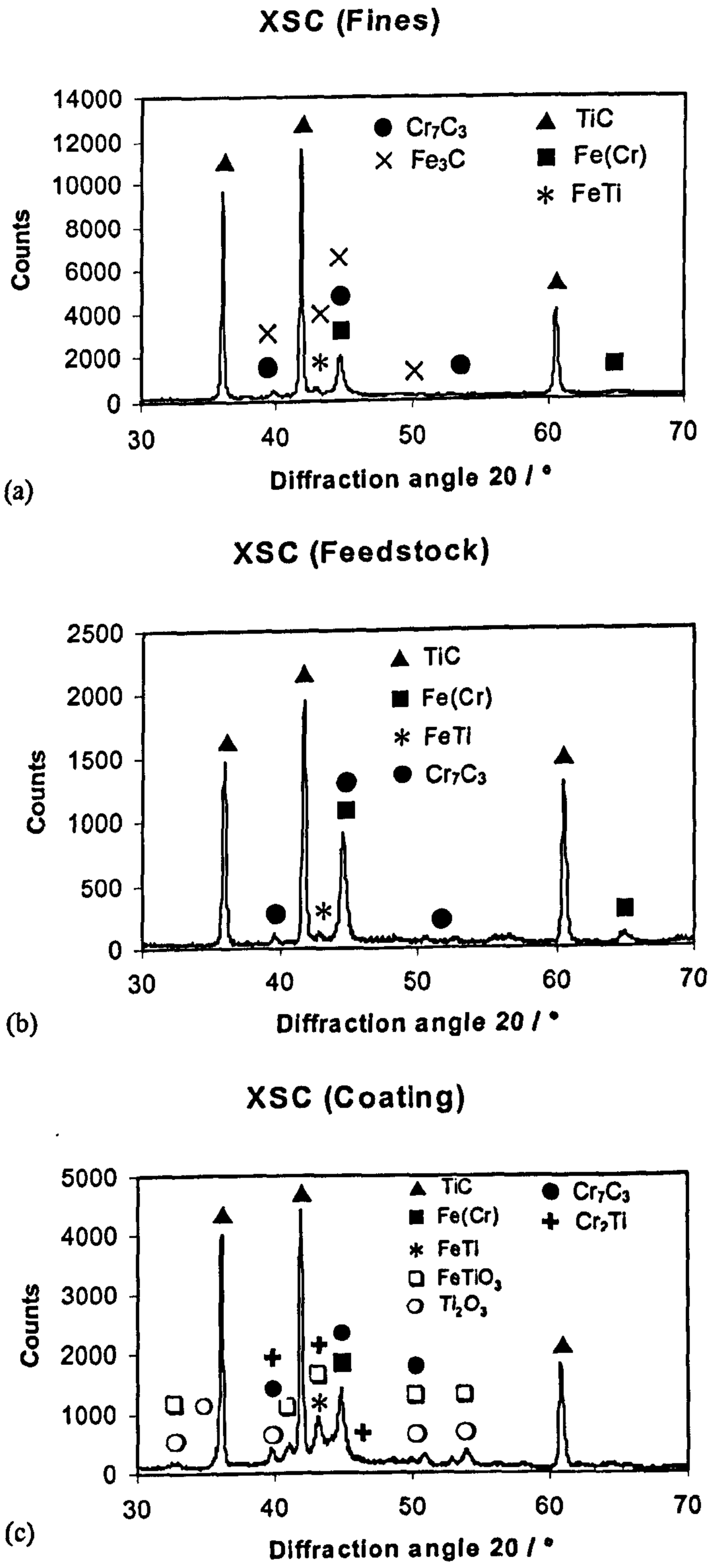

Figure 8.5 : XRD patterns of 30% FeCr-TiC (Excess C) (a) powder fines, (b) feedstock powder and (c) coating

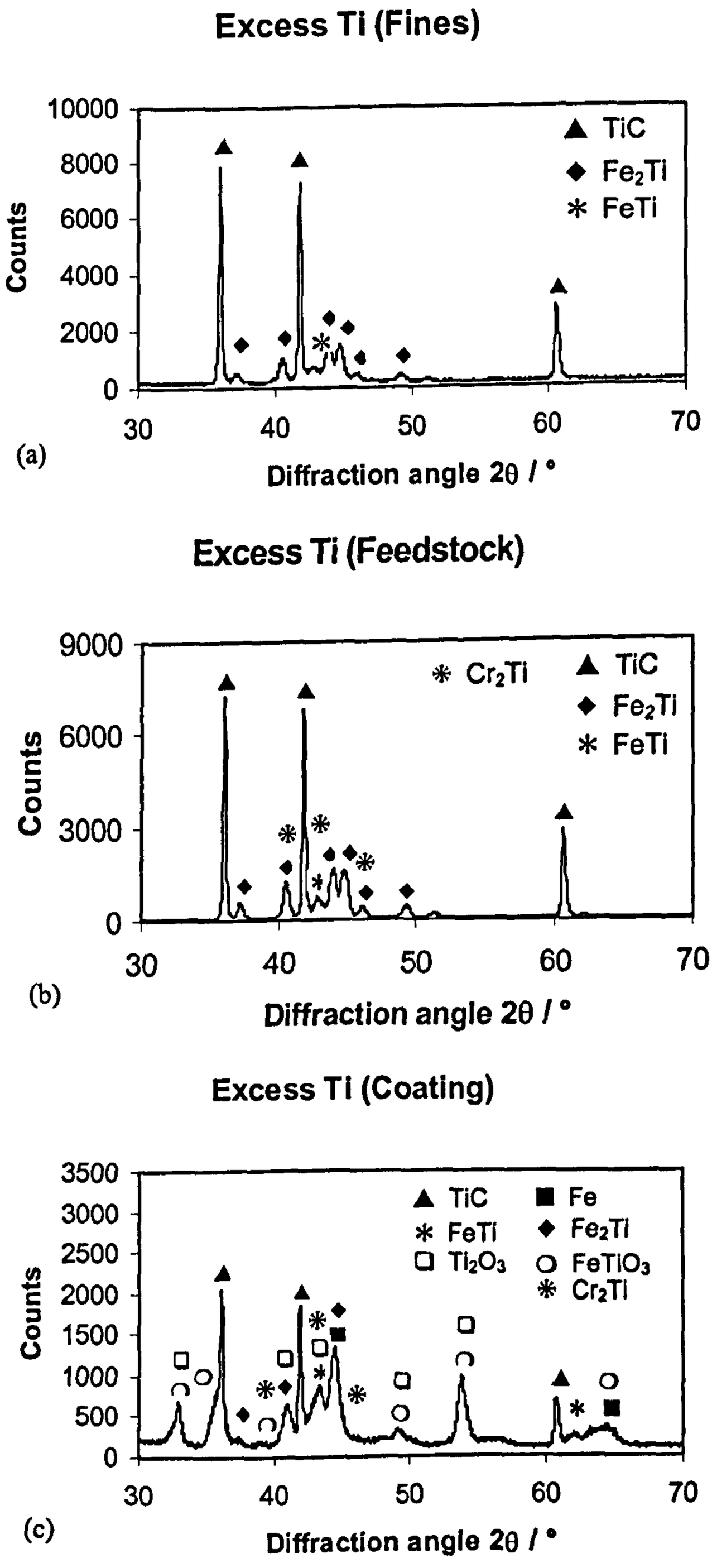

Figure 8.6 : XRD patterns of 30% FeCr-TiC (Excess Ti) (a) powder fines, (b) feedstock powder and (c) coating

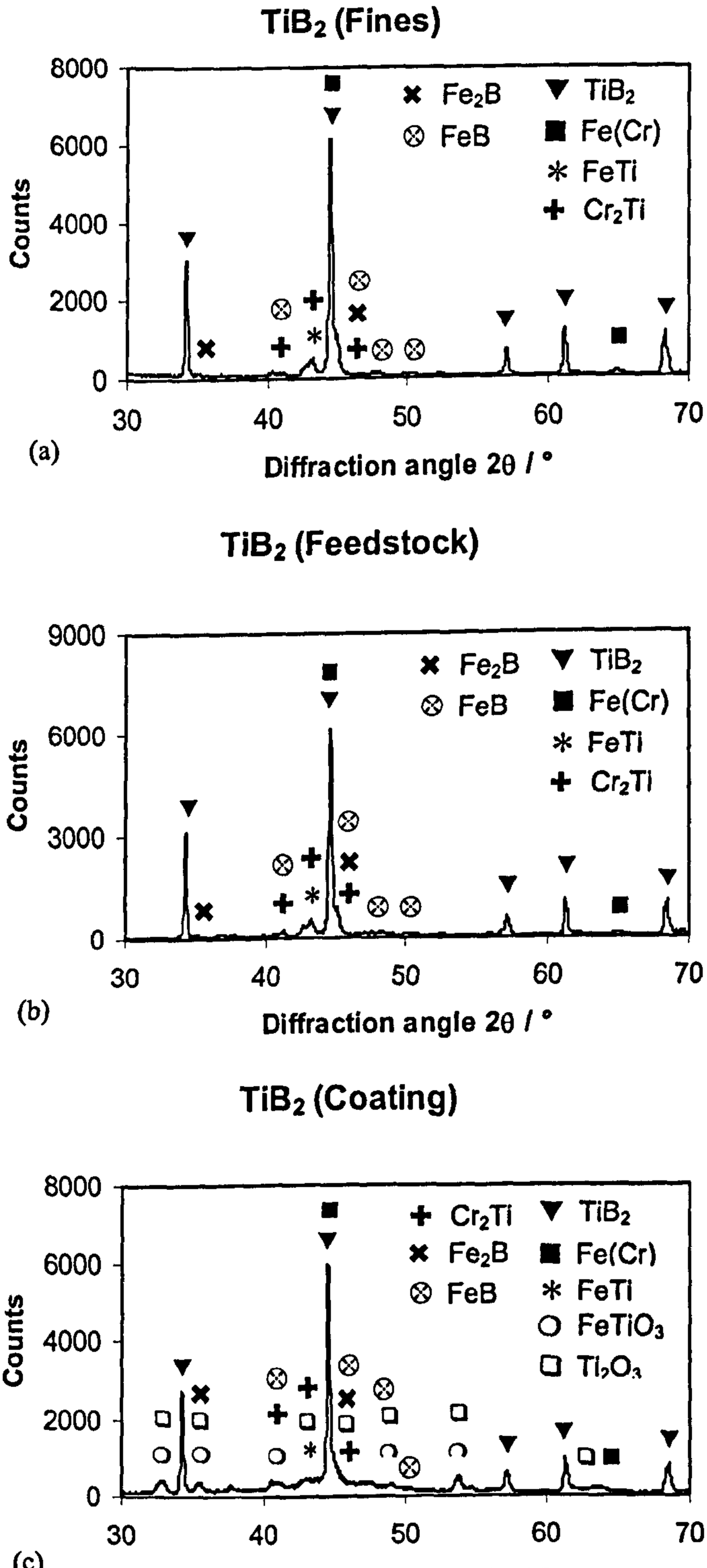

Figure 8.7 : XRD patterns of 30% FeCr-TiB_2 (a) powder fines, (b) sprayable feedstock powder and (c) coating

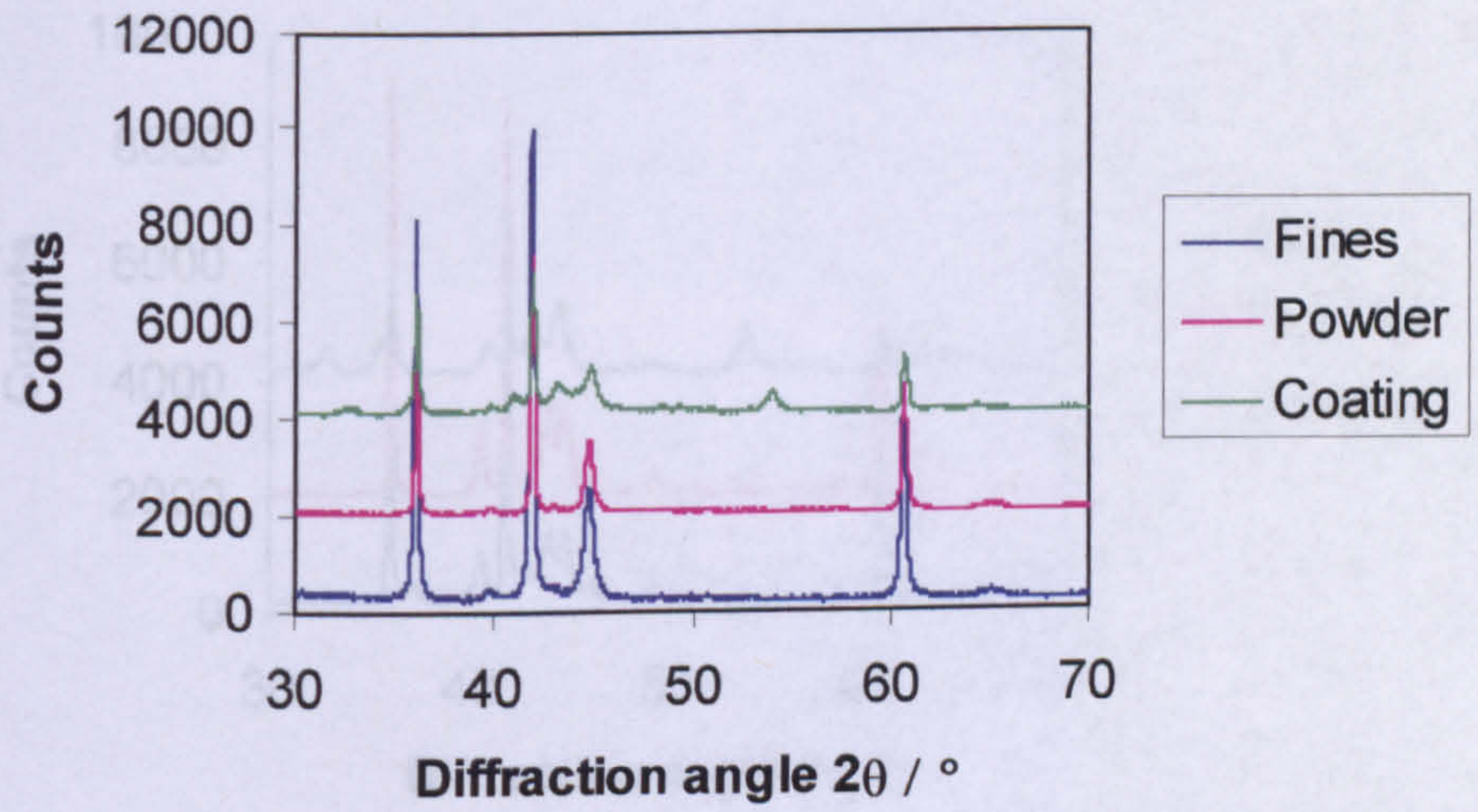

Figure 8.8: XRD traces of equimolar TiC powder fines, feedstock and coating

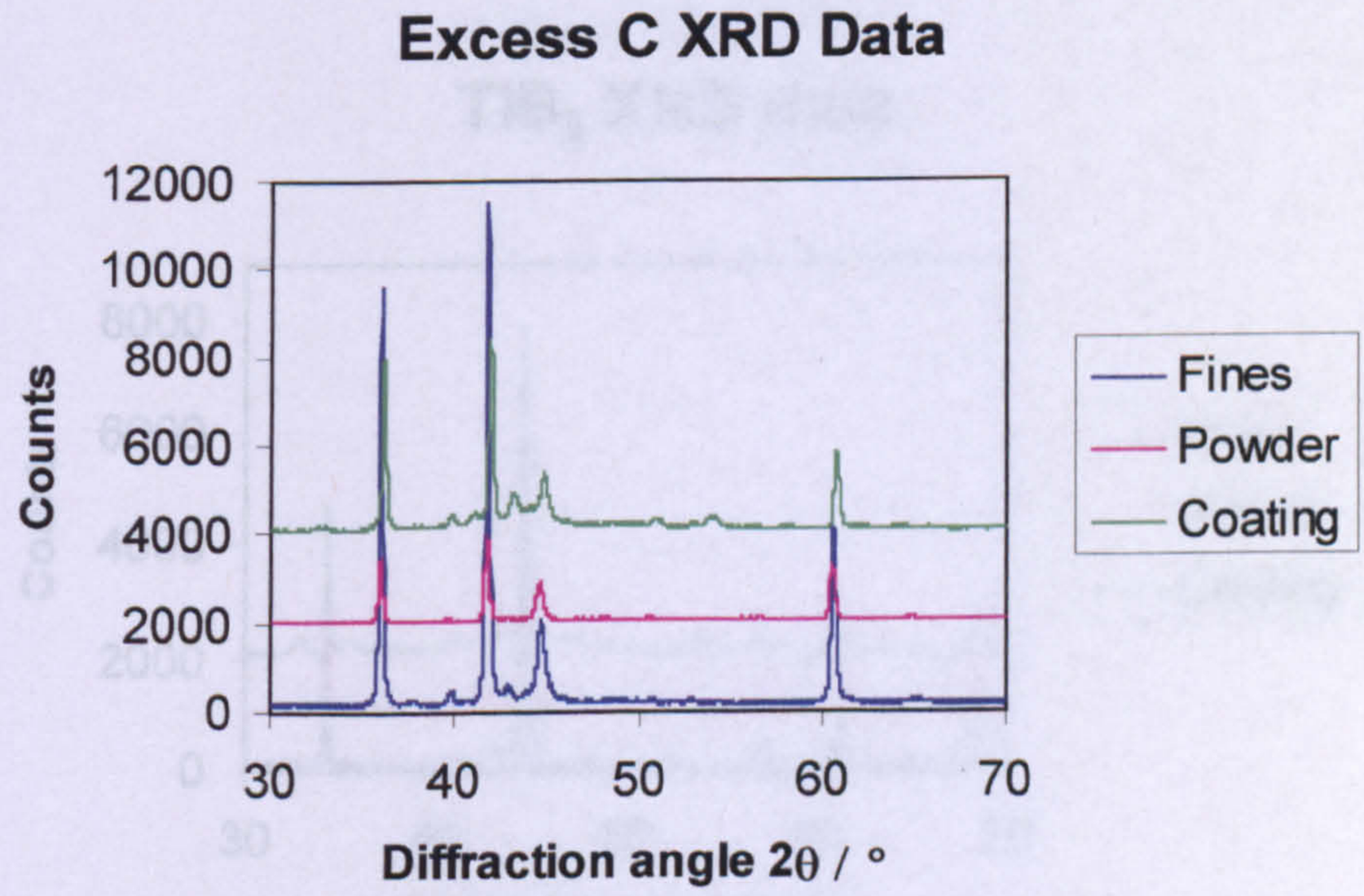

Figure 8.9: XRD traces of excess carbon powder fines, feedstock and coating

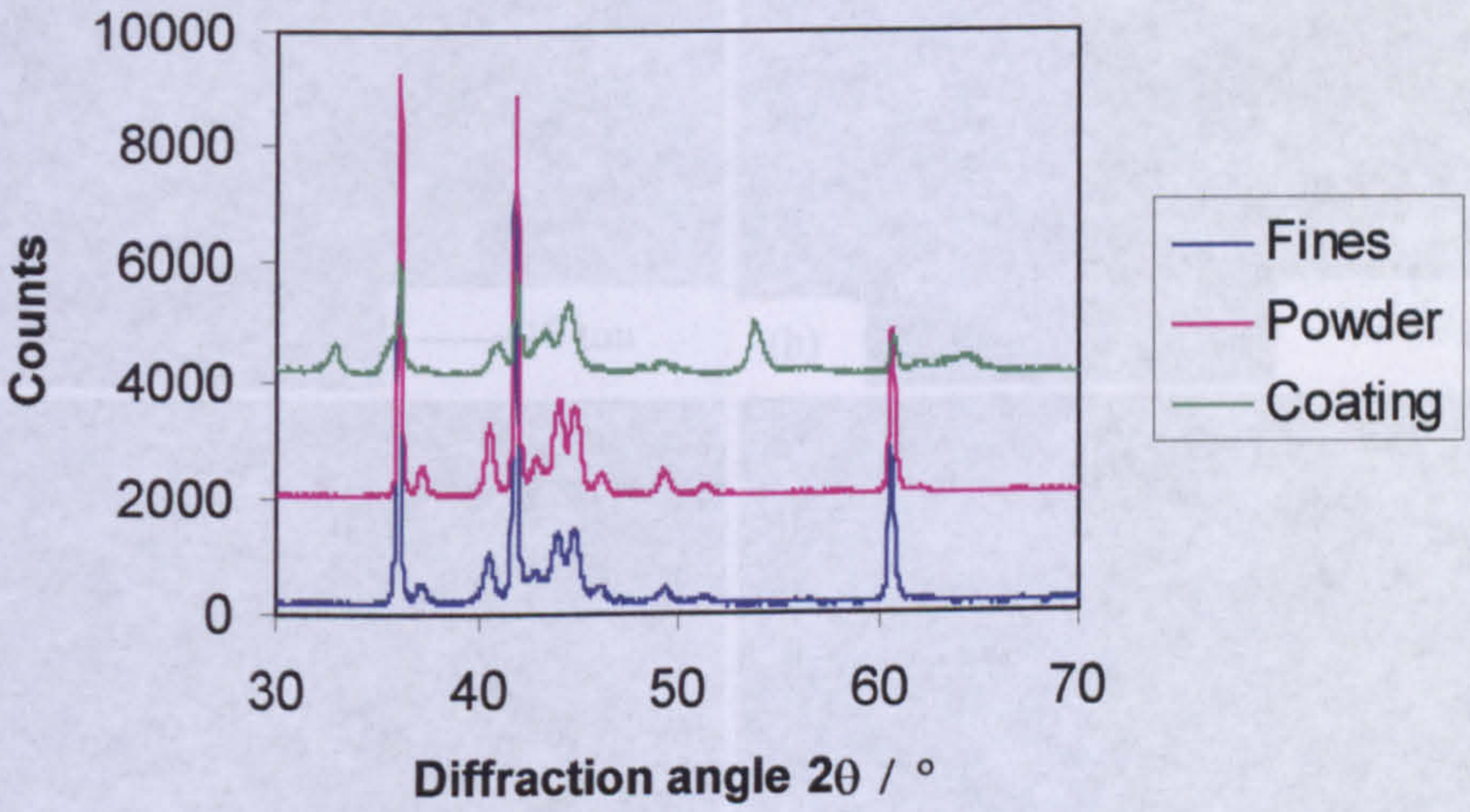

Figure 8.10: XRD traces of excess titanium powder fines, feedstock and coating

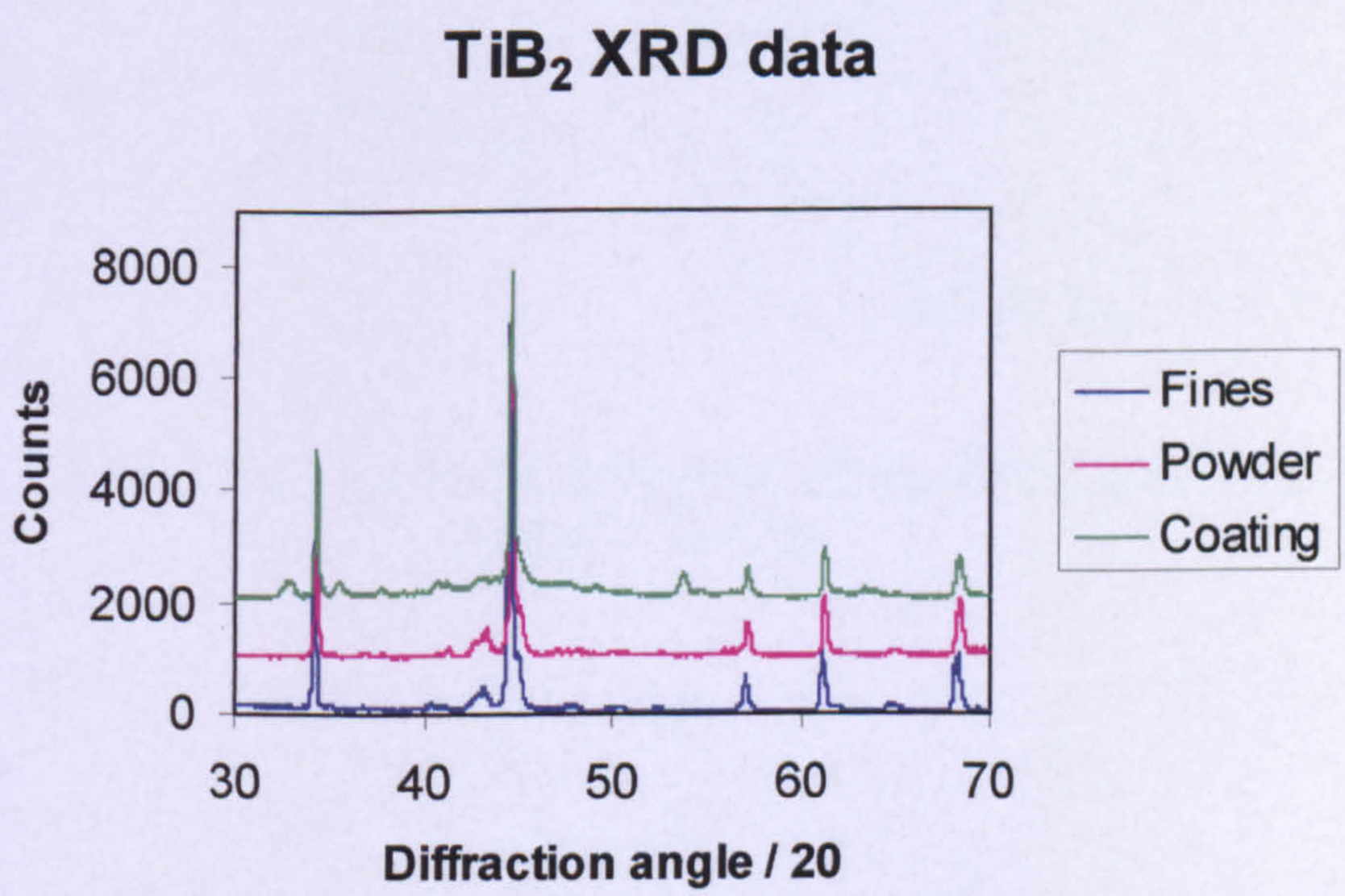

Figure 8.11: XRD traces of TiB_2 powder fines, feedstock and coating

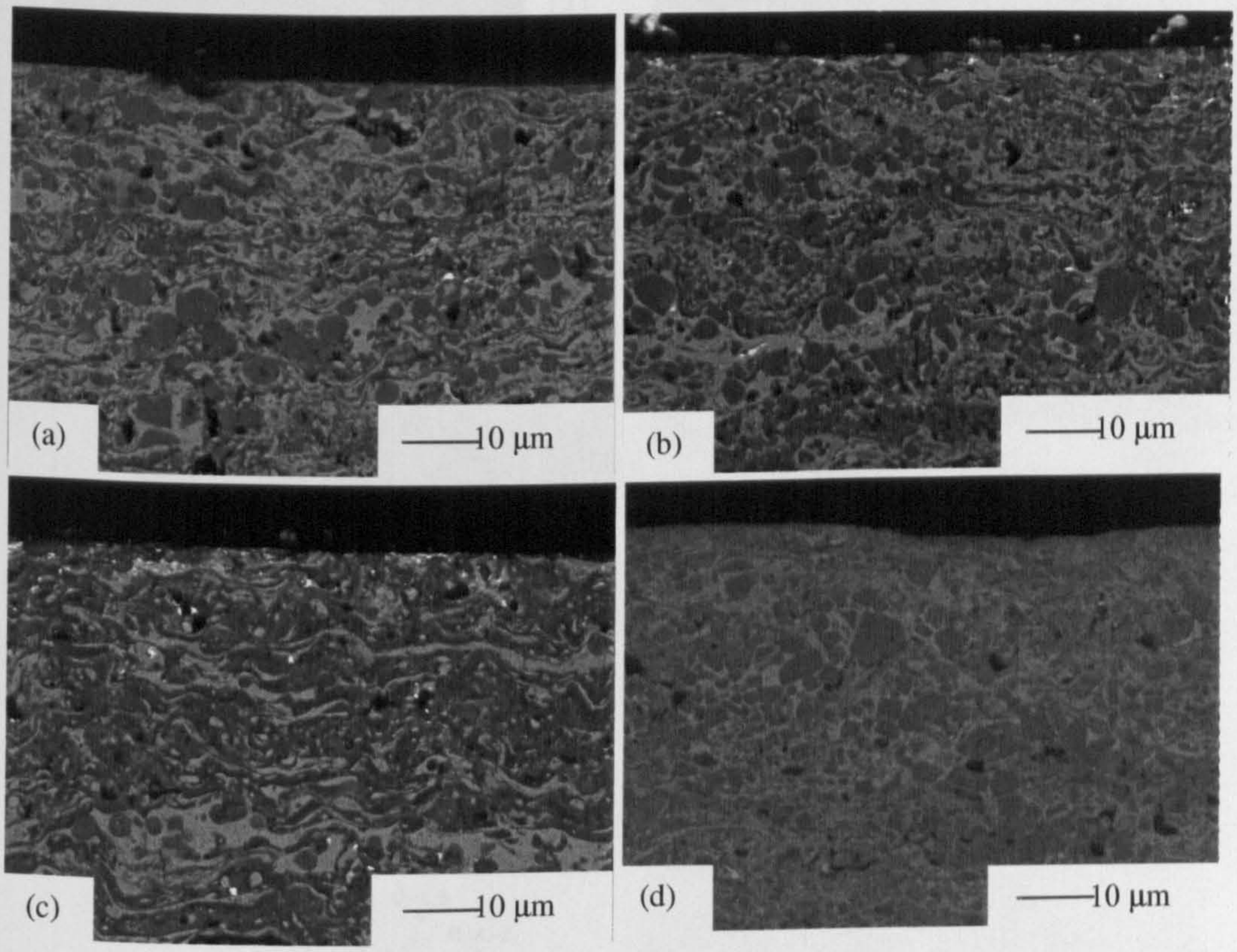

Figure 8.12 : BSE images of cross-sections of (a) 30% FeCr-TiC (Equimolar), (b) 30% FeCr-TiC (Excess C), (c) 30% FeCr-TiC (Excess Ti) and (d) 30% FeCr-TiB_2 coatings

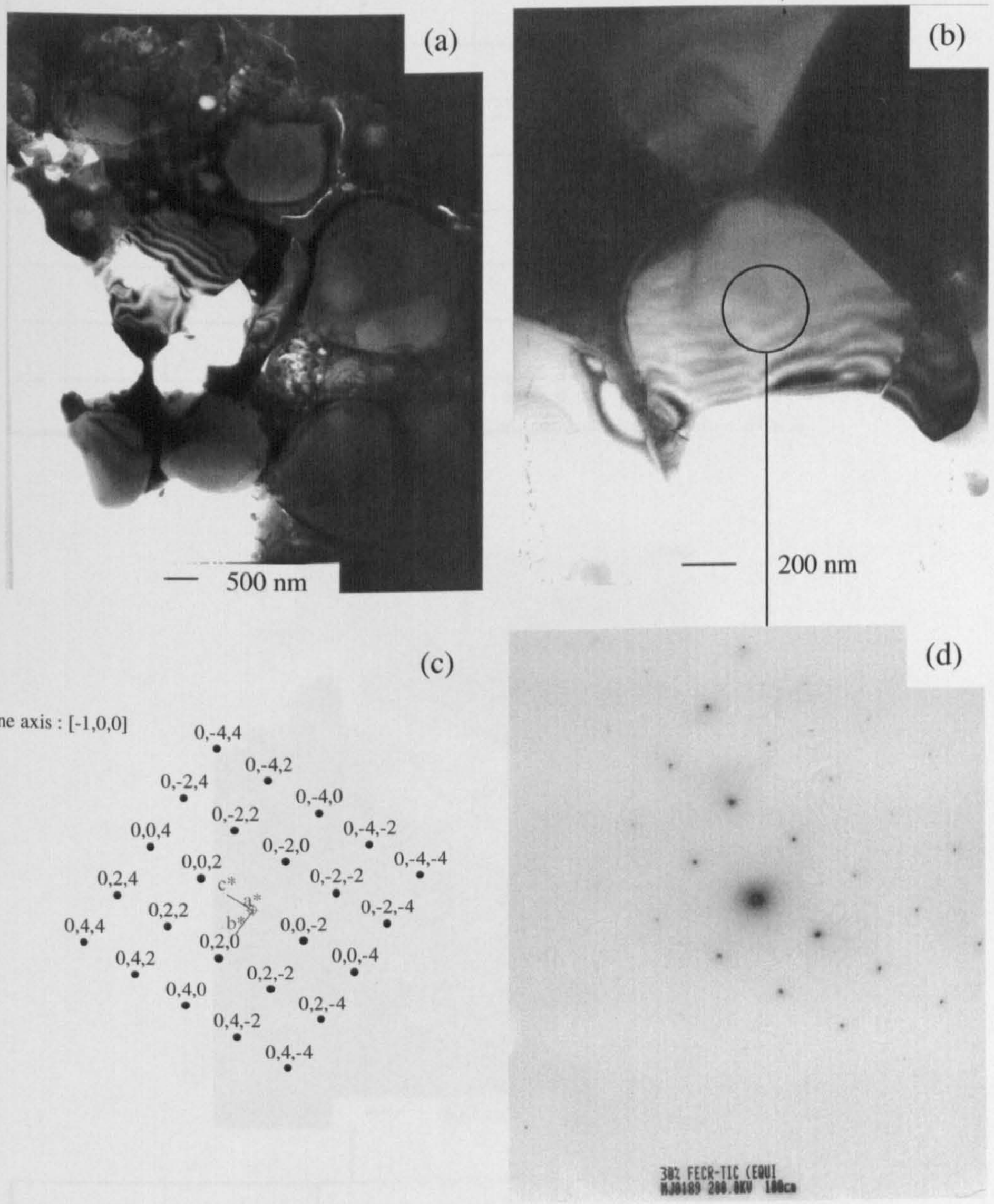

Figure 8.13: TEM images and diffraction pattern of TiC particles in equimolar coating

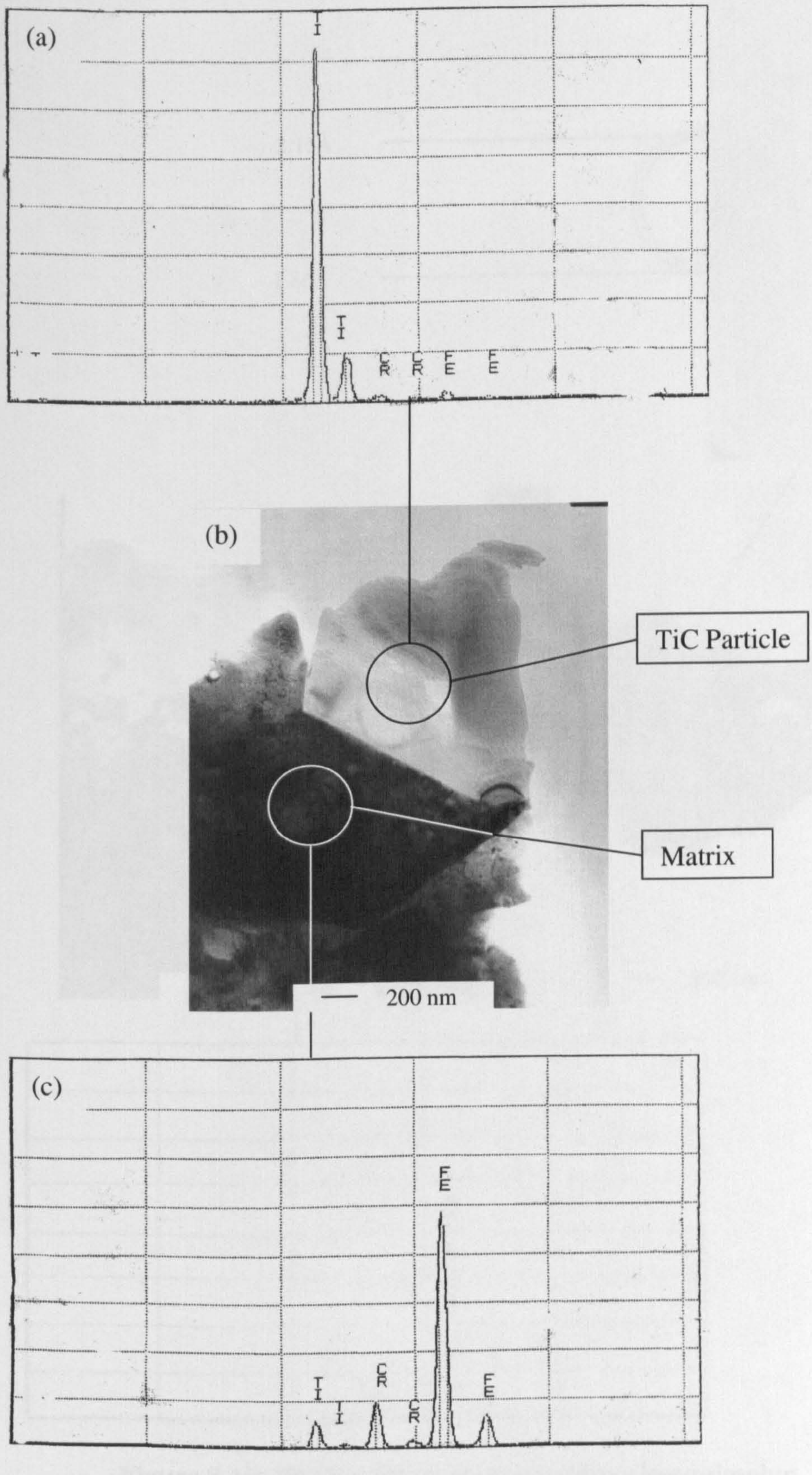

Figure 8.14: EDX analysis of TiC particle and matrix in equimolar coating

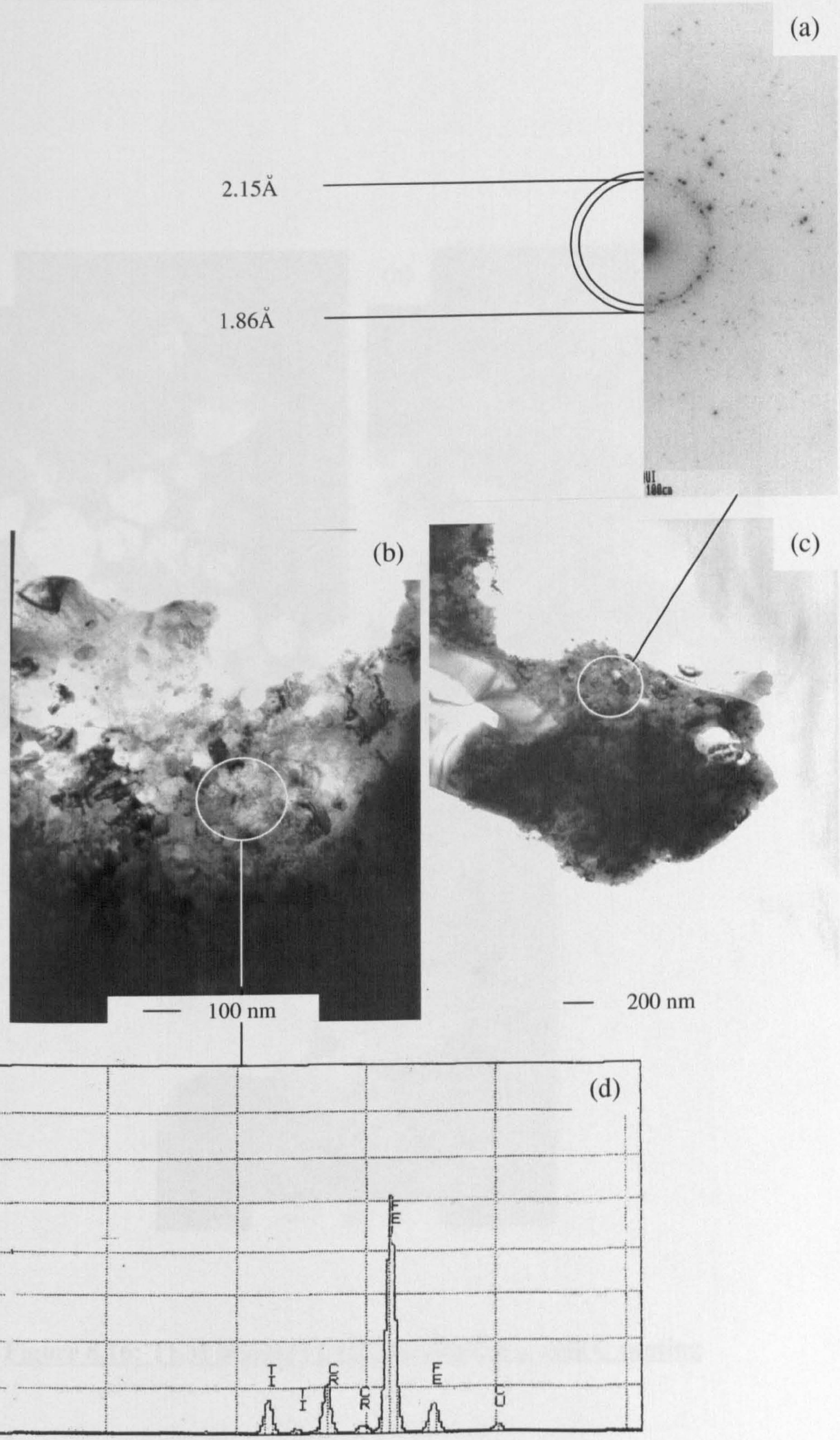

Figure 8.15: TEM analysis of matrix phase in equimolar coating

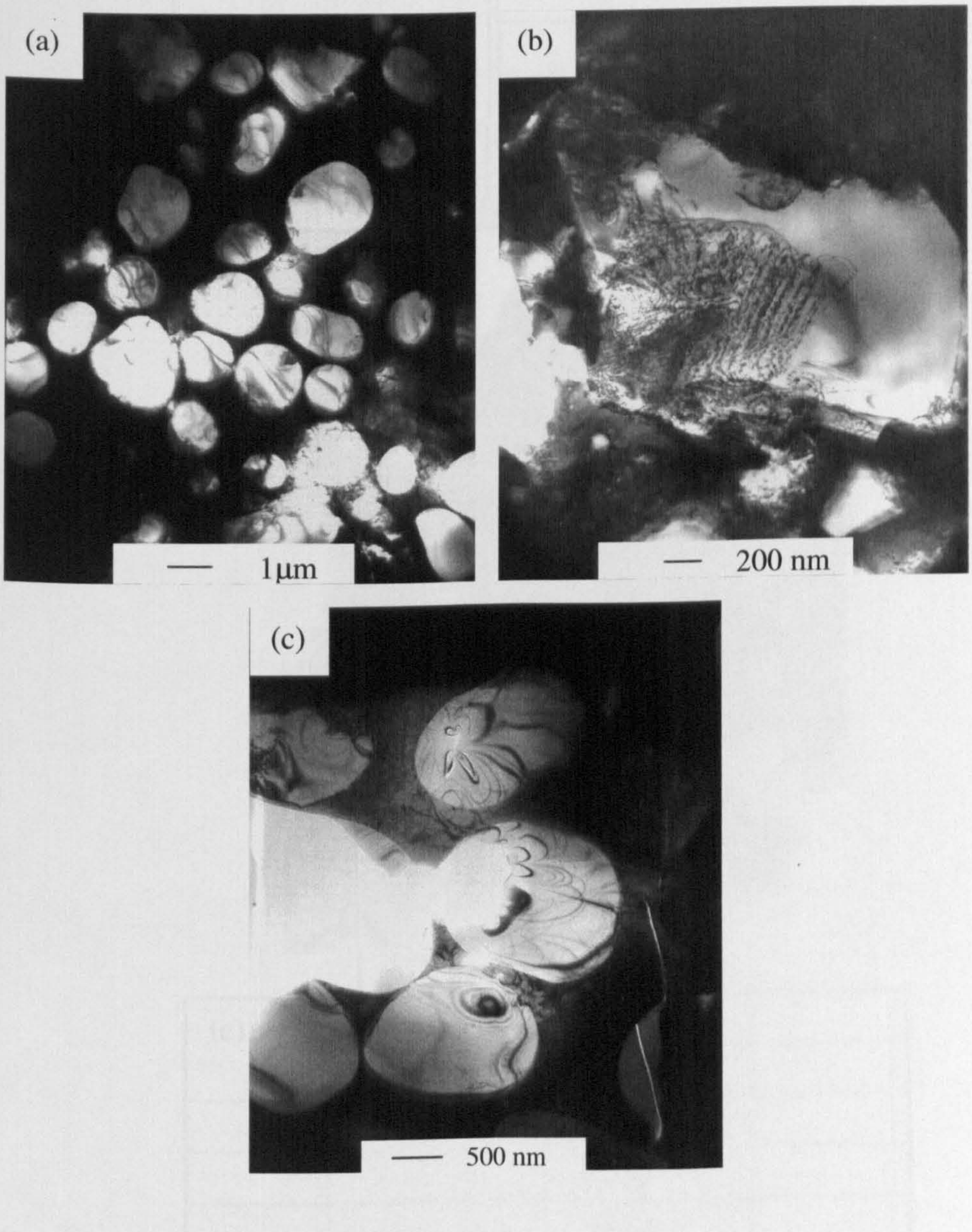

Figure 8.16: TEM images of TiC particles in excess C coating

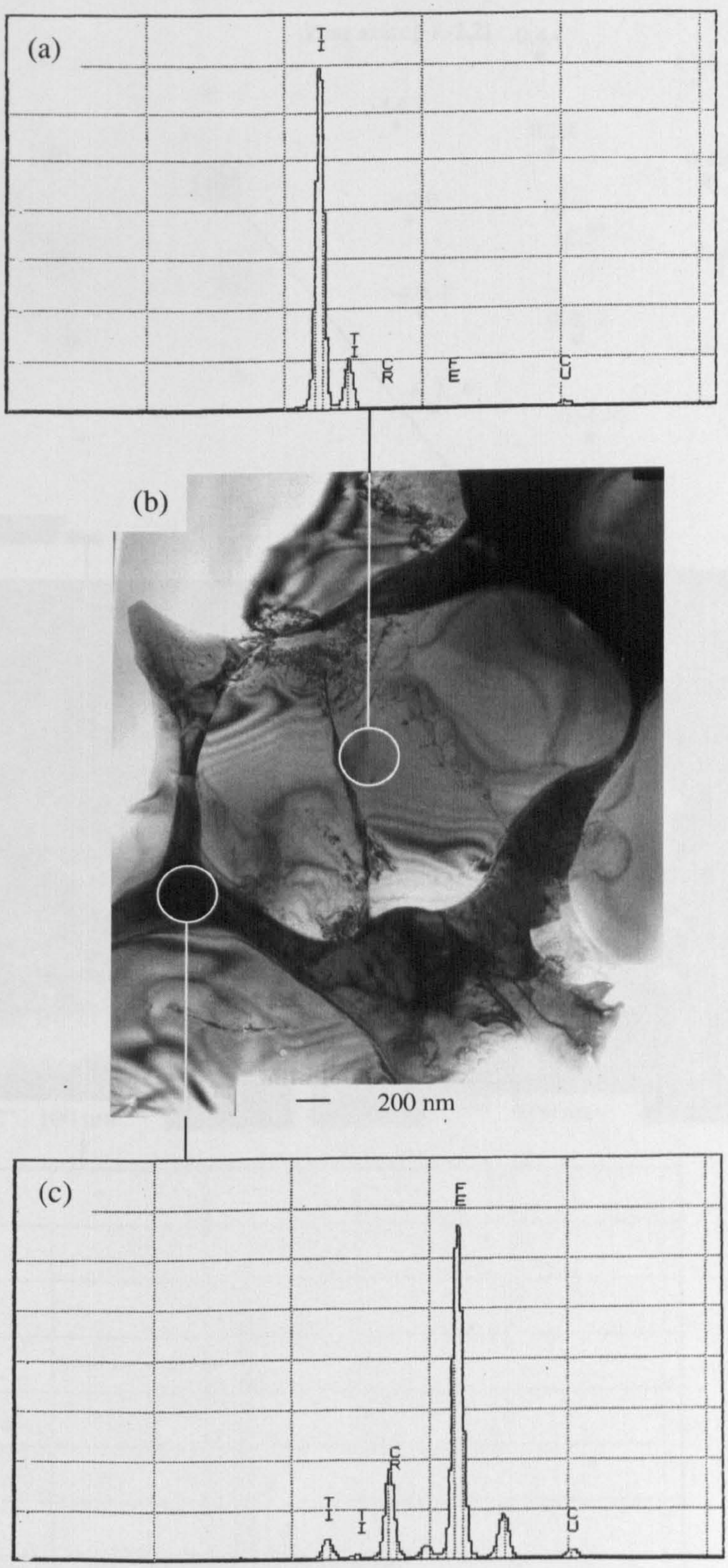

Figure 8.17: Image of TiC particles and matrix of excess C coating

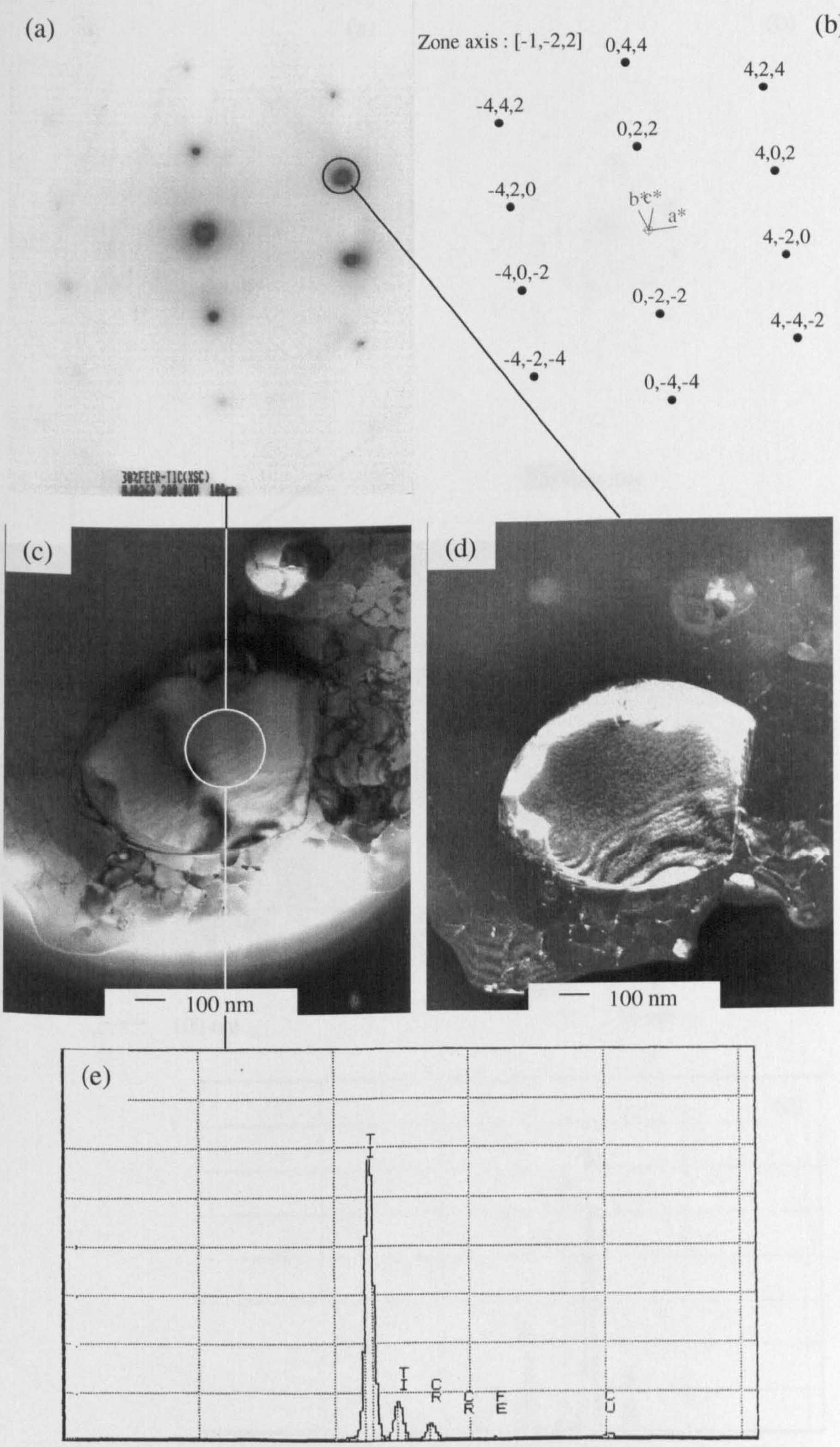

Figure 8.18: Bright-field (c) and, Dark-field (d) images of TiC particle and matrix in excess C coating

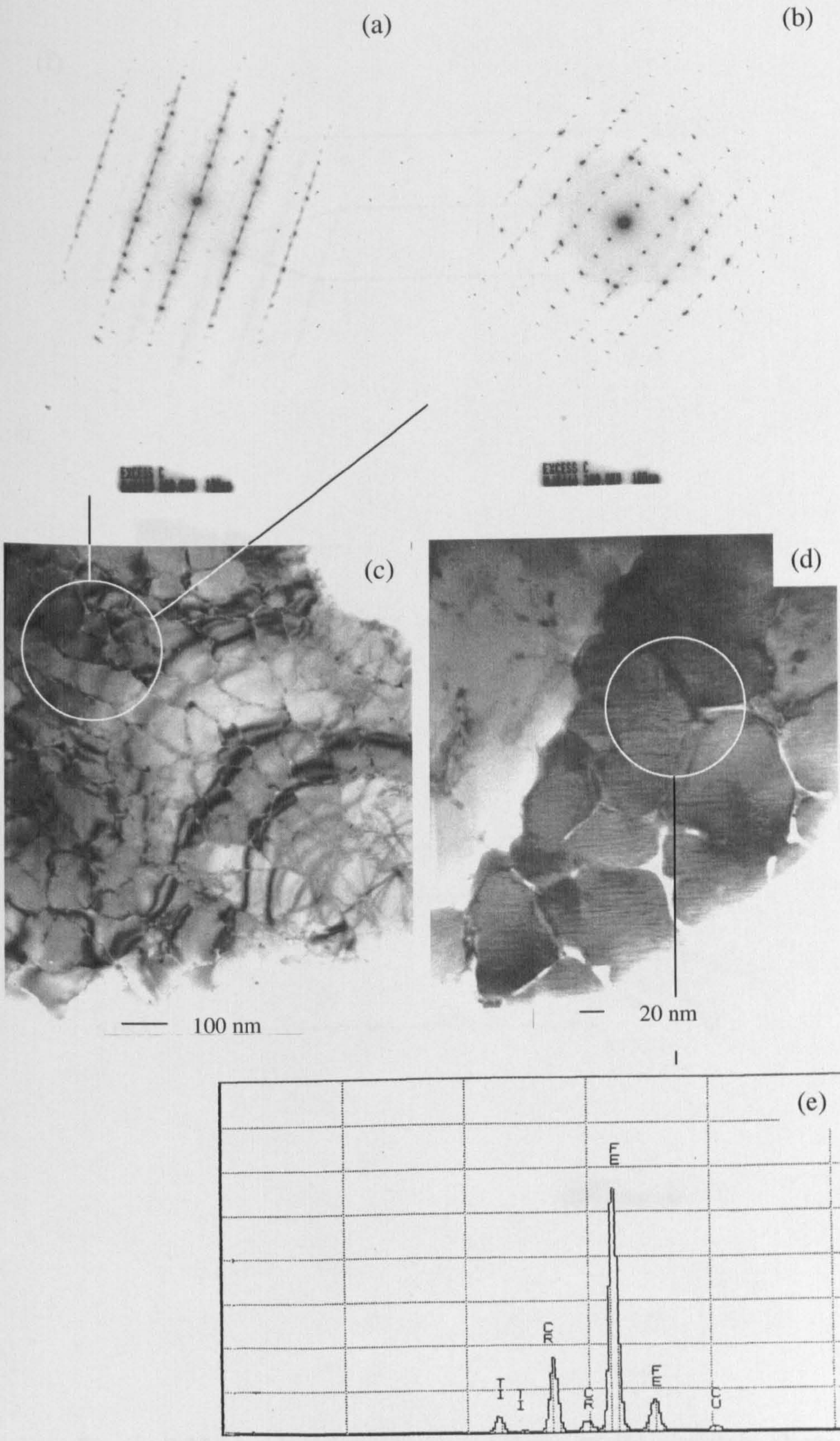

Figure 8.19: TEM analysis of matrix phase in excess C coating

(f)

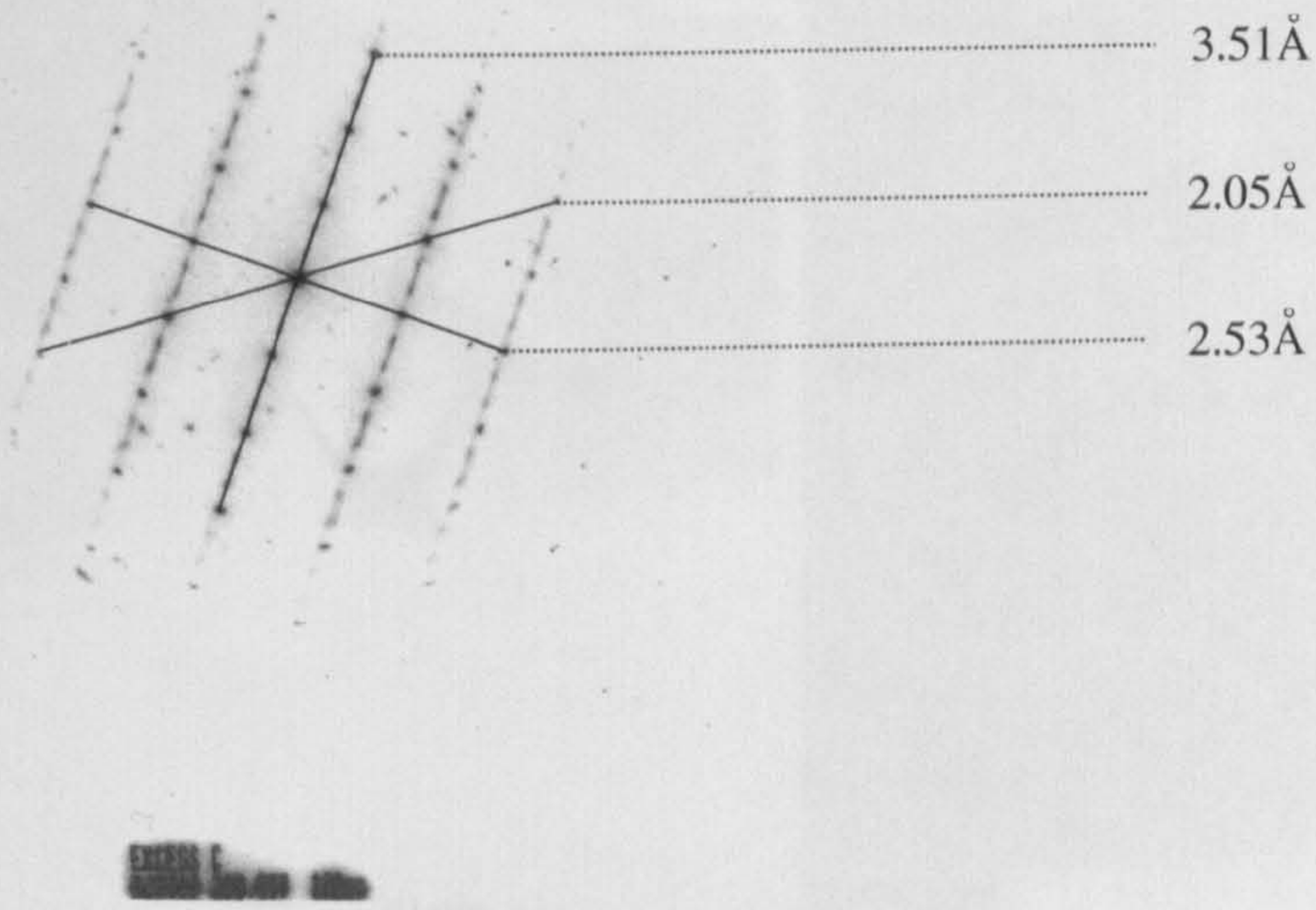

(g)

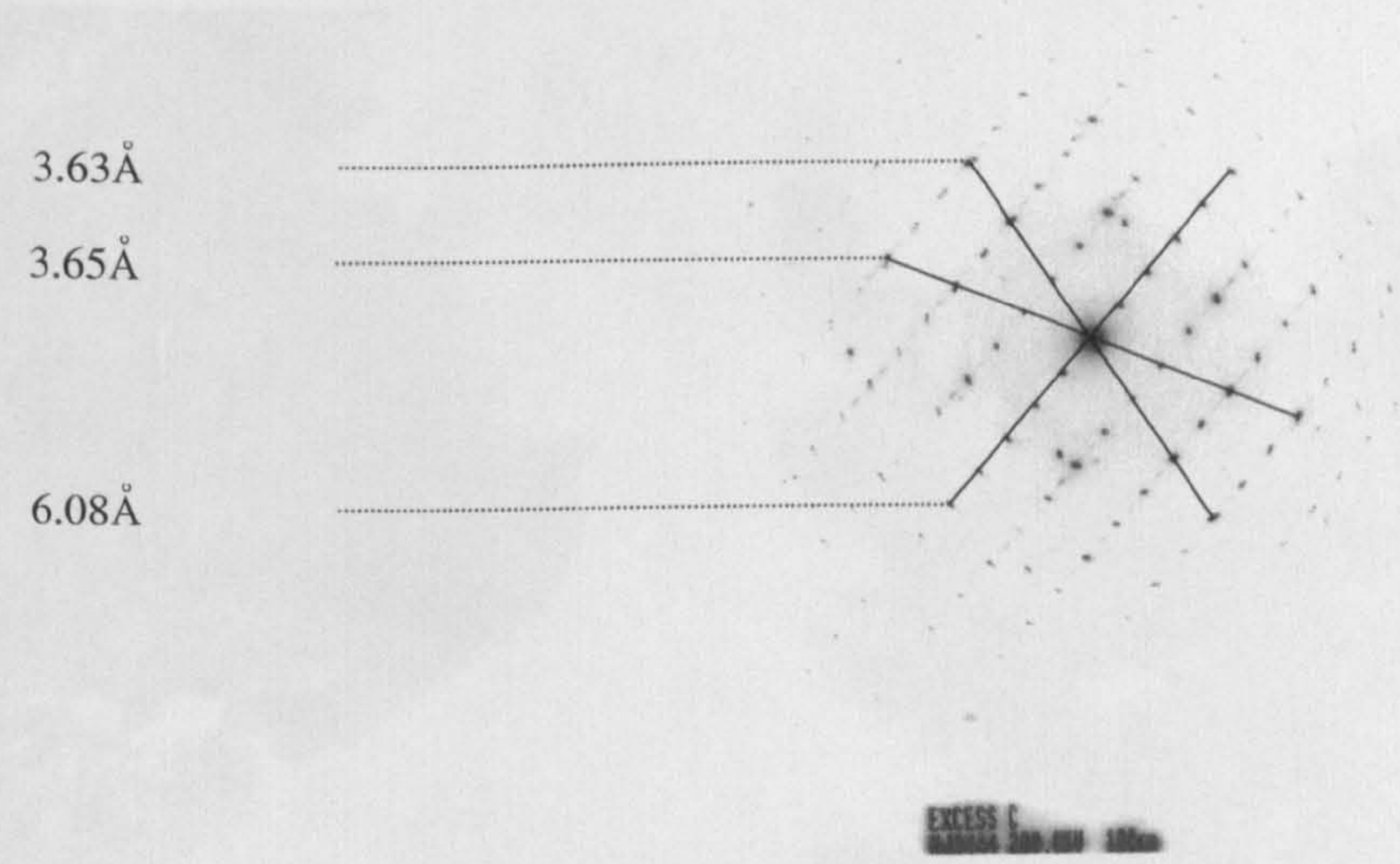

Figure 8.19: Analysis of diffraction patterns from matrix phase

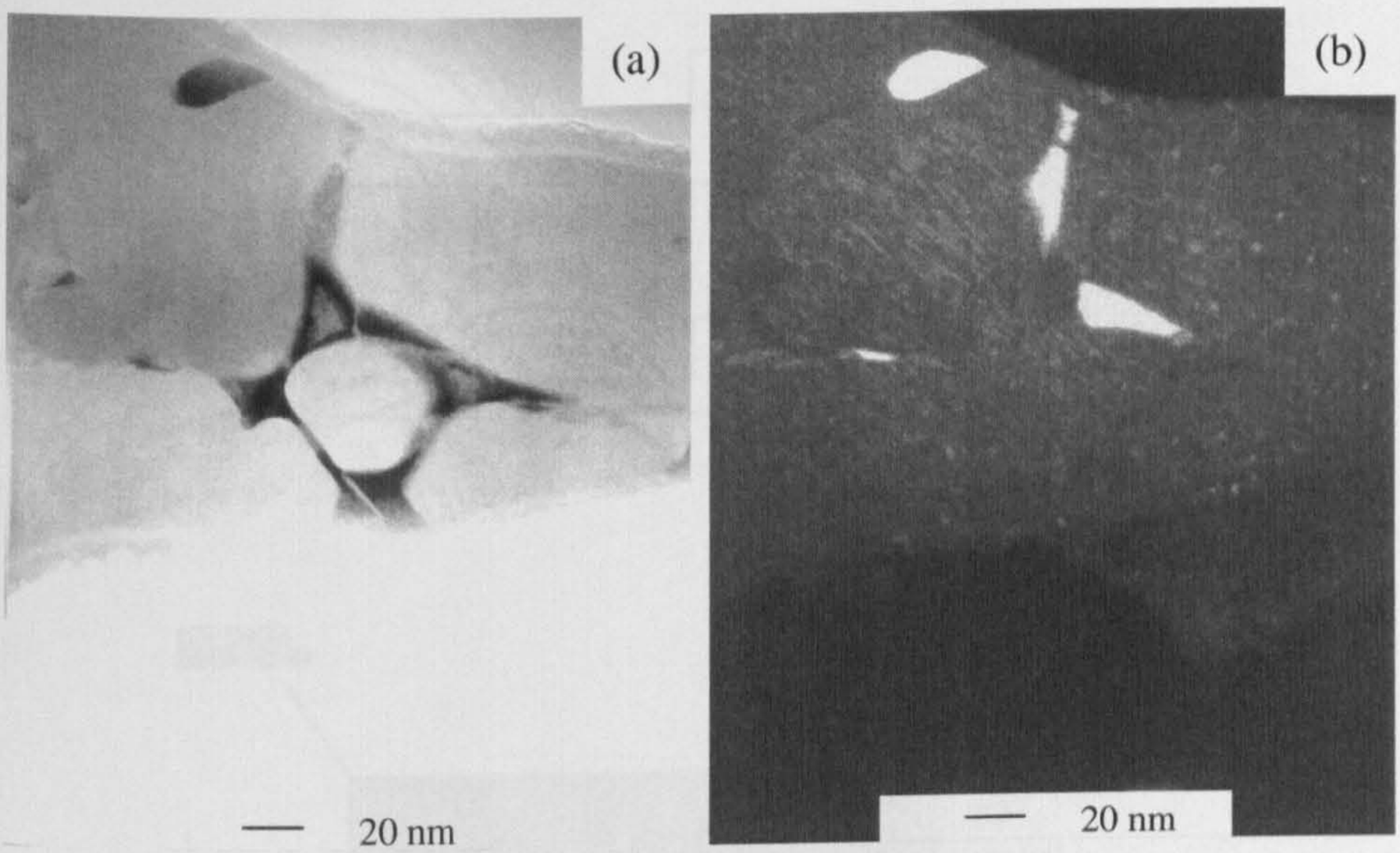

Figure 8.20: (a) Bright-field and, (b) Dark-field images of matrix phase in excess C coating

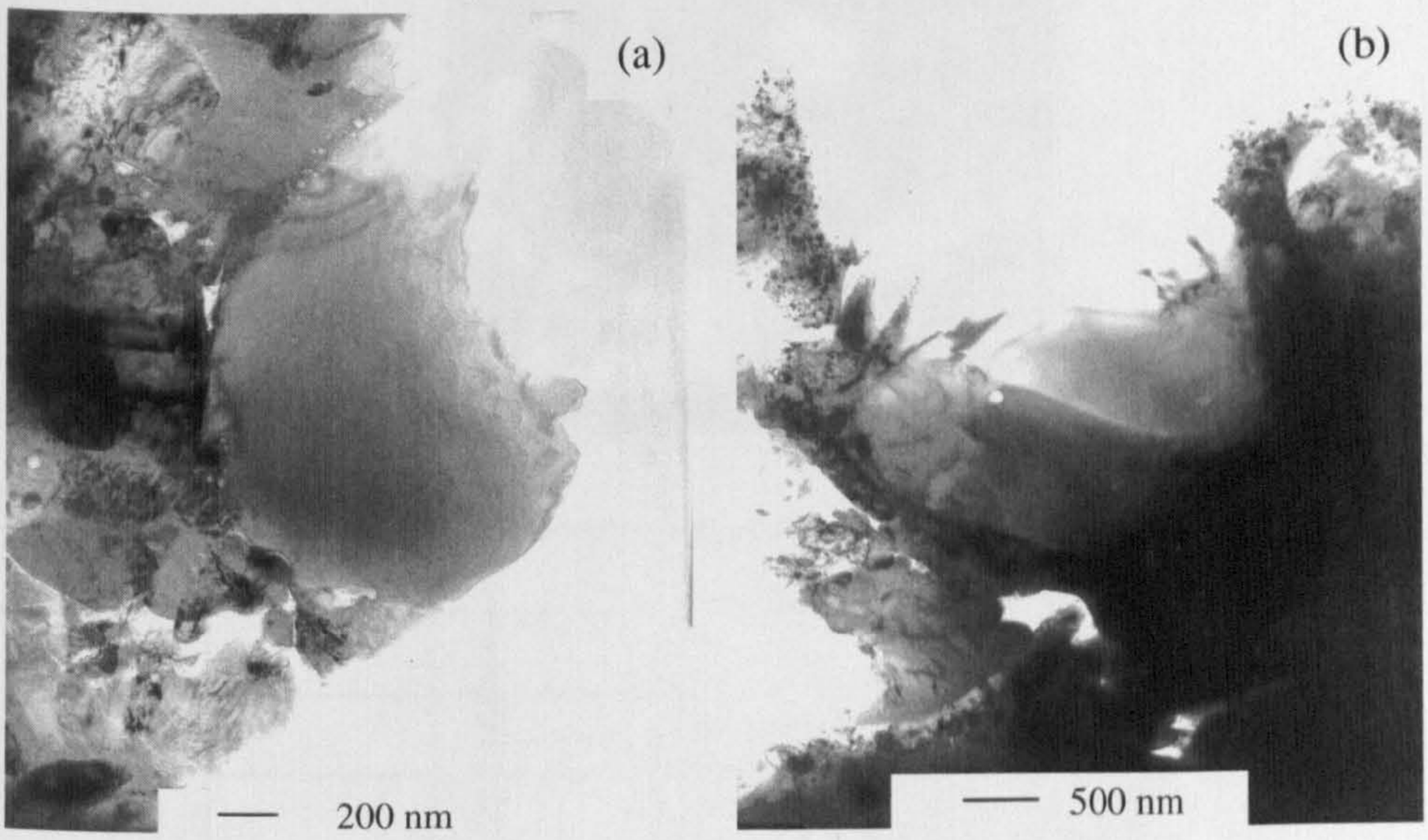

Figure 8.21: TiC particles in matrix of excess Ti coating

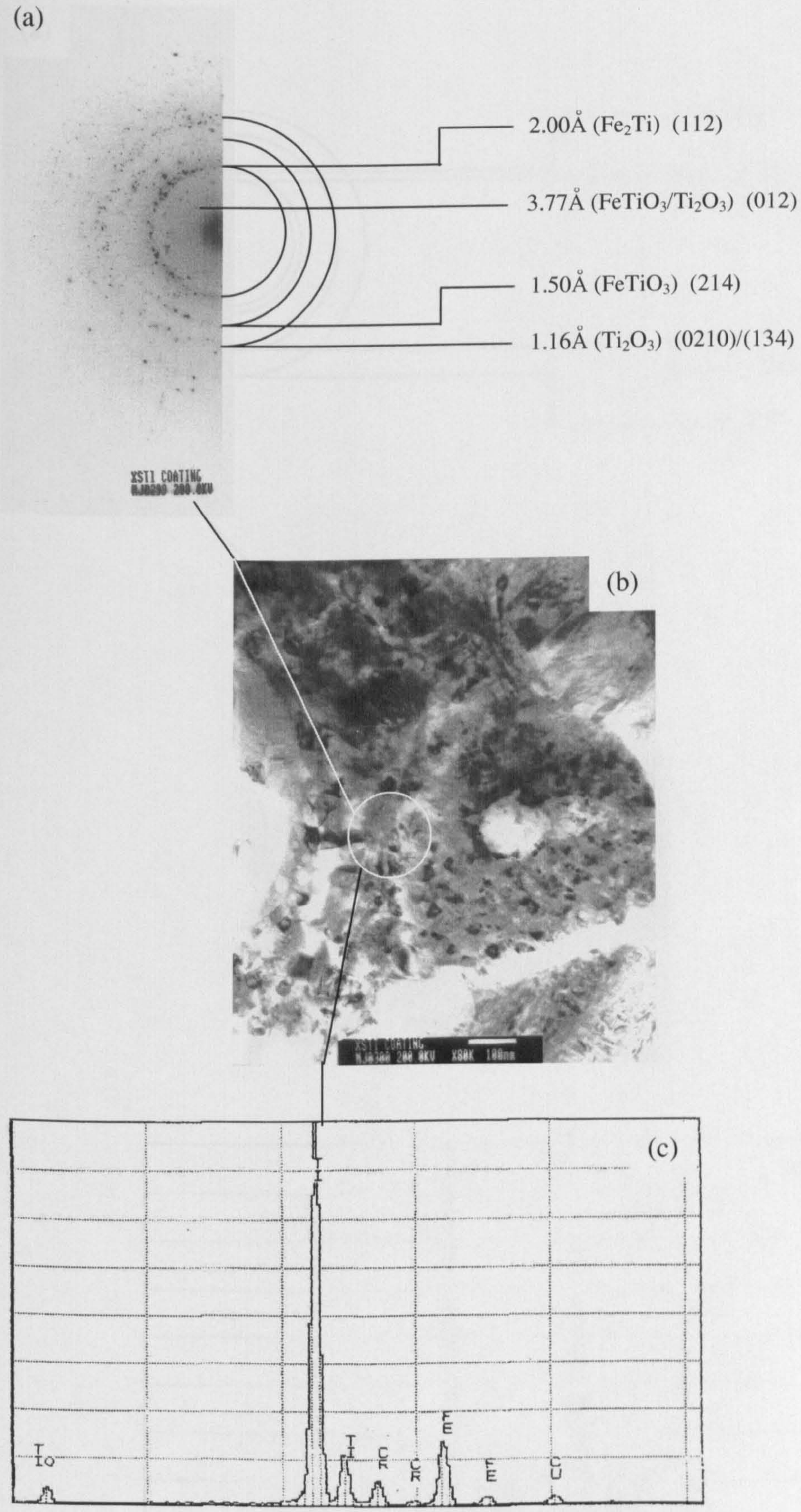

Figure 8.22: Image of oxide and intermetallic phases in excess Ti coating

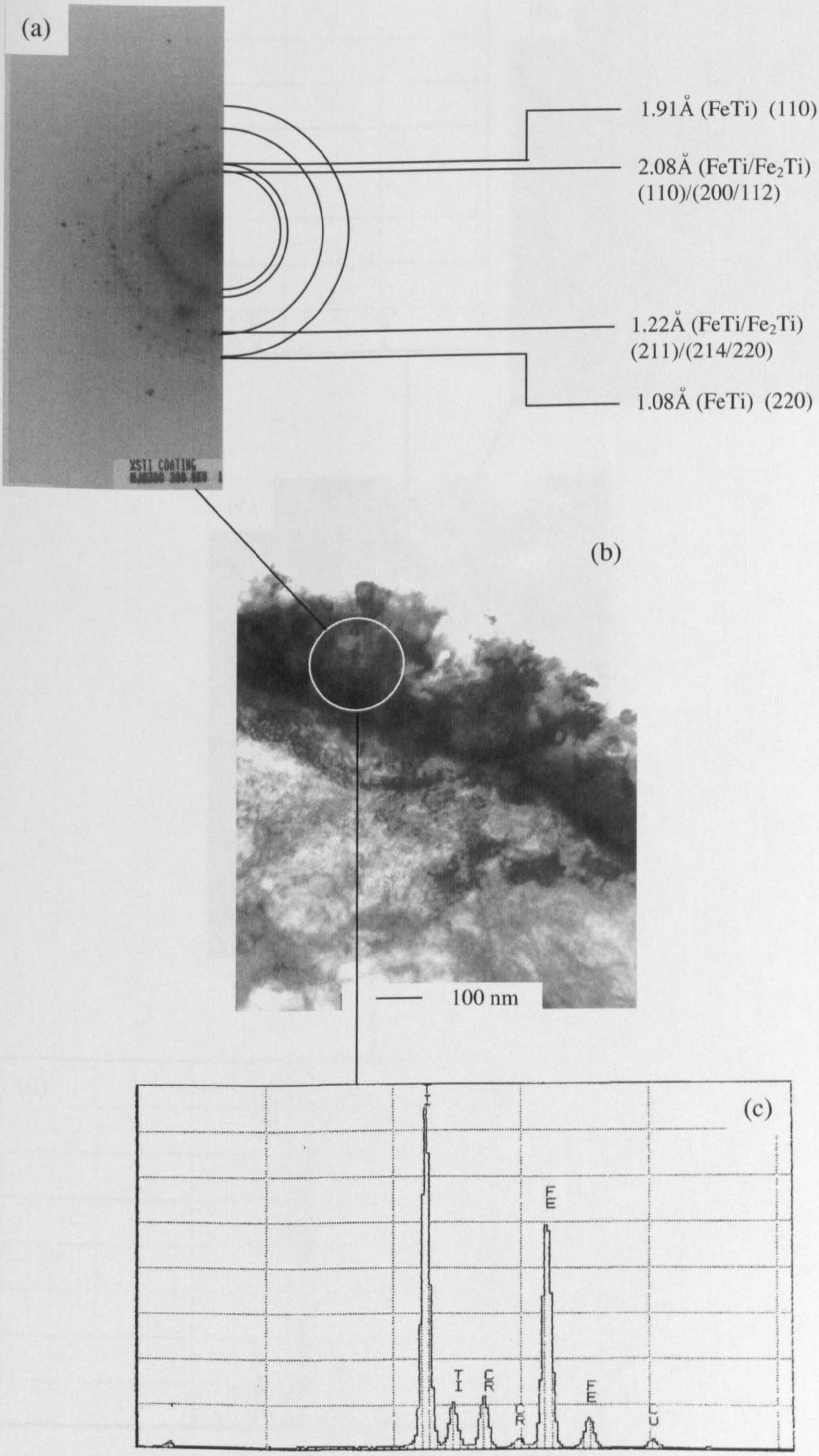

Figure 8.23: Intermetallic phases in excess Ti coating

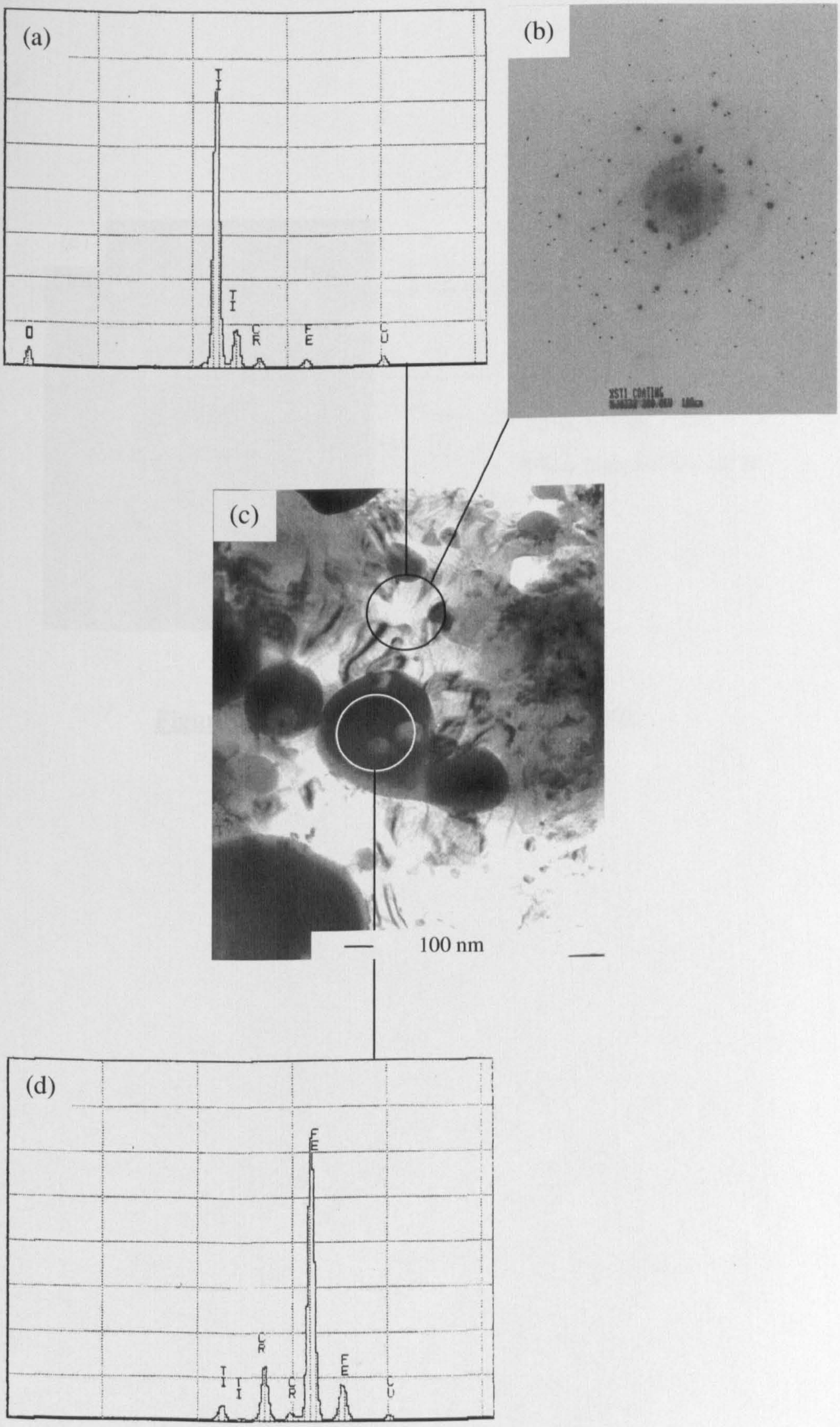

Figure 8.24: Image of globular regions and oxides in excess Ti coating

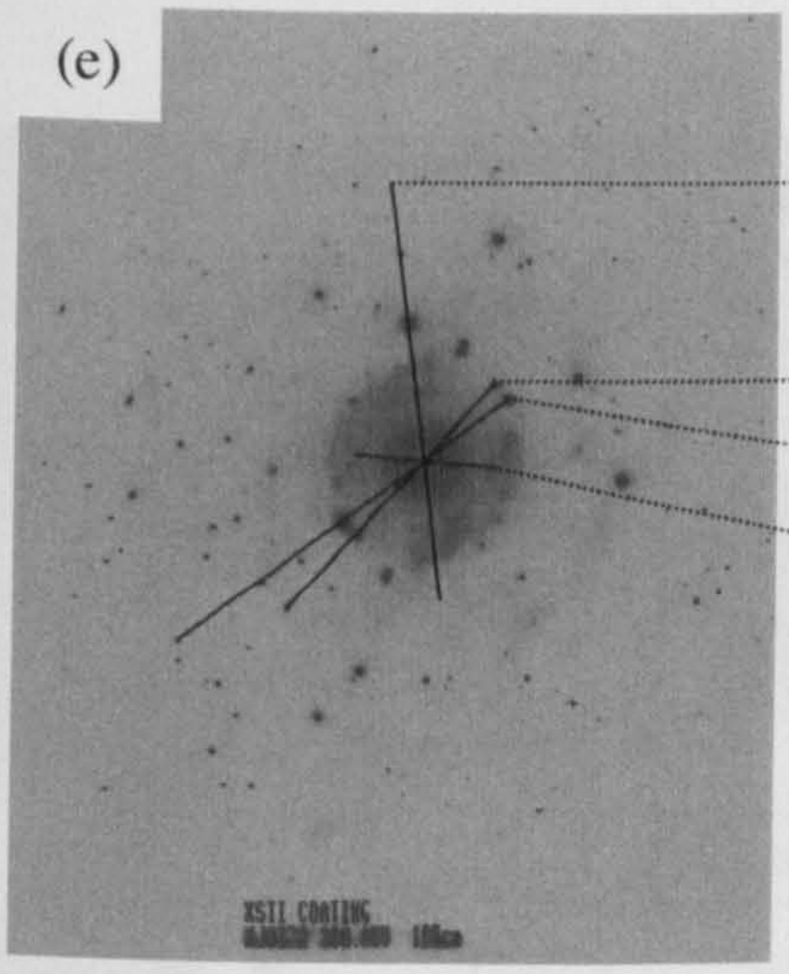

Figure 8.24: Analysis of diffraction pattern

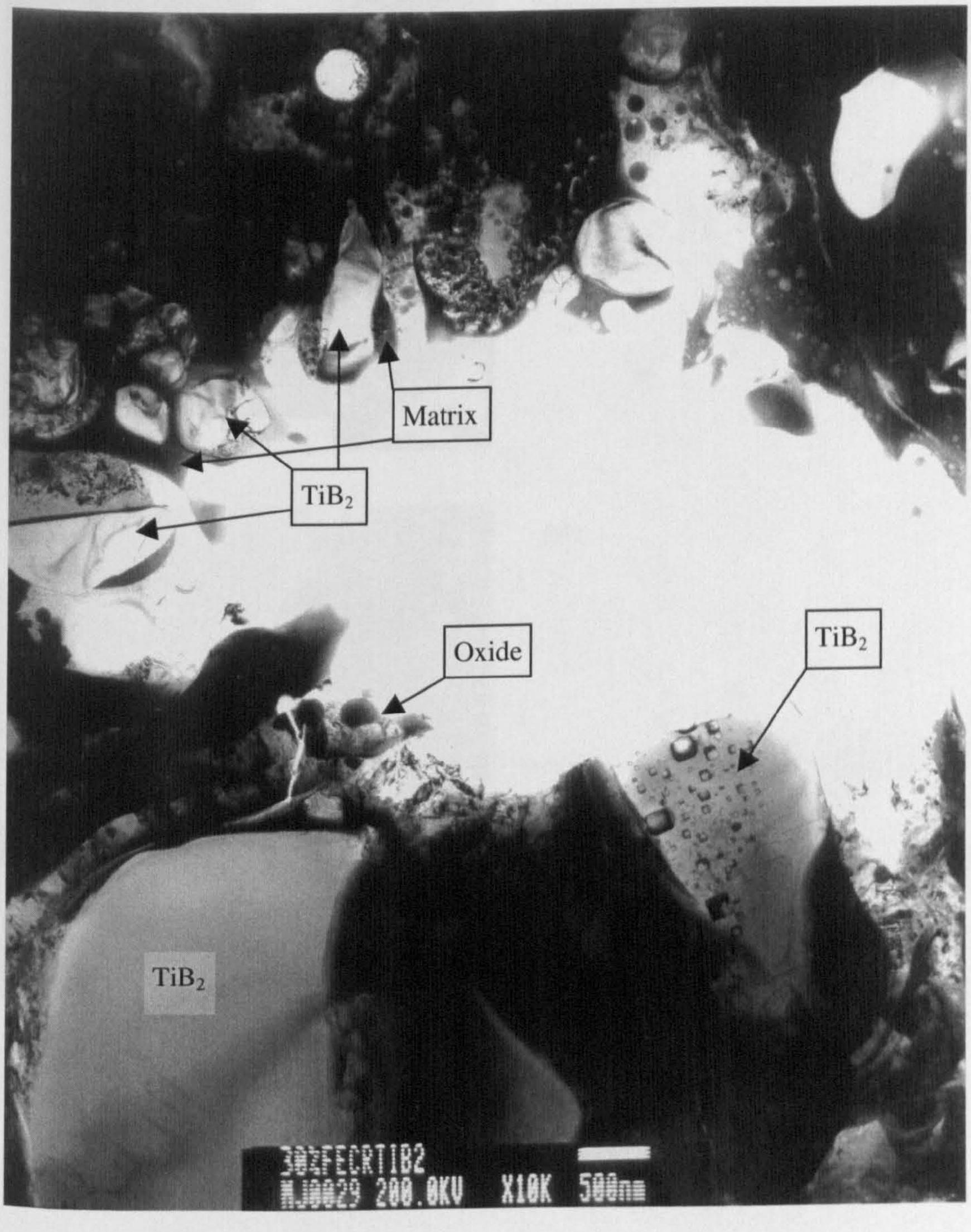

Figure 8.25: General view of TiB_2-based coating

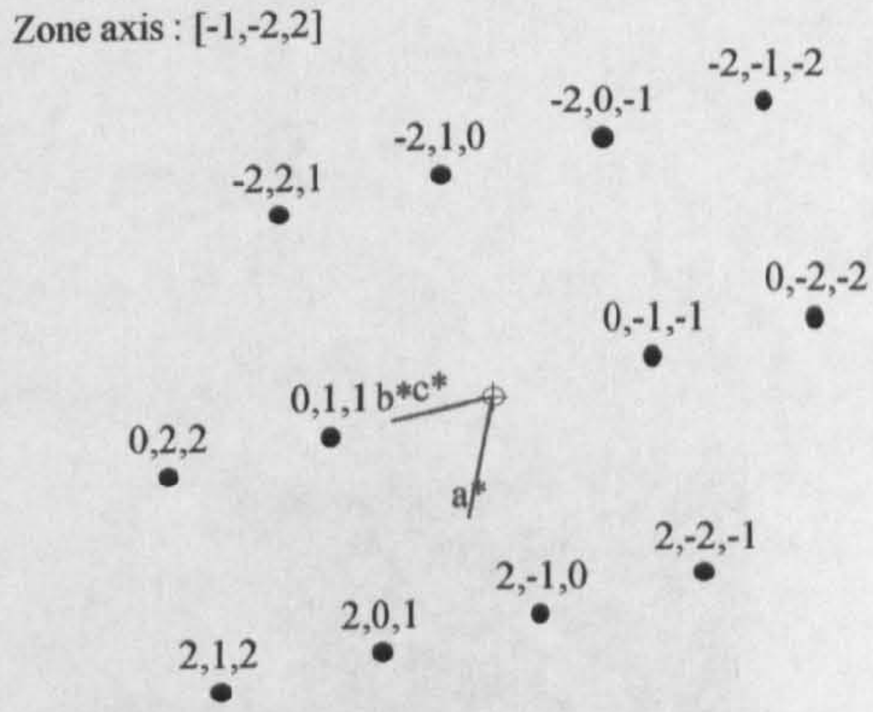

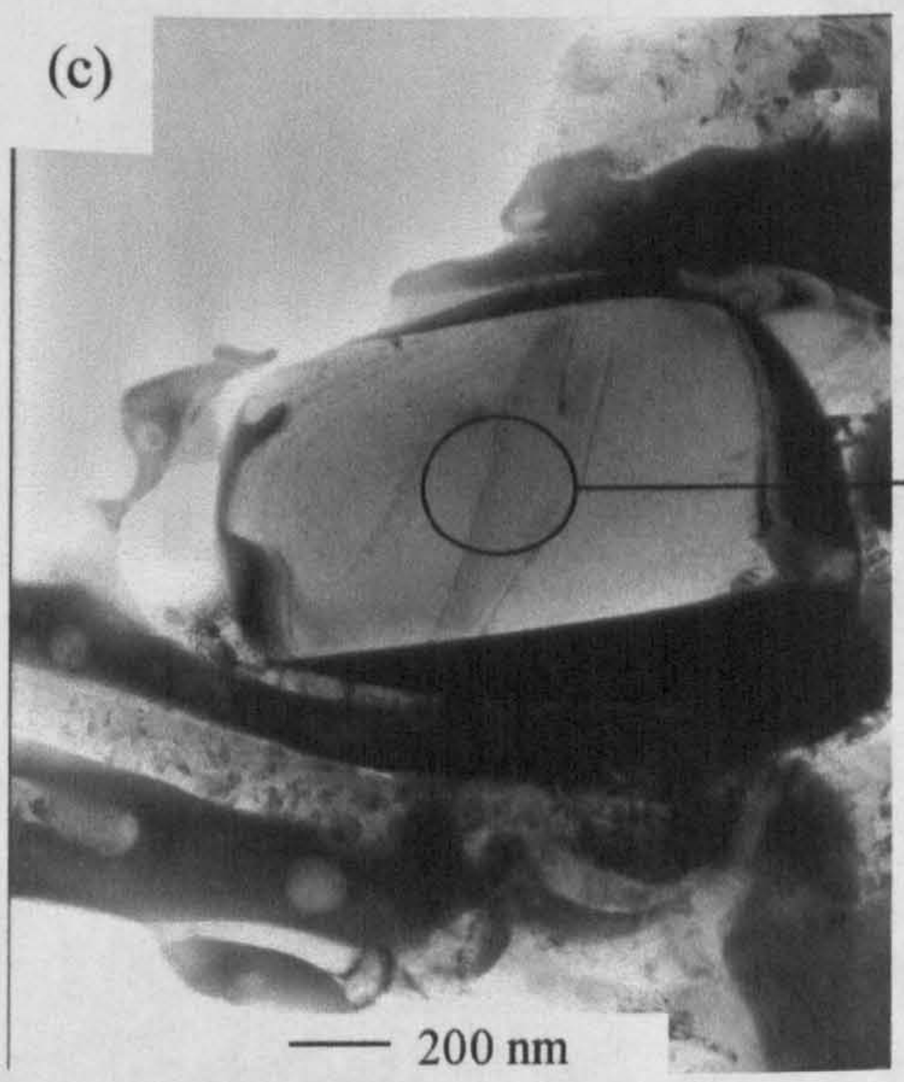

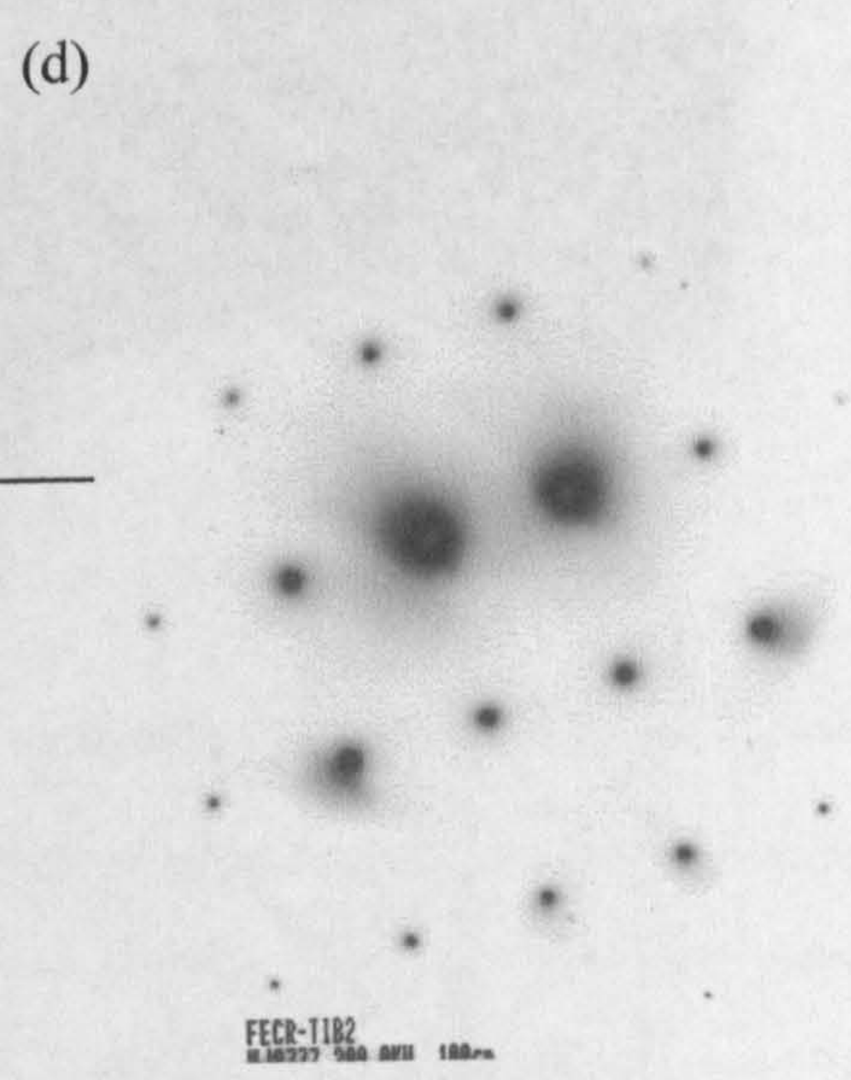

Figure 8.26: Analysis of TiB_2 particles

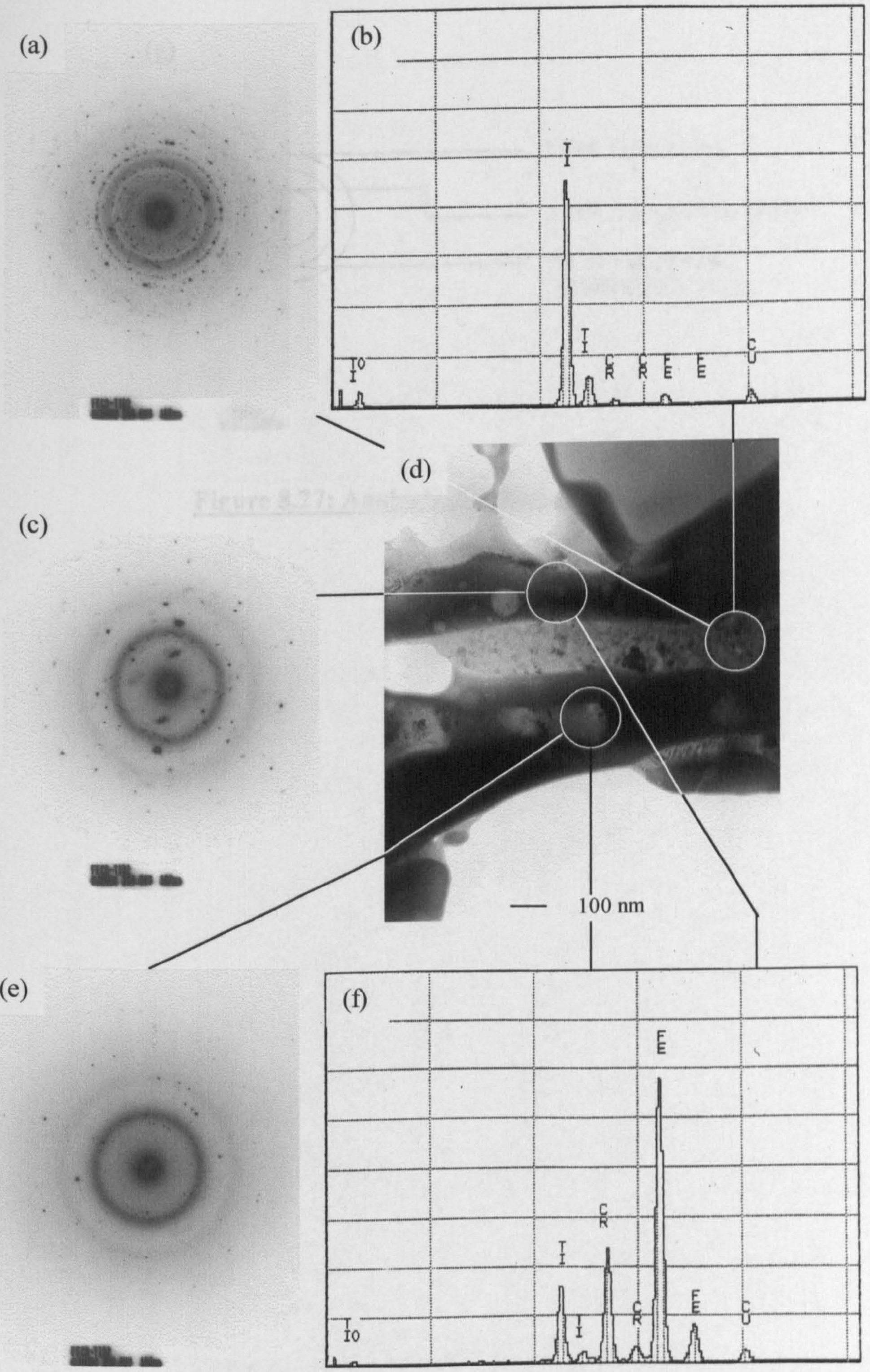

Figure 8.27: Amorphous and crystalline phases in TiB_2-based coating

(g)

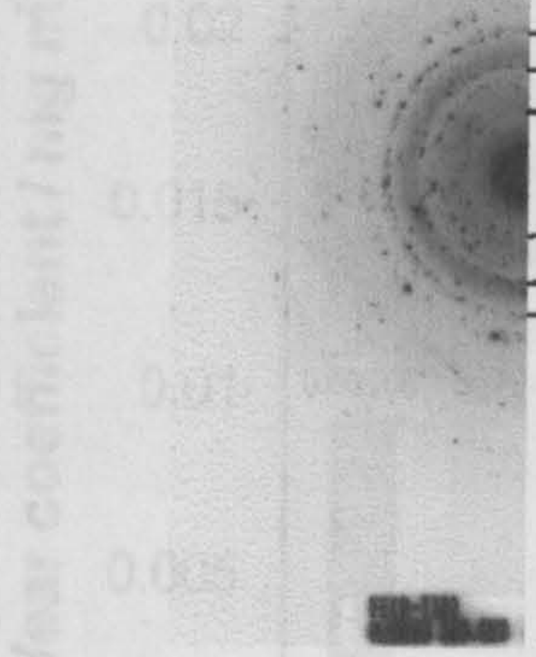

Figure 8.27: Analysis of diffraction pattern

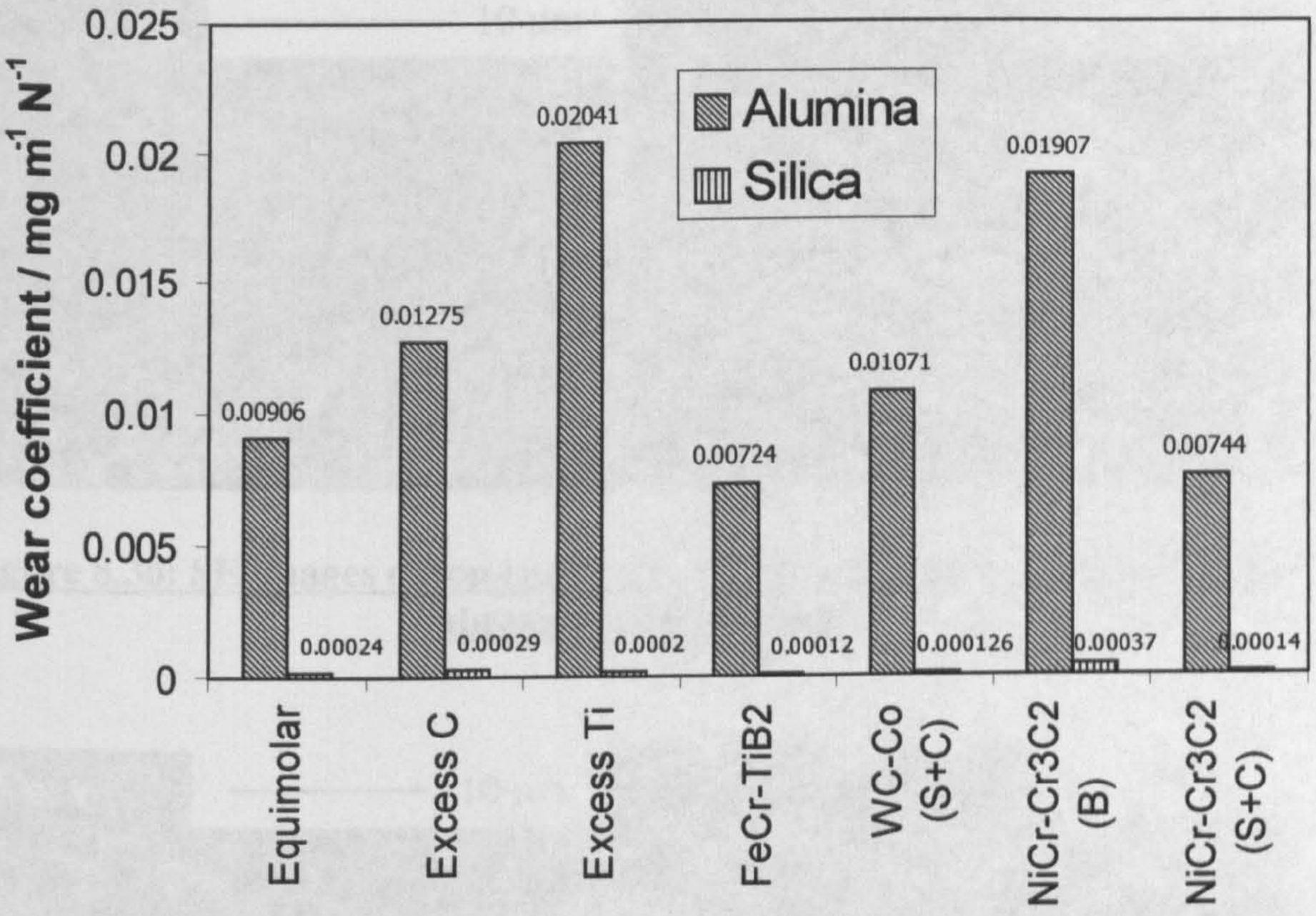

Figure 8.28: Abrasive wear coefficients of coatings tested with an applied force of 54N and an abrasive particle size range of 500-600μm

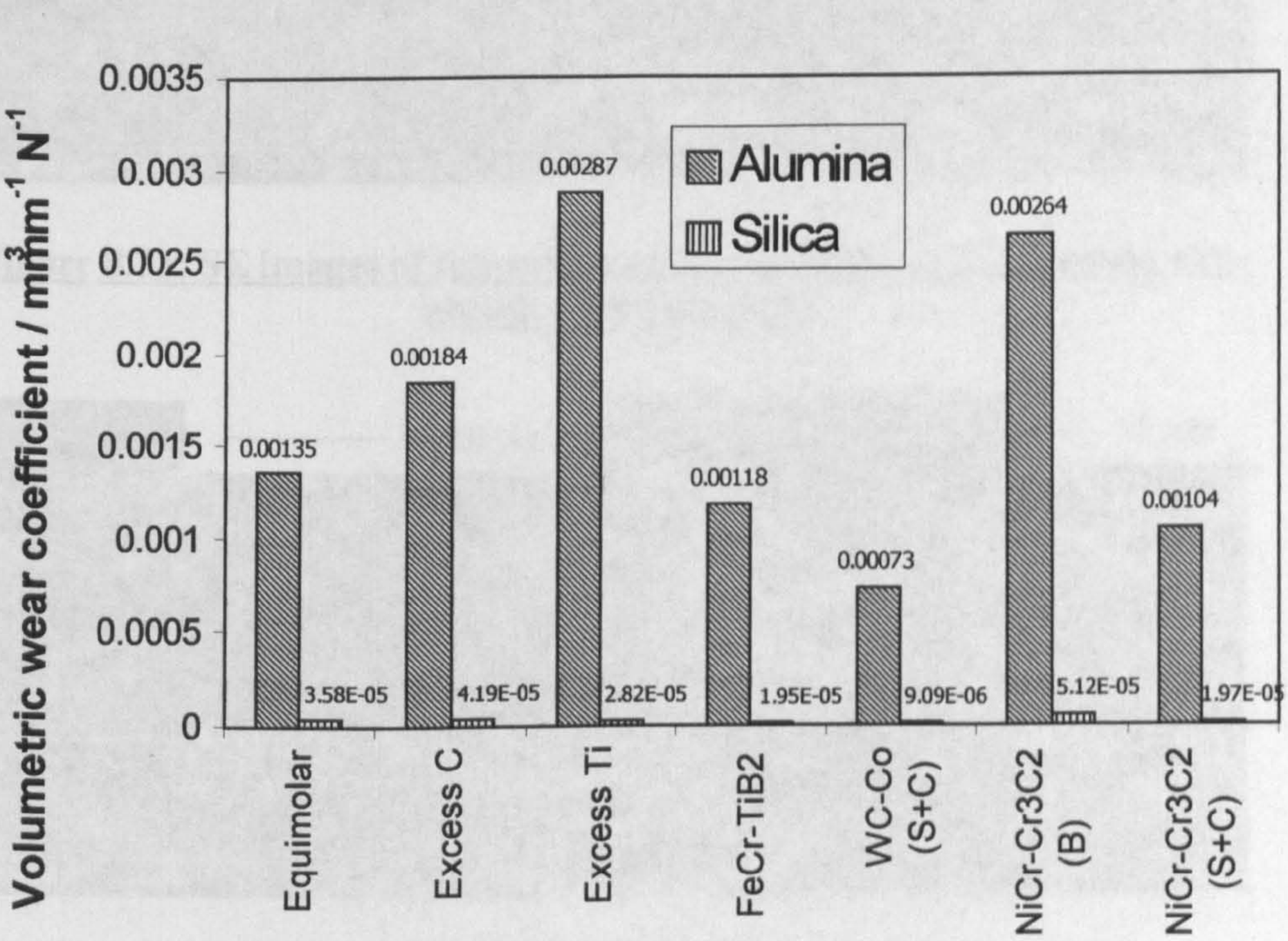

Figure 8.29: Volumetric wear coefficients of coatings tested with an applied force of 54N and an abrasive particle size range of 500-600μm

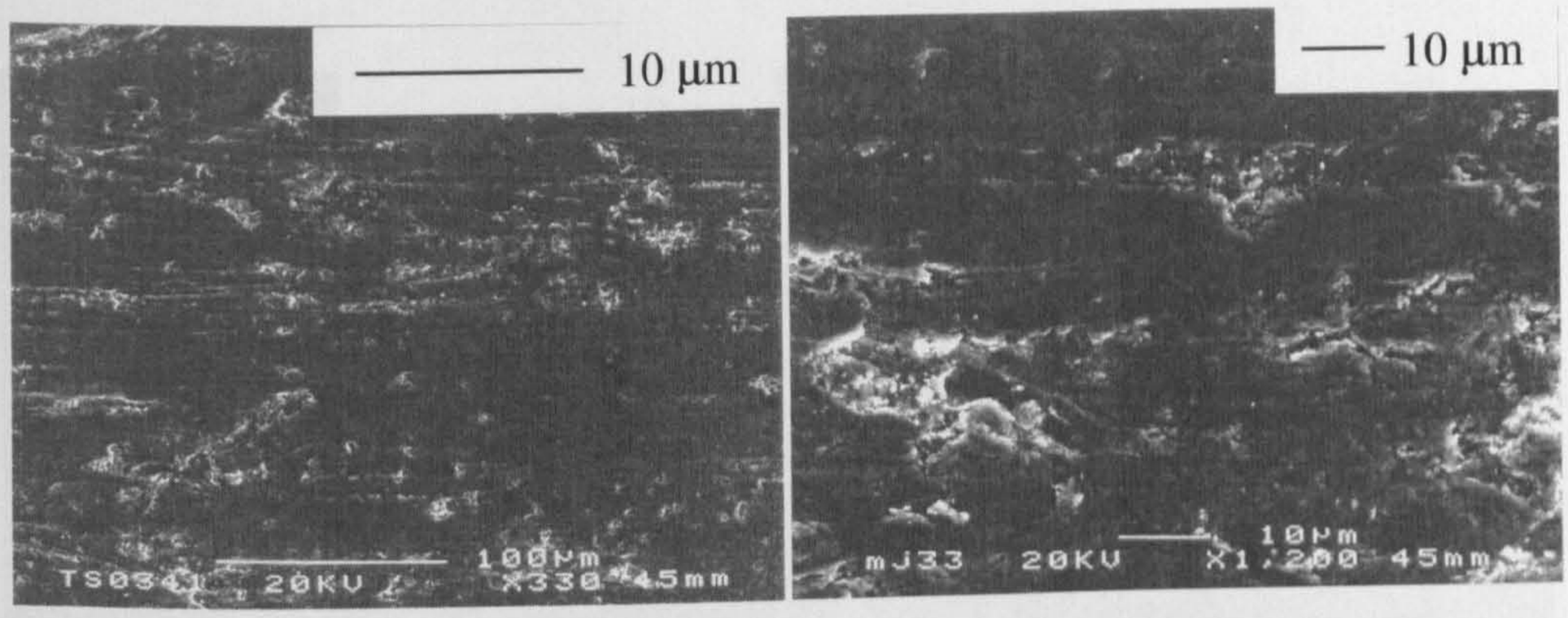

Figure 8.30: SE images of top-surface wear scars of equimolar coating after abrasion with alumina

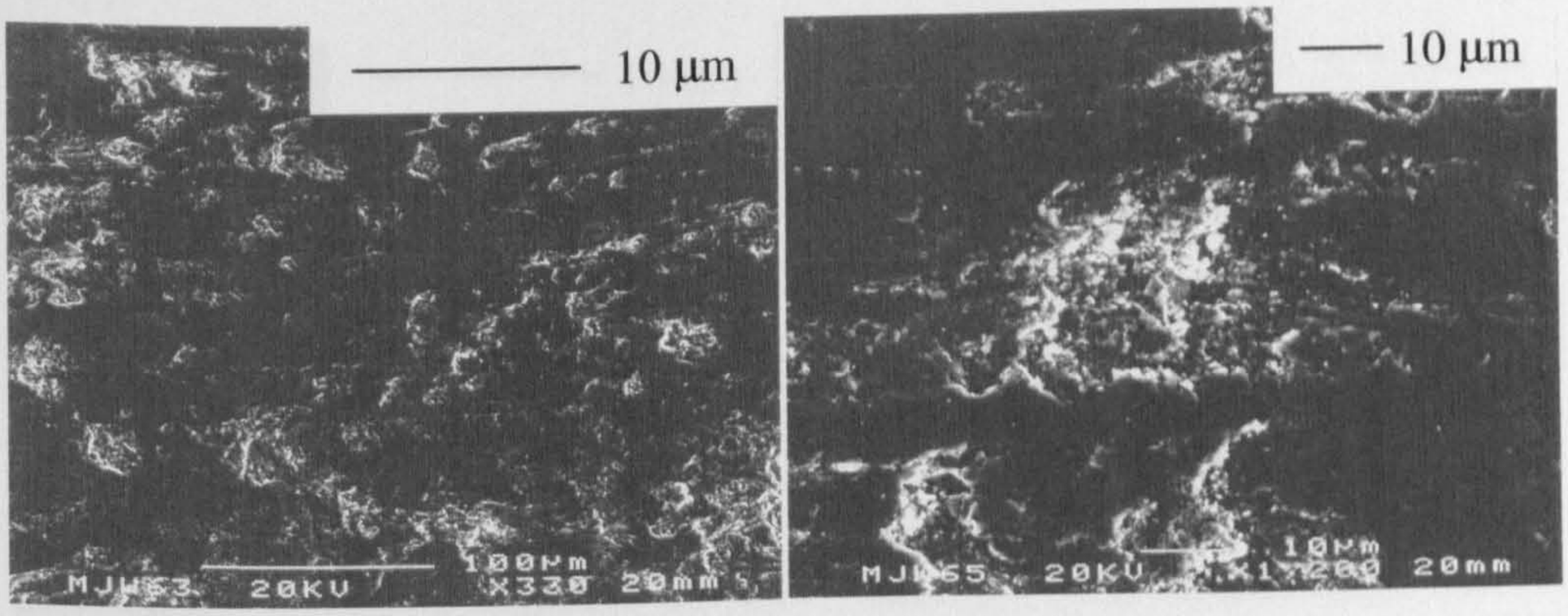

Figure 8.31: SE images of top-surface wear scars of excess C coating after abrasion with alumina

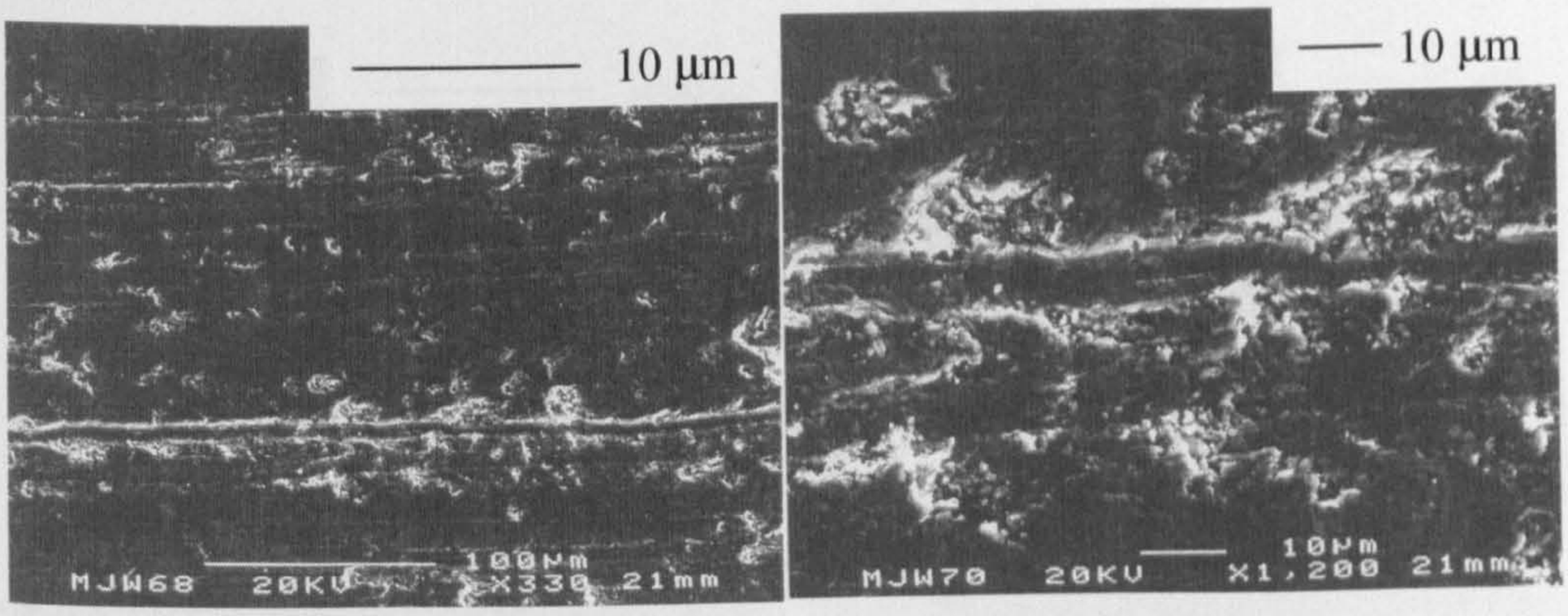

Figure 8.32: SE images of top-surface wear scars of excess Ti coating after abrasion with alumina

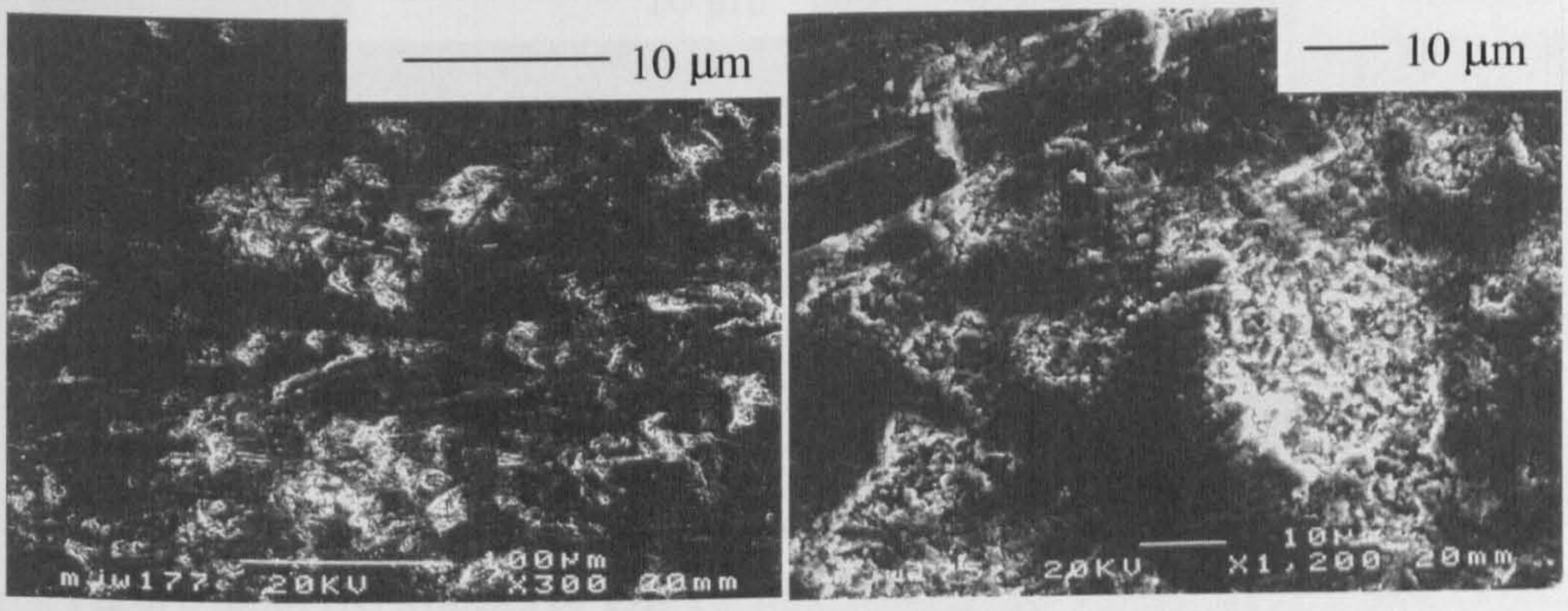

Figure 8.33: SE images of top-surface wear scars of TiB_2-based coating after abrasion with alumina

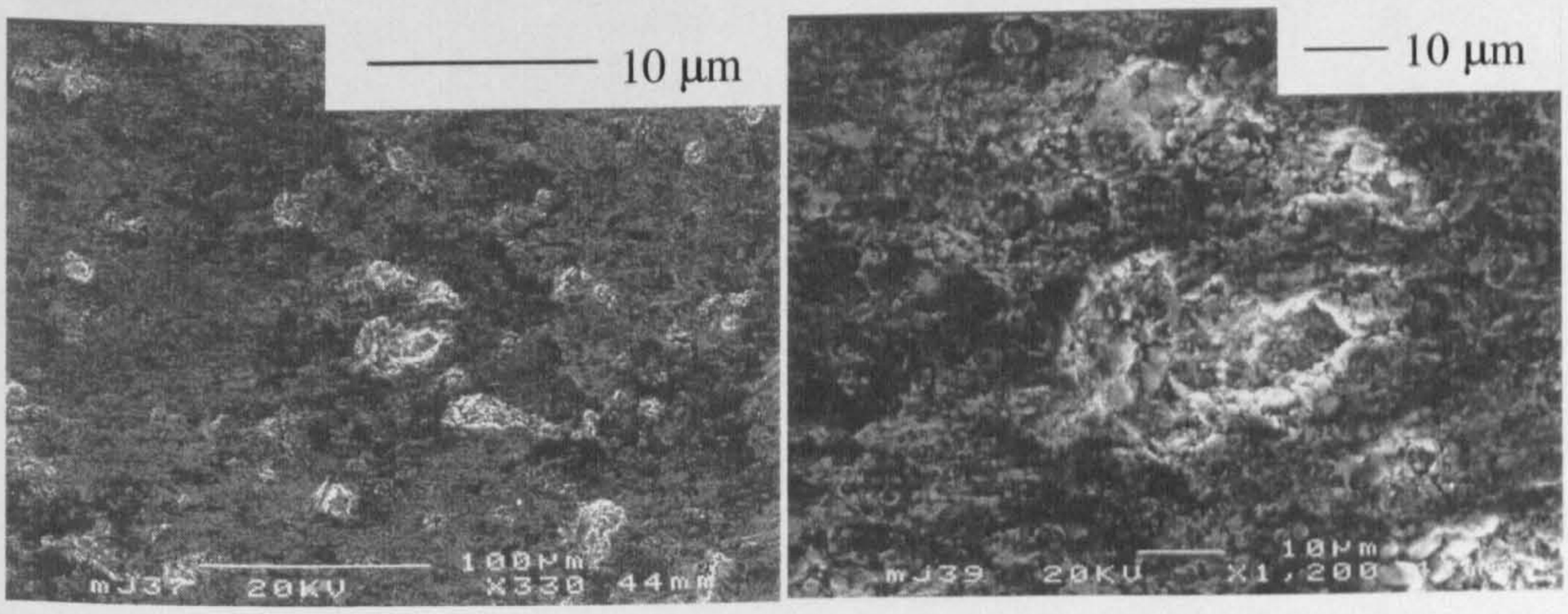

Figure 8.34: SE images of top-surface wear scars of equimolar coating after abrasion with silica

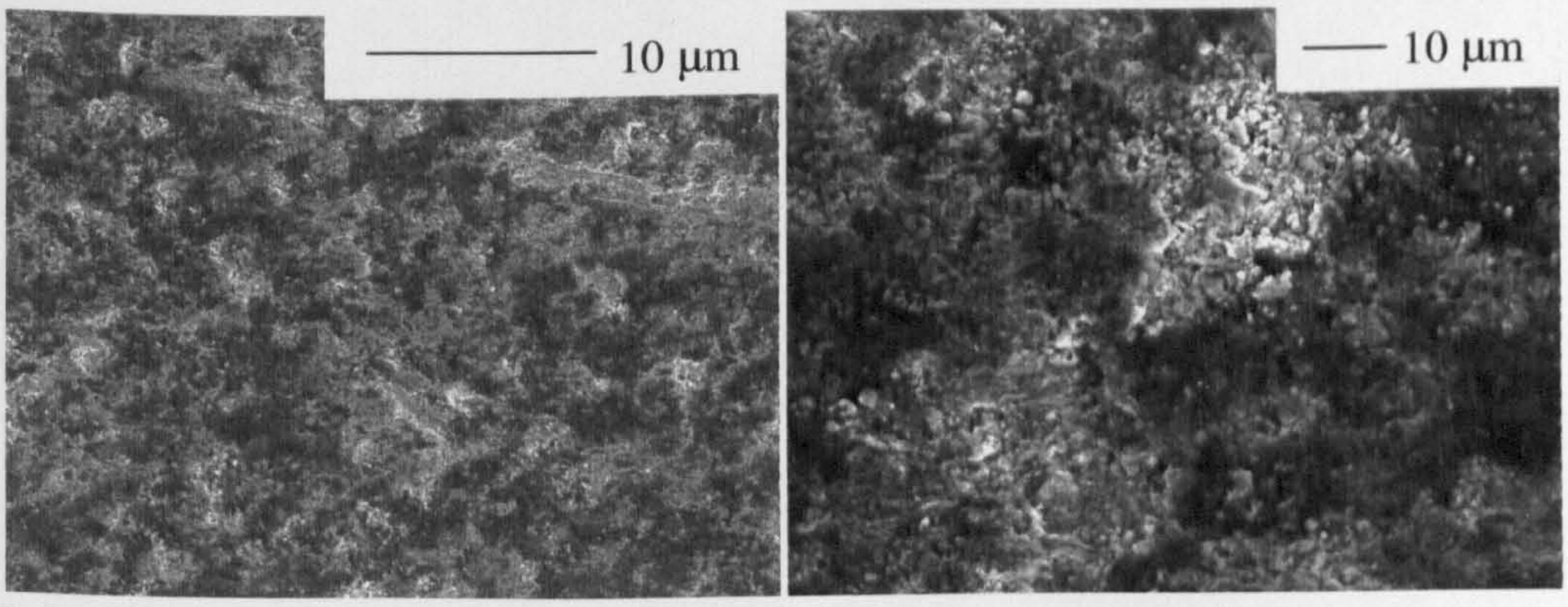

Figure 8.35: SE images of top-surface wear scars of excess C coating after abrasion with silica

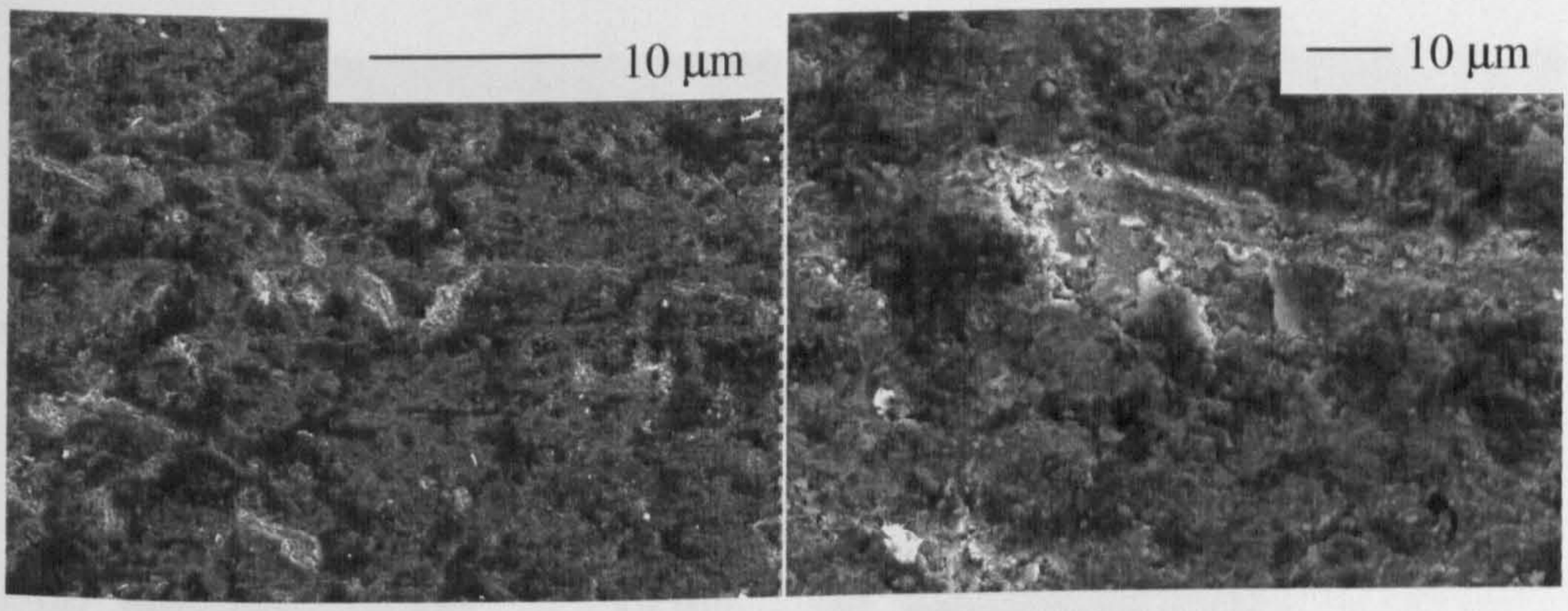

Figure 8.36: SE images of top-surface wear scars of excess Ti coating after abrasion with silica

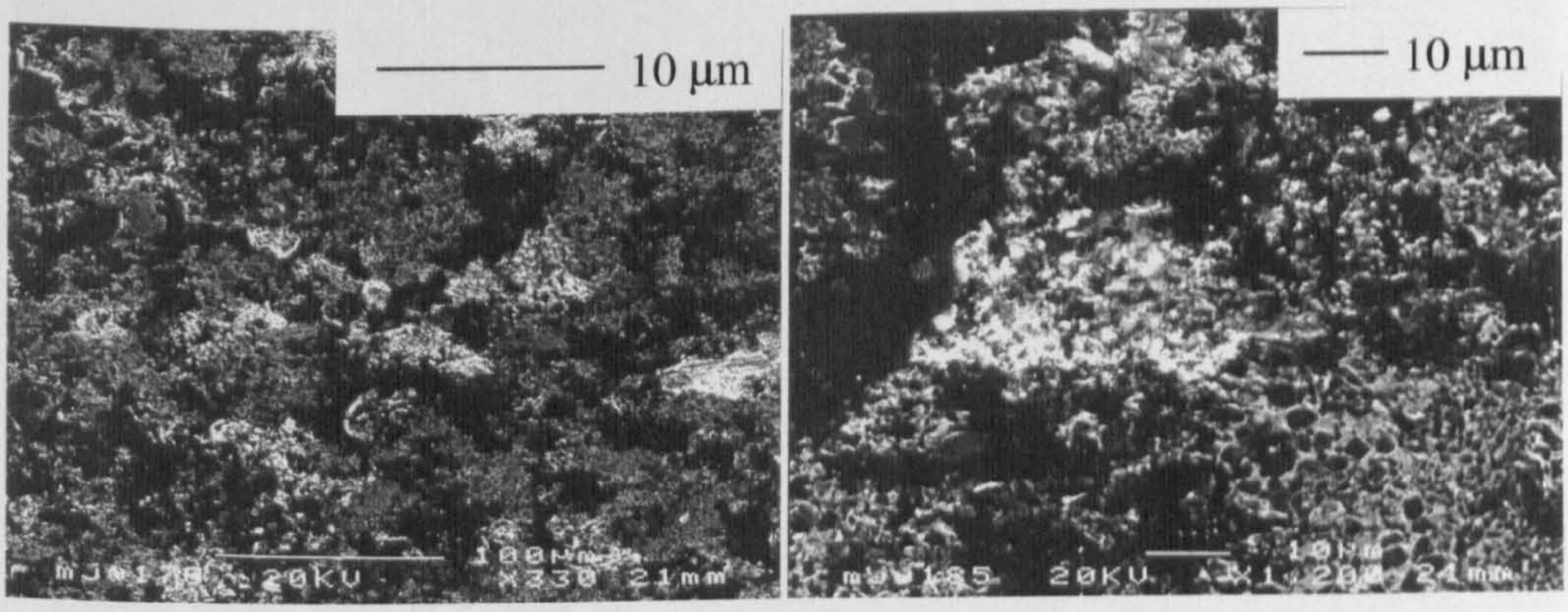

Figure 8.37: SE images of top-surface wear scars of TiB_2-based coating after abrasion with silica

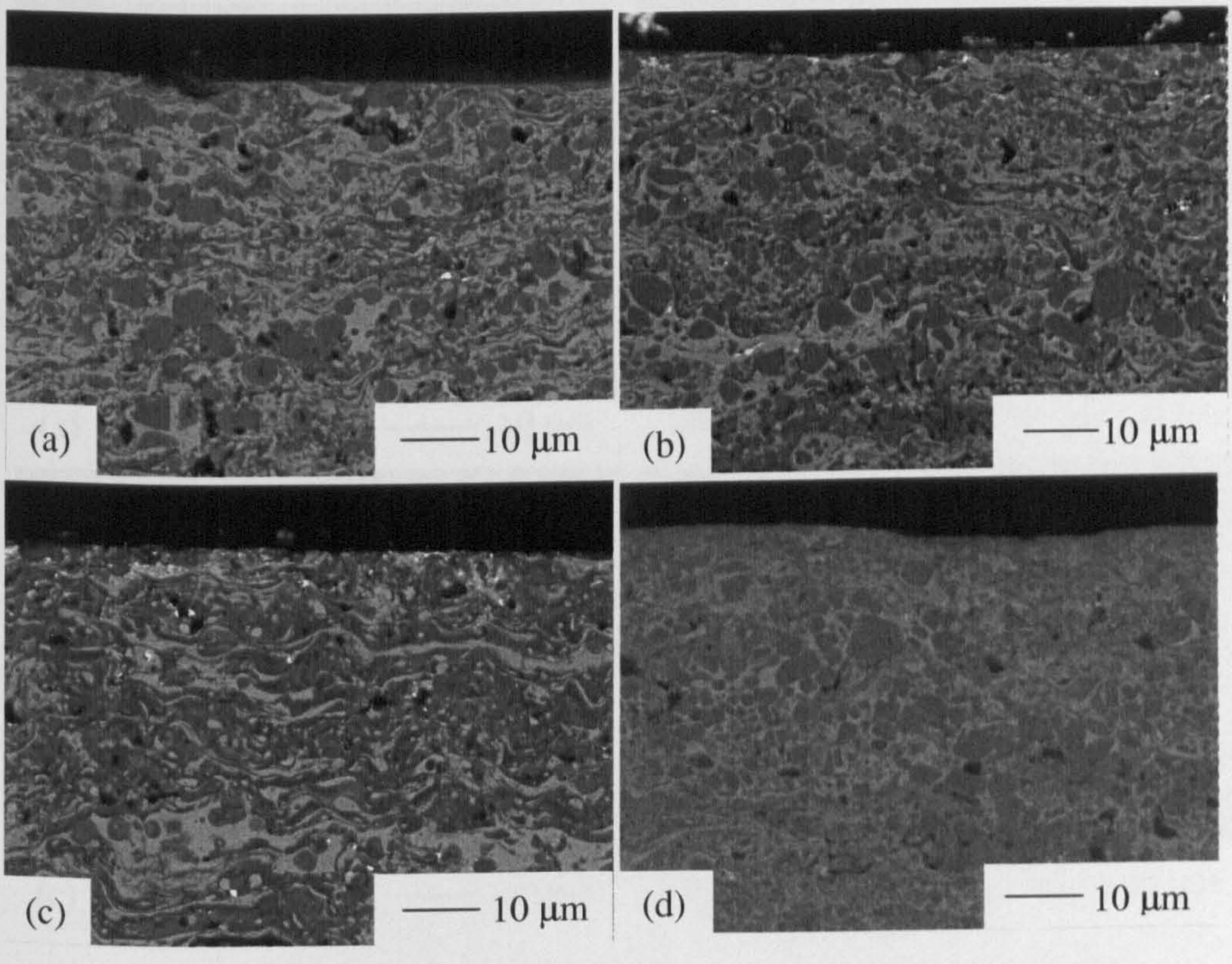

Figure 8.38: BSE images of cross-sections of wear scars of (a) equimolar, (b) excess C, (c) excess Ti and (d) TiB_2-based coatings following abrasion with alumina

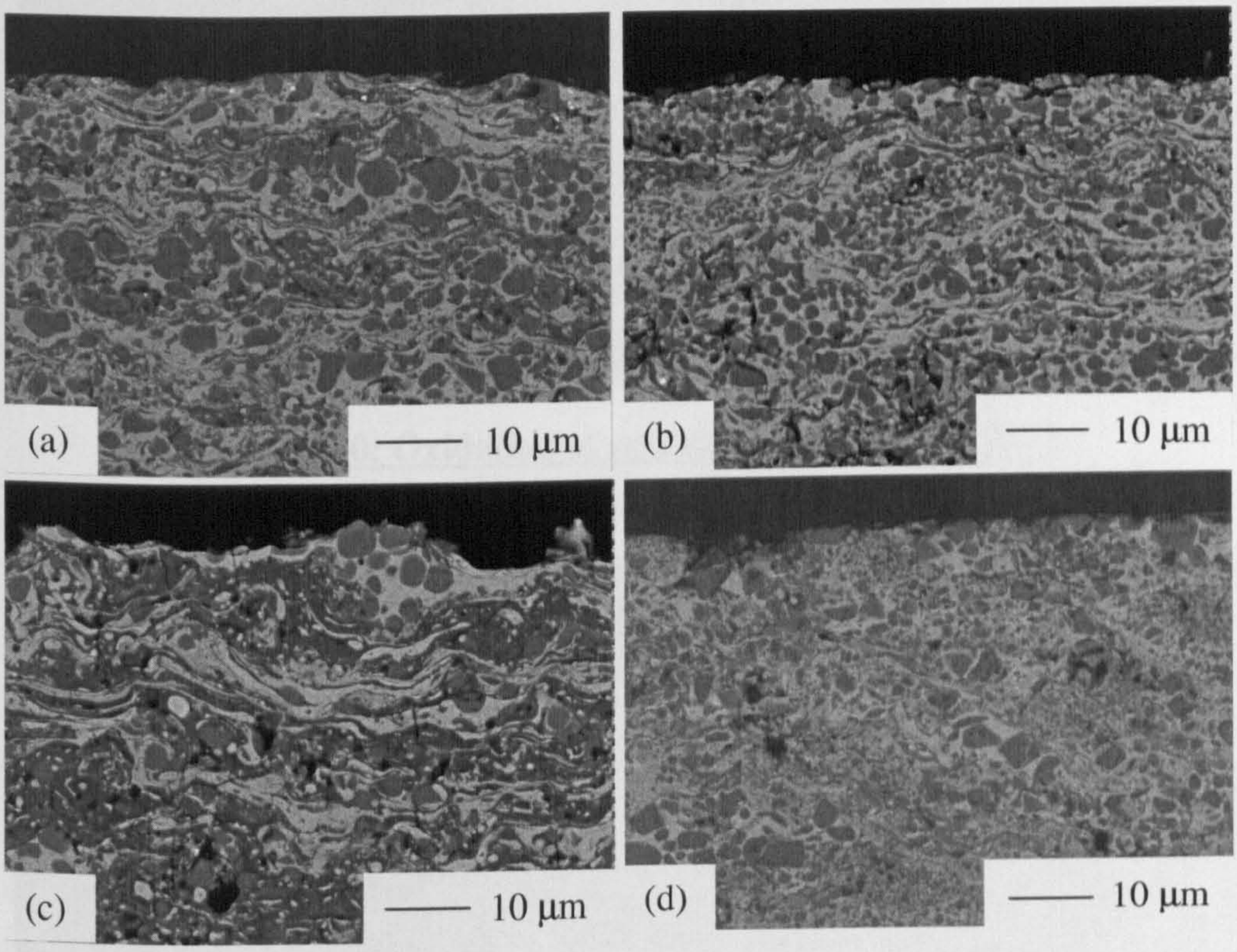

Figure 8.39: BSE images of cross-sections of wear scars of (a) equimolar, (b) excess C, (c) excess Ti and (d) TiB_2-based coatings following abrasion with silica

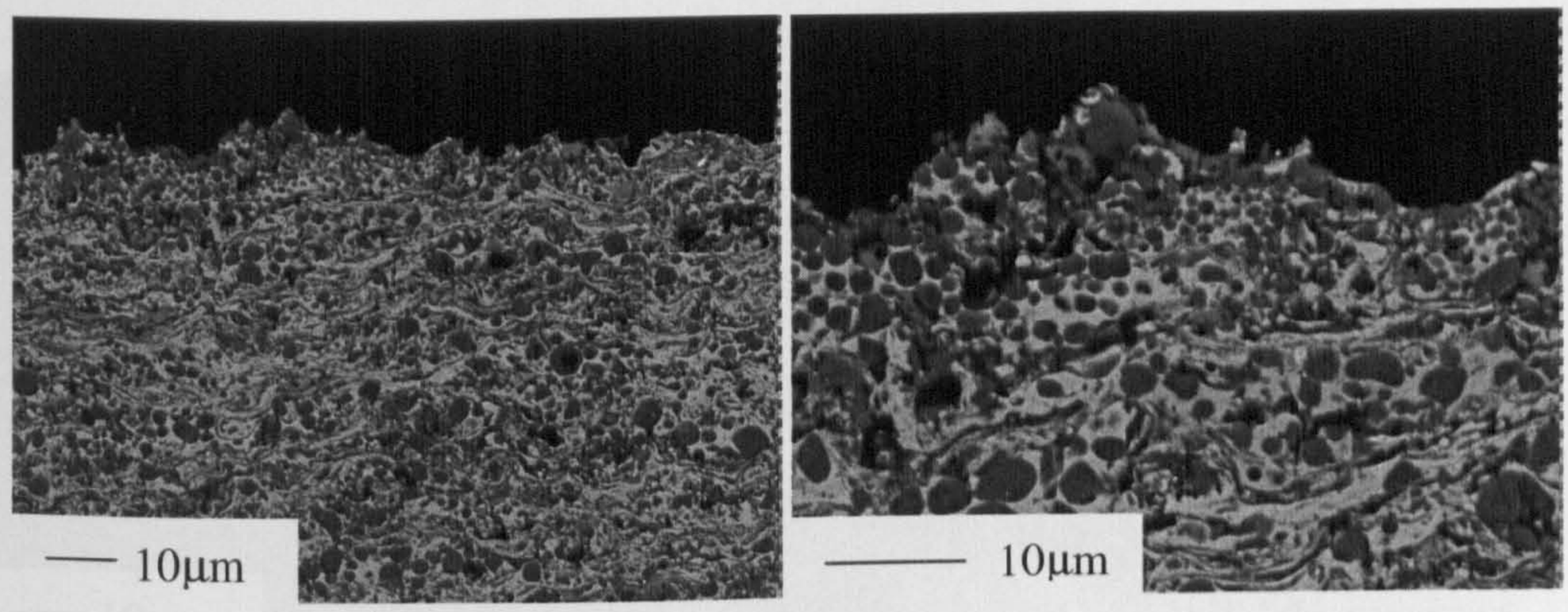

Figure 8.40: Oxidation of equimolar coating at 500°C

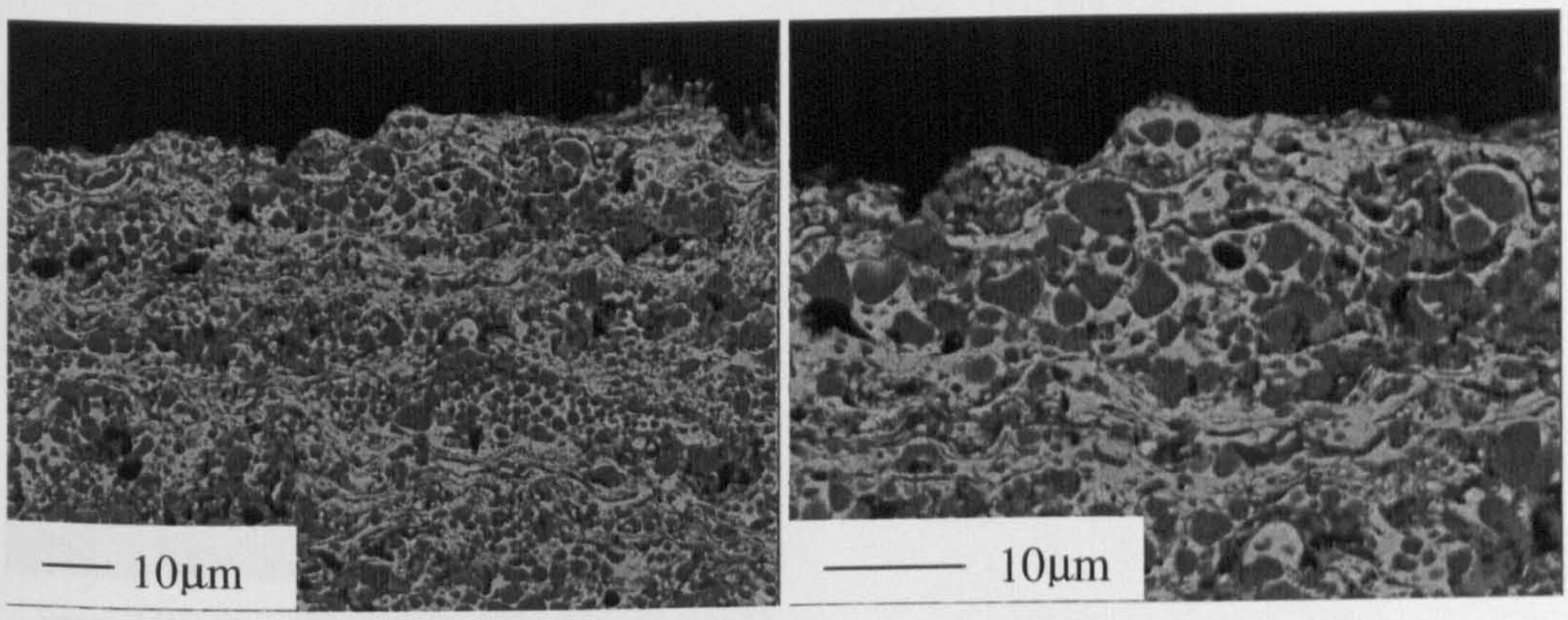

Figure 8.41: Oxidation of excess C coating at 500°C

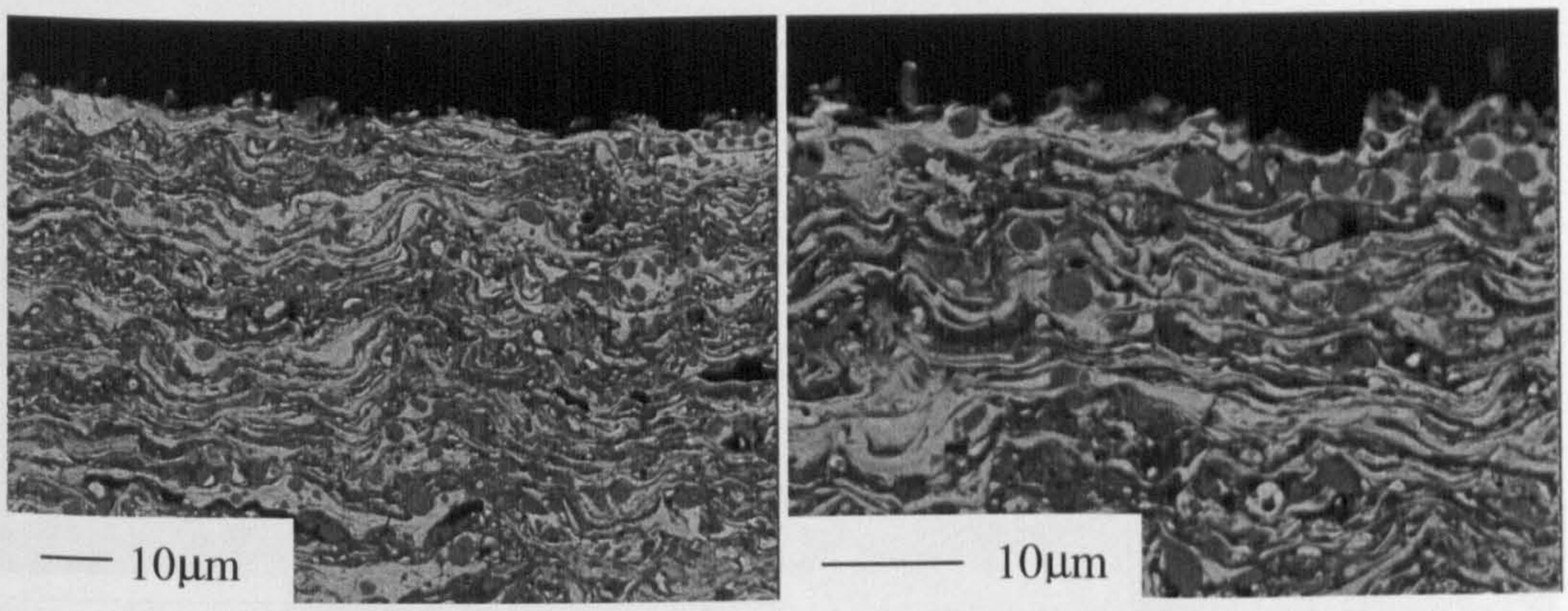

Figure 8.42: Oxidation of excess Ti coating at 500°C

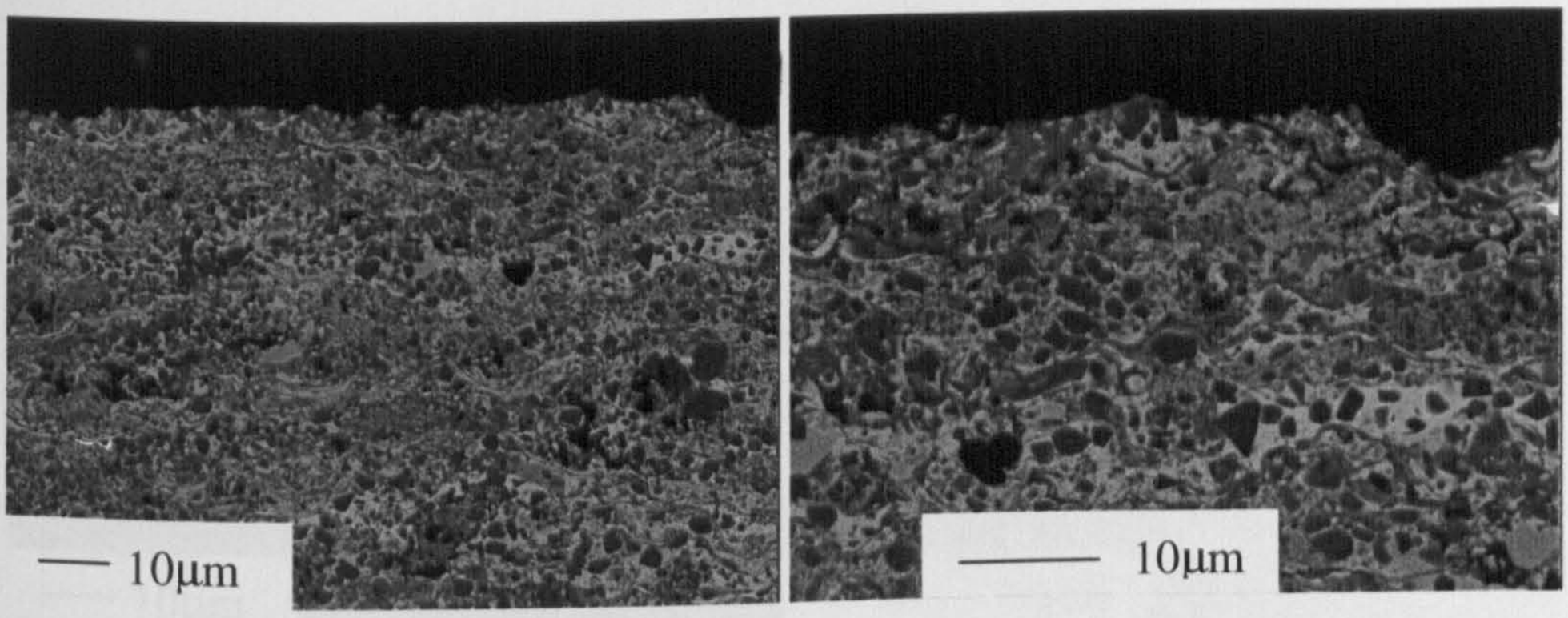

Figure 8.43: Oxidation of TiB_2-based coating at 500°C

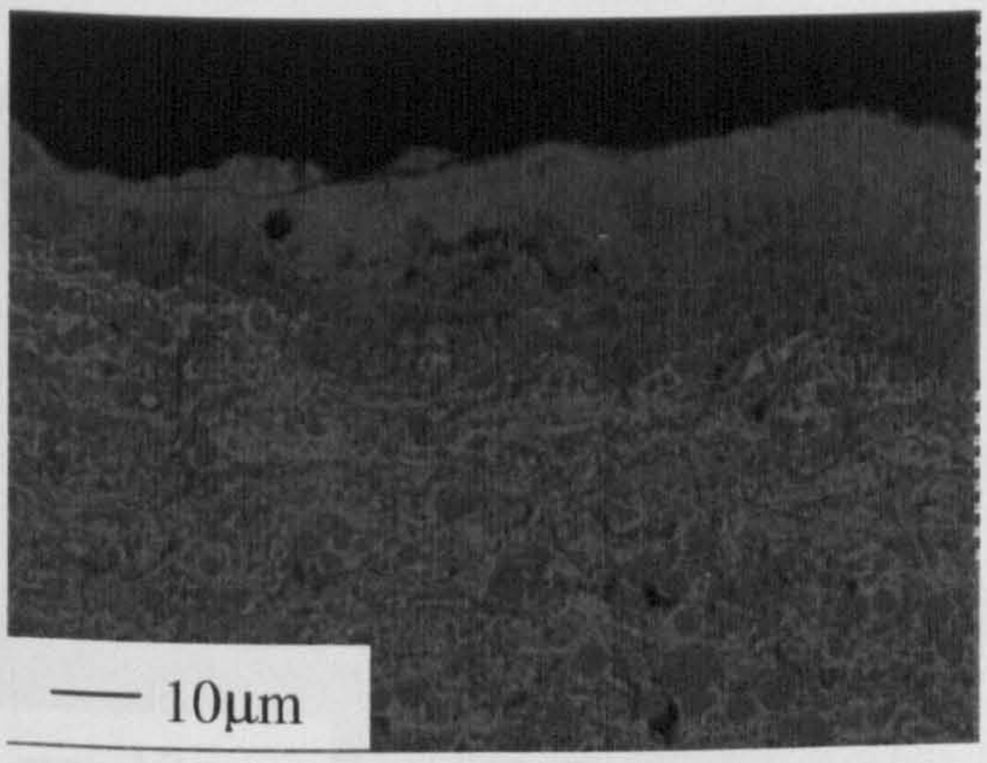

Figure 8.44: Oxidation of equimolar coating at 700°C

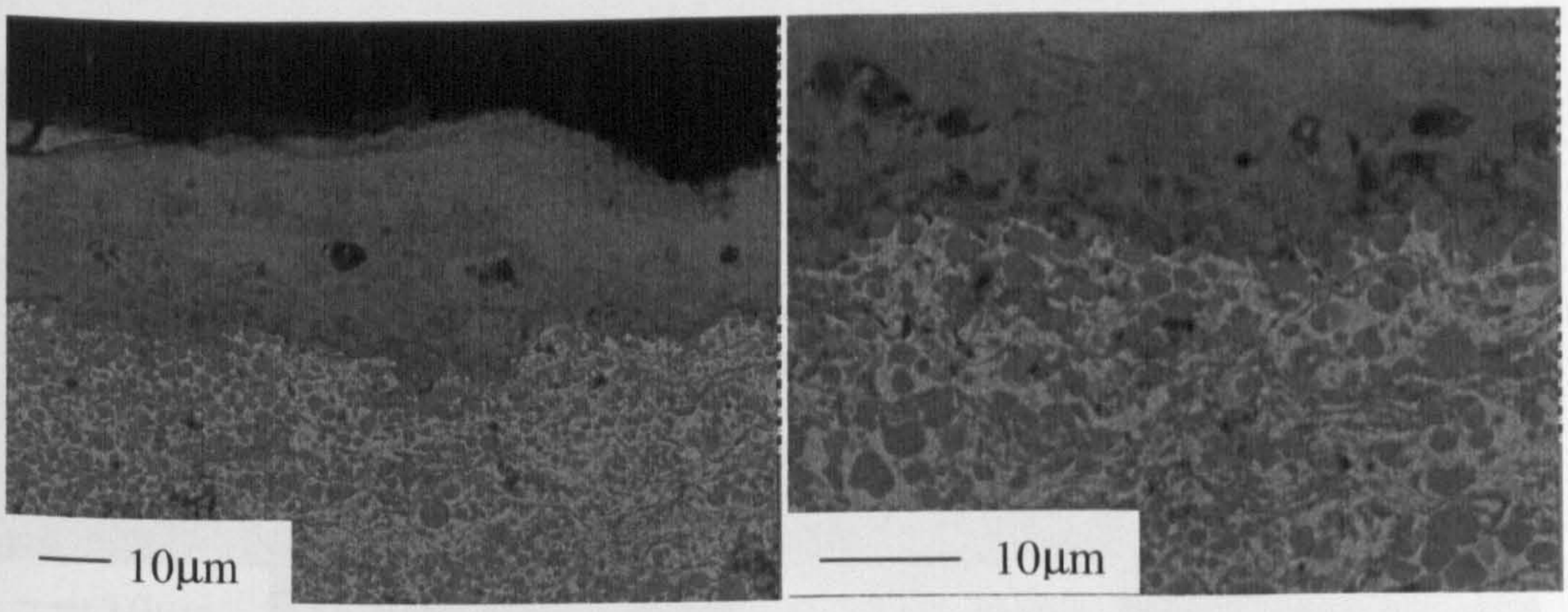

Figure 8.45: Oxidation of excess C coating at 700°C

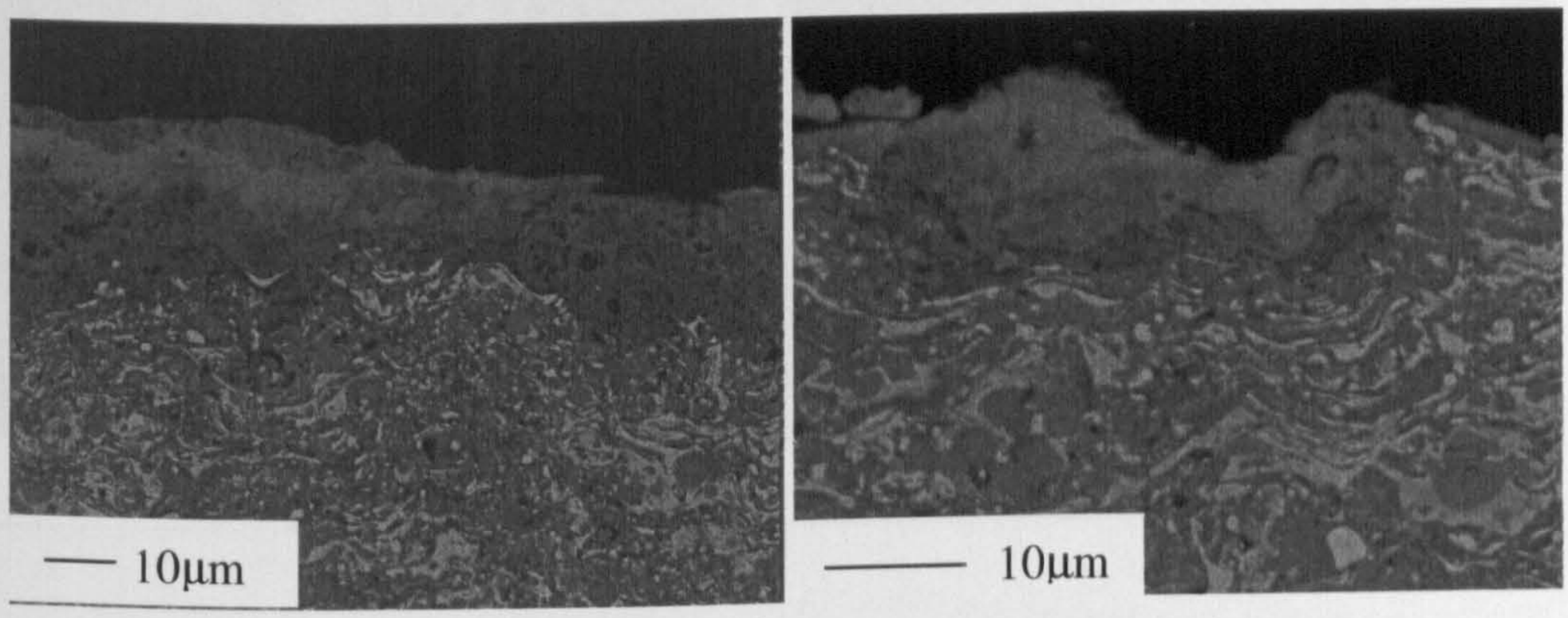

Figure 8.46: Oxidation of excess titanium coating at 700°C

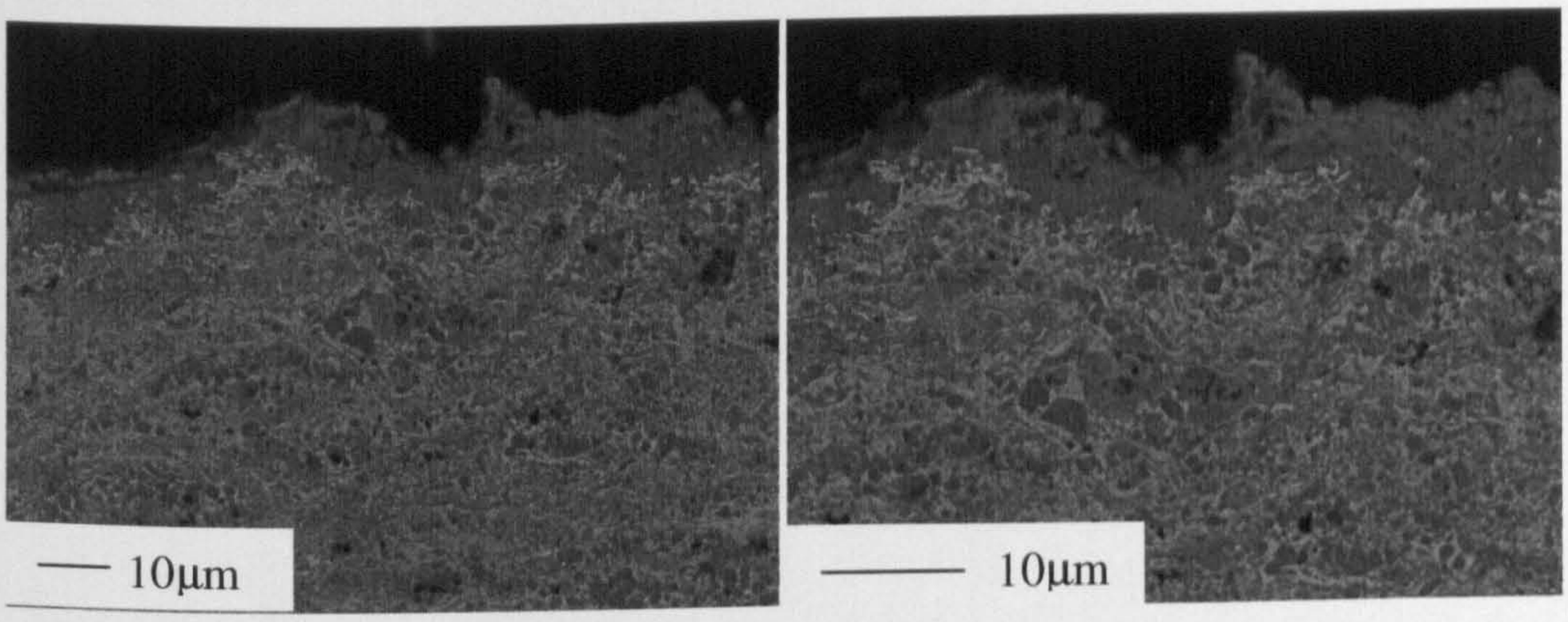

Figure 8.47: Oxidation of TiB_2-based coating at 700°C

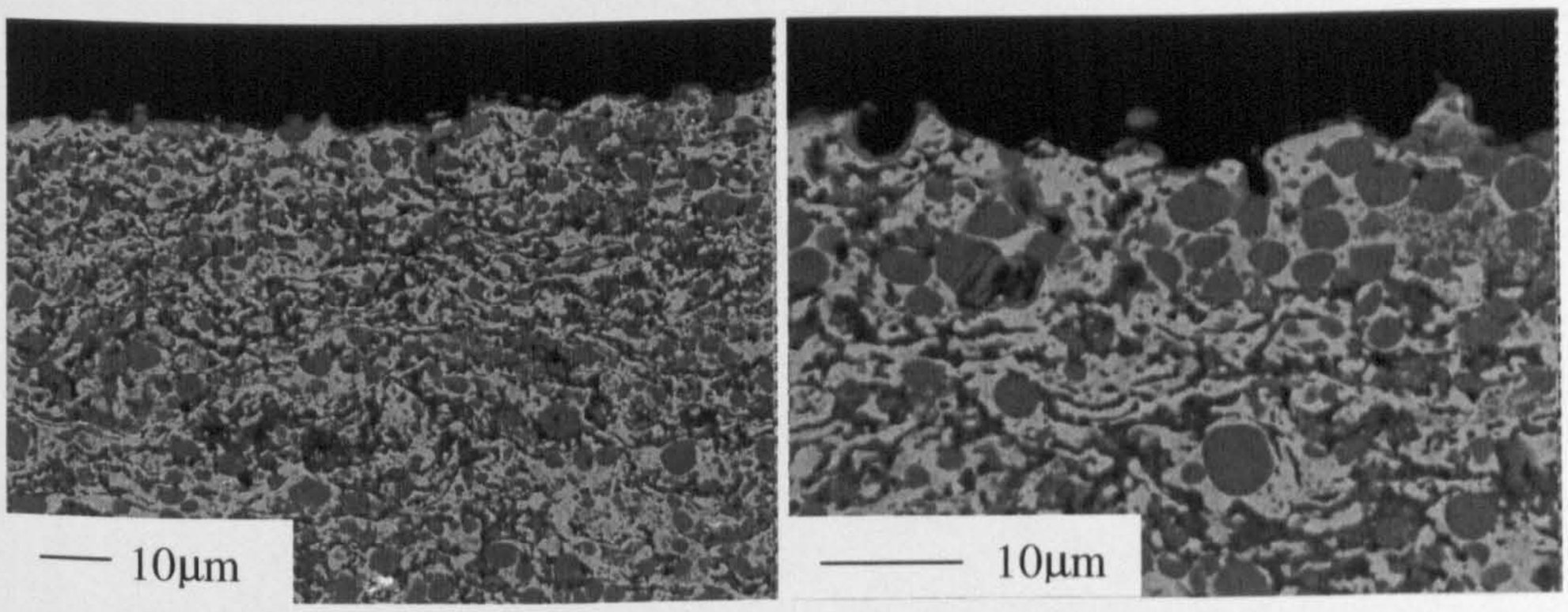

Figure 8.48: Oxidation of equimolar coating at 900°C

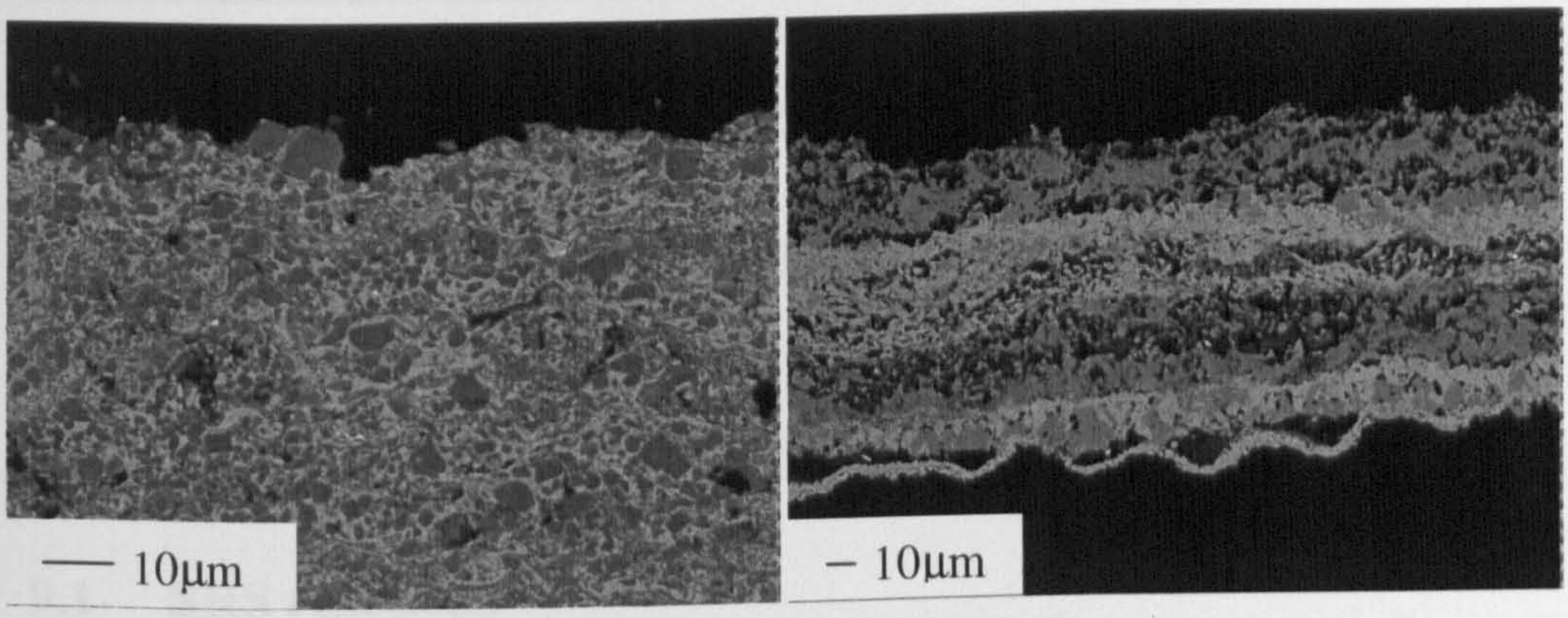

Figure 8.49: Oxidation of TiB_2-based coating at 900°C

9 Discussion

This chapter discusses the results obtained from the various experimental work performed.

9.1 SHS reactions

The cermet compacts were produced by a reaction called self-propagating high-temperature synthesis (SHS) (Chapter 2) where the reaction utilised the heats of combustion when Ti and C or B reacted. As previously mentioned in Chapter 7, the cermet powders were produced by reaction of pre-mixed elemental Fe, Cr, Ti, C or B. The initial elemental composition of the equimolar, excess C, excess Ti and TiB_2-based feedstock powders are shown in Tables 8.2 to 8.5 respectively. As mentioned in Chapter 7.2, elemental powders were added as to obtain a cermet with an FeCr matrix phase consisting of 30wt%. This matrix phase had an elemental distribution of 24wt% Fe, and 6wt% Cr in order to provide adequate oxidation resistance. The elemental powder composition of the TiB_2-based was done so in order to obtain stochiometric TiB_2 hard phase. The TiC-based compositions, however, contained differing amounts of titanium and carbon in order to evaluate the effect of the C:Ti ratio of TiC on the overall integrity of the powders and coatings produced. The three compositions of the TiC-based starting reactants were referred to as equimolar, excess C and excess Ti. It has been previously reported (Chapter 4.2.1) that TiC exists over a wide C:Ti ratio, $TiC_{0.47}$ to $TiC_{0.97}$ and its mechanical properties are highly dependent upon this ratio. Holleck [1986] states that the hardness of TiC increases with increasing carbon,

i.e. tending towards $TiC_{0.97}$, and Ramqvist [1965] reports that the bonding between TiC and Cu increases with a decrease in carbon, i.e. tending towards $TiC_{0.47}$. This is also reported in work performed by Eustathopoulos [1991] (Table 4.3). It is therefore evident that changing the C:Ti ratio of TiC can change its mechanical properties.

9.1.1 Equimolar

The equimolar composition was designed to produce a ceramic phase with $TiC_{0.96}$ which had the highest C:Ti ratio and thus the highest hardness. However, it was recognised that during SHS production or HVOF thermal spraying, carbon could be lost from the carbide phase by a number of mechanisms, such as its dissolution in the matrix or oxidation, resulting in a lower C:Ti ratio than expected.

9.1.2 Excess C

The excess C mix contained a C:Ti ratio of 2:1 and this high carbon content was designed to force the C:Ti ratio of the TiC to its highest level ($TiC_{0.96}$), inspite of any carbon loss. Despite the high carbon level, it would be incorrect to assume that martensite (of a similar composition to that of, e.g. 440-C) may have formed. In order for martensite to form, the steel must be quenched from the austenite phase. As well as iron and carbon, chromium and titanium are also present in the TiC-based material, and each will have an effect on the γ-loop and therefore austenite formation (Figures 4.3 to 4.5). As shown in Figure 4.3, chromium and titanium are ferrite stabilizers, i.e. they close the γ-loop. A 20% Cr addition

closes the γ-loop to a large extent, and even with the extra carbon additions, which open the γ-loop (Figures 4.4 to 4.5) it is not expected that martensite formation occurred in either the excess C feedstock powder or coating, due to the high Cr level. It is possible for 440-C steel to form a martensitic matrix as it is held in the austenitic regime until everything is fully austenitic and subsequently quenched. Therefore, another reason why martensite would never form in the excess C powders or coating is due to the extreme cooling rates present which do not allow the iron to be held in the austenitic regime for any period of time.

9.1.3 Excess Ti

The excess Ti mix contained a C:Ti ratio of 1:2 in an attempt to form a primary carbide with a lower C:Ti ratio, which, whilst it is less hard than $TiC_{0.96}$, may exhibit stronger bonding with the matrix phase and thus may produce superior wear properties.

9.1.4 TiB_2-based

As mentioned earlier in this section, the Ti and B proportions were added, in a B:Ti ratio of 2:1, in order to produce stoichiometric TiB_2.

9.1.5 Comparison of SHS reactions

The combustion temperatures achieved for each composition are shown in Table 8.1. The highest combustion temperature of 1996°C was achieved by the TiB_2-based cermet followed by the equimolar, excess C and finally the excess Ti

cermet. It was expected that the TiB_2-based cermet would have the highest combustion temperature as TiB_2 is reported by Cutler [1991] to have an adiabatic temperature of 3225°C when reacted via the SHS process. Titanium carbide is reported to have a combustion temperature of 2930°C [Holt,1991] and thus the combustion temperatures of the TiC-based cermets were lower than the TiB_2-based counterpart. All four cermets have a considerably lower combustion temperature than the actual ceramics, which is due to the presence of the FeCr binder phase (Chapter 2.4.2). After initiation, in order for the reaction to "self-propagate", melting of the Fe and Cr must occur which absorbs the heat produced and thus lowers the combustion temperatures of the reactions.

When comparing the combustion temperatures of the three TiC-based cermets it can be seen that the C:Ti ratio of the ceramic phase has a considerable effect on the combustion temperatures achieved. This can be rationalized in terms of the proportion of TiC formed. Table 9.1 shows the maximum proportions of TiC that can be formed for each composition assuming that only $TiC_{0.98}$ is formed. Whilst this assumption is not ideal, the heats of formation of TiC as a function of its stoichiometry are not known and the actual proportions of the TiC phase in the powders are unknown due to the variable stoichiometry of TiC. For the equimolar sample, as equal proportions of Ti and C are present, the maximum TiC content will be 81.2 at% and will have the highest combustion temperature. The excess C sample has 28.5 at% Ti and 55.6 at% C, therefore only a maximum of 57 at%TiC will be formed. For the excess Ti sample, 51.7 at% Ti and 26.6 at% C are present and will therefore form 53.2 at%TiC and will thus have the lowest

combustion temperature. It should also be made clear that not all of the titanium in the powders has formed TiC, as the XRD traces of the feedstock powders show amounts of intermetallic (Figures 8.4b to 8.7b) which will affect the C:Ti ratio of the TiC and hence the combustion temperatures. Also, for the excess Ti sample, it is unclear if any Ti_2C phase is present.

9.2 Feedstock powders

After SHS reaction, the cermet compacts were crushed, sieved and air-classified to obtain a powder size range of 15-45μm as this range is supplied by many HVOF powder suppliers (Praxair Surface Technologies) and other researchers have also used this range [Smith,1995]. Other reasons for selection of this particle size range are shown in Section 7.2.4.

9.2.1 Feedstock powder morphology and size

The powder morphologies of each composition are shown in Figure 8.1 and it can be seen they can be seen to be fairly angular, which is undesirable for thermal spraying (Chapter 3.4.2). Figure 8.2 shows the particle sizes of each composition and all show a similar distribution. The powder cross-sections are shown in Figure 8.3 and the three TiC-based powders all contain spherical-like TiC_x particles surrounded by a Fe-based matrix, whilst the TiB_2-based powder exhibits a hard phase with an angular morphology, this is because the TiB_2 particles undergo faceted growth, where the growth rate is highly dependent upon crystal orientation. The TiC particles have undergone non-faceted growth where the rate

of growth is less dependent upon crystal orientation, resulting in a spherical-like appearance. The equimolar powder exhibits the highest volume fraction of hard phase in the powders (Table 8.6) with 72%. When compared with the excess C, 69%, and excess Ti, 63%, this was expected as there are smaller amounts of reactants available to produce TiC in the excess C and excess Ti powders. The TiB_2 powder exhibits a volume fraction of hard phase of 64%.

9.2.2 XRD analysis

XRD analysis of the equimolar, excess C, excess Ti and TiB_2-based powder fines (after air classification) and feedstock powders are shown in Figures 8.4 to 8.7 respectively. The equimolar feedstock powders (Figure 8.4b) contain TiC, an iron-based phase, (to which EDX analysis indicates that Cr is mainly partitioned), a small quantity of FeTi intermetallic and Cr_7C_3. It is also believed that free C is present, but it is not evident in the XRD trace as it is amorphous. When compared with the powder fines (Figure 8.4a), it can be seen that no single phase is being lost preferentially. The excess C feedstock powders (Figure 8.5b) contain TiC, an iron-based phase and small amounts of FeTi intermetallic and Cr_7C_3. The excess C powder fines (Figure 8.5a) contain all of these phases and also, brittle Fe_3C. It is believed that free C is also present in this system but is not evident on the trace due to it being amorphous. The proportion of the TiC phase is higher in the fines than in the feedstock, which is not evident in the equimolar or excess Ti powders and suggests a preferential loss of TiC during crushing. The excess Ti feedstock powders (Figure 8.6b) contain TiC, Cr_2Ti, and two intermetallic phases,

predominantly Fe_2Ti intermetallic and some FeTi intermetallic, which have formed due to the excess Ti reacting with iron-based matrix. It is notable that there is no iron-based phase in these powders. The analysis of the powder fines contains all of the phases in the feedstock powder, apart from Cr_2Ti. There appears to be a switch in TiC peak intensities at 36° and 42° when compared with the equimolar and excess C powders, and may be an indication of the differing C:Ti ratio present within the TiC particles in the excess Ti powder. This is in conflict with Table 8.7 which suggests that the C:Ti ratios of the three TiC-based powders are very similar, but this issue is yet to be resolved. The TiB_2-based feedstock powder (Figure 8.7b) contains TiB_2, an iron-based matrix, FeB, Fe_2B, Cr_2Ti, and some FeTi intermetallic. These phases are also present in the powder fines (Figure 8.7a).

When comparing the phases present in the TiC-based feedstock powders with the liquidus projection ternary phase diagram of Fe-Ti-C (Figure 9.1); it is evident that some of the phases in the phase diagram are also present in the powders. Firstly, it must be noted that as this is a phase diagram of Fe-Ti-C, all phases are in equilibrium, so there will be differences in phases due to the fact that chromium is present in the powder and also that non-equilibrium cooling occurs when producing the powders. When the compositions of the three powders are superimposed on the phase diagram, it is evident that for equimolar and excess Ti coatings that TiC will precipitate out of solution first, along with free C for the excess C sample. The equimolar coating should follow the line to e_2, where

ferritic iron and TiC are formed, and are also present in the XRD traces of the powders (Figure 8.4a and b), although some deviation will occur as the C:Ti ratio is not 1:1. The excess C sample will follow the valley down to E_2 and produce austenitic iron, TiC and free C. XRD analysis (Figure 8.5a and b) indicates that TiC is evident in the powders, and it is also thought that free C is present, but is not visible in the trace, as it is amorphous. The austenitic iron was not present due to the high chromium levels, which encourages the formation of ferrite. The excess Ti sample will follow to the right of the centre line and will form Fe_2Ti and FeTi, which are both evident in the XRD traces of the powders (Figure 8.6a and b).

Two pseudobinary phase diagrams of Fe-Ti-B are shown in Figures 4.20 and 4.21. Figure 4.20 shows that TiB_2 will precipitate out of solution first, and form austenite, followed by ferrite. Again, the austenite will not form due to the high levels of chromium present. Figure 4.21 shows a phase diagram of the effects of impurities, such as C or O, when FeTi and FeB are reacted. It is evident that the final composition formed contains ferritic iron, TiB_2 and Fe_2B, which are all present in the powder.

9.2.3 C:Ti ratios of TiC-based powders

The C:Ti ratios of the three TiC-based powders are shown in Table 8.7 and it can be seen that although the excess C powder exhibits the highest ratio and the excess Ti ratio exhibits the lowest ratio, there appears to be little difference. The excess C sample exhibits only a C:Ti ratio of 0.711 instead of the desired, $TiC_{0.96}$.

The presence of Fe_3C in the powder fines and Cr_7C_3 in the feedstock powder, along with amorphous, free C in both powders, suggests that a proportion of carbon is not reacting to form TiC. The excess Ti sample was designed to obtain a C:Ti ratio nearing 0.47, again this was not realised and is thought to be due to the titanium forming Fe_2Ti and FeTi intermetallics and thus not fully contributing to the formation of TiC. Alternatively, the intensity of the TiC peaks in the excess Ti XRD traces, and the appearance of the fractured TiC particles in the powder cross-sections (Figure 8.3c) indicates that the TiC particles are different and that there may be a bigger difference in stoichiometry than is calculated in Table 8.7.

9.2.4 Chemical analysis of feedstock powders

Chemical analyses of the fines and feedstock powders of the four compositions are shown in Table 8.2 to 8.5.

9.2.4.1 Equimolar

Chemical analysis of the equimolar fines and feedstock powders (Table 8.2) indicate that there is a reduction in Ti and C contents from the reactant to the feedstock powders. This reduction is thought to be due to the loss of TiC from the matrix during grinding, which is then removed during air-classification and sieving. This reduction is validated by the higher Ti and C weight% in the powder fines when compared with the feedstock powders. It must also be noted from the XRD trace of the powder fines (Figure 8.4a), that the iron-based phase,

FeTi, Fe_3C and Cr_7C_3 are also being lost. It is also evident that the Fe and Cr weight%, from reactant to feedstock powders, increases due to the reduction in Ti and C. In the feedstock powder, the atom% of Ti and C are very similar, but according to Table 8.7, the C:Ti ratio of TiC is 0.710. This therefore suggests that a proportion of C may be forming Cr_7C_3, as Ti is also contributing to the formation of FeTi (Figure 8.4b). A small proportion of free C may also be in the system but is not evident in the XRD trace as it is amorphous.

9.2.4.2 Excess C

The chemical analyses of the excess C fines and feedstock powders are shown in Table 8.3. It can be seen that a significant loss of C has taken place from reactant to feedstock powders. The fact that the loss of Ti is not commensurate with the loss of C indicates that C is being lost independently from Ti. It is proposed that there is a proportion of free C in the SHS reacted compacts, some of which is lost during removal from the graphite reaction tube and during crushing into powder form. Although not easily identified in the chemical analysis, the XRD pattern of the powder fines (Figure 8.5a) indicates that Fe(Cr), TiC, FeTi, Fe_3C and Cr_7C_3 are also being lost. It is also evident that the Fe and Cr weight% from reactant to feedstock powders increase due to the reduction in Ti and C. In the feedstock powder, the Ti:C ratio is 1:1.27 which again suggests that C has been lost during removal of the cermet compact from the graphite tube, and also during crushing and air-classification. The calculated C:Ti ratio of the TiC in the feedstock powder is 0.711 (Table 8.7) and suggests that a proportion of the C must be in the

form of Cr_7C_3, as some of the Ti will also be contributing towards the formation of FeTi as shown in Figure 8.5b. It is also assumed that the feedstock powders contain a quantity of free C which is not evident in the XRD trace due to it being amorphous. The carbon will not be in solution with the iron due to the low solubility of C in the ferritic matrix.

9.2.4.3 Excess Ti

Table 8.4 shows the chemical analyses of the fines and feedstock powders. Again, the weight% of Ti and C is reduced from reactant to feedstock powders which is thought to be due to loss of TiC during grinding and air-classification. This is validated by the higher content of the Ti and C in the powder fines when compared with the feedstock powder. The XRD trace of the powder fines also shows that FeTi and Fe_2Ti are being removed (Figure 8.6a). The ratio in the reactant powders was 2:1, as expected, and is the same for the feedstock powder. As the C:Ti ratio of the TiC in the feedstock powder is 0.709 (Table 8.7), it is assumed that not all of the Ti is combined with C to form TiC and is shown to be forming FeTi, Fe_2Ti and Cr_2Ti in Figure 8.6b.

9.2.4.4 TiB_2-based

Table 8.5 shows chemical analysis of the fines and feedstock powders. The chemical analysis of the powder fines and feedstock powders shows that Ti is being lost preferentially to B, but the XRD trace of the powder fines (Figure 8.7a) shows that TiB_2, as well as Fe(Cr), FeB, Fe_2B, Cr_2Ti and FeTi are being lost.

Therefore, the reduction in the Ti level is thought to be due to some sort of preferential loss of TiB_2. Again, the weight% of Fe and Cr are increasing from reactants to feedstock as a result of the reduction in Ti and B. In order to form TiB_2, the atomic ratio of Ti and B must be 1:2, as shown in the chemical analysis of the reactant powders (Table 8.5). The ratio of Ti:B in the powder fines is 1:1.88 which shows that Ti must also be reacting to form other compounds, namely, FeTi and Cr_2Ti (Figure 8.7a). The ratio in the feedstock powders is 1:2.37, indicating that a proportion of the B may be forming FeB and Fe_2B. This theory is validated as the two phases mentioned were present in the XRD trace of the feedstock powder (Figure 8.7b). The boron may also be going into solution in the iron and forming an amorphous matrix, as is evident in the TEM images of this coating (Figures 8.25 to 8.27).

9.3 Coating characterisation and properties

9.3.1 Coating microstructure formation

Figure 8.12 shows SEM images of the four coatings. All four coatings exhibit a proportion of retained hard phase within the coatings, a lighter region, which is believed to be the iron-based matrix, and also stringer-like features, which EDX has indicated are oxides. For the three TiC-based coatings (Figure 8.12a-c), the TiC size range is between 1-5μm, and the TiB_2-based coating (Figure 8.12d) exhibits a TiB_2 size range from sub-micron to 6μm (Table 8.6). Whilst the hard phase size ranges appear not to have changed, the volume fractions of the hard phase in the coatings, when compared with the feedstock powders, have changed

significantly. Table 8.6 shows that the TiC volume fraction in the equimolar coating has reduced by a factor of two, whilst the volume fractions of TiC in the excess C and excess Ti coatings have dropped by a greater proportion. The TiB_2-based coating has a much lower reduction, approximately 18% of the proportion in the feedstock powder. Whilst it can be concluded that these reductions may be partly due to the hard phase bouncing off the substrate during spraying, another mechanism is also proposed by Stewart [1999] who reports that ceramic phases, such as WC can dissolve in molten metal during spraying. It is therefore proposed that both TiC and TiB_2 have undergone dissolution into the liquid phase during spraying. The TiB_2-based coating appears to have a bi-modal distribution of hard phase, indicating that some TiB_2 dissolved into the liquid melt during spraying, but re-precipitated upon cooling, which accounts for the smaller reduction in hard phase. The TiC-based coatings have a much lower volume fraction in the coatings when compared with the TiB_2-based coating, which indicates that dissolution of the TiC occurred with little subsequent re-precipitation on cooling. This is validated by the fact that the TiC-based coatings do not exhibit this bi-modal distribution to the same extent. The re-precipitation of TiB_2 from solution may be driven by its large free energy of formation (-319 kJ mol^{-1}). The fact that Ti and C remain in solution in the binder phase may result from its comparatively lower free energy of formation (-181kJ mol^{-1}) (Table 4.9). Another result of the dissolution of the hard phase during spraying is the proportion of oxide in the coatings. When TiC or TiB_2 dissolve into the matrix, a liquid phase with a high proportion of Ti and metalloid results. The high level of

reactive titanium in the molten metal may be responsible for the levels of oxide in the coatings as Ti in solution will oxidise far faster than TiC or TiB_2. Comparison of levels of hard phase (Table 8.6), with the oxygen levels found in the coatings (Tables 8.2 to 8.4) demonstrates that the highest reduction of hard phase (excess Ti coating) is accompanied by the highest level of oxide present in the coating (Table 8.4). The equimolar coating has a higher reduction of hard phase than the TiB_2-based coating and subsequently has a higher oxide level (Tables 8.2 and 8.5, respectively). The second highest reduction in hard phase (excess C) however, is accompanied by the lowest oxide level, which indicates that it is not only hard phase dissolution that contributes to the oxides in the coatings and is discussed further in section 9.3.5.

9.3.2 XRD analysis

The XRD traces of the four coatings are shown in Figures 8.4c-8.7c. The equimolar and excess C traces (Figures 8.4c and 8.5c) both show that the coatings consist of TiC, Fe(Cr), FeTi, $FeTiO_3$, Ti_2O_3, Cr_2Ti and Cr_7C_3. Some free C may also be present in the excess C coating, but is not evident in the trace as it is amorphous. The excess Ti coating does not contain Cr_7C_3, as in the equimolar and excess C coatings, but contains an Fe_2Ti intermetallic. The excess Ti feedstock powder does not contain Fe, as the extra titanium in the system forms Fe_2Ti and FeTi. During spraying, it is proposed that a proportion of the titanium from the intermetallic phases is oxidizing to form $FeTiO_3$ or Ti_2O_3, leaving Fe to form in the coating. The TiB_2-based coating (Figure 8.7c) contains the same

phases as the feedstock powder, along with two additional oxide phases, $FeTiO_3$ and Ti_2O_3, thought to be predominantly the product of titanium oxidation due to TiB_2 dissolution in the matrix.

9.3.3 TEM characterisation of coatings

TEM pictures from the four coatings are shown in Figures 8.13 to 8.27. Some of the phases present in the XRDs traces of the coatings have been found by TEM analysis.

9.3.3.1 Equimolar

Figures 8.13 to 8.15 show TEM pictures of the equimolar coating and it can be seen from Figure 8.13a that the TiC particles are dispersed throughout the matrix phase. The diffraction pattern of the hard phase (Figure 8.13d) confirms that it is titanium carbide. Figure 8.14b illustrates the form of matrix within the coating, which TEM-EDX (Figure 8.14c) indicates is FeCr-rich with a small quantity of Ti. Figure 8.15b shows a higher magnification image of the matrix, which again EDX (Figure 8.15d) indicates is FeCr-rich, with a small quantity of Ti, which is thought to be in solution in the iron, as up to 10 atom% titanium can go into solution according to the Fe-Ti phase diagram (Figure 4.16). It must be noted that the Cu content in the EDX is from the sample holder. It is also evident that the matrix has a granular appearance, and the diffraction pattern (Figure 8.15a) exhibits two ring patterns which have d-spacings of 2.155Å and 1.868Å, but do not match Fe or FeCr PDF files. The diffraction angles have also been calculated

from the d-spacings and matched to the XRD trace and were found to be masked by other peaks. It is proposed that the FeCr phase in the coating has a tetragonal unit cell, as PDF cards show that many FeCr phases exhibit this unit cell type and also exhibit a variety of d-spacings depending on the other alloying elements present. The FeCr phase present in the coating exhibits a d-spacing that has not previously been reported for FeCr phases.

9.3.3.2 Excess C

TEM analysis of the excess C coating is shown in Figures 8.16 to 8.20. Figures 8.16a, 8.16c and 8.18c show the spherical-like carbides in the coating, which were also evident in the SEM images (Figure 8.12). Figures 8.16b and 8.17b show TiC particles exhibiting dislocation networks, which are assumed to be a result of the impact with the substrate during spraying. EDX of the matrix phase (Figure 8.17c) again shows that it is FeCr-rich with a small quantity of Ti. It must be noted that, in this case, there is uncertainty as to whether the Ti is a contribution from the TiC particles and not from the matrix. Figure 8.18c and d show higher magnification bright-field (BF) and dark-field (DF) images of a TiC particle surrounded by the granular matrix, which is very similar to the matrix found in the equimolar coating (Figure 8.15). High magnification images of the granular matrix are also shown in Figure 8.19, and it is again evident from the EDX (Figure 8.19e) that the matrix is FeCr-rich with a small quantity of Ti. The grains in Figure 8.19d appear to be exhibiting a lamellar-type effect in the grains at the same orientation and it is not yet known why these are present. The two

diffraction patterns from the matrix were taken from two zone axes (Figures 8.19a and b), hence their different spot patterns. The streaking in Figure 8.19a is thought to be a result of the lamellar effect in the grains and is perpendicular to the lamellar structure found in the grains. Extinction contours are also visible in Figure 8.19c indicating that each cell is in a similar orientation as the next and suggests that it is not a random polycrystalline material. Indexing of the two diffraction patterns has proved to be very difficult. Diffraction pattern a, has d-spacings of 3.5085Å, 2.5369Å and 2.0577Å (Figure 8.19f), whilst diffraction pattern b, has d-spacings of 6.0857Å, 3.6506Å and 3.6383Å (Figure 8.19g). It is clear that the granular matrix is FeCr-based, but has not matched any Fe or FeCr-based phase fully. It was originally thought that the Cr may be expanding the iron unit cell, thus increasing the d-spacing, but after comparison with the d-spacing attained from 434L stainless steel (16-18% Cr), it is unlikely that 20% Cr would increase the d-spacings to the extent found in diffraction pattern, b. Again, it is proposed that the FeCr phase in the coating has a tetragonal unit cell of unknown dimensions. The diffraction angles were again calculated from the d-spacings and matched to the XRD trace and were found to be masked by other peaks or existed out of the range of the trace. Figure 8.20 shows high magnification BF and DF images of the granular phase and whilst it is not absolutely clear what material exists between the grains, it is evident that a phase is present. Diffraction patterns of the intergranular regions were taken but have proved to be not indexable at present.

9.3.3.3 Excess Ti

Figures 8.21 to 8.24 show TEM images of the excess Ti coating. Figure 8.21 shows TiC particles in the matrix. The excess Ti coating had the highest level of oxide (Table 8.4), and the oxides present are shown in Figure 8.22, which EDX (Figure 8.22c) indicates is titanium, iron and oxygen-rich, along with some chromium. The diffraction pattern (Figure 8.22a) shows spotted rings, with spots at a range of different radii within each ring, and this indicates that a number of phases are present in the material. The indexed patterns reveal that a mixture of Fe_2Ti and $FeTiO_3/Ti_2O_3$ phases are present in the coating. More evidence that FeTi and Fe_2Ti are present in the coating is shown in Figure 8.23. The EDX analysis (Figure 8.23c) indicates that the material is predominantly Ti and Fe-rich and the diffraction pattern indicates that FeTi and Fe_2Ti are present. Figure 8.24c shows a TEM image that exhibits dark, spherical regions. EDX analysis (Figures 8.24a and d) indicates that these regions are predominantly iron-rich and are surrounded by regions that are titanium and oxygen-rich, which the indexed diffraction pattern indicates is Ti_2O_3 and $FeTiO_3$ (Figure 8.24e). It is proposed that, during spraying, the Fe_2Ti and/or FeTi phases have melted and undergone oxidation, where a proportion of the titanium and iron have formed Ti_2O_3 or $FeTiO_3$, and the remaining Fe has precipitated to form spherical, iron-rich phases, on cooling. The re-appearance of the iron-phase is validated by its presence in the XRD trace of the coating (Figure 8.6c).

9.3.3.4 TiB_2-based

Figures 8.25 to 8.27 show TEM images of the TiB_2-based coating. A low magnification image of the coating is shown in Figure 8.25, where TiB_2 particles, matrix phase and oxide are present. A higher magnification image of angular TiB_2 particles in the matrix is shown in Figure 8.26. Figure 8.27d shows a region of the coating that contains amorphous matrix and oxide. EDX indicates that the matrix phases are predominantly iron and chromium-rich, with a quantity of titanium that is probably from the lighter, titanium-rich phase. The matrix is thought to be amorphous as the diffraction patterns exhibit diffuse rings. This amorphous phase is thought to result from the presence of boron as it is a well-known amorphous phase promoter. The diffraction pattern of the titanium-rich phase (Figure 8.27g) indicates that it is a mixture of Ti_2O_3 and $FeTiO_3$.

9.3.4 Coating properties

Table 8.8 shows the thickness, hardness and roughness of the four, sprayed coatings. The TiB_2-based coating has the highest hardest, with the lowest hardness attributed to the excess Ti coating. The equimolar and excess C coatings have similar hardness's and is another indication that martensite has not formed in the excess C coating. It was aimed to have a coating thickness of around 100μm and Table 8.8 shows that this has been achieved. The roughness of the coatings show that there is a difference between the TiC-based and TiB_2-based coatings. The TiB_2-based coating exhibits a greater roughness and may be attributed to a larger amount of unmelted particles in the coating. These unmelted particles are

assumed to be in the form of the hard phase and it is evident that more dissolution of the hard phase has occurred in the TiC-based coatings (Table 8.6). The reduction in the degree of melting may be due to the lower solubility of TiB_2 in the molten matrix (Section 9.3.1).

9.3.5 Chemical analysis

The chemical analyses of the four coatings are shown in Tables 8.2 to 8.5 respectively.

9.3.5.1 Equimolar

Chemical analysis of the equimolar coating (Table 8.2) indicates that there is a reduction in Ti and C contents from the reactant powders to the coating. It is also evident that the Fe and Cr weight% of the coating has increased due to the reduction in Ti and C. The loss of Ti and C from the feedstock powder to coating is a result of the spraying process. It is assumed that Ti and C are being lost in the form of TiC particles, as it cannot be lost from the coating in any other form, e.g. formation of oxides would not remove the titanium. The TiC particles are thought to be bouncing off the substrate, upon impact. Oxidation of the C into CO may also be occurring due to the levels of oxygen in the flame. The increase in the oxygen content is due to the oxidation of TiC and FeTi, as solids or solution, during the spraying process, resulting in the formation of Ti_2O_3 and $FeTiO_3$. In the coating, the atom% of C is lower than the Ti. The C:Ti ratio of TiC in the coating is 0.711, and as titanium is also contributing towards the formation of

FeTi, Cr_2Ti, $FeTiO_3$ and Ti_2O_3 phases, C may also be forming Cr_7C_3 (Figure 8.4c). A schematic diagram showing the various phases formed and mechanisms during powder and coating production is shown in Figure 9.2.

9.3.5.2 Excess C

The chemical analysis of the excess C coating is shown in Table 8.3. In the coating, a reduction in both Ti and C is witnessed, which is assumed to be in the form of TiC. This reduction is thought to be due to TiC particles bouncing off the substrate during spraying. It is also evident that the Fe and Cr weight% of the coating has increased due to the reduction in Ti and C. The Ti and C atomic ratio decreases from reactant powders to coating. In the coating, the Ti:C atomic ratio is 1:1.12 (c.f. 1:1.27 in feedstock powder) which shows that C is being lost, this time, due to oxidation during the spraying process, subsequently forming carbon monoxide. The C:Ti ratio of the TiC in the coating is 0.717 and suggests that some of the C is forming Cr_7C_3 as a proportion of the Ti will be in the form of FeTi, Cr_2Ti, $FeTiO_3$ and Ti_2O_3. The excess C coating has the lowest oxygen content of the four coatings and is thought to be due to oxidation of the extra C within the feedstock powders during spraying, thus protecting the other elements in the melt from oxidation. A schematic diagram showing the various phases formed and mechanisms during powder and coating production is shown in Figure 9.3.

9.3.5.3 Excess Ti

Table 8.4 shows the chemical analysis of the excess Ti coating. The loss of Ti and C from the feedstock powder to the coating is due to the spraying process. The majority of the Ti and C is being lost in the form of TiC which is thought to be rebounding off the substrate, and oxidation of the C, forming CO, may also be occurring. The loss of Ti and C from reactant powders to the coating is the reason for the increase in the weight% of the Fe and Cr. The Ti and C ratio increases from reactant powders to the coating. After spraying, the ratio of Ti to C is 2.26:1 (c.f. 2:1 in feedstock powder). As the calculated C:Ti ratio is 0.62 (Table 8.7), the remaining excess Ti must be reacting to form other phases such as FeTi, Fe_2Ti, Cr_2Ti, $FeTiO_3$ and Ti_2O_3, as shown in Figure 8.6c. A schematic diagram showing the various phases formed and mechanisms during powder and coating production is shown in Figure 9.4.

9.3.5.4 TiB_2-based

The chemical analysis of the TiB_2-based coating is shown in Table 8.5. As with the TiC-based powders and coatings, there is a gradual decrease in Ti and B from reactant powders to the coating. The coating chemical analysis exhibits a reduction of Ti and B, when compared with the feedstock powder, and is thought to be a result of the spraying process, where the TiB_2 particles were rebounding off the substrate. Oxidation of B may also be occurring, in the form of B_2O_3, which may then vapourise during spraying as its boiling point is 1860°C [Kaye,1972]. Again, the weight% of Fe and Cr are increasing from reactants to

the coating as a result of the reduction in Ti and B. In the coating, the ratio is 1:1.86 which suggests that Ti is contributing to the formation of FeTi, Cr_2Ti, $FeTiO_3$ and Ti_2O_3 during spraying, as shown in Figure 8.7c. A schematic diagram showing the various phases formed and mechanisms during powder and coating production is shown in Figure 9.5.

9.4 Abrasive wear of coatings

Figure 8.28 shows the wear coefficients of the coatings, in terms of mass loss, when subjected to abrasion with alumina and silica. When comparing wear loss of coatings with differing phases, it is more appropriate to compare volume losses as this accounts for the varying densities of the phases. Figure 8.29 shows the volumetric wear coefficients of the coatings for abrasion with both alumina and silica.

9.4.1 Abrasion of TiC and TiB_2-based coatings by alumina

For the TiC-based coatings, when subjected to hard, alumina abradent, the equimolar coating exhibited the lowest volumetric wear coefficient. The hardnesses of the equimolar and excess C samples are approximately the same (Table 8.8), and thus the differences in wear resistance cannot be attributed to this. Comparison of the Figure 8.38a and b again do not show a change in mechanism of wear. The higher wear coefficient of the excess C sample may be associated with the stoichiometry of the titanium carbide ($TiC_{0.717}$) and the effect that this has on the hardness and bonding of the carbide with the binder phase. It

is more likely to be due to the lower volume fraction of hard phase, when compared with the equimolar coating (32vol% c.f. 36vol%). The proportion of oxide in the coatings appear to have little effect on their abrasive properties, as the weight% of oxide in the excess C coating is half of that in the equimolar coating. The highest volumetric wear coefficient is observed for the excess Ti coating. This is the softest coating and exhibits a high wear coefficient, which may be due to the high volume fraction of brittle oxide phase and the low volume fraction of primary carbide. Although, no clear change in the wear mechanism can be seen when comparing Fig. 8.38c with Fig. 8.38a and b, Figure 8.32 shows that there is considerably more ploughing on the coating surface when compared with Figures 8.30 and 8.31, where the material at the edges of the grooves appear to be fracturing.

When subjecting the TiB_2-based coating to the alumina abradent, the coating showed signs of ploughing and delamination (Figure 8.33). When compared with the equimolar coating it can be seen that there appears to be more delamination in the TiB_2-based coating. This is thought to be due to the harder TiB_2 particles in the coating offering more resistance to the cutting action of the alumina abrasive. The TiB_2-based coating exhibits superior abrasive wear properties than the TiC-based coatings (Figure 8.29) and is thought to be due to a number of factors. Firstly, TiB_2 is harder than TiC (3650 kgf mm^{-2} [Cutler, 1995], compared with 3200 kgf mm^{-2} [Holleck, 1986]) and may therefore have an intrinsically superior resistance to abrasion. Secondly, there is a larger volume fraction of hard phase

present in the TiB_2-base coating than the TiC-based coatings (Table 8.6). Thirdly, the boride based cermet also exhibits, what appears to be, a bi-modal distribution of hard phase; this has previously been reported to be favourable for the resistance of TiC-based cermet coatings to sliding wear due to the larger carbides resisting penetration and acting as a bearing surface, and the smaller carbides strengthening the matrix [Smith, 1995]. This may also be the case in the FeCr-TiB_2 cermet system under the abrasive conditions reported here.

9.4.2 Abrasion of TiC and TiB_2-based coatings by silica

The cross-sectional images of the coatings subjected to silica (Figure 8.39) are rougher than those subjected to alumina and is due to the abrasive nature of the alumina and silica. Previous work [Stewart, 1999] has shown that whilst angular alumina indents and cuts coatings, wear by rounded silica causes subsurface propagation of cracks and pull out of carbides. For the TiC-based coatings subjected to silica, the order of wear resistance is different than with alumina (Figure 8.29). The excess C coating exhibits the highest wear coefficient and Figure 8.39b shows that the surface is extensively cracked with evidence of carbide pullout and matrix loss. The equimolar coating shows the least damage in cross-section (Figure 8.39a) although it is the excess Ti coating that exhibits the highest wear resistance. Some surface cracking is observed on the surface of this sample (Figure 8.39c) but good carbide retention, which is not evident in the equimolar and excess C coatings, is observed at the surface which may be due to the low C:Ti ($TiC_{0.62}$) ratio expected in these coatings. The presence of the large

amount of oxide has not proven to be as deleterious to its wear resistance as it was when alumina abradent was employed.

The TiB_2-based coating exhibits the lowest volumetric wear coefficient when compared with the TiC-based coatings (Figure 8.29). The coating also shows signs of pitting and delamination when subjected to abrasion with silica (Figure 8.37). Figure 8.39d shows that the TiB_2-based coating has 2-5μm sized diboride particles at the surface that appear to be well bonded to the matrix; indeed the borides appear to be chipping at their edges resulting in a relatively rough surface with micropits between the diboride particles at the surface. One larger pit can be seen to the left of Figure 8.39d which may have resulted from the loss of a cluster of poorly bonded borides or from a pore in the original coating. These larger pits are those visible on the plan view (Figure 8.37). The wear surface is rougher than that of the TiC-based coatings (Figure 8.39) and it is thought that the silica observed on the top surface wear image (Figure 8.37) may be adhering to the surface by being keyed into the microcavities between the diborides. The silica deposits are not evident in the cross section and may indicate that the silica layer is thin. As such, silica deposition is not expected to affect the mass loss measurements from which the wear rates were calculated.

9.4.3 Abrasion of coatings from commercially available powders

Figure 8.29 also shows the volumetric wear coefficients of cermet coatings produced from commercially available powders, namely, sintered and crushed WC-17%Co and two types of 25%NiCr-Cr_3C_2, sintered and crushed, and blended.

9.4.3.1 Abrasion by alumina

In terms of abrasion with alumina, it is evident that the WC-Co coating has the lowest volumetric wear coefficient, followed by the sintered and crushed NiCr-Cr_3C_2 and then the TiB_2-based coatings. The equimolar coating has a superior coefficient to the blended NiCr-Cr_3C_2. The excess Ti coating has the highest volumetric wear coefficient which is rationalised in terms of the high oxide content and low volume fraction of carbide. The second highest is the blended NiCr-Cr_3C_2 and is thought to be due to the fact that there is no intimate mixing of the hard phase and matrix phase before spraying which can result in the powders traveling independently of one another and producing poor adhesion between matrix and hard phase (Section 2.8.1). Poor coating microstructure, hardness, deposition efficiency and wear abrasion can also result [Wirojanupatump, 1999].

9.4.3.2 Abrasion by silica

When considering abrasion by silica, it is evident that the WC-Co coating exhibits the lowest wear coefficient, followed by the TiB_2-based coating, and sintered and crushed NiCr-Cr_3C_2. Whilst not as good as sintered and crushed WC-Co, it is evident that a TiB_2-based coating produced from SHS powders has superior wear

properties when compared with coatings produced from sintered and crushed NiCr-Cr_3C_2 powders. The coating with the highest wear coefficient is blended NiCr-Cr_3C_2 which is a result of the afore-mentioned reasons.

The above abrasion tests were all performed at room temperature, as high-temperature wear facilities were not available in the department. It is important to note, however, that Figures 4.9 and 4.12 show the high temperature capabilities of TiC and TiB_2, in terms of hardness. The figures show that the TiB_2 ceramic phase retains a higher hardness at high temperatures and thus may exhibit a superior wear resistance.

9.5 Oxidation of coatings

Figures 8.40 to 8.49 show the coating microstructures when subjected to temperatures of 500, 700 and 900°C, and Table 8.10 gives the weight gain per unit area for each coating. When tested at 500°C hardly any oxide is evident on the surface of the coatings and XRD analysis indicates that, for the TiC-based coatings, a small amount of TiO_2 (Rutile), Fe_2O_3 (Hematite) and Cr_2O_3 (Eskolaite) were present. This suggests that both the Fe-Cr matrix and TiC were being oxidised. The TiB_2-based coating also exhibited these phases as well as B_2O_3.

At 700°C, all four coatings show signs of oxide build-up at the surface. The hematite in equimolar and excess C coatings appears to have undergone further reaction to form $Fe_2Ti_3O_9$ (Pseudorutile). This phase is also evident in the excess

Ti coating, but some hematite remains. The TiB_2-based coating, exhibits the same oxides as the equimolar and excess C coatings but with B_2O_3 also present.

The microstructures of the coatings are shown in Figure 8.40 to 8.49 and for all coatings subjected to temperatures of 500°C and 700°C, no subsequent change in microstructure is evident. Figures 8.48 and 8.49 show the microstructures of the equimolar and TiB_2-based coatings subjected to 900°C, respectively. Whilst there is no change in the appearance of the TiB_2-based coating, the equimolar coating shows some signs of microstructure change in the form of black stringer-like features. XRD analysis of the coatings indicates new phases at 30.5° and 35.5° which correspond to iron oxide ($Fe_{21.34}O_{32}$) and maghemite titanian ($Fe_{0.23}(Fe_{1.95}Ti_{0.42})O_4$). The corresponding PDF numbers for these oxides are 80-2186 and 84-1595 respectively.

The weight gains of the coatings are shown in Table 8.10 and it is evident that the excess Ti coating exhibits the best oxidation resistance. This may be due to the fact that a larger proportion of oxide was already present, after HVOF spraying, and may have formed an impermeable surface layer. The TiB_2-based coating exhibits the second best oxidation resistance and this can be attributed to the fact that TiB_2 has a superior oxidation resistance to TiC [Macdonald,1959]. The equimolar and excess C coatings are reasonably similar as they contain a very similar microstructure. The theories put forward are very preliminary and a more detailed series of experiments and examination of the coatings are required.

	At% Ti	At% C	At% TiC
Equimolar	40.6	40.6	81.2
Excess C	28.5	55.6	57.0
Excess Ti	51.7	26.6	53.2

Table 9.1: Maximum proportions of TiC formation

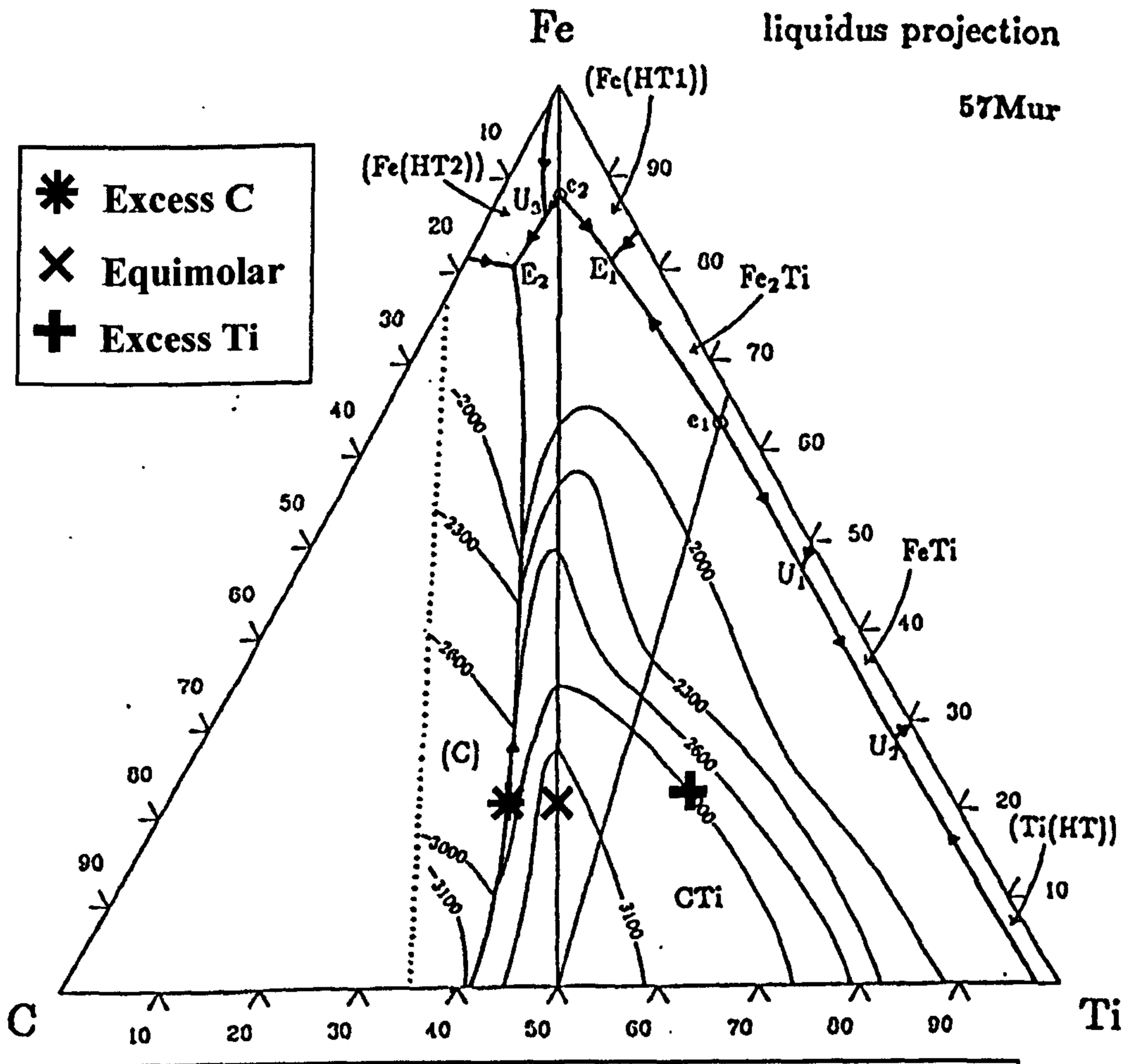

Reaction Scheme

e_1 :	$l \leftrightarrow TiC + Fe_2Ti$	1520°C
e_2 :	$l \leftrightarrow TiC + (Fe(HT1))$	~1350°C
E_1 :	$L \leftrightarrow TiC + (Fe(HT1)) + Fe_2Ti$	1340°C
E_2 :	$L \leftrightarrow (C) + TiC + (Fe(HT2))$	~1130°C
U_1 :	$L + Fe_2Ti \leftrightarrow TiC + FeTi$	1300°C
U_2 :	$L + TiC \leftrightarrow FeTi + (Ti(HT))$	1100°C
U_3 :	$L + (Fe(HT1)) \leftrightarrow TiC + (Fe(HT2))$	1320°C

*NB - (Fe(HT1)) is bcc
- (Fe(HT2)) is fcc

Figure 9.1: Fe-Ti-C ternary phase diagram [Murakami,1957]

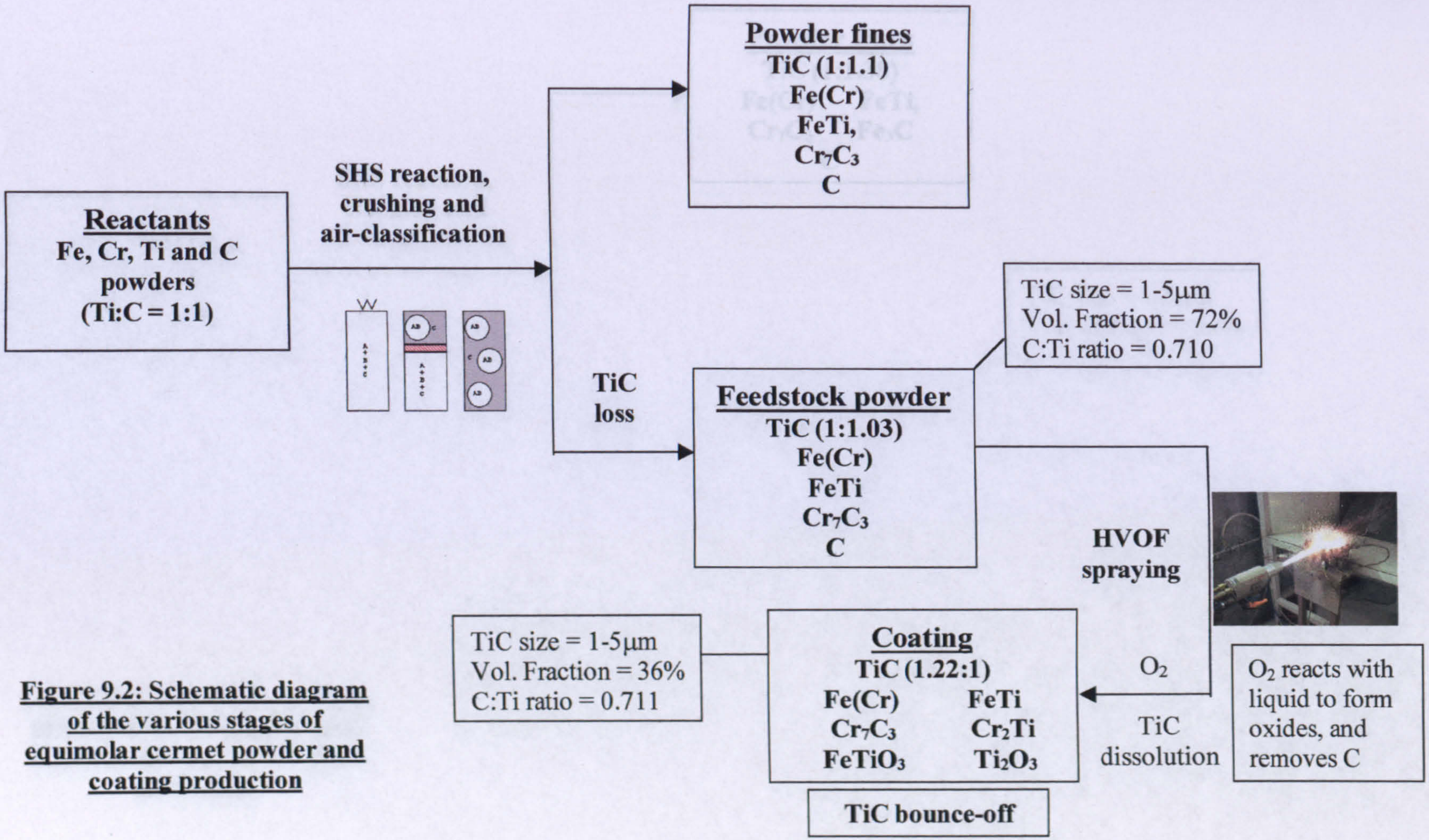

Figure 9.2: Schematic diagram of the various stages of equimolar cermet powder and coating production

Reactants
Fe, Cr, Ti and C powders
(Ti:C = 1:2)

SHS reaction, crushing and air-classification

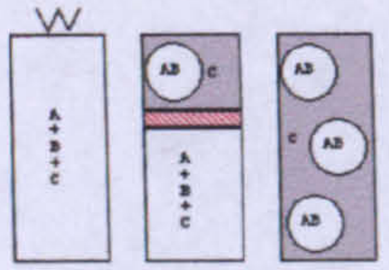

Powder fines
TiC (1:1.38)
Fe(Cr) FeTi,
Cr_7C_3 Fe_3C
C

TiC loss

TiC size = 1-5μm
Vol. Fraction = 69%
C:Ti ratio = 0.711

Feedstock powder
TiC (1:1.27)
Fe(Cr)
FeTi
Cr_7C_3
C

HVOF spraying

O_2

O_2 reacts with liquid to form oxides, and removes C

TiC dissolution

Coating
TiC (1:1.12)
Fe(Cr) FeTi
Cr_7C_3 Cr_2Ti
$FeTiO_3$ Ti_2O_3

TiC size = 1-5μm
Vol. Fraction = 32%
C:Ti ratio = 0.717

TiC bounce-off

Figure 9.3: Schematic diagram of the various stages of excess C cermet powder and coating production

Reactants
Fe, Cr, Ti and C powders
(Ti:C = 2:1)

SHS reaction, crushing and air-classification

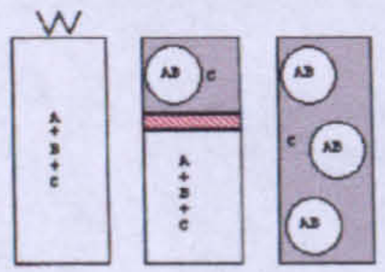

Powder fines
TiC (1.61:1)
Fe_2Ti
FeTi

TiC size = 1-5μm
Vol. Fraction = 63%
C:Ti ratio = 0.709

TiC loss

Feedstock powder
TiC (2:1)
Fe_2Ti
FeTi
Cr_2Ti

HVOF spraying

O_2

TiC dissolution

O_2 reacts with liquid to form oxides, and removes C

Coating
TiC (2.26:1)
Fe FeTi
Fe_2Ti Cr_2Ti
$FeTiO_3$ Ti_2O_3

TiC size = 1-5μm
Vol. Fraction = 26%
C:Ti ratio = 0.62

TiC bounce-off

Figure 9.4: Schematic diagram of the various stages of excess Ti cermet powder and coating production

Reactants
Fe, Cr, Ti and B powders (Ti:B = 1:2)

SHS reaction, crushing and air-classification

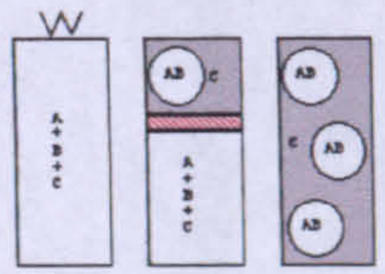

Powder fines
TiB_2 (1:1.88)
Fe(Cr) FeTi
FeB Fe_2B
Cr_2Ti

TiB_2 loss

TiC size = sub-6μm
Vol. Fraction = 64%

Feedstock powder
TiB_2 (1:2.37)
Fe(Cr) FeTi
FeB Fe_2B
Cr_2Ti

HVOF spraying

O_2

O_2 reacts with liquid to form oxides, and removes C

TiB_2 dissolution

Coating
TiB_2 (1:1.86)
Fe(Cr) FeTi
FeB Fe_2B
$FeTiO_3$ Ti_2O_3
Cr_2Ti

TiC size = sub-6μm
Vol. Fraction = 52%

TiB_2 bounce-off

Figure 9.5: Schematic diagram of the various stages of TiB_2-based cermet powder and coating production

10 Conclusion

This study aimed to produce, characterise, and evaluate the oxidation and abrasive wear properties of four HVOF sprayed coatings. The four coatings, three TiC-based and one TiB_2-based, were sprayed from cermet powders produced via SHS reaction from elemental Fe, Cr, Ti and C or B powders. Each TiC-based composition contained differing C:Ti ratios in order to change the properties. The coatings were wear tested using the dry sand rubber wheel (DSRW) abrasive wear tester and were compared with coatings produced from commercially available coatings, namely WC-17%Co and 25%NiCr-Cr_3C_2. The coatings were then subjected to high temperature oxidation tests for 100 hours at 500°C, 700°C and 900°C. The following conclusions were made:

10.1 SHS reactions

- SHS reaction of the four cermets were successful.
- The highest combustion temperature was achieved by the TiB_2-based cermet, followed by equimolar, excess C and finally excess Ti, titanium carbide-based materials.
- Varying the C:Ti ratio of the starting powder changed the microstructure and thus the wear resistance of the coatings.

10.2 Feedstock powders

- The TiC-based powders exhibited a spherical-like hard phase, while the TiB_2-based powder was more angular.

- The equimolar powder contained the highest volume fraction of hard phase, followed by excess C powder, TiB_2-based powder and finally the excess Ti powder.
- The TiC-based powders exhibited the same hard phase size range, whilst the hard phase in the TiB_2-based powder exhibited a smaller size range.
- The phases present in the equimolar and excess C feedstock powders were TiC, an iron-based phase, to which chromium was mainly partitioned, and small quantities of FeTi and Cr_7C_3. It is also believed that the excess Ti feedstock powders contained TiC, Fe_2Ti, FeTi and Cr_2Ti, and the TiB_2 feedstock powders contained TiB_2, an iron-based matrix, FeB, Fe_2B, Cr_2Ti and FeTi.
- The planned C:Ti ratios of the carbides in the TiC-based powders were not reflected in the calculations from the XRD traces. In fact, the ratios of the three powders were almost identical. This is in conflict with the different appearance of the hard phase in the excess Ti powders, and the differing peak intensities of the TiC in the excess Ti XRD traces. It is proposed that there may be discrepancies in the C:Ti ratio calculations.

10.3 Coating characterisation

- For both TiC and TiB_2 systems, microstructure, and oxidation and wear performance of the HVOF sprayed coatings depended upon the powder characteristics.

- The TiB_2-based coating exhibited the highest volume fraction of hard phase, followed by the equimolar coating, excess C coating, and finally the excess Ti coating. The volume fractions in all four coatings were lower than that in the powders and is thought to be due to dissolution of the hard phase during spraying. The high volume fraction of hard phase present in the TiB_2-based coating is due to the large free energy of formation of TiB_2, which limits dissolution and drives the re-precipitation of the hard phase during cooling.
- The hard phase size range for all coatings were the same as the relevant feedstock powders, but in different proportions.
- XRD analysis indicates that the equimolar and excess C coatings contain TiC, Fe(Cr), FeTi, $FeTiO_3$, Ti_2O_3, Cr_2Ti and Cr_7C_3. Free C is also thought to be present in the excess C coating but was not evident in the XRD trace as it is amorphous. The excess Ti coating contained all of the phases present in the equimolar and excess C coatings, apart from Cr_7C_3, but also contained Fe_2Ti intermetallic. The TiB_2-based coating exhibited the same phases present in the powder along with two oxides, namely $FeTiO_3$ and Ti_2O_3.

10.4 Abrasive wear properties of coatings

- Of the four coatings produced, the TiB_2-based coating exhibited superior properties when subjected to abrasion with alumina and silica. This is due to TiB_2 being harder than TiC, the larger volume fraction of hard phase

present in the TiB_2-based coating than the TiC-based coatings, and the bi-modal distribution of hard phase in the TiB_2-based coating.

- Of the TiC-based coatings, the equimolar coating exhibited superior properties when subjected to abrasion with alumina and is thought to be mainly due to the larger volume fraction of hard phase present and the different C:Ti ratios of the TiC. When subjected to abrasion with silica, the excess Ti coating exhibited superior wear properties and is thought to be due to the good carbide retention in the coating and may be a result of the low C:Ti ratio.
- The abrasive properties of the four coatings were compared with coatings produced from commercially available cermet powders. In terms of mass loss, the TiB_2-based coating exhibited the best wear resistance when subjected to both alumina and silica. When the wear results were presented in terms of volumetric loss, the WC-Co sample exhibited the best wear resistance when subjected to both alumina and silica.
- It is evident from the wear results that coatings produced from the SHS combustion method have comparable if not better wear properties to those produced from sintered and crushed, and blended powders of a commercially available NiCr-Cr_3C_2 system.

10.5 Oxidation properties of coatings

- At 500°C, all four coatings showed little sign of oxide build-up at the surface and there were no signs of microstructure change. At 700°C,

oxide layers were present on all four coatings but no change in microstructure was evident. At 900°C, only the equimolar and TiB_2-based coatings were examined and it was evident that significant oxidation had taken place and that the oxide layers were detached from the coatings. The equimolar coating showed signs of microstructure changes in the form of black-stringer-like features, whilst the TiB_2-based coating exhibited no changes in microstructure.

- The excess Ti coating exhibited the best oxidation resistance and may be due to the large proportion of oxide already present and may have formed an impermeable layer. This is only a preliminary theory and requires further examination.

11 Future work

The main topics for future work are recommended as follows:

- It was pointed out in this work that a martensitic matrix would not be formed in the excess C powder or coating despite the high carbon level present in the reaction mixture. This was due to the high levels of chromium present. It is therefore proposed that nickel be added to the reaction mixture as it opens the γ-loop and may allow the formation of martensite from the austenite during cooling.
- A full analysis of the coating properties must be addressed, such as the adhesive strength between the coating and the substrate, and the cohesive strengths of the splats in the coating.
- Further work needs to be done on the oxidation properties of the coatings, such as the oxidation rate of each coating at different temperatures.
- A study of the wear behaviour of the coatings at elevated temperatures must also be addressed, as this is the environment for which these coatings were produced.
- A study of the feasibility of large-scale production of the cermet powders for thermal spraying may also be required.

Acknowledgements

The author wishes to thank:

Dr P. H. Shipway for his advice and encouragement throughout this work.

The University of Nottingham for the funding they provided for the duration of study.

Prof. D.G. McCartney, Dr P. D. Brown and Dr A. Horlock for their advice and help.

The staff of the Wolfson building for the training and guidance they provided.

Dr R. Nixon at London and Scandinavian Metals Co. Ltd. for providing equipment.

His family for their continual love and support.

References

Advani, A.H., Thadhani, I.N., Grebe, H.A., Heaps, R. and Coffin, C., Dynamic Modelling of Material and Process Parameter Effects on Self-propagating High-Temperature Synthesis of Titanium Carbide Ceramics, Chapman and Hall, (1992) 3309-3317.

Agarwal A. and Dahorte B., Characterisation of Tribological Behaviour of Composite Boride Coating Deposited on Steel using Lazer Surface Engineering, Elevated Temperature Coatings: Science and Technology III, (1999), 273-284.

Agarwal, A. and Dahotre, N.B., Synthesis of Boride Coating on Steel using High Energy Density Processes: Comparative Study of Evolution of Microstructure, Materials Characterization, 42 (1999) 31-44.

Agarwal, A., Katipelli, L.R. and Dahotre, N.B., Elevated Temperature Oxidation of Laser Surface Engineered Composite Boride Coating on Steel, Metallurgical and Materials Transactions A, 31A (2000) 461-473.

Alison, P.J. and Wilman, H., The Different Behaviour of Hexagonal and Cubic Materials in their Friction, Wear and Work Hardening During Abrasion, British Journal of Applied Physics, vol. 15 (1964) 281-289.

Ananthapadmanabhan, P.V. and Taylor, P.R., Titanium Carbide-Iron Composite Coatings by Reactive Plasma Spraying of Ilmenite, Journal of Alloys and Compounds, 287 (1999) 121-125.

Andrievski R. A., Mechanical Properties of TiB_2 Wear Resistant Materials, Proceedings of Powder Metallurgy World Congress 8, June 1992, San Francisco, California, USA, pp. 293-298.

Askeland, D.R., The Science and Engineering of Materials, Third Edition, Chapman and Hall, London, 1996.

Avery, H.S., The Measurement of Wear Resistance, Case Report 340-10, Dept. Report 9-AE-134, American Brake Shoe Company (1961).

Azatyan, T.S., Mal'tsev, V.M., Merzhanov, A.G. and Seleznev, V.A., Spectral-Optical Investigation of the Mechanism of the Combustion of Mixtures of Titanium and Carbon, Combust. Explos. Shock Waves USSR, 13 (1977) 156-158.

Bandyopadhyay, D., Sharma, R.C. and Chakraborti, N., The Ti-Cr-C (Titanium-Chromium-Carbon) System, Journal of Phase Equilibria, 20(3) (1999) 325-331.

Barandika, M.G., Echeberria, J.J., Sanchez, J.M. and Castro, F., Oxidation Resistance and Microstructure of the Oxide Layers for TiB_2-based Cermets, Journal of Materials Chemistry, 8(8) (1998) 1851-1857.

Barandika, M.G., Echeberria, J.J. and Castro, F., Oxidation Resistance of Two TiB_2-based Cermets, Materials Research Bulletin, 34(7) (1999) 1001-1011.

Bartuli, C., Smith, R.W. and Shtessel, E., SHS Powder for Thermal Spray Applications, Ceramics International, 23 (1997) 61-68.

Berger, L.-M., Hermel, W., Vuoristo, P., Mantyla, T., Lengauer, W. and Ettmayer, P., Structure, Properties and Potentials of WC-Co, Cr_3C_2-NiCr and TiC-Ni-Based Hardmetal-like Coatings, Thermal Spray: Practical Solutions for Engineering Problems, C. C. Berndt (Ed.), ASM International, OH, USA (1996) 89-96.

Berger, L.-M., Vuoristo, P., Mantyla, T. and Gruner, W., A Study of Oxidation Behaviour of WC-Co, Cr_3C_2-NiCr and TiC-Ni-based Materials in Thermal Spray Processes, 15th International Thermal Spray Conference, Nice, France, May (1998) 75-82.

Bhaumik, S.K., Divakar, C., Singh, A.K. and Upadhyaya, G.S., Synthesis and Sintering of TiB_2 and TiB_2-TiC Composite Under High Pressure, Materials Science and Engineering, A279 (2000) 275-281.

Bhushan, B. and Gupta, B.K., Handbook of Tribology: Materials, Coatings, and Surface Treatments, Krieger Publishing Company, Floride, (1997).

Birks, N. and Meier, G.H., Introduction to High Temperature Oxidation of Metals, Edward Arnold, London, (1983).

Capaldi, M.J. and Wood, J.V., Production and Characterisation of TiC-Containing Materials by Self-Propagating High-Temperature Synthesis, Journal of Materials Synthesis and Processing, 4(4) (1996) 245-253.

Capaldi, M.J., Saidi, A. and Wood, J.V., Reaction Synthesis of TiC and Fe-TiC Composites, ISIJ International, 37(2) (1997) 188-193.

Champagne, B. and Dallaire, S., Plasma Spray Synthesis of TiB_2-Fe Coatings, Journal of Vacuum Science Technology, A3 (6) (1985) 2373-2377.

Chang, D.K., Won, C.W., Chun, B.S. and Shim, G.C., Purifying Effects and Product Microstructure in the Formation of TiC Powder by the Self-Propagating High-Temperature Synthesis, Metallurgical and Materials Transactions B, 26B (1995) 176-179.

Chawla, S.L. and Gupta, R.K., Materials Selection for Corrosion Control, ASM International, OH, USA (1993).

Choi Y and Rhee S, Equilibirum in the Reaction of Ti and C to form Substoichiometric TiC_x, Journal of Materials Letters, 13 (1994) 323-325.

Cutler R. A., Engineering Properties of Borides, Engineering Materials Handbook: Ceramic and Glasses, 4 (1991), 787-803.

Department of Trade and Industry, Wear Resistant Surfaces in Engineering, London, HMSO, (1986).

Dorfman, M.R., Kushner, B.A., Nerz, J. and Rotolico, A.J., A Technical Assessment of HVOF, 12th International Conference on Thermal Spraying, The Welding Institute, London, UK, 17 (1988) 291-302.

Dunmead, S.D., Readey, D.W. and Semler, C.E., Kinetics of Combustion Synthesis in the Ti-C and Ti-C-Ni Systems, Journal of American Ceramics Society, 72(12) (1989) 2318-2324.

Eustathopoulos, N., Chatain, D. and Coudurier, L., Wetting and Interfacial Chemistry in Liquid Metal-Ceramic Systems, Materials Science and Engineering, A135 (1991) 83-88.

Evans, A.V., The Science of Ceramic Machining and Surface Finishing II, National Bureau of Standards Sp., Pub. 562, US Government Printing Office, (1979) 1-14.

Eyre, T.S., Wear Characteristics of Metals, Tribology International, 10 (1976) 203-212.

Fan, Q., Chai, H. and Jin, Z., Microstructural Evolution in the Combustion Synthesis of Titanium Carbide, Journal of Materials Science, 31 (1996) 2573-2577.

Fan, Q., Chai, H. and Jin, Zhihao, Role of Iron Addition in the Combustion Synthesis of TiC-Fe Cermet, Journal of Materials Science, 32 (1997) 4319-4323.

Goetzel, C.G., Cermets, ASM Hanbook, (1991) 798-815.

Gilles, C.S. and Daillaire, S, 3rd National Thermal Spray Conference, Long Beach, CA, USA, May (1990), 761-765.

Grebe, H.A., Advani, A., Thadhani, N.N. and Kottke, T., Combustion Synthesis and Subsequent Explosive Densification of Titanium Carbide Ceramics, Metallurgical Transactions A, 23A (1992) 2365-2372.

Halling, J., Principles of Tribology, MacMillan Press Ltd., (1975).

Halling, J., Introduction to Tribology, Wykeham Publications Ltd., London, (1976).

Harvey, D., The Tough Truth – Wear-resistant Coatings using High Velocity Oxy-Fuel, Industrial Lubrication and Tribology, vol. 48, 2 (1996) 11-16.

Herman, H. and Sampath, S., Thermal Spray Coatings, Metallurgical and Ceramic Protective Coatings, London, Chapman & Hall, (1996) 274-289.

Holleck H, Material Selection for Hard Coatings, Journal of Vacuum Science Technology, A4 (6), Nov/Dec (1986), 2661-2669.

Holt, J.B., Kingman, D.D. and Bianchini, G.M., Kinetics of the Combustion Synthesis of TiB_2, Materials Science and Engineering, 71 (1985) 321-327.

Holt, J.B., Self-Propagating High-Temperature Synthesis, Engineered Metals Handbook, Volume 4: Ceramics and Glasses (1991), ASM International.

Honeycombe, R.W.K and Bhadeshia, H.K.D.H., Steels: Microstructure and Properties, Second Edition, Edward Arnold, London, 1995.

Hutchings, I.M., Tribology: Friction and Wear of Engineering Materials, Edward Arnold, London, (1992).

Jarosinski, W.J., Gruninger, M.F. and Londry, C.H., Characterization of Tungsten Carbide Cobalt Powders and HVOF Coatings, National Thermal Spray Conference, Anaheim, USA (1993) 153-157.

Kato, K., Wear Mode Transitions, Scripta Metall., Vol. 24 (1990) 815-820.

Kaye, G.W.C and Laby, T.H., Tables of Physical and Chemical Constants, Longman, London, (1972).

Kecskes, L.J., Kottke, T. and Niile, A., Microstructural Properties of Combustion-Synthesized and Dynamically Consolidated Titanium Boride and Titanium Carbide, Journal of American Ceramic Society, 73(5) (1990) 1274-1282.

Kogan, Y.D., Sereda, B.P. and Kostogorov, E.P., Preparing Boronized Coatings under the Conditions of Self-propagating High-temperature Synthesis, Metal Science and Heat Treatment, 38(1-2) (1996) 20-22.

Kosolapova, T. Ya., Carbides: Properties, Production and Applications, Plenum Press, New York, (1971).

Krepski, R. E., Thermal Spray Coating Applications in the Chemical Process Industries, MTI, St. Louis, USA (1993).

Kubarsepp, J., Klaasen, H. and Pirso, J., Behaviour of TiC-base Cermets in Different Wear Conditions, Wear, 249 (2001) 229-234.

Lansdown, A.R. and Price, A.L., Materials to Resist Wear: A Guide to their Selection and Use, Pergamon Press, Oxford, (1986).

Laul, K. and Dorfman, M., New Chromium Carbide-Nickel Chrome Materials for High Temperature Wear Applications, Thermal Spray: Surface Engineering via Applied Research, ASM International, Ohio, USA, (2000) 561-566.

Lawn, B.R. and Swain, M.V., Journal of Materials Science, 10, (1975) 113-122.

Lee, W-C. and Chung, S-L., Ignition Phenomena and Reaction Mechanisms of the Self-Propagating High-Temperature Synthesis Reaction in the Ti+C System, Journal of Materials Science, 30 (1995) 1487-1494.

Liao, P. K. and Spear, K. E., Boron-Iron Binary Phase Diagram, Binary Alloy Phase Diagrams, 351-356.

Liao H., Normand, B. and Coddet, C., Influence of Coating Microstructure on the Abrasive Wear Resistance of WC/Co Cermet Coatings, Surface and Coatings Technology, 124 (2000) 235-242.

Macdonald, N.F. and Ransley, C.E., The Oxidation of Hot-pressed Titanium Carbide and Titanium Boride in the Temperature Range 300-1000°C, Powder Metallurgy, 3 (1959) 172-176.

Mantyla, T.A., Niemi, K.J., Vuoristo, P., Barbezat, G. and Nicola, A.R., Abrasion Wear Resistance of Tungsten Carbide Coatings Prepared by Various Thermal

Spraying Techniques, 2nd Plasma-Technik Symposium, Lucerne, Switzerland, 1 (1991) 287-297.

Mohanty, M. and Smith, R.W., Plasma Spray Processing of TiC-Reinforced Coatings for Wear Protection, 8th National Thermal Spray Conference, Houston, TX, USA, September (1995) 561-566.

Moore, M.A., Materials in Engineering Applications 1, (1978) 97-111.

Moore, M.A., Fundamentals of Friction and Wear of Materials, Rigney, D.A. (Ed.), ASM, (1981) 73-118.

Morozova, M.P., Khiripun, M.K. and Ariya, S.M., Enthalpy of Formation of Titanium Carbides and Oxycarbides, Journal of Gen. Chem., 32(7) (1962) 2050.

Murakami, Y., Kimura, H. and Nishimura, Y., An Investigation on the Titanium-Iron-Carbon System (3rd Report), Journal of the Japan Institute of Metals, 21 (1957) 712-716.

Murray, J.L., Fe-Ti (Iron-Titanium) Phase Diagram, Binary Alloy Phase Diagrams, 1117-1119.

Murray, J. L., Liao, P. K. and Spear, K. E., Boron-Titanium Binary Phase Diagram, Binary Alloy Phase Diagrams, 387-392.

Nicoll, A.R., Gruner, H., Prince, R. and Wuest, G., Thermal Spray Coatings for High Temperature Protection, Surface Engineering, 1 (1985) 59-71.

Pawlowski, L., The Science and Engineering of Thermal Spray Coatings, John Wiley, (1995).

Ramberg, J.R. and Williams, W.S., High Temperature Deformation of Titanium Diboride, Journal of Materials Science, 22 (1987) 1815-1826.

Ramqvist, L., Wetting of Metallic Carbides by Liquid Copper, Nickel, Cobalt and Iron, International Journal of Powder Metallurgy, 1(4) (1965) 2-21.

Rogachev, A.S., Mukas'yan, A.S. and Merzhanov, A.G., Dokl. Phys. Chem. (English Translation), 297 (1987) 1240.

Rohatgi, P.K., Liu, Y. and Ray, S., Friction and Wear of Metal-Matrix Composites, University of Wisconsin, Milwaukee, USA, (1991) 801-811.

Roy, S.K., Biswas, A. and Banerjee, S., Self-propagating High-temperature Synthesis of Titanium Borides, Bulletin of Materials Science, 16(5) (1993) 347-356.

Saidi, A., Chrysanthou, A., Wood, J.V. and Kellie, J.L.F., Characteristics of the Combustion Synthesis of TiC and Fe-TiC Composites, Journal of Material Science, 29 (1994) 4993-4998.

Saidi, A., Chrysanthou, A., Wood, J.V. and Kellie, J.L.F., Preparation of Fe-TiC Composites by the Thermal-Explosion Mode of Combustion Synthesis, Ceramics International, 23 (1997) 185-189.

Scussel, H.J. and Valentine, G.T.E., Friction and Wear of Cemented Carbides, Volume 18: Friction, Lubrication, and Wear Technology, ASM Handbook, (1991) 795-800.

Shaffer, P.T.B., Engineering Properties of Carbides, 804 – 811.

Smith, R.W., Harzenski, E. and Robisch, T., High Velocity Oxy-Fuel Spray Wear Resistant Coatings of TiC Composite Powders, 3rd National Thermal Spray Conference, Long Beach, CA, USA, 20-25 May (1990) 617-623.

Smith, R.W., Mutasim, Z., Lugscheider, E., Limbach, R., Jungklaus, H., Roos, J., Celis, J.P., DeBonte, M. and Economou, S., Wear Test Characterization of TiC Reinforced Thermal Spray Coatings, 4th National Thermal Spray Conference, Pittsburgh, PA, USA, 4-10 May (1991) 59-66.

Smith, R.W., Mohanty, M., Stessel, E. and Verstak, A., Self Propagating High Temperature Synthesis (SHS) of Thermal Spray Powders, International Thermal Spray Conference, Kobe, Japan, (1995) 1121-1126.

Sobolev, V.V. and Guilemany, J.M., Oxidation of Coatings in Thermal Spraying, Materials Letters, 37 (1998) 231-235.

Somaraju, K.R.C., Srinivasarao, D, Sivakumar, D., Sen, D., Rao, G.V.N. and Sundararajan, G., The Influence of Powder Characteristics on the Properties of Detonation Sprayed Cr_3C_2-25NiCr Coatings, Thermal Spray: Surface Engineering via Applied Research, ASM International, Ohio, USA, (2000) 309-316.

Stachowiak, G.W., Particle Angularity and its Relationship to Abrasive and Erosive Wear, Wear, 241 (2000) 214-219.

Steffens, H.D. and Nassenstein, K., Thermal Spraying : A Review of 1993, vol. 25, 6 (1993) 280-284.

Steinhauser, S., Wielage, B., Hofmann, U., Schnick, Th., Ilyuschenko, A. and Azarova, T., Plasma-sprayed Wear-resistant Coatings with Respect to Ecological Aspects, Surface and Coatings Technology, 131 (2000) 365-371.

Stewart, D., Studies on the Abrasive Wear Behaviour of HVOF WC-Co Coatings, Ph.D. Thesis, University of Nottingham, UK, (1998).

Stewart, D., Abrasive Wear Behaviour of Conventional and Nanocomposite HVOF-sprayed WC-Co Coatings, Wear, 225-229 (1999) 789-798.

Sturgeon, A., Thermal Spraying Gives a New Look to Substrate Design, Bulletin 4, The Welding Institute, London, UK, 35 (1994) 84-87.

Tan, J.C., Looney, L. and Hashmi, M.S.J., Component Repair Using HVOF Thermal Spraying, Journal of Materials Processing Technology, 92-93 (1999) 203-208.

Tanaka, K. and Saito, T., Phase Equilibria in TiB_2-Reinforced High Modulus Steel, Journal of Phase Equilibria, 20(3) (1999) 207-214.

Tjong, S.C. and Lau, K.C., Abrasion Resistance of Stainless-Steel Composites Reinforced with Hard TiB_2 Particles, Composite Science and Technology, 60 (2000a) 1141-1146.

Tjong, S.C. and Lau, K.C., Abrasive Wear Behaviour of TiB_2 Particle-Reinforced Copper Matrix Composites, Materials Science and Engineering, A282 (2000b) 183-186.

Tondu, S., Schnick,T., Pawlowski, L., Wielage, B., Steinhauser, S. and Sabatier, L., Laser Glazing of FeCr-TiC Composite Coatings, Surface and Coatings Technology, 123 (2000) 247-251.

Tylczak, J.H., Abrasive Wear, ASM Handbook, (1991) 184-190.

Vadchenko, S.G., Grigor'ev, Y.M. and Merzhanov, A.G., Combust. Explos. Shock Waves (English Translation), 12 (1976) 606.

Valente, T. and Bartuli, C., Thermal sprayed hard Cr_3C_2-NiCr coatings for wear protection, Thermal Spray 2001: New surfaces for a new millennium, ASM International, Ohio, USA, (2001) 1075-1084.

Varma, A. and Lebrat, J.P., Chem. Eng. Sci., 47(9) (1992) 2179.

Subrahmanyam, J. and Vijayakumar, M., Journal of Material Science , 27 (1992) 6249.

Verstak, A., Vitiaz, P., Lugscheider, P., Remer, P., Smith, A.R., Beljaev, A., Talako, T., Azarova, T. and Koval, V., New Coatings for Elevated Temperature Erosion Application, Thermal Spray Conference, DVS 175 (1996) 71-75.

Vitiaz, P., Verstak, A., Azarova, T. and Talako, T., Titanium Carbide in Wear Resistant Coatings, Thermal Spray: Practical Solutions for Engineering Problems, Berndt, C.C.{Ed.), ASM International, OH, USA, (1996) 169-176.

Voitovich, V.B., Mechanism of the High Temperature Oxidation of Titanium Carbide, High Temperature Materials and Processes, 16(4) (1997) 243-253.

Vuoristo, P., Stenberg, T., Mantyla,T., Bereger, L.-M. and Nebelung, M., Microstructure and Properties of Thermally Sprayed TiC-Ni and (Ti,Mo)C-NiCo Coatings, Thermal Spray: Practical Solutions for Engineering Problems, C.C. Berndt (Ed.), ASM International, OH, USA (1996) 729-734.

Wirojanupatump, S. and Shipway, P.H., Abrasion of Mild Steel in Wet and Dry Conditions with the Rubber and Steel Wheel Abrasion Apparatus, Wear, 239 (2000) 91-101.

Wirojanupatump, S., Characterisation and Wear Performance of HVOF sprayed Cr_xC_y-NiCr Coatings, Ph.D. Thesis, University of Nottingham, UK, (1999).

Wirojanupatump, S., Shipway, P.H. and McCartney, D.G., The Influence of HVOF Powder Feedstock Characteristics on the Abrasive Wear Behaviour of Cr_xC_y-NiCr Coatings, Wear, 249 (2001) 829-837.

Yen C. F., Yust C. S. and Clark G. W., Enhancement of Mechanical Strength in Hot-pressed TiB_2 Composites by the Addition of Fe and Ni, Proceedings of TMS-AIME, New Developments and Applications in Composites, St Louis, Missouri, (1978), 317-330.

Yi, H.C. and Moore, J.J., J. Mater. Sci., 25 (1990) 1159.

Zimmermann, S. and Kreye, H., Chromium Carbide Coatings Produced with Various HVOF Spray Systems, Thermal Spray: Practical Solutions for Engineering Problems, ASM International, Ohio, USA, (1996) 147-152.

Appendix A

In order to calculate the volume wear coefficients of the wear results from the mass wear coefficients, the average density of the cermets must be estimated. This value can be calculated using the volume fraction or mass fraction of the matrix and hard phase.

Assuming the cermet contains only two phases (i.e. no oxides), namely, matrix (e.g. Fe and Cr), A, and hard phase, B (e.g. TiC).

Calculating from the volume fractions of the phases:

Volume of A = $v_A.m^3$

Volume of B = $v_B.m^3$

Total volume, $V = v_A + v_B$

Therefore,

Volume fraction of A = $\frac{v_A}{V}$

Volume fraction of B = $\frac{v_B}{V}$

Mass of A = $v_A.\rho_A$

Mass of B = $v_B.\rho_B$

Total mass = $v_A.\rho_A + v_B.\rho_B$

Therefore,

$$\text{Average density} = \frac{v_A.\rho_A + v_B.\rho_B}{v_A + v_B}$$

$$= \frac{v_A.\rho_A + v_B.\rho_B}{V}$$

$$= \frac{v_A}{V}.\rho_A + \frac{v_B}{V}.\rho_B$$

Calculating from the mass fractions of the phases:

Mass of A = m_A

Mass of B = m_B

Total mass, M = $m_A + m_B$

Therefore,

$$\text{Mass fraction of A} = \frac{m_A}{M}$$

$$\text{Mass fraction of B} = \frac{m_B}{M}$$

$$\text{Volume of A} = \frac{m_A}{\rho_A}$$

$$\text{Volume of B} = \frac{m_B}{\rho_B}$$

$$\text{Total volume} = \frac{m_A}{\rho_A} + \frac{m_B}{\rho_B}$$

Therefore,

$$\text{Average density} = \frac{(m_A + m_B)\rho_A\rho_B}{m_A\rho_B + m_B\rho_A}$$

$$\frac{1}{\text{Av.density}} = \frac{m_A\rho_B + m_B\rho_A}{(m_A + m_B)\rho_A\rho_B}$$

$$= \frac{\text{mass fraction A}}{\rho_A} + \frac{\text{mass fraction B}}{\rho_B}$$

Now that the average density has been established the volume losses can be calculated by dividing the mass loss of the coatings during wear testing by the average density. The wear rate can subsequently be calculated by dividing this figure by the total distance travelled.

$$\text{Volume loss} = \frac{mass\ loss}{average\ density}$$

$$\text{Wear rate} = \frac{volume\ loss}{wear\ distance}$$

The wear coefficient can then be calculated by dividing the wear rate by the applied force.

$$\text{Wear coefficient} = \frac{wear\ rate}{applied\ force} = \frac{mm^3.m^{-1}}{N}$$